

WATER DYNAMICS IN SOFT CONFINEMENT  
- NEUTRON SCATTERING INVESTIGATIONS ON REVERSE MICELLES -



Vom Fachbereich Physik  
der Technischen Universität Darmstadt

zur Erlangung des Grades  
eines Doktors der Naturwissenschaften  
(Dr. rer. nat.)

genehmigte Dissertation von  
DIPL.-PHYS. TINKA LUISE SPEHR  
geboren in Albany, USA

Darmstadt 2010  
D17

Referent: Prof. Dr. Bernd Stühn  
Korreferent: Prof. Dr. Michael Vogel

Tag der Einreichung: 14.12.2009  
Tag der Prüfung: 25.01.2010

WATER DYNAMICS IN SOFT CONFINEMENT:  
NEUTRON SCATTERING INVESTIGATIONS ON REVERSE MICELLES

**Abstract:** In the present experimental study we investigate the dynamical behaviour of water in soft confinement. As a model system we choose the AOT (sodium bis[ethylhexyl] sulfosuccinate) based water-in-oil droplet microemulsion which we pre-characterize in detail. Using small angle neutron scattering we determine the microemulsion structure as a function of composition. Spherical water droplets (reverse micelles) coated by a monomolecular layer of the surfactant are dispersed in the continuous oil matrix. By variation of the molar ratio of water to surfactant one may control the droplet size between a few Ångström and several nanometers. We extend the phase diagram to temperatures far below the freezing point of bulk water to determine the range of structural stability of the droplets as a function of water loading. The supercooling of the confined water is investigated by means of elastic fixed window scans on neutron backscattering. The freezing point of the confined water as well as the lower stability temperature decrease with decreasing droplet size. Moreover we use neutron-spin-echo spectroscopy to measure droplet diffusion and form fluctuations, whereof we deduce the temperature dependency of the bending modulus of the surfactant shell. The influence of confinement on the water mobility is then studied using two systems with different droplet sizes. We access the water dynamics over three orders of magnitude from pico- to nanoseconds by the combination of neutron backscattering and time-of-flight spectroscopy. We analyze the data taking into account rotation and jump diffusion. We find the water diffusion inside the droplets on average to be considerably slowed down with respect to bulk water. The translational mobility further decreases with decreasing droplet size. We extract values for rotational and translational diffusion coefficients. Dependent on water loading, two dynamically separated water fractions inside the droplets are resolved, one probably corresponding to surfactant bound water and the other one corresponding to less hindered water in the middle of the droplet core. We determine the absolute number of tightly bound water molecules per AOT molecule.

**Keywords:** Neutron Scattering (61.05.fg), Microemulsions (47.57.jb), Interfacial properties of microemulsions (68.05.Gh), Diffusion of water (66.30.jj), Neutron spectroscopy (29.30.Hs)



**Zusammenfassung:** In der vorliegenden experimentellen Studie untersuchen wir das dynamische Verhalten von Wasser in weicher eingeschränkter Geometrie. Die Eigenschaften von geometrisch eingeschlossenem Wasser sind außer für das grundsätzliche Verständnis auch in Bereichen der biologischen, pharmazeutischen oder chemischen Anwendung von Bedeutung. Als Modellsystem wählen wir eine auf dem anionischen Tensid AOT (sodium bis[ethylhexyl] sulfosuccinate) basierte Wasser-in-Öl Mikroemulsion in der Tröpfchenphase, die wir ausführlich vorher charakterisieren. Anhand von Neutronenkleinwinkelstreuung bestimmen wir die Struktur in Abhängigkeit von Konzentration der Komponenten. Sphärische Wasserkerne sind umschlossen von einer monomolekularen Schicht des Tensids; diese sogenannten Wasser-geschwollenen inversen Mizellen sind in einer kontinuierlichen Ölmatrix dispergiert. Wir bestätigen, dass der Radius des Wasserkerns durch geeignete Wahl der Zusammensetzung kontrolliert zwischen wenigen Ångström und einigen Nanometer variiert werden kann. Wir weiten das Phasendiagramm bis zu Temperaturen weit unterhalb des Gefrierpunktes von freiem Wasser aus und bestimmen den Stabilitätsbereich der Tröpfchenphase ihrer Größe. Die Unterkühlbarkeit der Wasserkerne wird anhand von elastischen Temperatur-Scans mit Neutronenrückstreuung untersucht. Sowohl der Gefrierpunkt des eingesperreten Wassers, als auch die untere Stabilitätstemperatur der Tröpfchen liegen umso tiefer, je kleiner die Tröpfchen bei Raumtemperatur sind. Weiterhin nutzen wir Neutronen-Spin-Echo Spektroskopie, um die Diffusion der gesamten Tröpfchen und deren Schalenfluktuation zu messen, und daraus die Temperaturabhängigkeit des Biegemoduls der Tensidmembran zu bestimmen. Den Einfluß der Einschränkung auf die Mobilität des Wassers testen wir anhand von zwei Systemen mit Tröpfchen unterschiedlicher Größe. Die Kombination von Neutronenrückstreu- und Flugzeitspektroskopie lässt uns die Wasserdynamik über drei Größenordnungen von Piko - bis Nanosekunden verfolgen. Die simultane Analyse der kombinierten Daten mit einem Rotations-Sprungdiffusions-Modell zeigt, dass die Wassertranslation innerhalb aller Mizellen im Mittel stark verlangsamt ist und mit kleiner werdendem Radius der Mizellen abnimmt. Wir bestimmen Rotations- und Translations-Diffusionskonstanten des Wassers. In Abhängigkeit der Tröpfchengröße sind zwei dynamisch separierbare Wasserfraktionen auflösbar, wobei die langsamere vermutlich Tensid-gebundenem Wasser entspricht.

**Stichwörter:** Neutronenstreuung (61.05.fg), Mikroemulsionen (47.57.jb), Mikroemulsionsgrenzflächen (68.05.Gh), Wasserdiffusion (66.30.jj), Neutronenspektroskopie (29.30.Hs)



---

DYNAMIQUE DE L'EAU SOUS CONFINEMENT SOUPLE:  
MICELLES INVERSES ETUDIÉES PAR DIFFUSION DES NEUTRONS

**Resumé:** Dans le cadre de cette thèse expérimentale, nous avons étudié le comportement de l'eau sous confinement souple. Comme système modèle nous avons choisi une microémulsion de type "eau-dans-huile" que nous avons caractérisé en détail. Nous avons déterminé la structure du système en fonction de la composition par diffraction des neutrons aux petits angles. L'eau se trouve dans le coeur sphérique de micelles inverses entourée d'une couche monoatomique d'agent tensioactif AOT (sodium bis[ethylhexyl] sulfosuccinate). Ces gouttelettes (les micelles) sont dispersées dans l'huile. Nous avons observé que la variation du rapport eau / AOT permet de régler le rayon du coeur d'eau de quelques Ångströms à plusieurs nanomètres. Le diagramme des phases a été élargi aux températures inférieures au point de congélation de l'eau afin de définir la gamme de stabilité des gouttelettes en fonction de leur taille. La surfusion de l'eau a été mesurée à l'aide de mesures par balayage élastique sur spectromètre à rétrodiffusion des neutrons. Moins les gouttelettes contiennent d'eau plus le point de congélation ainsi que la température minimale de stabilité des micelles sont diminués. De plus, nous avons utilisé la spectroscopie à écho de spin pour mesurer la diffusion des gouttelettes dans la matrice d'huile et leurs fluctuations de forme. Nous en avons déduit la dépendance en température du module élastique de la couche d'AOT. Pour tester l'influence du confinement sur la mobilité de l'eau, nous avons préparé deux systèmes avec des gouttelettes de tailles différentes. Combinant les techniques par rétrodiffusion et par temps de vol des neutrons nous avons eu accès à la dynamique de l'eau sur trois décades de temps de relaxation (de la picoseconde à la nanoseconde). L'analyse simultanée des données avec un modèle de rotation et de translation par sauts a confirmé le ralentissement de la diffusion de translation moyenne de l'eau avec la diminution de la taille des gouttelettes. De plus, deux types de dynamique de l'eau ont été observés, l'une probablement relative à l'eau liée au surfactant et l'autre décrivant la diffusion libre dans le coeur. Enfin, les coefficients de rotation et de translation de l'eau confinée ont été extraits et le nombre absolu de molécules d'eau apparaissant liées a été déterminé.

**Mots clés:** Diffusion des neutrons (61.05.fg), Microémulsions (47.57.jb), Propriétés de l'interface dans microémulsions (68.05.Gh), Diffusion de l'eau (66.30.jj), Spectroscopie neutronique (29.30.Hs)





# Contents

<b>1. Introduction</b>	<b>1</b>
1.1. Reverse micelles as model system to study soft confined water . . . . .	1
1.2. Outline of the thesis . . . . .	4
1.3. Microemulsions . . . . .	5
1.3.1. AOT based w/o droplet microemulsion . . . . .	5
1.3.1.1. Surfactant: AOT . . . . .	5
1.3.1.2. Microemulsion: water/AOT/oil . . . . .	6
1.3.1.3. Sample preparation . . . . .	9
1.4. Water in reverse micelles - state of the research . . . . .	9
<b>2. Neutron scattering - theory and practice</b>	<b>13</b>
2.1. Theory . . . . .	13
2.1.1. Double differential cross section . . . . .	15
2.1.2. Differential cross section . . . . .	18
2.1.3. Coherent and incoherent scattering . . . . .	20
2.2. Experimental reality . . . . .	21
2.2.1. Neutron backscattering spectrometry (BS) . . . . .	21
2.2.1.1. Principle . . . . .	22
2.2.1.2. Instruments: IN10, IN16 and Basis . . . . .	24
2.2.1.3. Primary data corrections . . . . .	24
2.2.2. Neutron time-of-flight spectrometry (TOF) . . . . .	26
2.2.2.1. Principle . . . . .	26
2.2.2.2. Instrument: IN5 . . . . .	28
2.2.2.3. Primary data corrections . . . . .	28
2.2.3. Neutron-spin-echo spectrometry (NSE) . . . . .	29
2.2.3.1. Principle . . . . .	29
2.2.3.2. Instrument: IN15 . . . . .	32
2.2.3.3. Primary data corrections . . . . .	33
2.2.4. Neutron small angle scattering (SANS) . . . . .	34
2.2.4.1. Principle . . . . .	34
2.2.4.2. Instruments: D11 and D22 . . . . .	35

---

2.2.4.3. Primary data corrections . . . . .	35
2.2.5. Energy resolution . . . . .	37
2.2.6. The choice of the instrument . . . . .	38
<b>3. Structure of the pure microemulsion</b>	<b>39</b>
3.1. Core-shell model for the structure . . . . .	40
3.2. Experimental details . . . . .	43
3.3. Series 1: $\omega$ -variation . . . . .	44
3.3.1. Results and discussion . . . . .	45
3.4. Series 2: $\phi$ -variation . . . . .	48
3.4.1. Results and discussion . . . . .	49
3.5. Series 3: $T$ -variation . . . . .	51
3.5.1. Results and discussion . . . . .	51
3.5.1.1. Reversibility upon heating . . . . .	54
3.5.1.2. Pure AOT micelles . . . . .	56
3.5.1.3. Remaining water core at low temperatures . . . . .	58
3.6. Summary and conclusions . . . . .	59
<b>4. Freezing behavior of water in reverse micelles</b>	<b>61</b>
4.1. Experimental details . . . . .	61
4.2. Results and discussion . . . . .	63
4.2.1. Supercooling of confined water . . . . .	65
4.2.2. Relation between water freezing and droplet instability . . . . .	67
4.3. Summary and conclusions . . . . .	68
<b>5. Dynamics of microemulsion droplets</b>	<b>69</b>
5.1. Micelle shell fluctuations and diffusion measured by NSE . . . . .	69
5.1.1. Helfrich model for the bending energy of membranes . . . . .	70
5.1.1.1. Droplet shell fluctuations . . . . .	70
5.2. Experimental details . . . . .	73
5.3. Results and discussion . . . . .	74
5.3.1. Droplet translation and bending modulus . . . . .	74
5.4. Droplet diffusion measured by DLS . . . . .	79
5.4.1. Experimental . . . . .	79
5.4.2. Results . . . . .	80
5.5. Summary and conclusions . . . . .	81
<b>6. Dynamical behavior of water in reverse micelles</b>	<b>83</b>
6.1. Theoretical description of water motion . . . . .	83
6.1.1. Vibrations . . . . .	84

6.1.2.	Translational diffusion . . . . .	85
6.1.3.	Isotropic rotation . . . . .	86
6.1.4.	Total model function . . . . .	87
6.1.4.1.	Fit function . . . . .	88
6.1.5.	QENS studies of water in AOT based microemulsions . . . . .	89
6.2.	Experimental results . . . . .	92
6.2.1.	Experimental details . . . . .	94
6.2.2.	Outline of the data analysis . . . . .	96
6.2.3.	Short times - fast processes: IN5 . . . . .	96
6.2.3.1.	Rotational motion of water . . . . .	96
6.2.3.2.	Translational motion of water as resolved by IN5 . . . . .	99
6.2.4.	Longer times - slower processes: Basis and IN16 . . . . .	103
6.2.4.1.	Number of water molecules bound per AOT molecule . . . . .	103
6.2.4.2.	Two dynamically separated water fractions . . . . .	105
6.2.4.3.	Alternative models . . . . .	108
6.2.5.	Do we see signs of geometrical confinement? . . . . .	109
6.3.	Summary and conclusions . . . . .	111
<b>7.</b>	<b>Perspective: polymer loaded micelles</b>	<b>113</b>
7.1.	PEO in reverse water swollen AOT micelles . . . . .	113
7.2.	Experimental results . . . . .	114
7.2.1.	Experimental details . . . . .	114
7.2.2.	PEO effect on droplet structure . . . . .	115
7.2.3.	Droplet diffusion and bending modulus - NSE . . . . .	118
7.3.	Summary and conclusions . . . . .	121
<b>8.</b>	<b>Summary</b>	<b>123</b>
8.1.	Zusammenfassung . . . . .	127
<b>A.</b>	<b>Appendix</b>	<b>131</b>
A.1.	Sample preparation . . . . .	131
A.2.	Properties of toluene, heptane, decane and water . . . . .	132
A.3.	Self absorption corrections for BS and TOF data . . . . .	134
A.4.	Correction macro for IN5 data . . . . .	136
A.5.	Sticky hard sphere structure factor . . . . .	137
A.6.	SANS data and fits for $T$ -variation . . . . .	139
A.7.	TOF data and fits . . . . .	142
A.8.	Structural characterization of PEO <sub>3000</sub> . . . . .	146
	<b>Bibliography</b>	<b>149</b>



# 1. Introduction

Water is present everywhere around us. Nevertheless and despite its utmost importance and ongoing research water is “a mystery that no one really understands”, to quote a recent review article [1]. It differs from most other liquids with respect to many physical properties with its phase diagram being maybe the most famous anomaly<sup>1</sup>. However, in nature water does not only exist in its free form, called bulk water, but often it is attached to substrates or it fills small nanometer sized cavities. Opposite to bulk water, one then speaks of confined water.

Many physical properties of confined water differ again substantially from those of bulk water. Thermodynamics [2], phase behaviour [3] and the molecular mobility of water have been observed to change upon confinement [4]. This spatially restricted water is involved in many physical, chemical and biological processes. It is e.g. thought to be essential for the stability and functionality of biological macromolecules [5], it plays a principal role in hardening and setting of cement [6,7], for oil recovery or heterogeneous catalysis [4]. These few examples can only be suggestive of the wide field of relevance of confined water. The topicality of this vast subject is maybe best reflected by the number of recent papers: *Web of Science* finds about 300 publications concerning confined water that have appeared during the last 5 years. A recent book [8] and a special section of papers [4] are dealing with interfacial and confined water. One general challenge for the study of confined water is to provide well-defined confining systems which allow for the variation of relevant external parameters like temperature and size to obtain a fundamental understanding of confinement induced changes of the water properties.

The purpose of this thesis is the thorough characterization of a system which will later be of use to systematically study confined water over a large range of temperatures and confining sizes.

## 1.1. Reverse micelles as model system to study soft confined water

Water and other liquids in hard confinement as realized for example by porous silica [7,9], clay materials [10] or carbon nanotubes [11] are subject of intense research [12–14]. How-

---

<sup>1</sup>An instructive overview of “water anomalies” together with references to literature can be found on <http://www.lsbu.ac.uk/water/anomlies.html>

ever, within recent years the great importance of wall interactions for confined liquids in general became evident [12–14]. The modification of the behaviour of water depends on the nature of the water-substrate interaction (hydrophilic or hydrophobic), as well as on its spatial range and on the geometry of the confinement [4]. With these observations the interest developed to modify wall properties either by coating the nanoporous host walls or more recently by studying liquids enclosed within soft walls [15]. One wants to find out how water molecules next to a soft matter interface behave and over which length scale their dynamics are affected by the interface. Such soft walls can be realized in microemulsions which are mixtures of polar and apolar liquids mediated by amphiphilic molecules called surfactants. One possible structure are spherical water droplets coated by a mono-layer of surfactant that are dispersed in a continuous oil matrix, sketched in Fig. 1.1. Pointing with their hydrophilic head groups towards the micellar core and with their hydrophobic tails towards the oil, the surfactant molecules form a soft shell that separates both liquids. The typical size of the enclosed water domains is in the order of Ångströms to nanometers.

These micellar systems offer the advantage that important parameters like degree of confinement (= micelle size), concentration of droplets and probably also the hardness of the confinement (= rigidity of the surfactant shell) may be varied in a systematic way. Moreover micellar systems are of special interest because of their similarity with systems of biological relevance. They are easy to prepare and to handle and with this respect an ideal model system for the study of soft confined water.

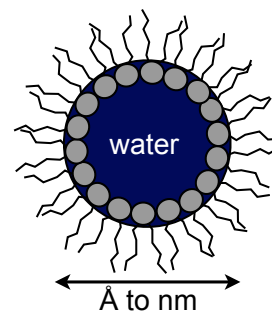


Figure 1.1.: Water containing reverse micelle.

On the other hand the complexity of these microemulsion systems - from a structural point of view as well as concerning their dynamical behavior - calls for a careful characterization. Prior to investigating possible confinement effects on enclosed water, structure, stability and self-dynamics of the reverse micelles need to be determined. A detailed knowledge about the temperature-dependent phase behaviour of the microemulsion is an essential precondition before one may focus on the water itself.

One of the best characterized water-in-oil droplet microemulsions is based on the anionic surfactant AOT (sodium bis[ethylhexyl] sodium sulfosuccinate) [16–18]. Around room temperature this system allows to control the size of the spherical water core in a very simple way: for a given surfactant concentration the droplets increase linearly with increasing water content [19]. These droplets are of moderate polydispersity,  $p \approx 15\% - 20\%$ , and one may vary the radius continuously between a few Ångströms

up to several nanometers for certain oils. Whereas the microemulsion structure around room temperature has been subject of numerous studies, no direct investigations at lower temperatures had been made.

Small angle neutron scattering (SANS) is a well suited experimental method for the study of microemulsion structures as it allows to probe the typical domain length scales of Ångströms to several hundreds of nanometers [20]. The sensitivity of neutrons to light elements and the possibility to highlight selected sample compounds by means of H/D exchange make the advantage of SANS over small angle X-ray scattering. SANS is an established method for the study of soft condensed matter. There exist approved models for the interpretation of scattering profiles from microemulsions which permit to determine their structure in a very direct way [21].

The dynamical behavior of confined water can be studied by quasi elastic neutron scattering (QENS) techniques [22]. Provided that the predominant incoherent contribution to the scattering is due to the water in the sample, QENS measures a quantity related through Fourier transforms to the self correlation function of the water protons [22]. The combination of different spectrometers allows to probe time scales from sub-picoseconds to nanoseconds with the spatial experimental resolution matching the spacings relevant for the water motion, so that rotational as well as translational diffusion of the water molecules may be investigated. Exploiting the range of accessible scattering vectors the distinction between different models for the motion becomes possible.

A further advantage of neutron scattering is it being a non-destructive method - structure and dynamics of the sample under investigation are unaltered by the scattering process and one may study the water without introducing a probe molecule as it has to be done e.g. with fluorescence probing [23]. These advantages are counterbalanced by the need of expensive large scale neutron scattering facilities and limited available beam time.

## 1.2. Outline of the thesis

The aim of this work was to investigate the suitability of reverse micelles as a model system for the investigation of water dynamics in soft confinement as it occurs e.g. in systems of biological relevance. For this purpose we chose the ternary microemulsion consisting of water, the anionic surfactant AOT (sodium bis[ethylhexyl] sodium sulfosuccinate) and oil where the degree of confinement may be varied in a controlled way between a few Ångströms and several nanometers. We characterized the microemulsion concerning its structure and dynamics in order to finally focus on rotational and translational motion of the confined water.

As main experimental methods we applied elastic and different quasi-elastic neutron scattering techniques. The theoretical background of neutron scattering and the experimental realization by different techniques as well as instrumental details are given in chapter 2. Furthermore we explain the instrument specific primary data corrections.

Prior to the investigation of confined water, a detailed knowledge about the confining structure is necessary. Chapter 3 presents results obtained by small angle neutron scattering (SANS). We determined phase behaviour and temperature range of structural stability of the water containing reverse micelles in dependence of their water loading.

As a next step towards a thorough characterization of the microemulsion, dynamics of the reverse micelles were studied by means of neutron spin echo spectroscopy (NSE). The translational diffusion of the entire droplets and form fluctuations of the AOT shell, both as a function of temperature, are subject of chapter 5.

Chapter 6 discusses quasi-elastic neutron scattering (QENS) investigations that were performed in order to elucidate the dynamical behavior of the confined water. The translational and rotational motion of the confined water were investigated as a function of confinement size and compared to the corresponding mobility of bulk water. Combining different QENS instruments we access three decades of time scales from picoseconds to nanoseconds. The large dynamic range and the spatial resolution matching the length scales of interest allow us to distinguish between different water fractions inside the micelles characterized by their average mobility.

A possible way to influence the structural properties of microemulsions in general and their surfactant membrane elasticity in particular is by addition of polymers. Regarding the study of confined water one may think of a tunable hardness of the confinement by modifying the water enclosing surfactant membrane with polymers. First experiments with the intent to study the influence of the hydrophilic homo polymer polyethyleneoxide (PEO) on droplet structure (SANS) and membrane elasticity (NSE) are depicted in chapter 7. Chapter 8 will complete this thesis with a summary.



## 1.3. Microemulsions

The term "microemulsion" was first used by *Schulman* and *Hoar* over 60 years ago to name the spontaneously forming isotropic solution of water, non-polar liquid, surfactant and a short-chained alcohol [24]. Together with *Winsor* they systematically investigated the phase behaviour of such mixtures [25]. Today microemulsions are more generally defined as an isotropic and macroscopically homogeneous mixture of a polar and an apolar liquid mediated by one or several surfactants. Domains of oil and water are separated from each other by mono-molecular layers of the surfactant and as these domains are small compared to the wavelength  $\lambda$  of visible light, microemulsions appear optically isotropic and transparent and their structure cannot be observed through an optical microscope. Contrary to emulsions, microemulsions are thermodynamically stable. Classified after their major component one speaks of water-in-oil (w/o) or oil-in-water (o/w) microemulsions. Depending on the nature of the surfactant, composition and many other parameters, e.g. temperature or pressure, a variety of different structures, including lamellar, droplet or bicontinuous phases can be formed. Microemulsions are of importance for a wide range of industries, as for example enhanced oil recovery, synthesis of nano-particles or cosmetics just to mention a few. Because of their selective solubilization properties, microemulsions have also attracted increasing attention as drug delivery systems. The theoretical background, including phase behaviour, microstructure and microemulsion formulation as well as applications of microemulsions are subject of a recent book [26]. In the following we will only discuss one special microemulsion system: we will introduce the w/o droplet microemulsion that has served as model system for this work.

### 1.3.1. AOT based w/o droplet microemulsion

The studied microemulsion is a ternary mixture composed of water, the anionic surfactant AOT and toluene, heptane or decane as oil.

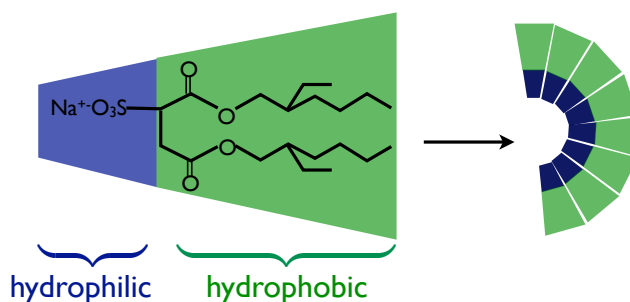
#### 1.3.1.1. Surfactant: AOT

Surfactants are amphiphilic molecules that unite a hydrophilic and a hydrophobic part in one molecule. The hydrophilic head can either be a charged or an uncharged polar group. According to the type of their polar head group, surfactants are categorized into ionic and nonionic. Ionic surfactants can then further be subdivided into anionic, cationic and zwitterionic. In contact with water the headgroup is ionized and the counterion is liberated into the water solution [27].

For this work we have used the common surfactant sodium bis[ethylhexyl] sulfosuccinate. Its commercial name Aerosol-OT (abbreviated to AOT) is a registered trademark of the American Cyanamid Company. AOT is an anionic double-tailed surfactant

whose chemical structure is shown in Fig. 1.2. The polar part is essentially composed of a negatively charged  $\text{SO}_3^-$  group and a positively charged  $\text{Na}^+$  counter-ion. Two identical ethylhexyl hydrocarbon tails form the apolar part of the molecule. Around room temperature AOT is a white waxy solid and it is soluble in a variety of different organic liquids. AOT is harmful if swallowed and irritating to the eyes, respiratory system and skin. The length of the apolar part of the AOT molecule is in the order of  $7.5 \text{ \AA}$ , for the polar head group a length of approximately  $3 \text{ \AA}$  is found [19].

Figure 1.2: Chemical structure of an AOT molecule. Due to its conical form the AOT surfactant film between water and oil has a spontaneous curvature towards the water, thus favors the formation of reverse water swollen micelles.



The protonated form (formula:  $\text{Na}^+\text{SO}_3^- \text{C}_{20}\text{H}_{37}\text{O}_4$ ) has a molar mass of  $M = 444.6 \text{ g/mol}$  with an density of  $\rho = 1.14 \text{ g/ml}$ .

For the partly deuterated form <sup>2</sup> (formula:  $\text{Na}^+\text{SO}_3^- \text{C}_{20}\text{H}_3\text{D}_{34}\text{O}_4$ ) we calculated the molar mass and density to  $M = 478.6 \text{ g/mol}$  and  $\rho = 1.21 \text{ g/ml}$  respectively.

Due to the conical form of the AOT molecule the surfactant film forming at the oil-water interface has a spontaneous curvature towards water and the formation of reverse micelles is favored. AOT is one of the most commonly used surfactants as it can form reverse micelles (hydrocarbon tails pointing to the outside) without a co-surfactant over a wide range of conditions. Around room temperature the critical micelle concentration<sup>3</sup> of AOT in non-polar solvents like decane, heptane or iso-octane was found to be in the order of  $\text{CMC} \approx 1 \text{ mM}$  [28]. Depending on the solvent up to 60 water molecules per AOT molecule may be solubilized [29]. The solution behaviour of AOT in non-polar solvents is in great detail reviewed in [28].

### 1.3.1.2. Microemulsion: water/AOT/oil

The room temperature phase diagram for the ternary mixture of water/AOT/decane is shown in Fig. 1.3 (after [17]). Phase diagrams for other oils e.g. iso-octane look similar [29]. For this work we will concentrate on the range of compositions marked by the dark red area in Fig. 1.3. In this region of the phase diagram the microemulsion consists of spherical water droplets coated by a mono-layer of AOT dispersed in the continuous oil

<sup>2</sup>Deuterated AOT was purchased by Prof. R Thomas, Oxford.

<sup>3</sup>Concentration of surfactants in liquid above which micelles are spontaneously formed.

matrix. Such a water swollen reverse micelle is shown on the right in Fig. 1.3. Different scattering methods including dynamic light scattering [18, 30], SANS [16, 17, 31] and SAXS [32, 33] have confirmed this structure around room temperature.

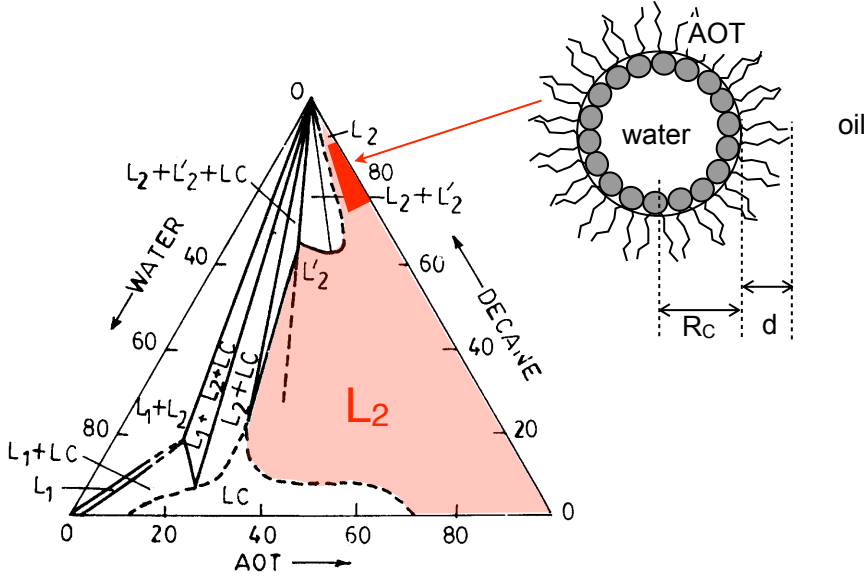


Figure 1.3.: Left: phase diagram of water/AOT/decane at ambient pressure and room temperature after [28]. Note the large part of the phase diagram covered by the  $L_2$  w/o droplet phase (light red area). In this region the microemulsion consists of water swollen reverse AOT micelles dispersed in the continuous oil matrix; such a reverse water swollen micelle is shown to the right. The range of compositions relevant for our study is marked with dark red. The region of  $L_2+L'_2$  is initially mono-phasic and phase separates by spinodal decomposition after a period of several months [28].  $L_c$  denotes the liquid crystal phase.

The composition of the microemulsion is commonly specified by two independent parameters<sup>4</sup>:

1. The **molar ratio**  $\omega$  is defined as the number of water molecules per AOT molecule:

$$\omega = \frac{n[\text{H}_2\text{O}]}{n[\text{AOT}]} \quad (1.1)$$

2. The droplet **volume fraction**  $\phi$  is defined as the ratio of water plus AOT volume over the entire volume:

$$\phi = \frac{V_{\text{H}_2\text{O}} + V_{\text{AOT}}}{V_{\text{oil}} + V_{\text{H}_2\text{O}} + V_{\text{AOT}}} = \frac{V_{\text{droplet}}}{V_{\text{tot}}} \quad (1.2)$$

<sup>4</sup>Understood that definitions 1.1 and 1.2 also hold in the case of deuterated ingredients.

Whereas the density of droplets (and hence the distance between droplets) depends on the choice of the volume fraction  $\phi$ , only the molar ratio  $\omega$  determines to a first approximation their size.

The radius of the droplets at room temperature can be related to the molar ratio  $\omega$  by simple geometrical considerations. Under the assumption of a spherical water core covered by a monomolecular shell of AOT (as shown in Fig. 1.3) the polar radius  $R_c$  composed of water and AOT headgroups can be calculated by combining the expressions for the volume and area of a droplet surrounded by  $n_s$  molecules of AOT :

$$\text{Droplet volume} : \frac{4}{3}\pi R_c^3 = n_s(v_w \cdot \omega + v_s) \quad (1.3)$$

$$\text{Droplet surface} : 4\pi R_c^2 = n_s \cdot A_s \quad (1.4)$$

with the AOT headgroup volume  $v_s \approx 50 \text{ \AA}^3$  and headgroup area  $A_s \approx 65 \text{ \AA}^2$  [19]. Taking the volume of a confined water molecule to be equal to that of a bulk water molecule  $v_w \approx 30 \text{ \AA}^3$  one finds the following linear relationship between the radius  $R_c$  and the molar ratio  $\omega$  [19]:

$$R_c = \frac{3}{A_s}(v_w \cdot \omega + v_s) \quad (1.5)$$

$$\approx (1.4 \omega + 2.3) \text{ \AA} \quad (1.6)$$

Equation 1.5 is derived based on the assumption of a constant and  $\omega$ -independent headgroup area  $A_s$  which was put into question by *Maitra* and co-workers who interpreted results from NMR as an increasing  $A_s$  with  $\omega$  [34].

Nevertheless relation 1.5 was experimentally verified and proved itself to be a good estimation for the droplet size at room temperature.

Assuming a random close packing of the droplets one may obtain a rough estimate for the mean center-to-center distance  $l$  between droplets [35]. With the entire droplet radius,  $R = R_c + d$ , and the volume fraction of closely packed spheres  $\rho_{cp} = 0.64$  we have:

$$l \approx 2R \sqrt[3]{\frac{0.64}{\phi}} \quad (1.7)$$

The maximum amount of water that can be solubilized by reverse AOT micelles depends on the surrounding oil due to the oil penetration into the surfactant shell which leads to an effectively increased volume of the surfactant tails [27]. Without a specific hydrocarbon-head group interaction, the hydrocarbons which are molecularly most similar to the surfactant tails will be able to penetrate the best and the solubility of water in AOT hydrocarbon solutions (equivalent to the maximum  $\omega$ ) was shown to decrease with increasing carbon number of the alkane [28].

### 1.3.1.3. Sample preparation

The preparation of the microemulsions is simple: required amounts of AOT, water and oil (decane, heptane or toluene) were mixed and shaken for several minutes until the samples were single-phase and optically clear. The detailed description of the sample mixing and the calculation of the composition is described in the appendix A.1. Special attention has been paid to the sealing of the sample holders as the used oils are very volatile.

## 1.4. Water in reverse micelles - state of the research

In reverse micelles, the effect of three-dimensional soft confinement and the strong interactions with the ionic AOT headgroups result in an environment for water which differs strongly from the bulk phase. The behavior of this interior core water is thus expected to differ significantly from free water and its variation with micelle size is of interest for fundamental but also for practical reasons. Reverse micelles have for example been studied because of their similarity to biological membranes and they have been exploited for their ability to solubilize enzymes and catalyze bio-organic reactions [36–38]. Moreover they have been applied for chemical catalysis, drug delivery or nano-particle synthesis. In this context the reverse micelles are sometimes referred to as "microreactors", because they provide a controlled small amount of water to the reactives [39].

The number of experimental studies on properties and applications of reverse AOT micelles is immense and *De* and *Maitra* [28] have reviewed them in great detail. While the predominant part of these investigations aimed at obtaining information about structure and properties of the micelles itself, there also exist an important number of studies focussing on the nature of the confined water. Applied techniques include infrared spectroscopy (IR) [40–48], fluorescence spectroscopy [49–51], vibrational spectroscopy [52, 53], nuclear magnetic resonance (NMR) [54–58], molecular dynamic (MD) simulations [59–65], dielectric spectroscopy [66, 67], QENS [63, 68] and differential scanning calorimetry (DSC) [55, 69].

A decrease of the average water mobility with decreasing micelle size has been observed by several techniques [63, 68, 70] - these techniques could not distinguish between water molecules at the surface layer of the droplets and those in the core. From these studies it therefore remained unanswered whether the mobility of water inside the reverse micelles decreases overall or if only water molecules located near the shell are retarded [71].

Results from other experimental techniques were interpreted in terms of two or more fractions of water - distinguishable by their differing dynamical behaviour and their ability to freeze [47, 50, 55, 67].

*Dokter* and co-workers used IR spectroscopy to investigate water inside reverse AOT micelles. They observed two types of water molecules differing in their mobility: water

molecules close to the micellar wall showed a much slower vibrational relaxation and a lower orientational mobility than water molecules in the core of the reverse micelles. The core water molecules were found to behave very similar to bulk water and the retarded water fraction corresponded to only a single layer of water molecules close to the AOT shell [71]. In agreement with this are recent results from MD simulations obtained by *Faeder* and co-workers who studied structure and dynamics of water inside reverse micelles of varying size. They observed a distinct molecular layer of water at the interface bound to the ionic headgroups which was characterized by a strongly reduced mobility. Away from the surfactant interface the water was found to regain its bulk properties very quickly within only a few molecular layers [65].

By means of DSC the amount of water hindered from freezing can be determined through the analysis of crystallization heats. Results differ, even though they were obtained using one and the same method: whereas *Boned* and coworkers found that no water freezing occurs for reverse AOT micelles dispersed in isooctane with  $\omega < 4$  [69], *Hauser* and co-workers observed a number of 6 un-freezable water molecules per AOT [55]. Complementary  $^2\text{H}$  NMR measurements on the same samples yielded a number of 13 bound water molecules per AOT molecule out of which molecules 2 appeared strongly bound, whereas the 11 others were found to be very weakly associated [55].

IR studies indicated that the number of bound water molecules depends on the molar ratio  $\omega$  [45]. In a later IR investigation, the interfacial layer was determined to consist of about 3 to 6 water molecules per AOT molecule; bulk-like water was observed only inside micelles with  $\omega > 12$  [42]. Very recently *Nucci* and co-workers distinguished 3 different water populations inside reverse AOT micelles by means of mid-IR spectroscopy. In their study, water with bulk characteristics was only seen for very large micelles with  $\omega > 40$  [40].

Vibrational spectroscopy using isooctane and cyclohexane as oil matrix showed that 3 to 6 water molecules are needed for the complete solvation of one AOT molecule [52]. 5 immobilized water molecules per AOT molecule were found by fluorescence spectroscopy.

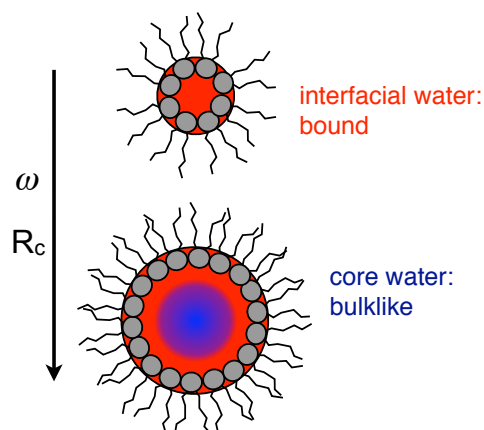


Figure 1.4.: Illustration of core-shell water model. Depending on the micelle size all water is bound to the AOT interface. This so-called shell water (red) is strongly retarded with respect to bulk water. With increasing micelle size, water in the middle of the core (blue) resembles bulk water.

For micelles with higher water content,  $\omega > 5$ , part of the contained water showed faster dynamics but even for the largest investigated micelles with  $\omega = 40$  the average water mobility was considerably slower than in the bulk state [51]<sup>5</sup>.

We summarize that whereas the decrease of the average water mobility inside the micelles seems to be a common observation, reported AOT headgroup coordination numbers are widely spread between 2 and 15 and up to now no consensus has been reached about the amount of bound water [28]. It is not yet clear if and to what extent the core water away from the shell is influenced by the micelle walls concerning its dynamical behaviour. Can water inside the micelles be regarded as a two-component system, where only those water molecules close to the AOT shell are retarded and those in the middle of the core behave like in the bulk (shown in Fig. 1.4), or is the entire water core influenced in the case of typical micelles sizes in the order of several nanometers? Both, experimental and theoretical studies of water at many different types of interfaces, show that most of the surface induced changes occur over a range of only a few molecular diameters and properties of the bulk have been found to re-emerge rapidly at greater distances from the surface. Indeed results for water inside reverse micelles, obtained by different experimental techniques, have successfully been analyzed by weighted sums of the respective bulk and bound water properties. On the other hand several of the above cited studies report about micelle core water behaving considerably different from bulk water even though the micelles under investigation were much larger than only a few molecular diameters.

---

<sup>5</sup>In this context one has to consider that fluorescence spectroscopy probes placed molecules that report about their local environment - this means that the probing molecules alter the water to some extent and interactions between water and the probing molecules need to be taken into account [57].





## 2. Neutron scattering - theory and practice

This chapter resumes the basics of neutron scattering. Rather than giving an exhaustive recapitulation of the theory, which can be found elsewhere [22, 72–74], the basic concepts required to follow the interpretation of the performed experiments are given. I will introduce the general formalism to describe the outcome of a neutron scattering experiment in general - the experimental realization differs from instrument to instrument and will be discussed after the theoretical part for the main techniques employed during this work. The used instruments are briefly presented together with the instrument-specific primary data corrections which have to be done to obtain the scattering functions. For actual and more detailed information on instruments and experimental possibilities I refer to the home page of the Institut Laue-Langevin (ILL, Grenoble)<sup>1</sup> and the Spallation Neutron Source (SNS, Oakridge)<sup>2</sup> and references given thereon.

### 2.1. Theory

Neutron scattering is an experimental technique for the investigation of both structure and dynamics of condensed matter. As shall be discussed in the following, this information is obtained by analyzing energy and momentum transfer between scattered neutrons and the probed sample. Neutrons are spin-1/2 particles with a magnetic moment of  $\mu = -1.923$  nuclear magnetons. Not bound inside the nucleus, a free neutron decays into a proton, an electron and an antineutrino with a lifetime of about 15 minutes. Neutrons can be described either as classical particles with a mass of  $m = 1.675 \times 10^{-27}$  kg or via the *de Broglie* formalism as a wave whose wavelength  $\lambda$  relates to the wavevector  $\mathbf{k}$  and the neutron velocity  $\mathbf{v}$  as:

$$\lambda = \frac{2\pi}{|\mathbf{k}|} = \frac{h}{m|\mathbf{v}|} \quad (2.1)$$

---

<sup>1</sup>[www.ill.eu](http://www.ill.eu)

<sup>2</sup><http://neutrons.ornl.gov>

with the *Planck* constant  $h = 2\pi\hbar = 6.626 \cdot 10^{-34}$  Js. The energy  $E$  of a free neutron then reads:

$$E = \frac{1}{2}mv^2 \quad (2.2)$$

$$= \hbar\omega = h\nu \quad (2.3)$$

$$= \frac{\hbar^2k^2}{2m} = \frac{h^2}{2m\lambda^2} \quad (2.4)$$

Classified after their energy one speaks of hot, thermal or cold neutrons when their average energy corresponds to about  $k_B T$  with average temperatures of  $T \approx 2000$  K, 300 K or 25 K respectively. The according range of neutron energies  $E$  and wavelengths  $\lambda$  corresponding this rough classification are presented in Tab. 2.1.

Table 2.1.: Classification of neutrons after their range of energy together with the corresponding temperature and wavelength [72].

	hot	thermal	cold
temperature $T$ (K)	1000 - 6000	60 - 1000	1 - 120
energy $E$ (meV)	100 - 500	5 - 100	0.1 - 10
wavelength $\lambda$ (Å)	1 - 0.4	4 - 1	30 - 3

It can be seen that at the same time the neutron energy  $E$  is in the energy range of excitations in condensed matter and the wavelength  $\lambda$  is comparable to interatomic distances. This fortunate match, for both, time scale and spacings, makes neutrons a unique probe for condensed matter structure and dynamics.

Neutrons are uncharged and therefore - contrary to electromagnetic radiation and electrons - they do not interact with the atomic charge distribution but directly with the atomic nucleus (via the strong nuclear force) and with magnetization density fluctuations (via their magnetic moment  $\mu$ ). The case of magnetic scattering will not further be subject of discussion as it is of no relevance for the here investigated samples. The range of the nuclear force is orders of magnitude smaller than the neutron wavelength and therefore the scattered wave is isotropic with its amplitude being proportional to the so-called scattering length  $b$ . The value of  $b$  does not only depend on the element but also on its isotope and the spin-state of the neutron-nucleus system<sup>3</sup>. In the absence of a theory for nuclear forces  $b$  is an experimentally determined quantity. Contrary to X-rays where the scattering strength increases with the number of electrons,  $b$  varies in a random way from element to element<sup>4</sup>.

---

<sup>3</sup> $b$  may be complex with the imaginary part of  $b$  corresponding to absorption. Here we will only deal with nuclei having an imaginary part negligibly small justifying to take  $b$  as a real quantity.

<sup>4</sup>For thermal and cold neutrons  $b$  is practically independent of the incident neutron energy.

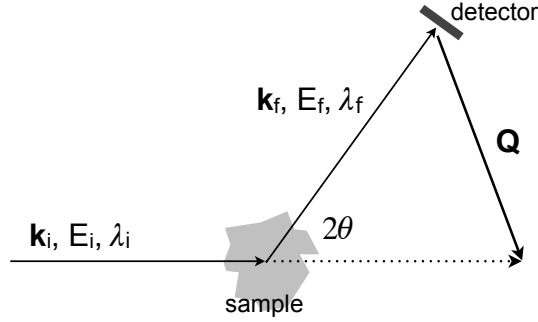


Figure 2.1.: Sketch of a general scattering experiment. Incoming neutrons with an incident wavelength  $\lambda_i$ , energy  $E_i$  and wave vector  $\mathbf{k}_i$  interact with the sample and are detected at an angle  $2\theta$  with a final  $\lambda_f$ ,  $E_f$  and  $\mathbf{k}_f$ . The scattering vector  $\mathbf{Q}$  is defined as the change in wave vector:  $\mathbf{Q} = \mathbf{k}_i - \mathbf{k}_f$ .

A general neutron scattering experiment consists of measuring the energy transfer  $\Delta E$  and momentum transfer  $\Delta \mathbf{k} = \mathbf{Q}$  between sample and neutron, visualized in Fig. 2.1.

$$\Delta E = E_i - E_f = \hbar\omega = \frac{\hbar^2}{2m}(k_i^2 - k_f^2) \quad (2.5)$$

$$\mathbf{Q} = \mathbf{k}_i - \mathbf{k}_f \quad (2.6)$$

These two quantities contain all the information about structure and dynamics of the sample.

### 2.1.1. Double differential cross section

Experimentally one accesses the number of neutrons that are scattered into a solid angle  $d\Omega$  around a given direction having a final energy between  $\hbar\omega$  and  $\hbar\omega + \hbar d\omega$  divided by the incoming neutron flux. This quantity is called the double differential cross section  $\frac{d^2\sigma}{d\Omega dE'}$ . Derived under the so-called Born approximation<sup>5</sup> it takes the following form [72]:

$$\frac{d^2\sigma}{d\Omega dE'} = \frac{k_f}{k_i} \frac{1}{2\pi\hbar} \sum_{i,j} \langle b_i b_j \rangle \int_{-\infty}^{\infty} \langle e^{-i\mathbf{Q}\mathbf{r}_i(0)} e^{i\mathbf{Q}\mathbf{r}_j(t)} \rangle \cdot e^{-i\omega t} dt \quad (2.7)$$

with  $\mathbf{r}_i(t)$  being the positions of scatterer  $i$  at the time  $t$ . Separating Eq. 2.7 into one part concerning the time correlations between  $N$  different scatterers ( $i \neq j$ ) and one for

<sup>5</sup>Holds if the perturbation of incident wave due to scattering is small and one can replace the scattered wave by the incident wave.

self-correlations ( $i = j$ ) one arrives at the following expression:

$$\begin{aligned} \frac{d^2\sigma}{d\Omega dE'} = & \frac{k_f}{k_i} \frac{1}{2\pi\hbar} \sum_{i \neq j} \langle b \rangle^2 \int_{-\infty}^{\infty} \left\langle e^{-i\mathbf{Q}\mathbf{r}_i(0)} e^{i\mathbf{Q}\mathbf{r}_j(t)} \right\rangle \cdot e^{-i\omega t} dt \\ & + \frac{k_f}{k_i} \frac{1}{2\pi\hbar} \sum_i \langle b^2 \rangle \int_{-\infty}^{\infty} \left\langle e^{-i\mathbf{Q}\mathbf{r}_i(0)} e^{i\mathbf{Q}\mathbf{r}_i(t)} \right\rangle \cdot e^{-i\omega t} dt \end{aligned} \quad (2.8)$$

We introduce the coherent and incoherent scattering cross sections  $\sigma_{\text{coh}}$  and  $\sigma_{\text{inc}}$  as:

$$\sigma_{\text{coh}} = 4\pi \langle b \rangle^2 = 4\pi b_{\text{coh}}^2 \quad (2.9)$$

$$\sigma_{\text{inc}} = 4\pi (\langle b^2 \rangle - \langle b \rangle^2) = 4\pi b_{\text{inc}}^2 \quad (2.10)$$

With these definitions the double differential cross section for purely nuclear scattering, Eq. 2.8, reads:

$$\frac{d^2\sigma}{d\Omega dE'} = \frac{1}{4\pi} N \frac{k_f}{k_i} (\sigma_{\text{coh}} S_{\text{coh}}(\mathbf{Q}, \omega) + \sigma_{\text{inc}} S_{\text{inc}}(\mathbf{Q}, \omega)) \quad (2.11)$$

In Eq. 2.11 we have defined the coherent and incoherent dynamic scattering functions,  $S_{\text{coh}}(\mathbf{Q}, \omega)$  and  $S_{\text{inc}}(\mathbf{Q}, \omega)$ , as:

$$S_{\text{coh}}(\mathbf{Q}, \omega) = \frac{1}{N} \frac{1}{2\pi\hbar} \sum_{i,j} \int_{-\infty}^{\infty} \left\langle e^{-i\mathbf{Q}\mathbf{r}_i(0)} e^{i\mathbf{Q}\mathbf{r}_j(t)} \right\rangle \cdot e^{-i\omega t} dt \quad (2.12)$$

$$S_{\text{inc}}(\mathbf{Q}, \omega) = \frac{1}{N} \frac{1}{2\pi\hbar} \sum_i \int_{-\infty}^{\infty} \left\langle e^{-i\mathbf{Q}\mathbf{r}_i(0)} e^{i\mathbf{Q}\mathbf{r}_i(t)} \right\rangle \cdot e^{-i\omega t} dt \quad (2.13)$$

The incoherent scattering corresponds to the scattering a system containing the same nuclei (position and motion) having all the average scattering length  $\langle b \rangle$  would give. The incoherent scattering arises from the random distribution of the deviations of the scattering length from their mean value, due to the fact that  $b$  varies with element, isotope and spin-state of the neutron-nucleus system.

Equations 2.12-2.13 contain Fourier transforms with respect to time:

$$S_{\text{coh}}(\mathbf{Q}, \omega) = \frac{1}{2\pi\hbar} \int_{-\infty}^{\infty} I_{\text{coh}}(\mathbf{Q}, t) \cdot e^{-i\omega t} dt \quad (2.14)$$

$$S_{\text{inc}}(\mathbf{Q}, \omega) = \frac{1}{2\pi\hbar} \int_{-\infty}^{\infty} I_{\text{inc}}(\mathbf{Q}, t) \cdot e^{-i\omega t} dt \quad (2.15)$$

where the transformed parts,  $I_{\text{coh}}(\mathbf{Q}, t)$  and  $I_{\text{inc}}(\mathbf{Q}, t)$ , are the coherent and incoherent intermediate scattering functions respectively:

$$I_{\text{coh}}(\mathbf{Q}, t) = \frac{1}{N} \sum_{i,j} \left\langle e^{-i\mathbf{Q}\mathbf{r}_i(0)} e^{i\mathbf{Q}\mathbf{r}_j(t)} \right\rangle \quad (2.16)$$

$$I_{\text{inc}}(\mathbf{Q}, t) = \frac{1}{N} \sum_i \left\langle e^{-i\mathbf{Q}\mathbf{r}_i(0)} e^{i\mathbf{Q}\mathbf{r}_i(t)} \right\rangle \quad (2.17)$$

Performing one more spatial Fourier transform on the coherent and incoherent intermediate scattering functions Eq. 2.16-2.17 one returns to real space and the pair- and the self correlation functions,  $G(\mathbf{r}, t)$  and  $G_s(\mathbf{r}, t)$ , are obtained:

$$G(\mathbf{r}, t) = \frac{1}{(2\pi)^3} \int_{-\infty}^{\infty} I_{\text{coh}}(\mathbf{Q}, t) \cdot e^{-i\mathbf{Q}\mathbf{r}} d\mathbf{Q} \quad (2.18)$$

$$G_s(\mathbf{r}, t) = \frac{1}{(2\pi)^3} \int_{-\infty}^{\infty} I_{\text{inc}}(\mathbf{Q}, t) \cdot e^{-i\mathbf{Q}\mathbf{r}} d\mathbf{Q} \quad (2.19)$$

These functions have the following concrete physical meaning<sup>6</sup>: given for  $t = 0$  there is a particle at the origin,  $G(\mathbf{r}, t)d\mathbf{r}$  is the probability that any particle is in the volume  $d\mathbf{r}$  around the position  $\mathbf{r}$  at the time  $t$ .  $G_s(\mathbf{r}, t)d\mathbf{r}$  is the probability, that the particle from the origin can be found in the volume  $d\mathbf{r}$  around the position  $\mathbf{r}$  at the time  $t$ . Note that  $G(\mathbf{r}, t)$  also contains  $G_s(\mathbf{r}, t)$ .

The coherent scattering thus corresponds to scattering from a system with scatterers having all the same average scattering length  $b_{\text{coh}}$ . It contains the correlation of the positions of different nuclei at different times. Hence it reflects interference effects and contains the time dependent structural information about the sample. The incoherent part on the other hand only depends on the time evolution of the position of one and the same nucleus, no information on the static structure is contained.

The relations between the functions  $S(\mathbf{Q}, \omega)$ ,  $I(\mathbf{Q}, t)$  and  $G(\mathbf{r}, t)$  as introduced in this section are recalled in Fig. 2.2:

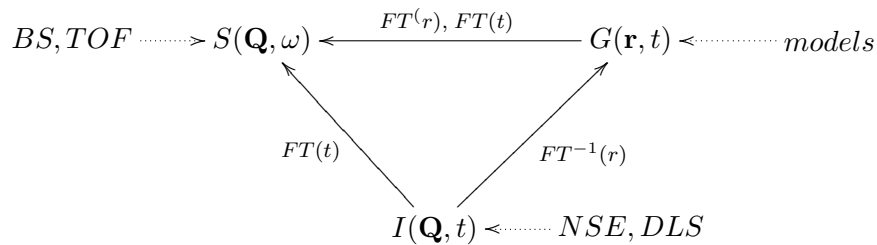


Figure 2.2.: Relation between dynamic scattering function  $S(\mathbf{Q}, \omega)$ , intermediate scattering function  $I(\mathbf{Q}, t)$  and pair (self) correlation function  $G(\mathbf{r}, t)$  and their accessibility by experimental methods.  $FT(x)$  denotes the Fourier transform with respect to the variable  $x$ .

In this context we anticipate some of the content of the next section by showing the accessibility of these functions by the applied scattering techniques. Whereas time-of-flight (TOF) and backscattering (BS) measure quantities that are directly proportional to the dynamic scattering function  $S(\mathbf{Q}, \omega)$  (frequency - reciprocal space domain), neutron-spin-echo (NSE) and dynamic light scattering (DLS) give access to the intermediate

<sup>6</sup>This holds only in the classical limit where one ignores that  $\mathbf{R}_i(0)$  and  $\mathbf{R}_j(t)$  do not commute.

scattering function  $I(\mathbf{Q}, t)$  in the time - reciprocal space domain.

As we are dealing with isotropic samples we will from now on drop the vectorial notation and replace  $\mathbf{Q}$  with  $Q$ .

### 2.1.2. Differential cross section

If one is only interested in the structure of the sample, the energy of the scattered neutrons is of no importance and only the number of neutrons scattered into the solid angle  $d\Omega$  around the direction  $\Omega$  has to be measured. This quantity is called differential cross section:

$$\frac{d\sigma}{d\Omega} = \int_0^\infty \frac{d\sigma}{d\Omega dE'} dE \quad (2.20)$$

and it is the integral of the double differential cross section, given by Eq. 2.7, over all possible final neutron energies. Accordingly the differential cross section of a system of  $N$  scatterers at positions  $\mathbf{r}$  can be expressed in terms of a coherent and an incoherent contribution:

$$\frac{d\sigma}{d\Omega} = b_{\text{coh}}^2 \cdot \sum_{i,j}^N \langle e^{-iQ(r_i - r_j)} \rangle + N \cdot b_{\text{inc}}^2 \quad (2.21)$$

$$= \left( \frac{d\sigma}{d\Omega} \right)_{\text{coh}} + \left( \frac{d\sigma}{d\Omega} \right)_{\text{inc}} \quad (2.22)$$

Whereas the information about form and spatial correlation of the scatterers is contained in the first term, the second term arises only from fluctuations in scattering length  $b$ .  $\left( \frac{d\sigma}{d\Omega} \right)_{\text{inc}}$  is independent of the position of the scatterers and therefore it does not contain any structural information about the sample.

We will assume that the incident energy of the neutrons is large compared to the change in energy they undergo during the scattering process and moreover that  $k_i \approx k_f$ , meaning  $Q$  is independent of  $\omega$ . Under this so-called quasi-elastic approximation the coherent scattering cross section reads:

$$\left( \frac{d\sigma}{d\Omega} \right)_{\text{coh}} \approx N \hbar \frac{\sigma_{\text{coh}}}{4\pi} \int_{-\infty}^{\infty} S_{\text{coh}}(Q, \omega) d\omega \quad (2.23)$$

For a liquid the quasi-elastic coherent cross section in the forward direction depends on the isothermal compressibility  $\kappa_T$  and the mass density  $\rho$  [74]<sup>7</sup>:

$$\lim_{Q \rightarrow 0} \left( \frac{d\sigma}{d\Omega} \right)_{\text{coh}} = N \hbar \frac{\sigma_{\text{coh}}}{4\pi} \rho \kappa_T k_B T \quad (2.24)$$

---

<sup>7</sup>At the critical point  $\kappa_T$  diverges which means that also the quasi-elastic forward scattering diverges.

As a quantity independent of the sample geometry one usually compares the scattered intensity per unit sample volume:

$$I(\text{cm}^{-1}) = \frac{1}{V} \frac{d\sigma}{d\Omega} \quad (2.25)$$

Going to a continuous distribution of scatterers we introduce the coherent scattering length density<sup>8</sup>:

$$\rho_{\text{coh}}(r) = \sum_i \rho_i(r) b_{\text{coh}}^i \quad (2.26)$$

with  $\rho_i(r)$  being the local density of atom  $i$ . This step is justified as at small  $Q$  we are not able to resolve individual atom positions. The amplitude of the scattered intensity is:

$$A(Q) = \int \rho_{\text{coh}}(r) e^{-iQr} d^3r \quad (2.27)$$

It is useful to split the scattering length density of the sample  $\rho(r)$  into a sum of a constant part  $\langle \rho \rangle$  and the deviation  $\delta\rho(r)$ :

$$\rho_{\text{coh}}(r) = \langle \rho_{\text{coh}} \rangle + \delta\rho_{\text{coh}}(r) \quad (2.28)$$

The scattering of the average term  $\langle \rho \rangle$  contributes only in the forward direction,  $Q = 0$ . It is called null scattering and experimentally unobservable. Therefore we may rewrite the scattering amplitude, Eq. 2.27, as:

$$A(Q) = \int \delta\rho_{\text{coh}}(r) e^{-iQr} d^3r \quad (2.29)$$

We first consider the intensity of a dilute and isotropic system of identical particles of constant coherent scattering length density  $\rho_{\text{coh},p}$  dispersed in a continuous matrix of coherent scattering length density  $\rho_{\text{coh},m}$ . Let  $V_p$  be the particle volume and  $n = N/V$  their number density then the coherent intensity normalized to the sample volume,  $I(Q) = [A(Q) \cdot A^*(Q)]/V$ , calculates to:

$$I(Q) = n \cdot (\Delta\rho_{\text{coh}})^2 \left[ \int_{V_p} e^{-iQr} d^3r \right]^2 \quad (2.30)$$

$$= n \cdot F(Q) \quad (2.31)$$

with the contrast,  $\Delta\rho = \rho_{\text{coh},p} - \rho_{\text{coh},m}$ , being the difference of scattering length density between particle and matrix.  $F(Q)$  is called the particle form factor, it contains the

<sup>8</sup>The incoherent scattering length density  $\rho_{\text{inc}}$  is calculated accordingly by replacing  $b_{\text{coh}}^i$  in Eq. 2.26 with  $b_{\text{inc}}^i$ .

information about the geometry of the individual scatterer<sup>9</sup>. In a more dense system of scatterers their positions are no longer independent; waves scattered by different particles interfere and Eq. 2.31 becomes:

$$I(Q) = n \cdot F(Q) \cdot S(Q) \quad (2.32)$$

with the structure factor  $S(Q)$  describing the spatial correlations of  $N$  individual scatterers with  $r_{ij}$  being the distance between particles  $i$  and  $j$ :

$$S(Q) = 1 + \frac{1}{N} \left\langle \sum_{i=1}^N \sum_{i \neq j}^N e^{-iQr_{ij}} \right\rangle \quad (2.33)$$

We summarize: the coherent SANS intensity of a solution of particles (e.g. reverse micelles dispersed in oil) is proportional to the product of the form factor, which reflects the geometry of the individual particle, and the structure factor as a measure for spatial correlations between different particles and hence their mutual interactions. For a dilute system the structure factor reduces to  $S(Q) \approx 1$ . Moreover it is important to realize that for  $Q \neq 0$  the coherently scattered intensity only depends on coherent scattering length density differences, called contrast, not on their absolute values. The incoherent scattering is independent of  $Q$  and contains no structural information, it forms the constant background on which the  $Q$ -dependent coherent scattering sits.

### 2.1.3. Coherent and incoherent scattering

A final remark concerns coherent versus incoherent scattering: in practice one always measures a combination of both; the weight of both contributions depends on the sample's composition (see Eq. 2.8). A way to adjust the relative strength of both coherent and incoherent scattering is by selective deuteration. Luckily for the scientists there is a big difference between coherent  $\sigma_{\text{coh}}$  and incoherent scattering cross sections  $\sigma_{\text{inc}}$  of  $^1\text{H}$  and  $^2\text{D}$ .

Table 2.2.: Coherent and incoherent cross sections for thermal and cold neutrons, as defined in Eqs. 2.9 and 2.10, of some common elements and isotopes which are contained in our sample compounds. Values are taken from [75]. ( $10^{-24}\text{cm}^2 = 1$  barn)

	$^1\text{H}$	$^2\text{D}$	C	O	$^{23}\text{Na}$	S
$\sigma_{\text{coh}} [10^{-24}\text{cm}^2]$	1.76	5.59	5.55	4.23	1.66	1.02
$\sigma_{\text{inc}} [10^{-24}\text{cm}^2]$	80.27	2.05	<0.01	<0.01	1.62	<0.01

---

<sup>9</sup>In literature the term form factor often refers only to the square of the integral over the particle volume not containing the contrast factor.



The values of  $\sigma_{\text{coh}}$  and  $\sigma_{\text{inc}}$  for some common "soft matter" elements are listed in Table 2.2. Note that while  $^1\text{H}$  has an incoherent cross section that is about 40 times bigger than the one of a deuteron with  $\sigma_{\text{inc}}(^2\text{D}) \approx 2$  barns the situation is inverted for coherent scattering and  $\sigma_{\text{coh}}(^2\text{D}) \approx 5.6$  barns  $>$   $\sigma_{\text{coh}}(^1\text{H}) \approx 1.8$  barns. This fact is widely exploited by exchanging protons with deuterons to mark different components of the samples/molecules under investigation. (Assuming that neither the measured structure nor dynamics are affected by replacing  $^1\text{H}$  with  $^2\text{D}$ , which is not always entirely true [21]). Depending on the aim of the investigation one will either use mainly deuterated or protonated components.

For structural investigations one will try to minimize the incoherent contribution to the differential cross section, Eq. 2.21. In dilute solutions, as for example here the "solution of droplets in oil", the main incoherent contribution comes from the solvent and hence it is preferable to work with deuterated oil. The same considerations hold when coherent dynamic processes, e.g. shell form fluctuations, are to be studied. If on the other hand the experimental intention is to measure the self dynamics of water, one will have to assure that mobile protons belong to the water under investigation to maximize the weight of its incoherent scattering relative to the entire scattering.

## 2.2. Experimental reality

Having outlined the basic theoretical notations necessary to understand the principles of neutron scattering we will move forward to the practical realization of measurements. In the following we will briefly describe the employed types of instruments and we give the instrument specific information about the working range. Except for one experiment all presented measurements have been performed on cold neutron instruments at the ILL, the European research reactor in Grenoble with 56 MW, where free neutrons are produced by fission. We will close this chapter by addressing the issue of resolution which is of importance for all measurement techniques. The presented techniques are compared.

### 2.2.1. Neutron backscattering spectrometry (BS)

Neutron backscattering (BS) has first been proposed by *Maier-Leibnitz* [76]. The technique exploits the fact that Bragg-reflection under an angle of  $90^\circ$  (or close to) leads to the decoupling to first order of resolution and divergency. Energy resolutions as high as  $\text{FWHM} \approx 0.1 \mu\text{eV} - 1 \mu\text{eV}$  can be obtained when Si(111) is used as analyzing and monochromating crystals. BS measures a quantity proportional to the dynamic scattering function  $S(Q, \omega)$  as introduced in section 2.1. The first BS instrument was built at the FRM (research reactor, Munich) in 1966 [77]; now BS instruments are installed at nearly all neutron scattering centers and spallation sources. Besides neutron-spin-

echo, which will be discussed in the following, BS is the leading high energy resolution technique<sup>10</sup>.

### 2.2.1.1. Principle

BS spectrometers are inverse geometry instruments where the energy transfer between neutron and sample is scanned by varying the incident neutron energy  $E_i$  whilst keeping the final energy  $E_f$  fixed. In practice  $E_i$  is changed either by thermal expansion of the monochromator crystals or by Doppler shifting the neutron wavelength. Figure 2.3 shows the principle BS set-up:

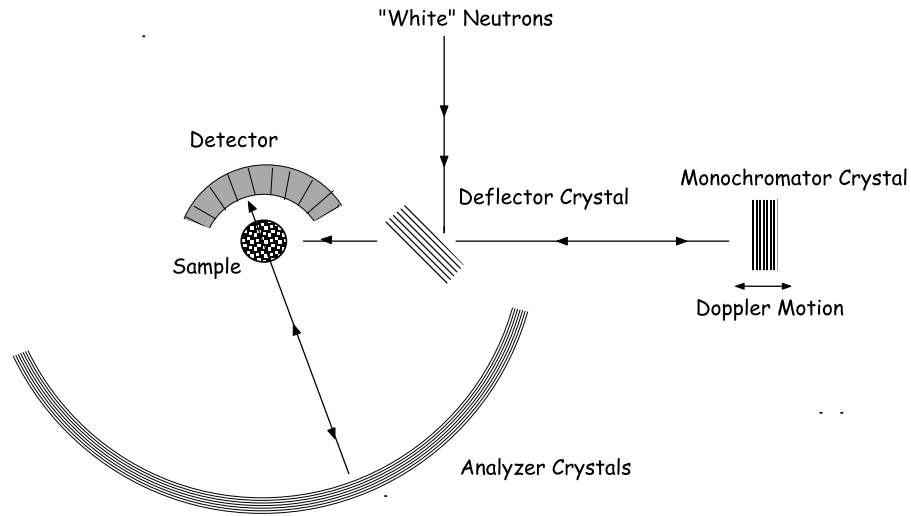


Figure 2.3.: Principle set-up of a backscattering spectrometer. Neutrons are monochromated by crystals mounted on a (periodically moving) Doppler drive. After being scattered by the sample only those neutrons are reflected back into the detectors which again fulfill the Bragg-condition.

Neutrons are reflected in backscattering geometry and thereby monochromatized by crystals on a Doppler drive moving parallel to the incident neutrons. Differentiating the Bragg-condition,  $\lambda = 2d \sin \theta$ , one sees that the reflected wavelength band  $\Delta \lambda$  becomes minimal for  $\theta = 90^\circ$ :

$$\frac{2\Delta\lambda}{\lambda} = \frac{\Delta E}{E} = \frac{2\Delta d}{d} + 2 \cot \theta \cdot \Delta\theta \quad (2.34)$$

where  $\Delta\theta$  contains the beam divergence and the angular deviation from backscattering and  $d$  is the lattice spacing of the crystals.  $\frac{\Delta d}{d}$  depends on the crystal quality. The

<sup>10</sup>A comprehensive introduction to BS providing also references to extensive information can be found under [http://www.ill.eu/other\\_sites/BS-review/](http://www.ill.eu/other_sites/BS-review/)

energy resolution is hence optimized when working with neutrons that are reflected in backscattering geometry.

After being scattered by the sample the neutrons hit the analyzers placed on a sphere around the sample. The analyzers usually consist of the same crystals as used for the mono-chromatization and thus all neutrons with wavelengths again fulfilling the Bragg-condition are reflected back and counted by the detectors. Two different types of measurements are done with a BS spectrometer:

**Elastic fixed window scans** provide a relatively quick overview about the molecular mobility in the sample as a function of temperature and therefore they are usually the starting point of every experiment. These scans are performed by keeping the Doppler still, resulting in fixed initial and final wavevectors,  $|\mathbf{k}_i| = |\mathbf{k}_f|$ , which is equivalent to  $\omega = 0$ . One thus counts within the instrumental resolution elastically scattered neutrons  $I^{\text{el}}(Q) = S(Q, \omega = 0)$  as a function of temperature.

As the energy width of the dynamic scattering function increases with increasing temperature, the elastic intensity decreases if the characteristic relaxation time becomes of the order or shorter than the instrumental resolution. For ILL's BS spectrometers the energy resolution is slightly better than  $1 \mu\text{eV}$  (FWHM), the corresponding time resolution can be estimated as  $\tau = h/1\mu\text{eV} \approx 4.14 \text{ ns}$  or, if compared to a relaxation, as  $\text{FWHM}/2/\omega \sim 1.3 \text{ ns/rad}$ . Depending on the activation energy of the dynamic processes and/or the relaxation time distribution the observation is then a more or less sharp step of the intensity in the temperature scan.

For the here investigated samples this means that at high temperature, where the microemulsions are liquid, the elastic incoherent scattering in the mentioned  $Q$ -range should go to zero if the energy resolution is good enough. However, for our microemulsions, which were about 80 vol% - 90 vol% deuterated, the coherent scattering is not negligible and it will add to the elastic signal as well. One important contribution arises from the integrated coherent static structure factor.

**Inelastic scans** are then carried out at a fixed temperature chosen based on the results from elastic scans. The energy of the incoming neutrons is modulated by a periodic movement of the Doppler in the flight direction of the neutrons. Depending on the actual velocity of the Doppler crystals at the moment of reflection the neutrons their energy changes periodically between  $(E_i - \Delta E)$  and  $(E_i + \Delta E)$ . Only those neutrons which have lost or gained exactly this energy change during the scattering process and have again the energy  $E_i$  are reflected back by the analyzer crystals to the detector. The flight time from monochromator over sample, analyzer to the detector is known exactly and therefore every time channel belongs to a known energy transfer at the doppler.

### 2.2.1.2. Instruments: IN10, IN16 and Basis

**IN10** is located at the cold neutron guide H15 at the ILL. It works in nearly perfect backscattering geometry. Si(111) crystals are used for monochromating and analyzing of the neutron beam:  $\lambda_i = 6.271 \text{ \AA}$  ( $E_i = 2.08 \text{ meV}$ ). The scattered neutrons are detected by 7  $^3\text{He}$  counters which cover an elastic  $Q$ -range of  $0.2 \text{ \AA}^{-1}$  to  $2 \text{ \AA}^{-1}$ . Energy transfers  $\Delta E = \hbar\omega$  between sample and neutron from  $-15 \text{ \mu eV}$  to  $15 \text{ \mu eV}$  with a resolution (FWHM) of  $\delta E \sim 1 \text{ \mu eV}$  are accessed in the standard set-up. In the IN10b configuration the incident neutron wavelength is varied by thermal expansion of the monochromator crystals in place of the Doppler driven crystals. Resulting energy transfers depend on the choice of the crystal.

**IN16** is located at a the cold neutron guide H53 at the ILL. It works in perfect backscattering geometry. In the standard set-up Si(111) crystals are used for monochromating and analyzing of the neutron beam:  $\lambda_i = 6.271 \text{ \AA}$  ( $E_i = 2.08 \text{ meV}$ ). The scattered neutrons are detected by 22  $^3\text{He}$  counters which cover an elastic  $Q$ -range of  $0.2 \text{ \AA}^{-1}$  to  $1.9 \text{ \AA}^{-1}$ . Energy transfers  $\Delta E$  from  $-15 \text{ \mu eV}$  to  $+15 \text{ \mu eV}$  with a resolution (FWHM) of  $\delta E < 1 \text{ \mu eV}$  are accessed. In addition 320  $^3\text{He}$  counters grouped by two are mounted below the analyzer crystals to allow for simultaneous diffraction measurements.

**Basis** is a new near-backscattering spectrometer at the neutron spallation source SNS in Oakridge, USA. In theory energy transfers  $\Delta E$  from  $-250 \text{ \mu eV}$  to  $+250 \text{ \mu eV}$  with a resolution (FWHM)  $\delta E$  of  $\sim 3.5 \text{ \mu eV}$  are accessed, when Si(111) crystals are used for analysis. Detectors cover an elastic  $Q$ -range of  $0.1 \text{ \AA}^{-1}$  to  $2 \text{ \AA}^{-1}$  [78].

### 2.2.1.3. Primary data corrections

The raw data from IN10 and IN16 are corrected using the standard ILL program *SQW* (*SQWel* in the case of fixed window scans) which corrects for self absorption, transmission, detector efficiency and normalizes to absolute intensities [79]. One needs to measure the intensities of sample in cell ( $I_{sc}^e$ ), empty cell ( $I_c^e$ ) and vanadium in cell ( $I_v^e$ )<sup>11</sup>. From these quantities the theoretical intensity from the sample alone ( $I_s$ ) is deduced which relates to the total differential scattering cross section  $\frac{d^2\sigma}{d\Omega d\omega} = \hbar \frac{d^2\sigma}{d\Omega dE'}$ :

$$I_s(Q, \omega) = n_s \cdot z_s \int \frac{d^2\sigma}{d\Omega d\omega} R(Q, \omega - \omega') d\omega' \quad (2.35)$$

where  $R(Q, \omega - \omega')$  is the instrumental resolution function.  $n_s$  and  $z_s$  denote the number density of scatterers and neutron path length in the sample respectively.

<sup>11</sup>With the superscript  $e$  we express the fact, that these intensities are experimentally determined quantities.

First the measuring time is eliminated by dividing the detector spectra by a monitor spectrum (energy channel by channel) that has been measured at the same time. This is important as the measuring duration for different doppler velocity channels (corresponding to different energy channels) are very different. Moreover intensity variations due to a possibly changing reactor power are thereby accounted for which may play a role as in BS typical counting times are in the order of 8 h - 24 h.

In a second step the varying analyzer surface and detector efficiencies are treated. For this purpose the elastic incoherent scattering of vanadium is measured under the same experimental configuration as the sample. For each detector this signal is corrected for absorption, the Debye-Waller factor, then integrated and used as a normalization standard for the sample signal.

In order to separate sample and cell scattering, one has to perform corrections for self-absorption in both, sample and cell. In the appendix A.3 the principle calculations performed by *SQW* are outlined.

The transmissions of the investigated samples were higher than 90% therefore no corrections for multiple scattering were applied.

BS does not distinguish between coherent and incoherent scattering; the final output of *SQW* is a "mixed" scattering function:

$$\begin{aligned}
 S_m(Q, \omega) &= \frac{4\pi}{\sigma_{\text{coh}} + \sigma_{\text{inc}}} \frac{k_i}{k_f} \int \frac{d^2\sigma}{d\Omega d\omega} R(Q, \omega - \omega') d\omega' \\
 &= \frac{4\pi}{\sigma_{\text{coh}} + \sigma_{\text{inc}}} \frac{k_i}{k_f} \frac{I_s(Q, \omega)}{n_s z_s}
 \end{aligned} \tag{2.36}$$

where  $z_s$  is the neutron path length in the sample,  $n_s$  denotes is the number density of scatterers and the cross sections are given per average scattering unit.

## 2.2.2. Neutron time-of-flight spectrometry (TOF)

TOF instruments are direct geometry instruments. Contrary to BS the energy of the incoming neutrons is constant and the energy transfer between sample and neutron is determined by measuring the velocity of the scattered neutrons. For this purpose neutron flight times over known distances are converted to neutron energies. TOF measures a quantity proportional to the dynamic scattering function  $S(Q, \omega)$  that was introduced in section 2.1.

### 2.2.2.1. Principle

Figure 2.4 shows a simplified TOF set-up:

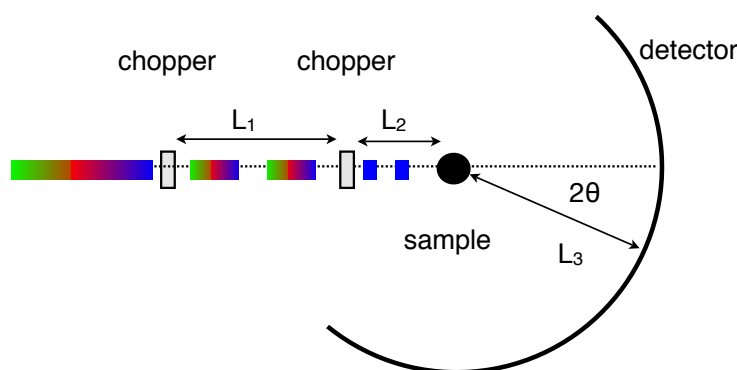


Figure 2.4.: Simple illustration of the TOF principle. A first chopper divides the continuous neutron beam into short neutron pulses. A second chopper selects the desired wavelength. The detector counts neutrons as a function of angle ( $2\theta$ ) and of their arrival time  $t$ . In reality further choppers are needed for the elimination of higher orders and to prevent very slow and very fast neutrons from overlapping (meaning that they arrive simultaneously at the detector).

Incoming neutrons are monochromatized by a number of choppers whose rotation frequencies, phases and positions in the neutron path determine the energy and the length of the neutron package: the desired wavelength  $\lambda$  is selected by the condition  $\lambda = (ht_1)/(mL_1)$  with  $t_1$  being the time between the opening and  $L_1$  the distance between the choppers. The second chopper sets a time-stamp for the departure time of the neutron pulse as its distance  $L_2$  to the sample is precisely known. Scattered neutrons then arrive at the detector after a time  $t$  corresponding to their velocity and hence their energy. The detector signal is a function of  $2\theta$  (see chapter 2.1) and neutron flight time  $t$  and it has to be converted to the  $Q$ - and  $\omega$ -space. The energy transfer  $\Delta\omega$  depends

in a non-linear way on the neutron flight time  $t$ :

$$\Delta E = \hbar\Delta\omega = \frac{1}{2} m (\Delta v)^2 = \frac{1}{2} m L_3^2 \left( \frac{1}{t_0} - \frac{1}{t} \right)^2 = \frac{1}{2} m L_3^2 \left( \frac{\Delta t}{t_0^2 + t_0\Delta t} \right)^2 \quad (2.37)$$

with  $L_3$  denoting the distance between sample and detector,  $t_0$  the flight time of elastically scattered neutrons and the TOF difference between inelastically and elastically scattered neutrons,  $\Delta t = t - t_0$ . (Note that the distance  $L_2$  between "stamp" chopper and sample is cancelled in the difference.) Contrary to BS where the small energy transfers probed allow to neglect the energy dependence of  $Q$  ( $|\mathbf{k}_i| \approx |\mathbf{k}_f|$  and the quasi-elastic approximation holds) in the case of TOF it has to be taken into account. With Eqs. 2.5 and 2.6,  $Q$ ,  $\omega$  and  $2\theta$  depend in the following way on each other:

$$\begin{aligned} \frac{\hbar^2 Q^2}{2m} &= \frac{\hbar^2}{2m} (k_i^2 + k_f^2 - 2k_i k_f \cos(2\theta)) \\ &= 2E_0 - \hbar\omega - 2\sqrt{E_0(E_0 - \hbar\omega)} \cos(2\theta) \end{aligned} \quad (2.38)$$

Figure 2.5 shows the relation between energy transfer and scattering vector for a given scattering angle  $2\Theta$ . For the data analysis the dynamic scattering function  $S(Q, \omega)$  as a function of different but constant  $Q$  and varying energy transfer  $\hbar\omega$  is of interest. In this case  $S(Q, \omega)$  can be constructed for a certain  $Q$  from count rates at different angles which corresponds to vertical cuts in Fig. 2.5. Especially when the TOF data is to be compared to data from other almost constant- $Q$  instruments (like BS) this re-construction is useful.

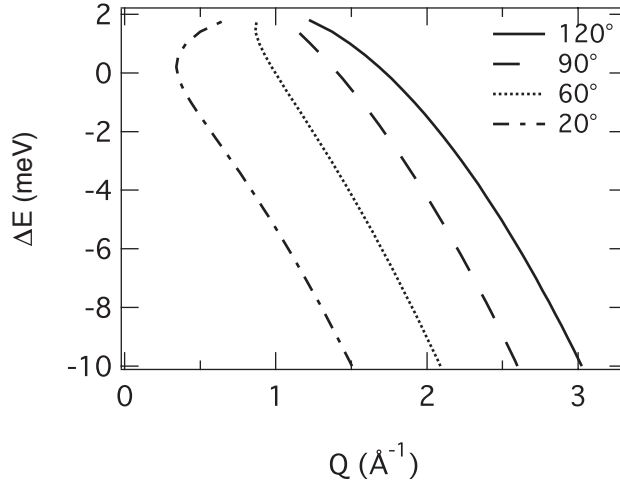


Figure 2.5.: Dynamic range for a TOF-instrument using incident neutrons of  $\lambda = 6.27 \text{ \AA}$ . Lines show the scattering vector  $Q$  - energy transfer  $\delta E$ - dependence for different scattering angles  $2\theta$ .

### 2.2.2.2. Instrument: IN5

**IN5** is a direct geometry disk chopper time-of-flight spectrometer located at the cold neutron guide H16 at the ILL. Resolution (of nearly Gaussian form), intensity and accessible  $Q$ -range depend on each other and can be varied by choosing the appropriate chopper speed<sup>12</sup>. Energy transfers between  $-1000 \text{ meV} < \Delta E = \hbar\omega < 0.6 \cdot E_i$  can be investigated with a wavelength dependent energy resolution in the order of  $\frac{\delta E}{E_i} = 1\% - 3\%$ . Incident wavelengths  $\lambda_i$  from  $1.8 \text{ \AA}$  to  $20 \text{ \AA}$  are possible and the resulting range of momentum transfer is given by the accessible scattering angles and ranges between  $0.28/\lambda_i \leq Q \leq 11.6/\lambda_i$  (for elastic scattering).

### 2.2.2.3. Primary data corrections

The raw data from IN5 have been converted to  $S(Q, \omega)$  by macros implemented in *lamp*. An exemplary data correction macro is shown in the appendix A.4<sup>13</sup>. For the corrections one needs to measure the sample ( $S$ ), empty cell ( $EC$ ) and vanadium ( $V$ ) which scatters almost purely incoherently and elastically. For a profound explanation of the theoretical background and the realization of the calculations see [79, 80] and the *lamp* manual<sup>14</sup>.

1. As a first step spectra from noisy detectors are removed (command: *remove\_spectra*).
2. The sample transmission  $T$  weighted empty cell spectra are then subtracted from the sample spectra:  $S - T \cdot EC$ .
3. The spectra are corrected for the dependence of detector efficiencies on energy and a flat background is removed (command: *corrtof (/background)*).
4. The spectra are corrected for self attenuation and self shielding (command: *safcorr*), see also appendix A.3 for the theoretical background of these corrections.
5. Steps 1. - 4. are repeated for the vanadium measurement  $V$ .
6. Due to the lattice vibrations the vanadium scattering decreases slightly with  $Q$  [74]. The vanadium spectra are explicitly corrected for this Debye-Waller factor [80].
7. The sample spectra are then normalized with respect to the corrected vanadium spectra (command: *vnorm*). Therefore vanadium spectra are integrated over the spectral region (channels) of the elastic peak and the corresponding sample spectra are divided by this integral.
8. The neutron counts per time channel are further transformed to neutron counts per unit energy (command: *t2e*).
9. The spectra are then regrouped to constant  $Q$ , see 2.38 (command: *sqw\_rebin*).
10. Finally the energy-binning can be modified to equidistant energy bins which is necessary for some fitting programs if convolutions are performed (command: *energy\_rebin*).

---

<sup>12</sup><http://www.ill.eu/instruments-support/instruments-groups/instruments/in5/set-up-help/>

<sup>13</sup>Data correction macro written by Jacques Ollivier, ILL

<sup>14</sup><http://www.ill.eu/instruments-support/computing-for-science/cs-software/all-software/lamp/>



### 2.2.3. Neutron-spin-echo spectrometry (NSE)

Neutron-spin-echo spectroscopy (NSE) has been proposed and developed by *Mezei* around 30 years ago [81]. NSE is based on measuring energy transfers by converting them into polarization changes of the neutron beam. Intensity and resolution are decoupled which allows for the use of a wide wavelength band. NSE is the neutron scattering technique with the highest energy resolution. Contrary to TOF and BS, NSE measures the intermediate scattering function  $I(Q, t)$  that was introduced in section 2.1.

#### 2.2.3.1. Principle

In a magnetic field  $\mathbf{B}$  the neutron spin component perpendicular to  $\mathbf{B}$  performs a precession around the direction of  $\mathbf{B}$ . The frequency  $\omega_L$  of the precession depends on the magnitude of  $\mathbf{B}$  and on the gyromagnetic ratio of the neutron  $\gamma = 2\pi \cdot 2913.07 \cdot 10^4 \text{ s}^{-1}\text{T}^{-1}$ :

$$\omega_L = \gamma B \quad (2.39)$$

Figure 2.6 shows the principle NSE set-up:

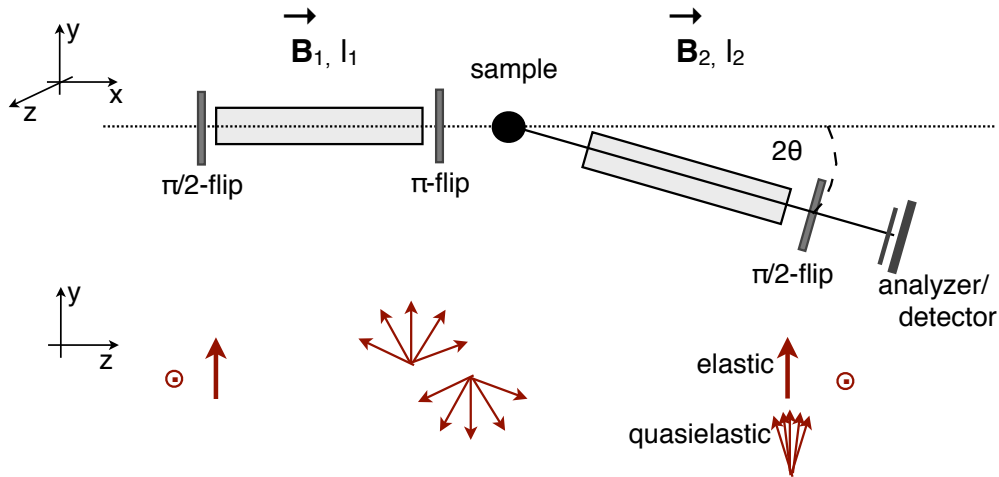


Figure 2.6.: Simple illustration of the NSE set-up. Upper part of the figure shows the main parts of the instrument, below is shown the corresponding orientation of the neutron spin. Neutrons enter the first magnetic field  $\mathbf{B}_1$  with their spin being perpendicular to it. Leaving the first coil of length  $l_1$ , the direction of each neutron's spin depends on the time spent in the coil and hence on the velocity of the neutron. After being flipped by  $\pi$  the scattered neutrons enter the second field  $\mathbf{B}_2 = \mathbf{B}_1$  of length  $l_2 = l_1$ . In the case of an elastic coherent scatterer the spins undergo the same number of precessions in both coils and the polarization measured at the detector is ideally  $P = 1$  whereas after a quasielastic scattering process the final polarization is reduced  $P < 1$ .

An incident non-polarized neutron beam is reflected by a magnetic multilayer mirror

which yields a longitudinally polarized neutron beam. This beam enters a so-called  $\pi/2$ -flipper which rotates the neutron spin such that on exit the neutrons are polarized perpendicular to their flight direction. They now enter a first magnetic field  $\mathbf{B}_1$  parallel to their flight direction. While traveling the time  $t$  through this first arm of length  $l_1$  of the NSE spectrometer they perform a number  $N_1$  of precessions corresponding to a precession angle of  $\alpha_1$ :

$$N_1 = \frac{\alpha_1}{2\pi} = \frac{\omega_L t}{2\pi} \quad (2.40)$$

The time  $t = l_1/v_i$  depends on the incident velocity  $v_i$  of the neutron and with Eq. 2.1 we can rewrite Eq. 2.40 to:

$$N_1 = \frac{\gamma B_1 l_1 m \lambda_i}{2\pi \hbar} = \frac{\gamma B_1 l_1}{2\pi v_i} \quad (2.41)$$

A  $\pi$ -flipper rotates the neutron spins by  $180^\circ$ , meaning that the up to now accumulated precession angle is transformed from  $\alpha_1 \rightarrow -\alpha_1$ . The neutrons are then scattered by the sample and with a final wavelength of  $\lambda_f = \lambda_i + \Delta\lambda$  they enter the second magnetic field  $\mathbf{B}_2$ , again parallel to their flight direction, where they continue to precess  $N_2$  turns (precession angle  $\alpha_2$ ):

$$N_2 = \frac{\alpha_2}{2\pi} = \frac{\gamma B_2 l_2 m \lambda_f}{2\pi \hbar} = \frac{\gamma B_2 l_2}{2\pi v_f} \quad (2.42)$$

If both magnetic regions are of equal length,  $l = l_1 = l_2$ , direction and magnitude,  $\mathbf{B}_1 = \mathbf{B}_2 = B$ , then the final precession angle  $\Omega$  for a neutron with initial wavelength  $\lambda_i$  and final wavelength  $\lambda_f = \lambda_i + \Delta\lambda$  is:

$$\begin{aligned} \Omega &= \alpha_2 - \alpha_1 = 2\pi(N_2 - N_1) \\ &= \frac{\gamma B l m}{\hbar} (\Delta\lambda) \end{aligned} \quad (2.43)$$

In principle one could also realize the NSE principle without the  $\pi$ -flipper by using two magnetic fields of equal length and magnitude but of *opposite* direction,  $\mathbf{B}_1 = -\mathbf{B}_2$ . In practice this is disadvantageous because this implies a region of zero magnetic field at the sample location which would cause beam depolarization<sup>15</sup>.

Coming back to 2.43 we are now expanding the energy transfer  $\omega$ , given by Eq. 2.5, in  $\frac{\Delta\lambda}{\lambda_i}$ . Taking into account only the leading order one obtains:

$$\Omega \approx \frac{\gamma B l \hbar}{m v_i^3} \omega \quad (2.44)$$

---

<sup>15</sup>A small "guide field" in the order of a few Gauss is mandatory in order not to lose the defined polarization.

Another  $\pi/2$  spin-flipper located after the second magnetic region converts the final precession angle to a longitudinal polarization component - the neutron "stop watch" is stopped. It follows an analyzer which accepts only the longitudinal polarization component and finally the detector measures the beam polarization  $P$ :

$$P = \langle \cos(\Omega) \rangle \quad (2.45)$$

where  $\langle \dots \rangle$  denotes the average over all scattered neutrons. In the case of coherent and elastically scattered neutrons the number of precessions in both arms is equal, hence  $\Omega = 0$  and the polarization is maximum  $P = 1$ . Inelastically scattered neutrons undergo a different number of precessions during their flight through  $\mathbf{B}_1$  and  $\mathbf{B}_2$ , therefore  $\Omega \neq 0$  and the final neutron beam polarization is reduced  $P < 1$ . For small energy transfers  $\frac{\Delta\lambda}{\lambda_i} \ll 1$  and  $\Delta E \ll k_b T$ ,  $S(Q, \omega)$  is an even function and the polarization  $P$  can be expressed as:

$$P(Q, t) = \frac{\int_{-\infty}^{\infty} S(Q, \omega) \cos(\omega t) d\omega}{\int_{-\infty}^{\infty} S(Q, \omega) d\omega} = \frac{I(Q, t)}{I(Q, 0)} \quad (2.46)$$

With the Fourier time  $t$ :

$$t = \frac{\gamma m^2 B l}{2\pi h^2} \lambda^3 = \frac{\gamma B l \hbar}{m v^3} \quad (2.47)$$

Note that the accessible Fourier time  $t$  depends on the third power of the wavelength  $\lambda$  and it is proportional to the magnetic field integral  $B l$ . The resolution may thus be increased by increasing either one of them.

Again the case of magnetic scattering, which includes a spin-flip, will not be discussed as all our samples were non-magnetic.

A typical NSE experiment consists in measuring the polarization  $P(Q, t)$  as a function of  $t$  for a scattering vector  $Q$  given by the angle  $2\theta$  of the second instrument arm with respect to the first arm.  $t$  is stepwise scanned by changing the current through the coils thus increasing the magnitude of  $B$ ; see Eq. 2.47. For each set of  $t$  and  $Q$ , the detector count rate has to be determined at the symmetry point, where field integrals before and after the scattering are equal.

Experimentally the symmetry point has to be located by means of a tunable extra current (phase current) through one of the coils. Figure 2.7 displays the schematic form of count rate as a function of phase current; at the symmetry point the count rate is maximum and there the amplitude  $A_{echo}$  is determined. The red line in Fig. 2.7 shows such an echo for a neutron beam with a Gaussian wavelength distribution with width  $\Delta\lambda$  centered at  $\lambda_0$ . The period of the echo is proportional to  $1/\lambda_0$  whereas the width of the envelope, shown by the broken line in Fig. 2.7, scales with  $1/\Delta\lambda$  [81]

Furthermore it has to be taken into account that the scattered intensity is always composed of coherent and incoherent contributions. While coherent scattering does not influence the spin orientation, for incoherent scattering the probability for a spin flip equals  $2/3$ . Incoherent scattering therefore changes the initial beam polarization to  $-1/3$ . Therefore at the beginning of a NSE measurement intensities for *spin-up* and *spin-down* have to be determined. For each value of  $Q$  one counts the scattered neutrons with  $\pi$ -flipper on and off respectively (a guide field maintains the beam polarization). Independent of  $B$  the maximal average polarization is calculated for every  $Q$ -value:  $\langle pol \rangle = \frac{up-down}{2}$  with  $up = I_{coh} + \frac{1}{3}I_{inc}$  and  $down = \frac{2}{3}I_{inc}$ .

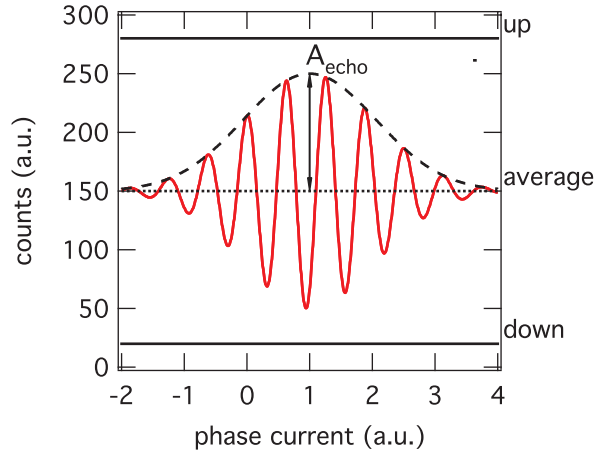


Figure 2.7: Schematic echo form: detector count rate as a function of phase current for a Gaussian wavelength distribution with width  $\Delta\lambda$  centered at  $\lambda_0$ . The echo is a cosine with a periode  $\propto 1/\lambda_0$ ; the width of the Gaussian envelope is inversely proportional to  $\Delta\lambda$ . See text for further explanations.

The echo amplitude  $A_{echo}$  (see Fig. 2.7) as a function of Fourier time  $t$  is then given by:

$$A_{echo} = I_{coh} \cdot f_{coh}(t) - \frac{1}{3}I_{inc} \cdot f_{inc}(t) \quad (2.48)$$

where  $f_{coh}$  and  $f_{inc}$  are normalized functions ( $f = 1$  for  $t = 0$ ) representing the dynamics of coherent and incoherent contributions. Finally we obtain the normalized intermediate scattering function:

$$\frac{I(Q, t)}{I(Q, 0)} = \frac{A_{echo}}{up - down} = \frac{I_{coh} \cdot f_{coh}(t) - \frac{1}{3}I_{inc} \cdot f_{inc}(t)}{I_{coh} - \frac{1}{3}I_{inc}} \quad (2.49)$$

where the division by  $(up - down)$  instead of the average intensity accounts for instrumental as well as incoherent polarization losses.

### 2.2.3.2. Instrument: IN15

**IN15** is located at the cold polarizing guide H511 at the ILL. Through a velocity selector the incident wavelength can be tuned between 6 and 25 Å with width of the

wavelength distribution FWHM  $\approx 15\%$ . The standard beam diameter at the sample is 40 mm. The  $^3\text{He}/\text{CF}_4$  multidetector is located at a distance of 4.6 m from the sample. It covers (32 cm·32 cm) and is build of  $32 \cdot 32$  pixel having each an are of  $1 \text{ cm}^2$ . With an angular resolution of  $2 \cdot 10^{-3}$  rad a scattering angle of  $2^\circ \leq 2\theta \leq 140^\circ$  can be accessed. The maximum field integral in the precession coils is  $2.7 \cdot 10^5$  Gcm.

### 2.2.3.3. Primary data corrections

The instrumental resolution is determined by measuring a purely coherent elastic scatterer (e.g. graphite). In the time domain the correction of the measured signal (subscript  $m$ ) for resolution (subscript  $res$ ) is then a simple division:

$$\left[ \frac{I(Q, t)}{I(Q, 0)} \right] = \left[ \frac{I(Q, t)}{I(Q, 0)} \right]_m \cdot \left[ \frac{I(Q, t)}{I(Q, 0)} \right]_{res}^{-1} \quad (2.50)$$

Furthermore we corrected the measured sample signal for scattering from the solvent and the sample holder. The scattering from the deuterated oil is coherent but out of the time window. It therefore only influences the counting rates for *up* and *down* but it gives no echo:  $f_{\text{coh}}(t)$  in Eq. 2.48 decays faster to zero than resolvable. The sample holder gives only an elastic contribution  $I_{\text{coh},c}$ :  $f_{\text{coh}}(t) = 1$  in Eq. 2.48. As the samples are nearly fully deuterated we neglect the incoherent scattering.

1. One measures the intermediate scattering function of sample (subscript  $s$ ) and sample holder (subscript  $c$ ) and solvent toluene-d8 (subscript  $t$ ) together:

$$\left[ \frac{I(Q, t)}{I(Q, 0)} \right]_{s+c+t} = \frac{I_{\text{coh},s} \cdot f_{\text{coh}}(t) + I_{\text{coh},c}}{\langle pol \rangle_{s+c+t}} \quad (2.51)$$

with the average  $Q$ -dependent polarization  $\langle pol \rangle = \frac{up-down}{2}$ .

2. As background the intermediate scattering function of toluene-d8 in the same sample holder is measured:

$$\left[ \frac{I(Q, t)}{I(Q, 0)} \right]_{c+t} = \frac{I_{\text{coh},c}}{\langle pol \rangle_{c+t}} = \text{elastic fraction} \quad (2.52)$$

And we want to determine the intermediate scattering function of the sample alone:

$$\left[ \frac{I(Q, t)}{I(Q, 0)} \right]_s = \frac{I_{\text{coh},s} \cdot f_{\text{coh}}(t)}{\langle pol \rangle_s} \quad (2.53)$$

With  $T$  being the transmission of sample ( $s+c+t$ ) with respect to that of the background ( $c+t$ ) the average polarization of neutrons scattered by the sample calculates from the *up* and *down* rates measured :

$$\langle pol \rangle_s = \langle pol \rangle_{s+c+t} - T \cdot \langle pol \rangle_{c+t} \quad (2.54)$$

With Eq. 2.51 we obtain the corrected intermediate scattering function of the sample:

$$\left[ \frac{I(Q, t)}{I(Q, 0)} \right]_s = \frac{\left[ \frac{I(Q, t)}{I(Q, 0)} \right]_{s+c+t} \langle pol \rangle_{s+c+t} - T \cdot \left[ \frac{I(Q, t)}{I(Q, 0)} \right]_{c+t} \langle pol \rangle_{t+c}}{\langle pol \rangle_{s+c} - T \cdot \langle pol \rangle_{c+t}} \quad (2.55)$$

## 2.2.4. Neutron small angle scattering (SANS)

The aim of SANS is the determination of the time averaged (static) structure of the sample. Contrary to the three quasi-elastic neutron scattering techniques studying dynamic processes, SANS gives information about shape and spatial organization of the scattering objects of size in the order of 1 nm to 100 nm. Small angle scattering was first explored about 70 years ago by *Guinier* who investigated metal alloys with X-rays [82]. The development of SANS instruments started about 20 years later in the 1960s. The big advantage of neutrons over the often complementary used X-rays, is neutrons being non-destructive and sensitive to light elements. Especially the difference in scattering length densities between hydrogen and deuterium is widely exploited to highlight special compounds of the sample. Today SANS is one of the most important techniques for the structural investigation of soft matter samples like polymers, surfactant aggregates or biological systems as for example membranes and protein solutions [21].

### 2.2.4.1. Principle

Figure 2.8 shows a schematic SANS diffractometer:

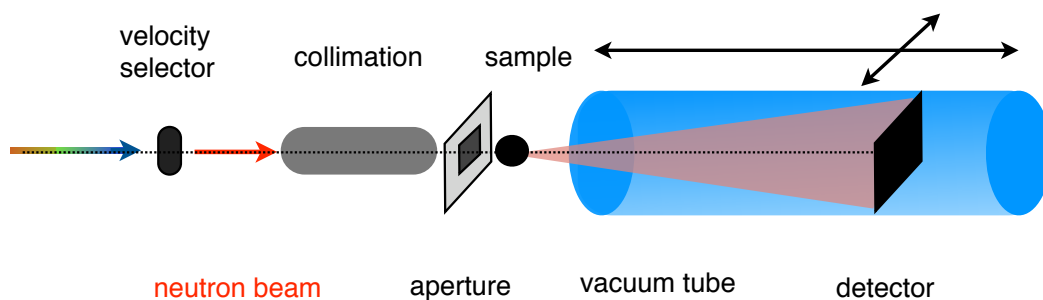


Figure 2.8.: Simple illustration of a SANS instrument.

Neutrons are monochromatized by a velocity selector which lets only the desired wavelength pass. After being further collimated the final beam size before the sample is defined by an aperture whose shape is chosen to match the specific sample geometry. The well defined neutron beam then hits the sample and is scattered. Depending on the  $Q$ -range of relevance the detector can be moved in the evacuated tube. In the case

of isotropic samples the detector may also be offset laterally to cover a larger  $Q$ -range. Usually several detector-collimation settings have to be combined to cover the  $Q$ -range of interest<sup>16</sup>.

#### 2.2.4.2. Instruments: D11 and D22

**D11** is a pinhole geometry SANS instrument installed at the cold neutron guide H15 at the ILL. Neutrons are monochromatized by a velocity selector. By choosing the appropriate selector velocity, neutron wavelengths  $\lambda$  between 4.5 Å and 40 Å with  $\Delta\lambda/\lambda \sim 0.1$  can be obtained. A (64 cm × 64 cm) <sup>3</sup>He multi-detector in an evacuated tube counts neutrons at a variable distance from the sample from 1.1 m to 36.7 m. The accessible scattering vector ranges between  $5 \cdot 10^{-4} \text{ Å}^{-1} \leq Q \leq 0.44 \text{ Å}^{-1}$ . The neutron flux at the sample is at maximum  $3.2 \cdot 10^7 \text{ cm}^{-2} \text{ s}^{-1}$ .

**D22** is located at the cold neutron guide H512 at the ILL. Neutrons are mono-chromatized by a velocity selector, which consists of a rotating drum with helically curved absorbing slits at its surface. By choosing the appropriate selector rotation speed neutron wavelengths between  $4.5 \text{ Å} \leq \lambda \leq 40 \text{ Å}$  with  $\Delta\lambda/\lambda \sim 10\%$  can be obtained. After the selector a set of vertical and horizontal slits follows to reduce the beam size. Then neutrons pass through a low efficiency detector, the monitor, its countrate is used for data normalization. The collimation consists of 8 guides which can be varied to yield a free flight path of 1.4 m to 17.6 m. Before hitting the sample the size of the neutron beam is defined by an aperture made of B<sub>4</sub>C covered by Cadmium, both strong neutron absorbers. Its shape is chosen to match the sample geometry. A (102 cm × 98 cm) <sup>3</sup>He multi-detector moveable in an evacuated tube of 2 m diameter counts neutrons at a variable distance from the sample from 1.1 m to 17.7 m. A beam stop made of B<sub>4</sub>C and Cadmium shields the detector from the direct beam. The accessible scattering vector ranges between  $5 \cdot 10^{-4} \text{ Å}^{-1} \leq Q \leq 0.44 \text{ Å}^{-1}$  without detector offset and up to  $0.85 \text{ Å}^{-1}$  with detector offset. With a maximum neutron flux at the sample of  $1.2 \cdot 10^8 \text{ cm}^{-2} \text{ s}^{-1}$  D22 is about ten times more intense than D11.

#### 2.2.4.3. Primary data corrections

The neutron intensity  $I$  as measured by the detector has to be corrected for background, detector efficiency, and normalized to a standard scatterer to obtain the differential cross-section  $\frac{d\sigma}{d\Omega}$ , see section 2.1.2. The structural information is then contained in its coherent part  $\left(\frac{d\sigma}{d\Omega}\right)_{\text{coh}}$ . The data is further divided by the sample volume  $V$  to give the

<sup>16</sup>A world directory of SANS instruments is available under: <http://www.ill.eu/instruments-support/instruments-groups/groups/lss/more/world-directory-of-sans-instruments/>

macroscopic cross section, a quantity that is independent of the sample size:

$$I(\text{cm}^{-1}) = \frac{d\Sigma}{d\Omega} = \frac{1}{V} \frac{d\sigma}{d\Omega} \quad (2.56)$$

Absolute intensity calibration and correction for detector efficiency are done using water as a secondary standard. Due to its predomination incoherent cross section water scatters uniformly over the whole  $Q$ -range. Comparison to vanadium spectra then allow to derive absolute scattering cross sections. Besides the wanted scattered neutrons the detector always also counts neutrons not coming from the incident beam and electronic noise. This background is measured by placing the neutron absorber  $\text{B}_4\text{C}$  instead of the sample.

Scattering and absorption of the sample holder are taken into account by measuring the transmission  $T_h$  and the scattered intensity  $I_h$  of an empty sample holder. The scattered sample intensity  $I_s$  then can be derived from the total measured intensity  $I_t$  and transmission  $T_t$  of sample and holder together:

$$I_s = I_t - \frac{T_t}{T_h} \cdot I_h \quad (2.57)$$

These primary data corrections were done using the following standard ILL software [83]:

- *det*: Determination of the beam center.
  - *rmask*: Creation of detector mask.
  - *windet*: Determination of transmissions.
  - *rnils*: Radial averaging.
  - *spolly*: Background subtraction and normalization to absolute intensity.
  - *smorger*: Merging of data from different settings and rebinning to constant  $Q$ -spacing.
- Finally the macroscopic scattering cross section  $\frac{d\Sigma}{d\Omega} = I(\text{cm}^{-1})$  is obtained.

A detailed and comprehensive treatise of SANS data correction and analysis can be found in [83].



### 2.2.5. Energy resolution

On an ideal instrument having perfect energy resolution one would measure in the frequency domain a quantity proportional to the double differential cross section  $\frac{d^2\sigma}{d\Omega d\omega}$  as given by 2.7. In reality this is not the case as experimentally the dynamic scattering function is convoluted with the instrument-specific resolution function  $R$  of the spectrometer:

$$S(\mathbf{Q}, \omega) = \int S(\mathbf{Q}, \omega') R(\omega' - \omega) d\omega' \quad (2.58)$$

Generally the resolution is a peaked function whose width  $\delta\omega$  depends on the specific instrumental set-up.  $\delta\omega$  determines how well the long time limit of  $G(\mathbf{r}, t)$  can be probed. This long time limit is of special interest as it gives information about the type of motion. E.g. one expects for a liquid no elastic scattering as  $G_s(\mathbf{r}, t) \rightarrow 0$  for  $t \rightarrow \infty$ . In contrast to this a slow translational diffusion (e.g. at low temperature) or spatially confined motions gives always rise to elastic scattering. In order to decide whether there is a real elastic intensity, one therefore needs a good instrumental resolution. Experimentally line broadenings of down to 15% of the resolution may be resolved.

## 2.2.6. The choice of the instrument

On the previous pages we have introduced different kinds of neutron spectrometers. The choice of the instrument depends on the dynamic process that one wants to observe. In Fig. 2.9 we show a rough comparison of time  $t$  and length  $L$  scale and accordingly momentum  $Q$  and energy  $\hbar\omega$  transfer range accessed by the introduced quasi-elastic instruments<sup>17</sup>. By light grey areas we mark the  $t$ - $L$ -range of interest for the dynamic processes that we are interested in. We show estimations for: (1) entire droplet diffusion, (2) droplet form fluctuations, (3) water rotation and (4) water translation<sup>18</sup>. It can be seen that water translation and rotation match the range accessed by TOF and BS, shell fluctuations need to be measured by NSE.

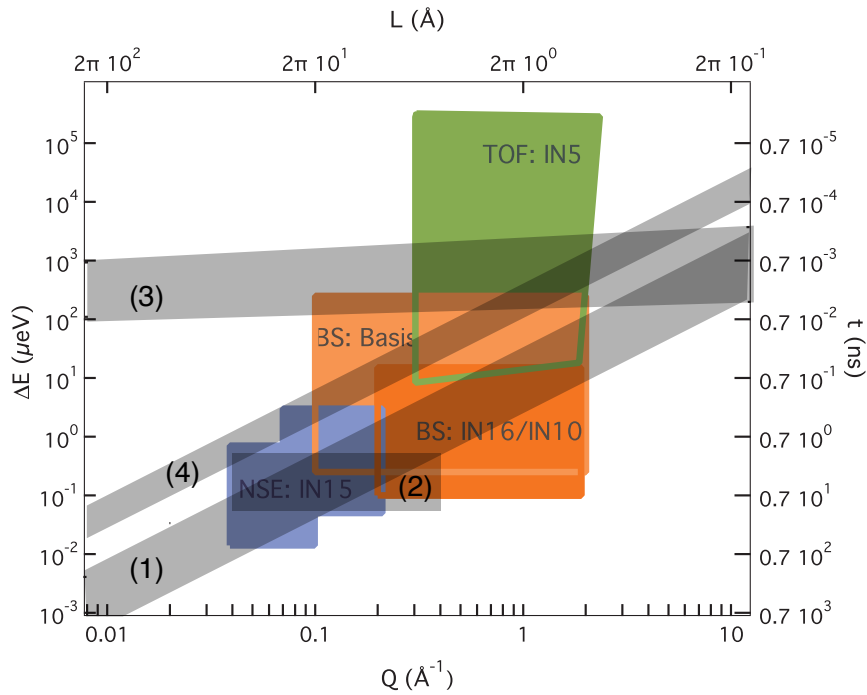


Figure 2.9.: Rough comparison of time and length scales probed by the QENS instruments used for this work. Note that we show the range accessed by configurations we used. Light grey areas correspond to the estimation of the  $t$ - $L$ -range relevant for the different dynamic processes that we will investigate: (1) droplet diffusion, (2) droplet form fluctuations, (3) water rotation and (4) water translation.

<sup>17</sup>Note that for each instrument we show the region corresponding to the instrumental setting applied for our experiments - different settings may give access to other  $t$ - $L$ .

<sup>18</sup>(1) and (2) are estimated after scaled parameters given in [84] for (3) and (4) we use results obtained for free water after [85].

### 3. Structure of the pure microemulsion

For the interpretation of the experiments on dynamics - both droplet self-dynamics or confined water dynamics - it is essential to first obtain an exact knowledge about the structure of the microemulsion.

From several studies around room temperature it is established that in the here relevant composition range, the water/AOT/oil microemulsion forms a w/o droplet structure. Spherical water droplets coated by a monolayer of AOT are dispersed in the continuous oil matrix [16,17,30]. But whereas the phase diagram from room temperature up to the high temperature phase border is well investigated, very little is known about the phase behavior and structure of this microemulsion for temperatures below the freezing point of bulk water.

This chapter presents SANS experiments that have been performed in order to characterize the microemulsion structure in detail as a function of composition and temperature.

We start with the description of the fitting model for the SANS data analysis and continue with the presentation of the results. The microemulsions structure under variation of the water loading for samples with  $0 \leq \omega \leq 40$  is subject of **series 1:  $\omega$ -variation**. After briefly discussing the effect of droplet density on the droplet structure, **series 2:  $\phi$ -variation**, studied for one sample with  $\omega = 8$  and droplet volume fractions between  $0.05 \leq \phi \leq 0.2$ , we will turn to the temperature dependent investigations. The structure of microemulsions with  $0 < \omega \leq 12$  and  $\phi = 0.2$  has been deduced from SANS measurements down to temperatures of  $T \approx 220$  K, **series 3:  $T$ -variation**. Moreover pure reverse micelles  $\omega = 0$  and  $\phi = 0.1$  were studied.

Part of these results are covered by two recent publications [86,87]

Table 3.1.: Overview of SANS measurements carried out on pure water/AOT/oil microemulsions to determine the structure as a function of molar ratio  $\omega$ , droplet volume fraction  $\phi$  and temperature  $T$ . The bold parameter is varied during the series.

Series	$\omega$	$\phi$	$T/\text{K}$	Section
1: $\omega$ -variation	<b>0 - 40</b>	0.05 - 0.2	$\approx 290$	3.3
2: $\phi$ -variation	8	<b>0.05 - 0.2</b>	$\approx 290$	3.4
3: $T$ -variation	0 - 12	0.2	<b>220 - 300</b>	3.5

### 3.1. Core-shell model for the structure

SANS is an ideal tool for the structural investigation of this microemulsion system: on the one hand it covers the  $Q$ -range of interest determined by the size of the droplets and on the other hand one can optimize the contrast of the sample by selective deuteration. The SANS raw data is corrected after the procedure described in 2.2.4.3. The resulting absolute intensity (normalized to the sample volume) is then fitted using the NIST package for analysis of SANS and USANS data [88] to the model explained in the following. For interacting polydisperse droplets of number density  $n$  with uncorrelated size and position the scattering cross section per unit volume  $I(Q)$  can be written as the product of the averaged droplet form factor  $\langle F(Q) \rangle$  and a structure factor  $S(Q)$  accounting for droplet-droplet interactions<sup>1</sup>:

$$I(Q) = n \cdot \langle F(Q) \rangle \cdot S(Q) + I_{inc} \quad (3.1)$$

$I_{inc}$  denotes the incoherent  $Q$ -independent background that is treated as a separate fitting parameter. Note that we deal with an isotropic system which means that  $I(\mathbf{Q}) = I(Q)$  holds.

It is established that in the chosen composition range the microemulsion consists of spherical water cores coated by a monolayer of AOT molecules dispersed in the oil matrix. In Eq. 3.1 we therefore use a form factor  $F(Q)$  for a spherical core-shell particle with core radius  $R_c$  and shell thickness  $d$  [20]:

$$F(Q) = \left[ 4\pi(\rho_c - \rho_s)R_c^3 \left( \frac{j_1(QR_c)}{QR_c} \right) \right. \quad (3.2)$$

$$\left. + 4\pi(\rho_s - \rho_m)(R_c + d)^3 \left( \frac{j_1(Q(R_c + d))}{Q(R_c + d)} \right) \right]^2 \quad (3.3)$$

where  $j_1$  denotes the spherical Bessel function of first order and subscripts  $c, s, m$  stand for core, shell and matrix respectively. The coherent scattering length densities  $\rho$  of each sample compound are calculated after:

$$\rho = \frac{1}{V} \sum_i b_{coh}^i \quad (3.4)$$

with  $V$  being the molecular volume and  $b_{coh}^i$  the coherent scattering length of atom  $i$  in the molecule [75]. The resulting values for  $\rho$  of the used solvents and water in protonated and deuterated form are listed in Table A.1.

---

<sup>1</sup>The factorization of  $F(Q)$  and  $S(Q)$  Eq. 3.1 strictly holds only for a system of monodisperse scatterers as the effect of polydispersity on  $S(Q)$  is in Eq. 3.1 neglected. For weak interparticle interferences as it is the case here the error in  $S(Q)$  is small and does not affect the formfactor parameters [89].

The droplet size polydispersity  $p$  is accounted for by using in Eq. 3.1 a formfactor  $\langle F(Q) \rangle$  that is averaged over Schultz-Zimm<sup>2</sup> distributed radii [90]:

$$f(R, z) = \left( \frac{z+1}{\langle R_c \rangle} \right)^{z+1} R_c^z \exp\left(-\frac{z+1}{\langle R_c \rangle} R_c\right) \frac{1}{\Gamma(z+1)}; \quad z > -1 \quad (3.5)$$

with the Gamma function  $\Gamma(x) = \int_0^\infty e^{-t} t^{x-1} dt$ . The parameter  $z$  relates to the droplet size polydispersity:

$$p = \frac{\sqrt{\langle R_c^2 \rangle - \langle R_c \rangle^2}}{\langle R_c \rangle} = \frac{1}{\sqrt{1+z}} \quad (3.6)$$

To describe droplet-droplet correlations a structure factor  $S(Q)$  for a hard sphere fluid with a narrow attractive well is used; the detailed form of this so-called Baxter sticky sphere structure factor is shown in the appendix A.5. In this model a perturbation parameter  $\epsilon$  is defined as the ratio of the width of the attractive well to the total particle radius (hard sphere radius plus attractive well) [91,92]. The strength of the attractive interaction is described in terms of the stickiness  $\tau$ ; the smaller  $\tau$  is the stronger is the attraction between the droplets, see A.5.

For the fitting procedure  $\epsilon$  is fixed to 0.05 and only the stickiness parameter  $\tau$  was varied. As we work with a moderate droplet volume fraction  $\phi \leq 0.2$  we do not see a strong effect of droplet interactions which would reveal itself by a structure factor peak at low scattering vector  $Q$ . Nevertheless the inclusion of a sticky hard sphere structure factor led to a significant increase of the fit quality at low  $Q$  as our model describes the scattering intensity in absolute units. A slight increase or decrease of the absolute intensity essentially at smaller  $Q$  is caused by droplet interactions. We found that the inclusion of the structure factor did not have a significant effect on the form factor parameters. We therefore do not further discuss the structure factor parameters (stickiness  $\tau$  and perturbation parameter  $\epsilon$ ) in the following but we include  $S(Q)$  in the fitting to obtain a better agreement between data and fits at the lowest  $Q$ -values.

For structural investigations samples with so-called shell contrast are best suited: by using heavy water  $D_2O$  and deuterated oil and only protonated surfactant AOT the coherent scattering length density profile exhibits a sharp step and the incoherent flat background  $I_{inc}$  is minimized. Figure 3.1 shows a sketch of a pure AOT micelle and a water swollen micelle together with the corresponding contrast profiles: since  $D_2O$ , the deuterated oil and the AOT headgroups have very similar coherent scattering length densities, the main contrast arises from the AOT tails. The droplet core radius  $R_c$  in Eq. 3.2 includes the water and the headgroups of the AOT and the shell of thickness  $d$

<sup>2</sup>Contrary to the Gauss distribution the Schultz-Zimm distribution is asymmetric; the physical non-sensical case of negative radii is excluded. For  $z \rightarrow \infty$  Eq. 3.5 becomes a  $\delta$ -peak centered at  $\langle R_c \rangle = R_c$ .

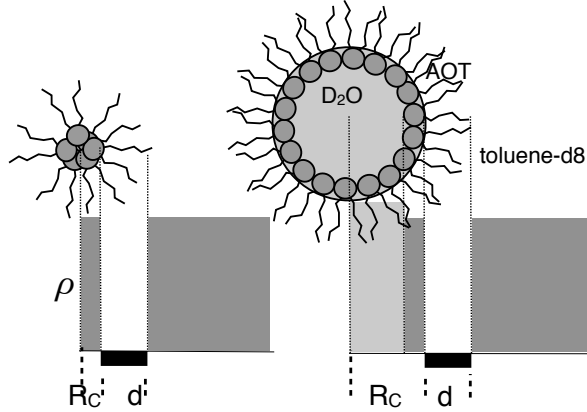


Figure 3.1.: Schematic coherent scattering length density  $\rho_{coh}$  profile of an AOT reverse micelle and a D<sub>2</sub>O swollen reverse micelle in toluene-d8 (shell contrast).

is made of the surfactant tails.

To stabilize the fit it is important to fix as many parameters as possible. For the fitting procedure in the case of shell-contrast samples the coherent scattering length densities  $\rho_c$  of D<sub>2</sub>O and  $\rho_m$  of the deuterated oil were therefore fixed to their theoretical values, whereas  $\rho_s$  of the AOT tails (shell) was allowed to vary between its calculated value and  $\rho_m$  as the oil is known to penetrate between the AOT tails.

Furthermore we want to emphasize that the absolute normalized intensity is fitted. This means, that the droplet number density  $n$  in Eq. 3.1 calculates from the droplet volume fraction  $\phi$  and the droplet volume  $V_d = 4/3\pi(R_c + d)^3$ :

$$n = \phi/V_d \quad (3.7)$$

In principle  $\phi$  is a known parameter defined by the prepared sample composition. Nevertheless it has to be treated as a free fitting parameter, as  $\phi$  depends sensitively on the correct absolute intensity. In the case of SANS data the normalization of the intensity is known to be possible only within an error of about 10%. Moreover transmissions have only been measured around room temperature. If the sample composition seen by the neutron beam (which hits the middle of the sample holder) changes with temperature, normalizing to the transmission measured at room temperature introduces a systematic error to the absolute intensity. Hence also the results of  $\phi$  and  $\rho_s$  for temperatures below the temperature where the transmission has been measured may be systematically wrong. Fitting results for  $\phi$  around room temperature were reasonably close to the real prepared  $\phi$ . In the case of the temperature-dependent study we will desist from a detailed discussion of the fitted  $\phi$  due to the above given arguments.

The Igor package allows to convolute the model curves with the known instrumental

resolution:

$$\Delta Q^2 = \Delta Q^2(\lambda) + \Delta Q^2(\theta) \quad (3.8)$$

$$= Q^2 \left[ \left( \frac{1}{2\sqrt{2\ln 2}} \frac{\Delta\lambda}{\lambda} \right)^2 \right] + \left[ \left( \frac{4\pi}{\lambda} \right)^2 - Q^2 \right] \Delta\theta^2 \quad (3.9)$$

where  $\Delta\lambda/\lambda$  is given by the wavelength distribution and  $\Delta\theta$  is related to the width and divergence of the collimated direct beam. Typical values for D11 and D22 are  $\Delta\lambda/\lambda \approx 10\%$  and  $\Delta\theta \approx 2 \cdot 10^{-3}$  rad. The inclusion of the instrumental resolution is mainly important for the correct determination of the polydispersity  $p$  [93].

### 3.2. Experimental details

SANS experiments were carried out on two small angle diffractometers at the ILL.

On **D11** a neutron wavelength of  $\lambda = 4.6 \text{ \AA}$  was used. The detector was placed at three different distances of 1.1 m, 5 m and 20 m from the sample with respective collimations of 8 m, 8 m and 20.5 m. These configurations covered a range of scattering vectors  $0.01 \text{ \AA}^{-1} \leq Q \leq 0.45 \text{ \AA}^{-1}$ . Samples were measured in Quartz cells with 1 mm sample thickness at a temperature of  $(287 \pm 1) \text{ K}$ .

On **D22** a neutron wavelength of  $\lambda = 6 \text{ \AA}$  was used. The detector was placed at a distance of 2 m from the sample with a collimation of 8 m. This configuration covered a range of scattering vectors  $0.025 \text{ \AA}^{-1} \leq Q \leq 0.47 \text{ \AA}^{-1}$ . All samples were measured in 1 mm thick flat aluminum holders<sup>3</sup> sealed with indium. A standard ILL orange cryostat was used for temperature control. The investigated microemulsions scatter that strongly that for the chosen instrumental configuration a counting time of 2 min was sufficient to obtain a smooth spectrum. This fact allowed to optimize the precious neutron beam time by cooling and counting simultaneously: the samples were cooled from  $T \geq 285 \text{ K}$  down to 220 K with a cooling rate of 0.5 K/min. While cooling, spectra were taken continuously with an accumulation time of 2 min/spectrum. This means that while taking one spectrum the sample temperature changes about 1 K. Transmission measurements were performed around room temperature before starting the cooling scan. Determining the transmission at every temperature - as it would be correct if the sample composition seen by the beam may change - is unfortunately too time consuming because the SANS spectra are measured in a continuous cooling scan and for transmission measurements the experimental set-up would have to be changed, thus the ramp would be interrupted each time. In the investigated temperature range all used solvents are liquid. Bulk freezing temperatures of the used solvents are listed in Tab. A.1.

<sup>3</sup>Sample holders were provided by M. Prager, Jülich

### 3.3. Series 1: $\omega$ -variation

In section 1.3.1.2 we presented simple geometrical considerations which led to a linear relationship between the droplet radius and the molar ratio  $\omega$  [19]. In this work we tested this predicted relation (Eq. 1.5) for the range of compositions that is of interest for the later study of water in soft confinement. The structure of a selection of water/AOT/oil microemulsions with varying oils (heptane-d8, decane-d10 and toluene-d7) and different compositions ( $0 \leq \omega \leq 40$  and  $0.05 \leq \phi \leq 0.2$ ) was measured by means of SANS. All investigated samples are listed in Tab. 3.2. Different surrounding oils have been used in order to span a wide range of droplet sizes and for changing the freezing point and the viscosity of the surrounding matrix. Whereas  $\text{H}_2\text{O}/\text{AOT}/\text{toluene}$  only forms a stable droplet microemulsion up to a molar ratio of  $\omega = 12$ , and therefore restricts the droplet radius to about 20 Å, decane as oil allows for droplet radii up to more than 60 Å. On the other hand decane crystallizes already around 240 K and thus the use of toluene or heptane, with freezing temperatures below 185 K, allows to expand the temperature range to lower temperatures.

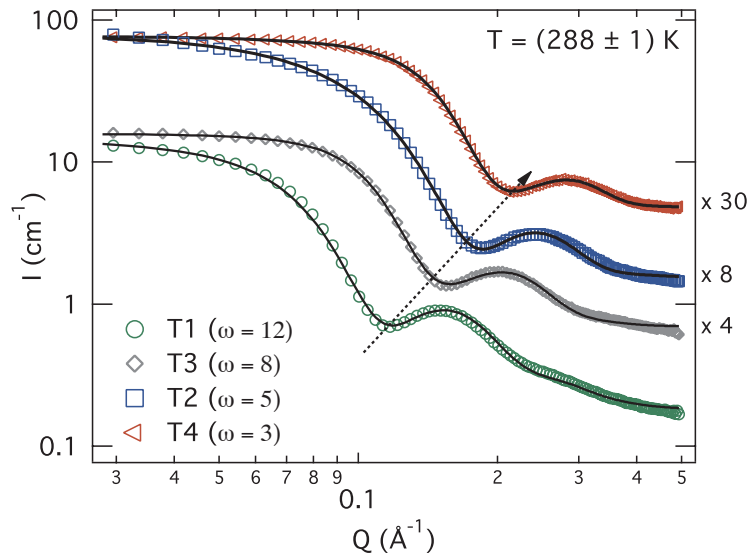


Figure 3.2.: SANS curves of four microemulsion samples with  $3 \leq \omega \leq 12$  at  $T = 288$  K. (Sample compositions are listed in Tab. 3.2.) Note that with decreasing  $\omega$  the minimum of the formfactor shifts to higher  $Q$ , indicated by the arrow. Solid lines are fits to the formfactor plus structure factor model explained in 3.1. The errors are smaller than symbols and curves are shifted vertically by the factor shown next to the right axis.

Figure 3.2 shows SANS curves of 4 shell contrast samples with different water loadings (T1, T2, T3 and T4). With decreasing molar ratio  $\omega$  the local intensity minimum shifts



Table 3.2.: Listing of sample compositions investigated for the structure studies on D22 and D11.  $\omega$  denotes the molar ratio of water to AOT,  $\phi$  is the prepared droplet volume fraction and under  $R_c^{290 K}$  we show the fitting result for the core radius at  $T \approx 290$  K. Samples T1 - T6 have been studied under  $T$ -variation.

Sample	Instrument	Composition	$\omega$	$\phi$	$R_c^{290 K}$
T1	D22	D <sub>2</sub> O/AOT/heptane-d16	12	0.2	19.2
T2	D22	D <sub>2</sub> O/AOT/heptane-d16	5	0.2	9.7
T3	D22	D <sub>2</sub> O/AOT/toluene-d8	8	0.2	11.9
T4	D22	D <sub>2</sub> O/AOT/toluene-d8	3	0.2	6.8
T5	D22	AOT/toluene-d8	0	0.2	2.1
T6	D22	AOT/decane-d22	0	0.2	2.7
	D11	D <sub>2</sub> O/AOT/toluene-d8	8	0.05	11.1
	D11	D <sub>2</sub> O/AOT/toluene-d8	8	0.1	12.2
	D11	D <sub>2</sub> O/AOT/toluene-d8	8	0.15	11.8

to higher  $Q$ -values, while all curves remain qualitatively similar. Independent of any model this indicates that all samples contain scattering particles with similar form but of decreasing size with decreasing  $\omega$ .

### 3.3.1. Results and discussion

By adjusting the core-shell model explained in section 3.1 we obtain fits which are shown as solid lines in Fig. 3.2. Resulting core radii  $R_c$  are plotted as a function of the molar ratio  $\omega$  in Fig. 3.3, values are listed in Tab. 3.2. The  $\omega$ -dependence of the other fit parameters, namely shell thickness  $d$ , droplet size polydispersity  $p$  and coherent scattering length density  $\rho_s$  of the shell, are plotted in Fig. 3.4. Note that there are 4 samples of similar composition ( $\omega = 8$  and toluene-d8), differing only in their droplet volume fraction  $\phi$ . In the next section we solely discuss the variation of the fitting parameters with  $\omega$ . The dependence of structure on  $\phi$  will be subject of section 3.4.

**Core radius  $R_c$ :** In addition to our SANS results we include  $R_c$  of four more samples with  $10 \leq \omega \leq 40$  (H<sub>2</sub>O/AOT/decane,  $\phi = 0.1$ ). These samples have previously been investigated by means of SAXS [94]. As expected from Eq. 1.5, the radius  $R_c$  increases linearly with increasing  $\omega$ . The predicted linear relationship is shown by the dotted line in Fig. 3.3 (note that it is not a fit to our results!). Except for the biggest droplets with  $\omega = 40$ , the radii of all samples are in agreement with Eq. 1.5. Moreover the SAXS results further confirm this relation. We did not conduct an extensive study under variation of the oil. Nevertheless within the errors we can say that the type of the oil has

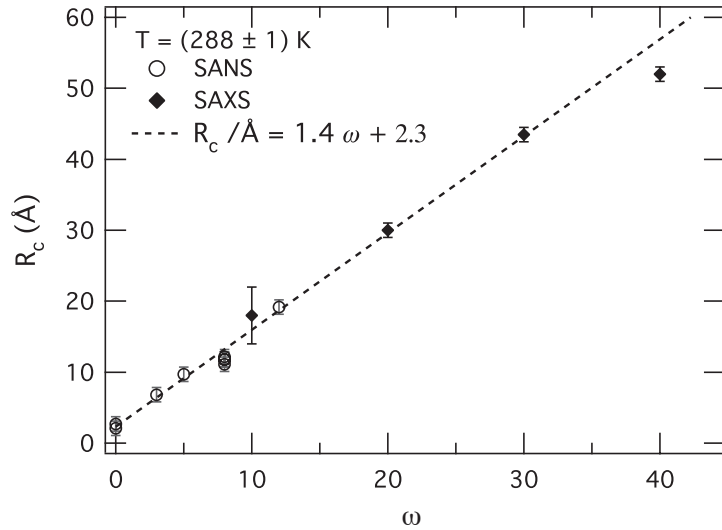


Figure 3.3.: Micelle core radius  $R_c$  obtained by SANS and SAXS [94] as a function of the molar ratio  $\omega$  at  $T = 288$  K. The dotted line shows the predicted linear relation (Eq. 1.5) between  $R_c$  and  $\omega$  after [19], see text.

no influence on the droplet size. Radii from microemulsions with toluene-d8, heptane-d16 and decane-d22 as matrix all follow within the accuracy of the measurements the same  $\omega$ -dependency. However  $d$  may change with oil. We conclude that the simple geometrical picture leading to Eq. 1.5 is sufficient for the description of the SANS results on  $R_c$  as a function of  $\omega$  around room temperature. Within errors our results confirm furthermore that AOT headgroup area  $A_s$  and volume  $V_s$  are independent of  $\omega$  and oil.

**AOT shell thickness  $d$ :** With increasing  $\omega$  the thickness  $d$  of the shell composed of the AOT tails shows a tendency to decrease, see Fig. 3.4 a). Whereas for the pure AOT reverse micelles  $d \approx 13$  Å the shell thickness is found to be only  $d \approx 10.5$  Å for the micelles with  $\omega = 12$ . For  $3 \leq \omega \leq 8$  no clear trend is observed, the shell thickness is within the errors rather constant  $d \approx 11$  Å – 12 Å.

Within the simple geometrical picture discussed before the space available for the AOT tails must be related to the size of the droplets. The smaller the droplets are the bigger is the curvature of the surfactant film and hence the bigger should be the spacing between tails. With increasing droplet size one could thus argue that the tails have to stretch out. This does not seem to be the case as we do see the contrary: a decrease of  $d$  with  $R_c \propto \omega$ . Keeping in mind on the one hand the big uncertainties of the fitting results for  $d$  and on the other hand the restricted number of data points we do not want to draw

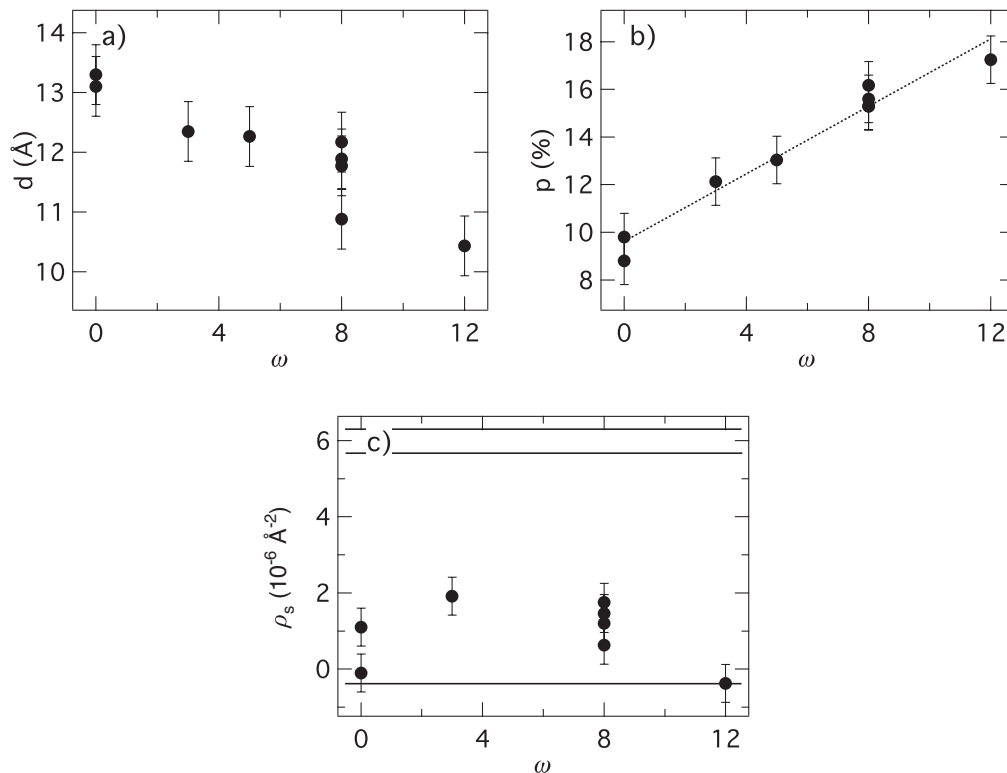


Figure 3.4.: a) Shell thickness  $d$ , b) size polydispersity  $p$  and c) coherent scattering length density  $\rho_s$  of the shell as a function of the molar ratio  $\omega$ . The solid lines in the bottom figure correspond to  $\rho$  of toluene-d8 and heptane-d16 and and the AOT tails. (Volume fractions range between  $0.05 \leq \phi \leq 0.2$ , see Tab. 3.2). See text for a further discussion.

any conclusions from this. Moreover we are not aware of similar observations described in literature. As a last point we note that we do not observe a systematic variation of  $d$  with surrounding oil as claimed in [28].

**Size polydispersity  $p$ :** We observe that the smaller the droplets are the more monodisperse they become. The droplet size polydispersity  $p$  decreases linearly with decreasing  $\omega$ , shown by the dotted line in Fig. 3.4 b). From  $p \approx 17\%$  at  $\omega = 12$  the polydispersity decreases to  $p \approx 9\%$  for water-free AOT micelles. *Kitchens* and co-workers investigated water swollen reverse AOT micelles in cyclohexane with  $\omega = 5, 10$  and  $18$ . Using SANS they observed a slight trend for  $p$  to decrease with increasing  $\omega$  [95]. Furthermore form fluctuations of these reverse micelles were measured by means of NSE and a constant elasticity of the AOT film was observed - this leads us to conclude that the fluctuation part in  $p$  does not depend on  $\omega$ . To our knowledge there does not exist any other

systematic study of the polydispersity variation with  $\omega$ . Polydispersity values for these systems have theoretically been predicted to be in the range of  $10\% \leq p \leq 20\%$  [96]. Experimentally determined  $p$  for w/o droplet microemulsions based on AOT mostly lie between 15% and 25% [31]. Our results for the polydispersity  $p$  agree very well with those values.

**Coherent scattering length density  $\rho_s$  of the shell:** In Fig. 3.4 c) we show  $\rho_s$  together with solid lines on the upper and lower border which mark the fitting constraints corresponding to the calculated scattering length density of the AOT-tails (bottom) and toluene-d8/heptane-d16 (top). For all samples we observe  $\rho_s$  differing from the theoretical value for AOT. This probably reflects the penetration of the shell by oil molecules. No systematic variation of  $\rho_s$  with  $\omega$  is observed.

### 3.4. Series 2: $\phi$ -variation

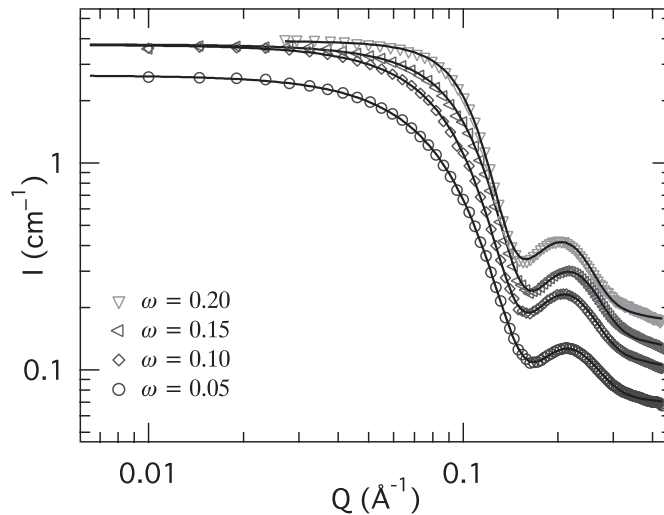


Figure 3.5.: SANS spectra and fits of  $D_2O/AOT/toluene-d8$  with  $\omega = 8$ . From bottom to the top curve the droplet volume fraction increases from  $\phi = 0.05$  to  $0.2$ . Note that the top curve was measured on D22 whereas the other samples were measured on D11, which explains the differing  $Q$ -range.

In literature it is mostly assumed that the droplet size is determined only by  $\omega$  (Eq. 1.5). Contrary there have also been observations of  $R_c$  changing with the droplet volume fraction  $\phi$  at a constant  $\omega$  [32, 33]. For a water/AOT/decane microemulsion with  $\omega = 40$  it was found that droplet size and droplet volume fraction  $\phi$  are independent parameters

only up to  $\phi \approx 0.12$ . For  $0.12 \leq \phi \leq 0.3$  the core radius was observed to decrease continuously [33]. In a different study the same slope for the decrease was found at higher volume fractions  $0.4 \leq \phi \leq 0.7$  [32], corresponding to  $\Delta R_c \approx 50 \text{ \AA} \cdot \Delta\phi$ .

In this context we did not aim to study in detail the relationship between  $R_c$  and  $\phi$ , but we only tested on one sample the variation of the droplet form over the  $\phi$ -range of interest for this work. We chose the D<sub>2</sub>O/AOT/toluene-d8 microemulsion with  $\omega = 8$  to investigate the relationship between droplet form factor parameters and volume fraction for four samples with  $0.05 \leq \phi \leq 0.2$ . The data was collected on D22 ( $\phi = 0.2$ ) and on D11 ( $0.05 \leq \phi \leq 0.15$ ) at a temperature of  $T = (289 \pm 1) \text{ K}$ .

Figure 3.5 shows scattering curves of the four investigated microemulsions. From bottom to top the curves belong to samples with droplet volume fractions of  $\phi = 0.05, 0.1, 0.15$  and  $0.2$  respectively. For  $Q > 0.1 \text{ \AA}^{-1}$  all curves run rather parallel and show the characteristic minimum of a form factor of a spherical particle, independent of droplet density located at  $Q \approx 0.16 \text{ \AA}^{-1}$ . If contrast and size of the scattering particles are independent of  $\phi$ , the coherent scattering intensity at medium  $Q$  values should be proportional to the number of scattering particles hence to  $\phi$ . For low  $Q$  we expect to see the effect of interference from different particles, the intensity will also be determined by the interactions of droplets which should become more important with increasing  $\phi$ . We therefore compare the intensity of the second oscillation of all curves after subtraction of the incoherent background estimated at the highest  $Q$ . Indeed we find a ratio 1 : 1.9 : 2.9 : 4 which is very close to the ratio of the prepared volume fractions 1 : 2 : 3 : 4. This leads us to conclude, even before having fitted the data, that indeed the size of the droplets is about the same, independently of  $\phi$ .

### 3.4.1. Results and discussion

For a quantitative analysis of the scattering we fit the curves to the model explained in section 3.1. The fits are shown as solid lines in Fig. 3.5 and the corresponding fitting results for the core radius  $R_c$ , shell thickness  $d$ , coherent scattering length density  $\rho_s$  of the shell and the droplet polydispersity  $p$  are shown in Fig. 3.6 as a function of droplet volume fraction  $\phi$ .

**Core radius  $R_c$  and shell thickness  $d$ :** The parameters extracted from the fits confirm that the overall radius (radius  $R_c$  of the core plus shell thickness  $d$ ) of the reverse swollen micelles is within the errors constant  $R_c + d \approx 23 \text{ \AA}$ . This goes with a radius of  $24 \text{ \AA}$  which has been reported for  $\omega = 8$  [97]. The thickness of the AOT shell (hydrocarbon tails) is with  $d \approx 11.5 \text{ \AA}$  in agreement with literature [98]. Both parameters do not show a systematic variation with  $\phi$  in the investigated range. Previously it was shown for a water/AOT/decane microemulsion with  $\omega = 40$  that droplet size and droplet volume

fraction  $\phi$  are independent parameters only up to  $\phi \approx 0.12$  [33]. For  $0.12 \leq \phi \leq 0.3$  the core radius was observed to decrease continuously. At  $\phi = 0.2$  the radius is about 7% smaller than the plateau value observed for low  $\phi$ .

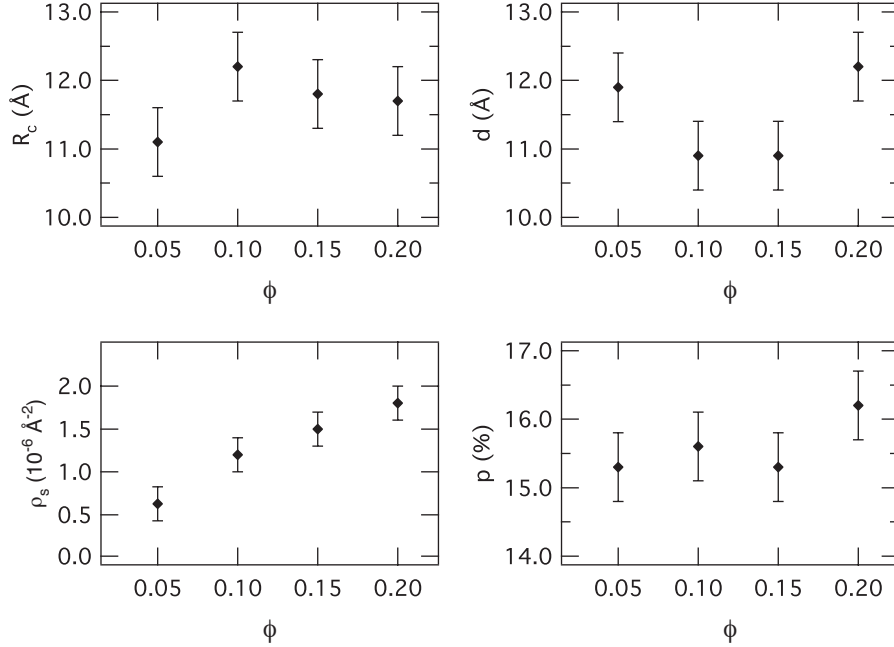


Figure 3.6.: Variation of core radius  $R_c$ , shell thickness  $d$ , coherent scattering length density  $\rho_s$  of the shell and polydispersity  $p$  with droplet volume fraction  $\phi$  for  $\text{D}_2\text{O}/\text{AOT}/\text{toluene-d8}$  ( $\omega = 8$ ,  $T \approx 288$  K).

**Size polydispersity  $p$ :** The size polydispersity of the droplets does not change systematically with changing  $\phi$  but it is for all samples 15% to 16.5%, a value that is close to what has been reported for similar systems [16,31].

**Coherent scattering length density  $\rho_s$  of the shell:** The only fitting parameter showing a systematic variation with the droplet volume fraction  $\phi$  is  $\rho_s$ . Within the investigated  $\phi$ -range the scattering length density  $\rho_s$  increases monotonically from about  $0.5 \cdot 10^{-6} \text{Å}^{-2}$  to  $1.7 \cdot 10^{-6} \text{Å}^{-2}$ . In this context we want to remark that fixing either the shell thickness  $d$  or  $\rho_s$  to an averaged value did not lead to satisfactory fitting results.

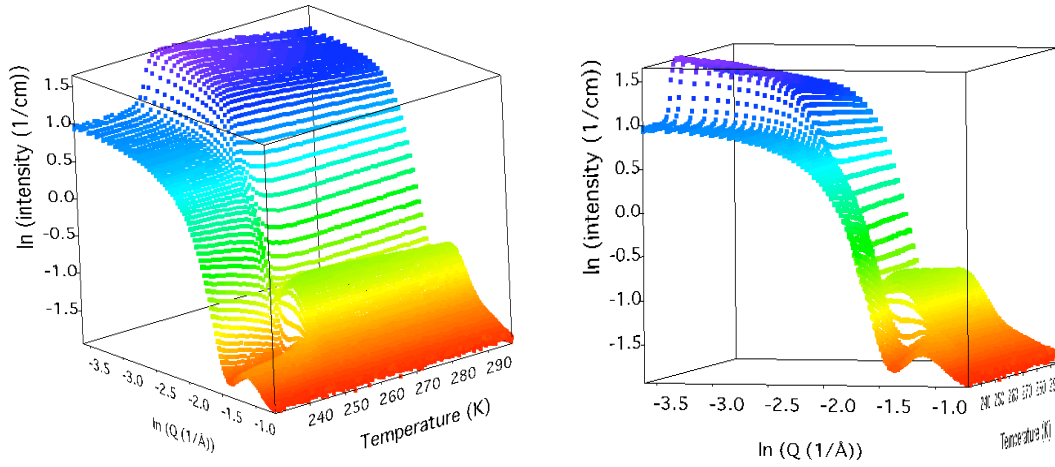


Figure 3.7.: Three-dimensional representation of the SANS curves of sample T3 ( $\text{D}_2\text{O}/\text{AOT}/\text{toluene-d8}$ ,  $\phi = 0.2$ ,  $\omega = 8$ ) as a function of temperature. Note that around  $T = 250$  K the form of the spectra abruptly changes and their local minimum shifts to higher  $Q$ -values.

### 3.5. Series 3: $T$ -variation

For a selection of microemulsions we performed a systematic SANS study to determine the temperature range of structural stability of the droplets. Water/AOT/oil microemulsions with different droplet sizes and toluene-d8 or heptane-d7 as oil were measured from room temperature down to  $T = 220$  K. Six samples with a molar ratio between  $0 \leq \omega \leq 12$  were chosen to determine size and polydispersity of the droplets as a function of temperature. This study allowed to extend the phase diagram of the microemulsion from room temperature down to temperatures far below the freezing point of bulk water. The investigated sample compositions are listed as T1 - T6 in Tab. 3.2, additional fits and resulting parameters are given in the appendix A.6.

#### 3.5.1. Results and discussion

All samples T1 - T6 (see Tab 3.2 for their composition) were investigated upon cooling. In Fig. 3.7 we show the 3-dimensional representation of the scattering curves versus temperature for sample T3, a microemulsion with middle-sized droplets. At a temperature of  $T \approx 250$  K we note the abrupt change of the scattered intensity, above 255 K and below  $T \leq 240$  K the spectra change only smoothly. As a next step every single curve is now fitted as explained in section 3.1. For each sample more than 70 spectra need to

be analyzed; the resulting fit parameters of one temperature are taken as the starting parameters for the next lower temperature. Turning the attention back to sample T3 we show resulting fits in Figure 3.8 for three temperatures of  $T = 297$  K, 250 K, and 230 K. A selection of scattering curves for all four investigated microemulsions are shown in the appendix A.6.

The above mentioned core-shell model describes the data very well over the whole investigated temperature range which implies that the reverse micellar structure seems to be preserved and only the size of the droplets changes. With decreasing temperature the droplet size shrinks causing a clear shift of the form factor minimum to higher  $Q$  as emphasized by the arrow in Fig. 3.8. From the fit the following parameters are

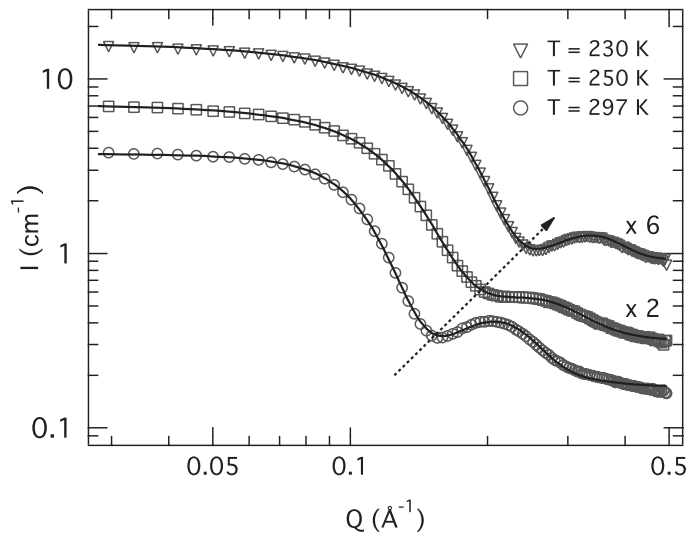


Figure 3.8.: Scattering from sample T3 ( $D_2O/AOT/toluene-d_8$ ,  $\phi = 0.2$ ,  $\omega = 8$ ) at three different temperatures. Solid lines are fits to the described formfactor plus structure factor model. For clarity curves are shifted vertically by a factor shown close to the right axis. With decreasing temperature the micelles decrease in size (shown by arrow, see text for further explanations). Errorbars are smaller than the symbols.

obtained: the core radius  $R_c$ , the thickness  $d$  of the shell formed by the AOT tails and the droplet size polydispersity  $p$ . Table A.3 lists fitting results for all samples at temperatures  $T = 290$  K, 250 K and 230 K. As the droplet volume fraction  $\phi = 0.2$  is moderate and we do not probe very low  $Q$ , we do not see a strong effect of droplet interactions which would reveal itself by a structure factor peak at low scattering vector. Nevertheless the inclusion of a sticky hard sphere structure factor led to a significant increase of the fit quality at low  $Q$  as the model describes the scattering intensity in absolute units. A slight increase or decrease of the absolute intensity essentially at



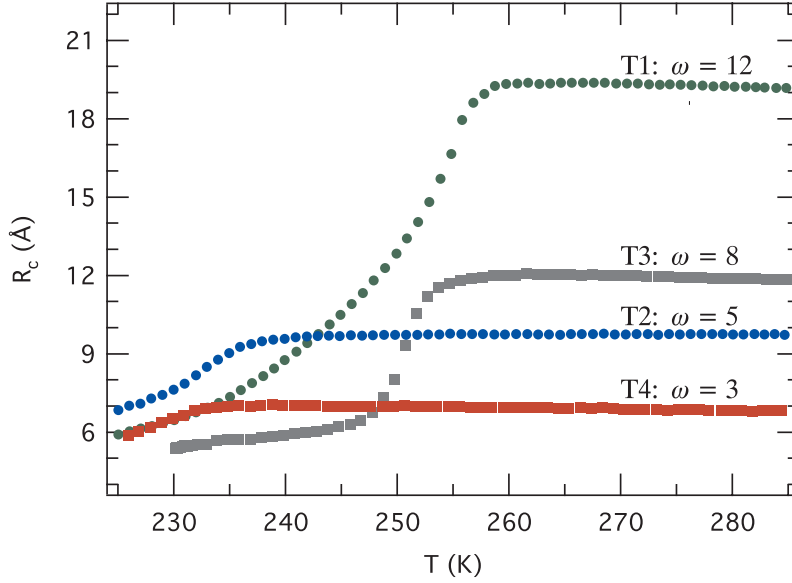


Figure 3.9.: Core radii of water swollen micelles as function of temperature. Sample names as introduced in Tab. 3.2 are written above each curve. Errorbars are smaller than the symbols.

smaller  $Q$  is caused by droplet interactions. The inclusion of the structure factor had no significant effect on the form factor parameters. Due to the rather flat structure factor no unambiguous conclusions can be drawn from the fitting parameters of the structure factor without further experiments under variation of  $\phi$ . Therefore structure factor parameters (stickiness  $\tau$  and perturbation parameter  $\epsilon$ ) are not further discussed in this context. The main objective of the temperature variation study is to characterize the confinement size as defined by the droplet core radius  $R_c$  with changing temperature. In Fig. 3.9  $R_c$  of all investigated samples is plotted as a function of temperature. It can be seen that the initial  $R_c$  remains unchanged with decreasing temperature even below the freezing point of bulk deuterated water. At a well defined temperature  $T_s$  the radii  $R_c$  abruptly start to decrease and then tend to a plateau value at low temperatures. We determined  $T_s$  as the temperature where the droplet core radius  $R_c$  drops  $0.3 \text{ \AA}$  below the high temperature average radius. Whereas the temperature  $T_s$  and the kinetics of shrinking (slope of the curve) depend on the sample composition,  $R_c$  seems to converge to the same low temperature  $R_c$  for all compositions. For all samples investigated we observe a remaining finite core radius of about  $R_c \approx 5 \text{ \AA}$  to  $6 \text{ \AA}$ . The temperature  $T_s$  is found to be a function of the molar ratio  $\omega$ . The smaller  $\omega$  is, i.e. the smaller the initial droplets are, the lower is the temperature  $T_s$  down to which the droplet size remains stable. The shrinking of the droplets below  $T_s$  is probably caused by water expulsion

as investigated in detail by [56]. A possible low temperature scenario would be that of small water crystallites frozen to the sample holder walls (bearing in mind the small wall to wall thickness of 1 mm). Due to the similar coherent scattering length densities of D<sub>2</sub>O, toluene-d<sub>8</sub> and heptane-d<sub>16</sub> (see Tab. A.1) we are not able to see this in our SANS data.

#### 3.5.1.1. Reversibility upon heating

On two samples (T3 and T4) the reversibility of the observed structural changes upon heating was tested. After 15 minutes of equilibrating at the lowest temperature the samples were heated back to  $T = 290\text{ K}$  with a heating rate of 0.5 K/min. In Fig. 3.10 the formfactor fit parameters for cooling and heating are compared for both samples. Full black symbols represent cooling results and hollow red symbols heating results as a function of temperature. Results for sample T3 and T4 are shown on top and bottom of the figure respectively. For both samples we find that the structure upon heating and cooling is different. They become similar only for temperatures above  $T = 270\text{ K}$ . The form factor fitting parameters show a pronounced hysteresis.

**Core radius  $R_c$**  falls back on its starting value after the cooling and heating cycle for sample T4, in the case of sample T3 the final radius lies about 1 Å below the initial value. Another important finding is that for both samples the droplets grow upon heating already from the lowest temperatures on. This means that far below the freezing point of bulk water the droplets rapidly incorporate the water that was ejected in the cooling scan. This is in contrast to observations by [56] who report a much slower water uptake corresponding to  $\omega = 1$  per day when the samples are not agitated which was also the case in our experiment. However, these results cannot be compared directly to ours as a different oil was used and the sample holder geometry can probably have an impact on the kinetic behavior of the samples.

**AOT shell thickness  $d$ :** For both droplet sizes cooling leads first to a small increase of the shell thickness  $d$ . This reflects the increasing rigidity of the hydrocarbon tails with decreasing temperature. Exactly at the temperature where we observe the shrinking of the droplet radius  $R_c$  the shell thickness  $d$  abruptly decreases for both samples. This finding may suggest that the hydrophobic AOT tails collapse when water is expelled. Upon heating the AOT tails continuously stretch out again until they reach their initial size around  $T \approx 275\text{ K}$ . Some influence of a change in scattering length density can not be excluded either. Above  $T \approx 275\text{ K}$  heating and cooling curves lie on top of each other.

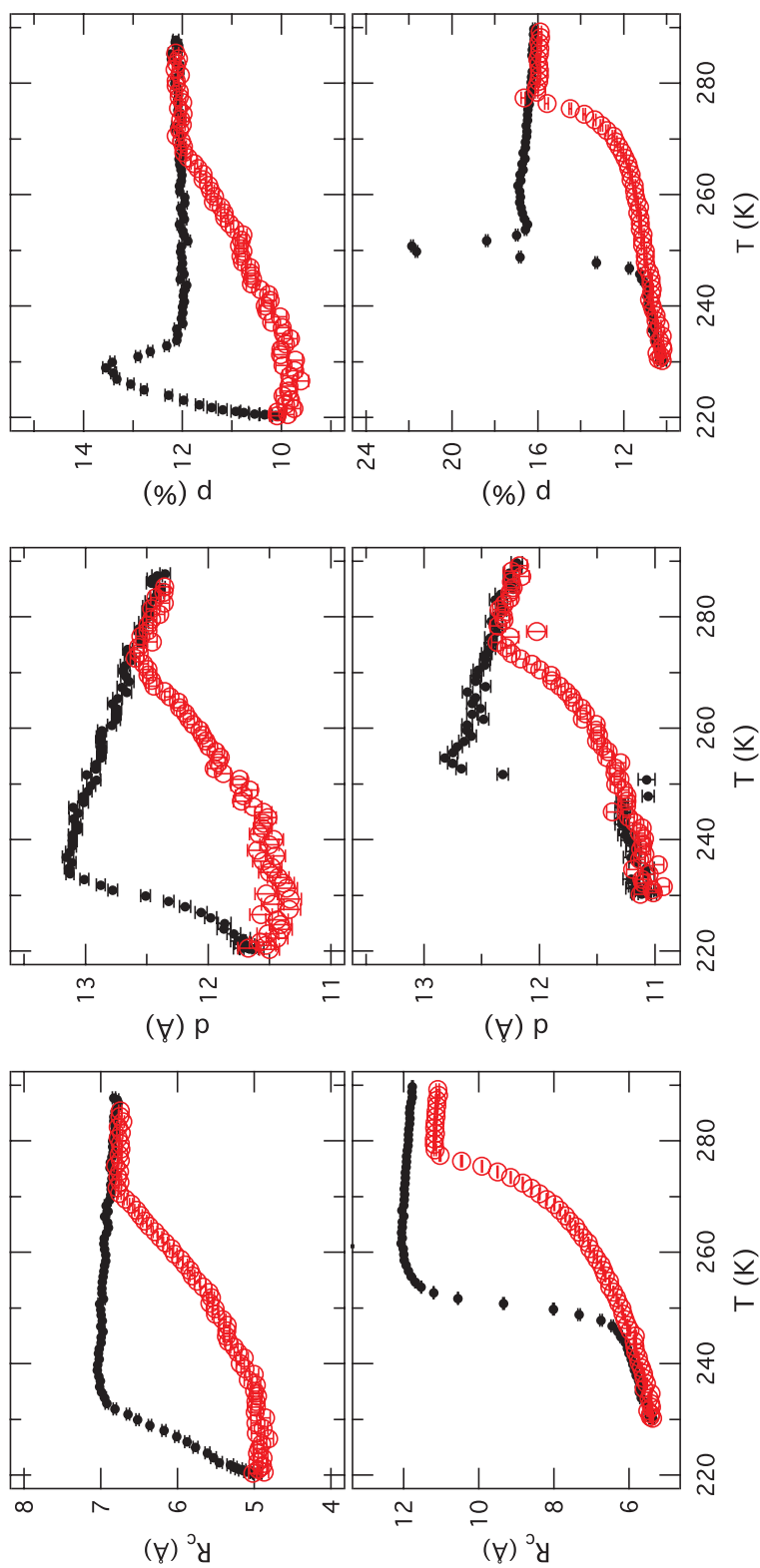


Figure 3.10.: Sample T4 (figures in first line) and sample 3 (figures in second line): radius  $R_c$ , shell thickness  $d$ , and polydispersity  $p$  upon cooling (full black symbols) and heating (hollow red symbols). Cooling and heating rates:  $0.5$  K/min. Note the hysteresis: cooling and heating curves are in good agreement only above  $T \approx 275$  K.

**Size polydispersity  $p$ :** Both samples show upon cooling a constant  $p$  down to roughly the respective shrinking temperature  $T_s$ . There we observe a sudden increase of the polydispersity  $p$ . This peak in  $p$  may be the signature of a system consisting of bigger and smaller droplets. Whereas the mean droplet radius  $R_c$  decreases from  $T_s$  on, the analysis of  $p$  reveals the coexistence of different sized droplets in the temperature range of transition from big to small droplets. Upon further cooling the polydispersity falls down to  $p \approx 10\%$  at the lowest investigated temperature. This value is still slightly bigger than that of pure AOT micelles which will be discussed in the following (pure AOT micelles dispersed in toluene-d8  $\rightarrow p \approx 9\%$ , see Fig. 3.12). Heating the samples up leads to a continuous increase of the polydispersity and again the values observed for  $p$  while cooling are reproduced above 275 K. Note that except for the slightly smaller final radius of sample T3 all other parameters fall back on the starting values after the cooling-heating cycle.

### 3.5.1.2. Pure AOT micelles

Pure reverse AOT micelles were studied to be compared with the shrunken water filled reverse micelles. We investigated samples with an AOT volume fraction  $\phi = 0.2$  in two different oils (toluene-d8 or n-decane-d22) were between  $T = 290$  K and 260 K. Figure 3.11 shows two representative spectra of both samples at  $T \approx 280$  K.

Again the data were fitted with a core-shell model for the form factor combined with a sticky hard sphere structure factor. This time the core is composed of only AOT heads, see Fig. 3.1. The scattering length densities of both, core and solvent (toluene-d8 or n-decane-d22), were fixed to the theoretical values. The scattering length density  $\rho_s$  of the shell was allowed to vary between its calculated value and the oil value  $\rho_m$ , as the oil can interpenetrate the chains.

Table 3.3 lists the temperature averaged fit results and Fig. 3.12 displays their variation with temperature. For the head group we find a thickness of about 2.5 Å, which compares well with values found by others [19, 33]. The thickness of the shell composed of the AOT chains seems to increase slightly with cooling starting at  $d = 13$  Å at  $T = 290$  K. This can be explained by the hydrocarbon chains becoming stiffer with decreasing temperature.

The average distance between the chains is determined by competition between van der Waals attraction and steric (entropic nature) repulsion. The former is less sensitive to temperature, whereas the latter decreases upon cooling (chain fluctuations responsible for steric repulsion are weaker for more rigid chains). Upon cooling the average inter-chain distance thus becomes smaller and the shell becomes less penetrable. This is also reflected by the decreasing scattering length density  $\rho_s$  of the shell. The higher absolute value for the scattering length density  $\rho_s$  of the AOT chains in toluene is due to the

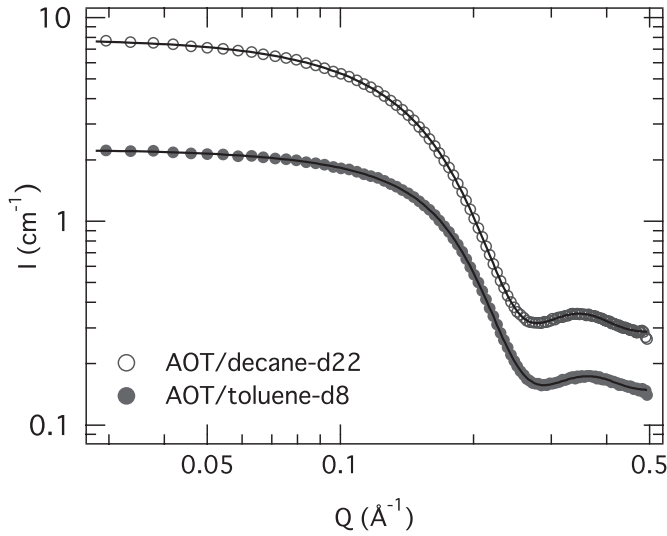


Figure 3.11.: Scattering from 20 vol% AOT reverse micelles dispersed in toluene-d8 ( $\bullet$ , sample T5,  $T = 278$  K) and decane-d22 ( $\circ$ : sample T6,  $T = 283$  K, shifted by a factor 2). Errorbars are smaller than the symbols. Solid lines are fits to a core-shell form factor combined with structure factor.

Table 3.3.: Summary of the temperature averaged fitting results for 20 vol% AOT reverse micelles dispersed in toluene-d8 (sample T5) and decane-d22 (sample T6).  $R_c$  denotes the core radius (AOT-head),  $d$  is the shell thickness (AOT-tail),  $\rho_s$  the coherent scattering length density of the shell,  $p$  the polydispersity.

sample	$R_c$ ( $\text{\AA}$ )	$d$ ( $\text{\AA}$ )	$\rho_s$ ( $10^{-6} \text{\AA}^{-2}$ )	$p$ (%)
T5: AOT/toluene-d8	$2.1 \pm 0.1$	$13.1 \pm 0.1$	$1.1 \pm 0.2$	$8.8 \pm 0.2$
T6: AOT/decane-d22	$2.7 \pm 0.1$	$13.3 \pm 0.3$	$-0.1 \pm 0.2$	$9.8 \pm 0.1$

better penetration of the chains by the smaller toluene molecule [99]. The size of the micelles ( $R_c + d$ )  $\approx 15 \text{\AA}$  (core and shell) lies close to the values published for the linear length of the AOT molecule of  $12 \text{\AA}$ . These findings compare well with results from DLS experiments on AOT micelles in iso-octane which showed a temperature independent micelle radius of  $15 \text{\AA}$  between  $T = 250$  and  $370$  K [30] and SANS measurements finding an AOT length of about  $16 \text{\AA}$  [100]. In both oils the micelles are very monodisperse: over the whole investigated temperature range we find a polydispersity in size of  $p = 9 - 10\%$ . Very recently frozen solutions of AOT/n-heptane have been investigated by small angle X-ray scattering (SAXS) [101]. These authors conclude that at  $T = 77$  K the reverse micelles structure is maintained and the micelles undergo a clustering pro-

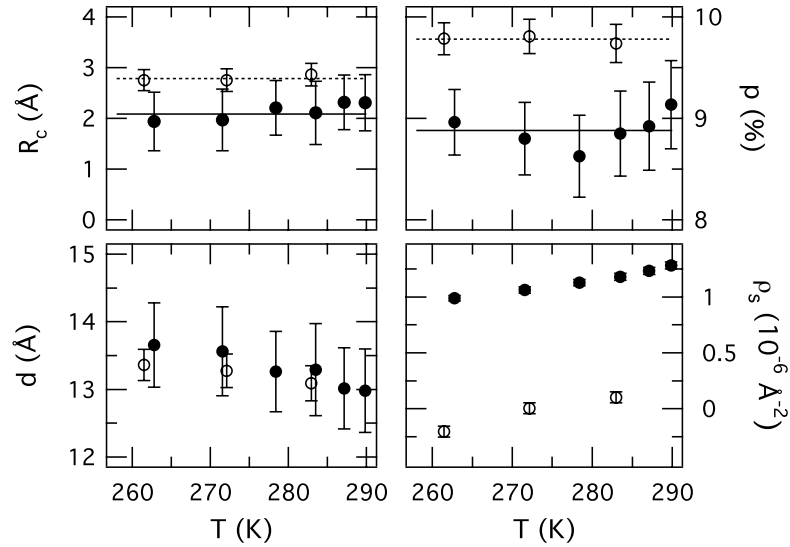


Figure 3.12.: Fitting parameters for AOT reverse micelles dispersed in toluene-d8 ( $\bullet$ , sample T5) and decane-d22 ( $\circ$ : sample T6). Core radius  $R_c$ , polydispersity  $p$ , shell thickness  $d$  and scattering length density  $\rho_s$  of the shell.

cess. The published value of around  $10 \text{ \AA}$  for the radius of the core consisting of the head groups disagrees with our results. Our findings are consistent with the established dimensions of AOT.

### 3.5.1.3. Remaining water core at low temperatures

All investigated microemulsion compositions agree in showing a remaining core radius of more than  $5 \text{ \AA}$  even at the lowest temperatures  $T = 220 \text{ K}$ . Due to the similar coherent scattering length densities  $\rho$  of  $\text{D}_2\text{O}$  and AOT head groups we cannot distinguish between them by means of SANS. The core radius determined for the water swollen micelles is thus composed of both. Only the direct comparison with the size of the AOT head group as identified by measuring the pure AOT micelles under the same conditions allows us to draw conclusions on the amount of remaining water. By subtracting  $2.7 \text{ \AA}$ , the maximum value determined for the size of the AOT head group, we know that a minimum water core of more than  $2.3 \text{ \AA}$  radius survives after the shrinking of the droplets. This value corresponds approximately to a number of 2 water molecules per AOT [19] and confirms the before discussed observations of 2 - 4 unfreezable water molecules per molecule AOT [102].

### 3.6. Summary and conclusions

The structure of water/AOT/oil microemulsions with different water loadings  $0 \leq \omega \leq 40$  was directly investigated over a wide range of temperatures by means of SANS. We summarize the main outcome for the following studies:

1. The droplet core radius varies linearly with the water to surfactant molar ratio  $\omega$  as  $R_c/\text{\AA} \approx 1.4 \cdot \omega + 2.4$  (Eq. 1.5). Thus one may control the droplet radius between a few Ångströms and several nanometers by choosing the appropriate composition. This means the degree of confinement for the water can be defined by preparing a microemulsion with  $\omega$  as given by Eq. 1.5.
2. We found the oil surrounding the droplets (heptane, decane or toluene) to have no significant influence on the microemulsion structure. Independent of the oil, the core radius  $R_c$  is simply defined by the molar ratio  $\omega$  expressed by Eq. 1.5. This means the softness of the confinement (related to the viscosity of the oil) may be varied whilst keeping the geometrical size of the confinement constant.
3. Over the relevant range of droplet volume fractions,  $0.05 \leq \phi \leq 0.2$ , we verified that the microemulsion droplet structure can be regarded as  $\phi$ -independent. Size and polydispersity of the droplets do not vary in a significant way with droplet density. Within these limits, one may adjust the relative amount of water in the sample to match the experimental requirements (for a given sample holder thickness one may for instance optimize the sample transmission to avoid multiple scattering).
4. Studies between  $220 \text{ K} \leq T \leq 300 \text{ K}$  proved that the microemulsion structure is stable over a wide temperature range down to temperatures far below the freezing point of bulk water (tested for toluene-d8 and heptane-d16 as surrounding oils). The smaller the initial droplets are the lower is the temperature  $T_s$  to which they remain stable. This means the confined water may be studied over this entire temperature range under constant confining geometry.
5. Even at the lowest investigated temperature  $T \approx 220 \text{ K}$  there seems to be a remaining amount of water inside the droplets corresponding to about 2 molecules per AOT molecule for all investigated  $\omega$ . This could be water closely bound to the AOT headgroups and thereby hindered from freezing.

We conclude that, from a structural point of view, this water/AOT/oil microemulsion in the droplet phase forms an appropriate model system for the investigation of soft confined water, in which the degree of confinement as well as the temperature may be varied over a wide range.





## 4. Freezing behavior of water in reverse micelles

Studying the temperature dependent structure of water swollen reverse AOT micelles by means of SANS, we have observed a shrinking of the droplets at temperatures below the freezing point of bulk water. The shrinking temperature  $T_s$  was found to depend on the initial size of the droplets: the smaller the initial droplets were, the lower was the temperature  $T_s$  down to which they remained stable. We are now interested if and how the structural instability of these reverse micelles relates to the freezing behavior of the water confined inside the micelles.

A way to monitor the water freezing is by means of elastic fixed window scans on BS, where the elastically scattered intensity is monitored as a function of temperature, see section 2.2.1.1. When the characteristic relaxation time of the probed molecules becomes of the order of or shorter than the instrumental resolution, one observes an increase of the elastic intensity. The signature of water freezing will thus be a step in the elastic intensity at the temperature where water molecules start to be immobilized. Here we report on  $Q$ -integrated elastic intensities.

For this study we focus on water confined to three different droplet sizes with a molar ratio of  $\omega = 40, 12$  and  $3$  and different surrounding oils. Using SANS we have determined the respective core radii to be  $R_c \approx 46 \text{ \AA}, 18 \text{ \AA}$  and  $7 \text{ \AA}$ . We discuss the relation between water supercooling and size of confinement. Moreover we compare these results to the observed shrinking of the droplets.

### 4.1. Experimental details

We have performed elastic fixed window scans in order to study the freezing behavior of water confined to reverse micelles. Six samples with different surrounding oils were prepared. The volume fraction was identical for all samples,  $\phi = 0.2$ , whereas the molar ratio was varied between  $3 \leq \omega \leq 40$ . The compositions of all investigated samples are listed in Tab. 4.1 together with the corresponding SANS contrast.

Elastic scans were carried out on the BS-instruments IN16 and IN10 (instruments were presented in section 2.2.1.2). The accessible  $Q$ -range of both instruments extends from  $0.2 \text{ \AA}^{-1}$  to  $1.9 \text{ \AA}^{-1}$  with an intensity resolution (FWHM) better than  $1 \mu\text{eV}$  corresponding to a resolution in time of about  $2 \text{ ns}$  to  $4 \text{ ns}$ .

Table 4.1.: Listing of sample compositions for the study of water freezing in soft confinement.  $R_c$  denotes the radius of the water core as determined by SANS,  $\Delta T_{BS}$  is the difference between the observed freezing point of the confined water and bulk water. Values with \* have not been measured with SANS, radii were estimated from linear interpolation.

Sample	Composition	SANS-Contrast	$\omega$	$\phi$	$R_c$ (Å)	$\Delta T_{BS}$ (K)
1	H <sub>2</sub> O/AOT/n-decane-d22	full droplet	40	0.2	45.6 ± 0.5	15.5 ± 4.0
2	H <sub>2</sub> O/dAOT/n-decane-d22	water core	40	0.2	*45.6 ± 1.0	20.1 ± 4.9
3	H <sub>2</sub> O/AOT/n-decane-d22	full droplet	12	0.2	*17.9 ± 1.0	31.2 ± 4.0
4	H <sub>2</sub> O/dAOT/n-decane-d22	water core	12	0.2	17.9 ± 0.5	31.8 ± 4.4
5	H <sub>2</sub> O/AOT/n-heptane-d16	full droplet	12	0.2	16.0 ± 0.5	27.3 ± 3.7
6	H <sub>2</sub> O/AOT/n-toluene-d8	full droplet	3	0.2	6.62 ± 0.5	50.7 ± 3.5

At high temperature the microemulsions are liquid, and the elastic incoherent scattering in the probed  $Q$ -range should go to zero if the energy resolution is good enough. However, for our microemulsions, which were 80 vol-% deuterated, the coherent scattering is not negligible and it will add to the elastic signal as well (only if the relaxation time is longer than 1 ns, i.e. the pair correlation decays slower). One important contribution arises from the integrated coherent static structure factor.

Samples were measured in hollow aluminum cylinders of sample thickness 0.1 mm sealed with indium. While counting the elastic intensity, samples were cooled from room temperature down below the freezing temperature of the respective oil and then heated again back to room temperature. For temperatures between  $T = 290$  K and 200 K (250 K in the case of sample 1) cooling rates were 0.33 K/min and heating rates were 0.5 K/min. The raw data was corrected as described in section 2.2.1.3. Calculated transmissions for all samples were in the order of 94% therefore no corrections for multiple scattering were applied. Note that at low temperatures the samples are partly crystallized and due to the resulting Bragg peaks we could not normalize to low temperature intensity as it is conveniently done for amorphous samples.

The composition dependent structure of this microemulsion was before in detail investigated; the corresponding results are presented in chapter 3. These investigations have been carried out using shell contrast samples, which are due to their sharp contrast profile and the minimized incoherent background best suited for structural investigations. Nevertheless additional structural investigations were carried out on exactly the samples investigated with BS, having either core or full droplet contrast.

These SANS experiments were carried out on the diffractometer D11 using a neutron wavelength of  $\lambda = 4.6$  Å. Three configurations were used to cover a range of scattering vectors from  $0.03 \text{ \AA}^{-1} \leq Q \leq 0.45 \text{ \AA}^{-1}$ . The detector-sample distances were 1.1 m, 5 m, and 20 m with collimations 8 m, 8 m and 20.5 m respectively. Samples were measured in rectangular quartz cells with 1 mm sample thickness at a temperature of

$T = (287 \pm 0.5)$  K. The raw data was corrected according to the procedure explained in section 2.2.4.3. After these corrections data from different experimental settings was merged without further changes and rebinned to a constant  $Q$  spacing of  $0.0045 \text{ \AA}^{-1}$ .

## 4.2. Results and discussion

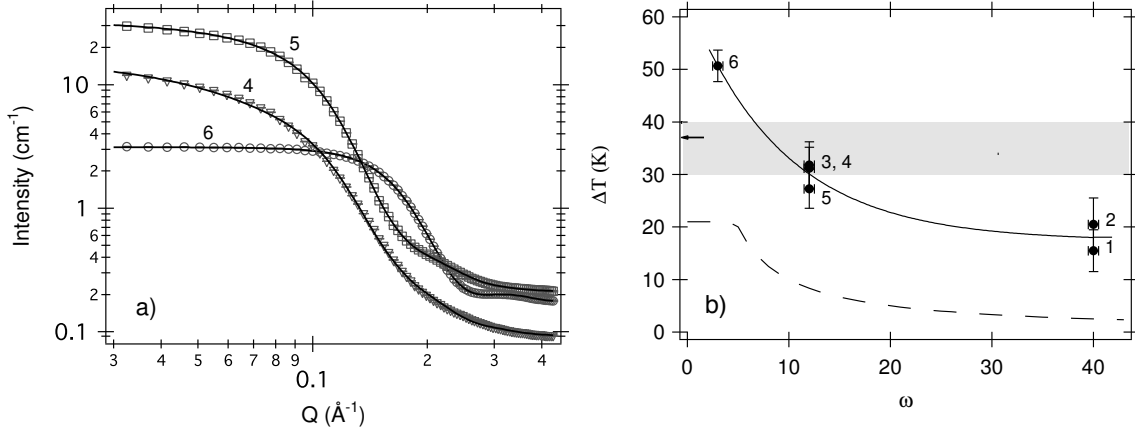


Figure 4.1.: a): SANS profile of samples 4, 5 and 6 at  $T = 287$  K, see table 4.1 for sample characteristics. Solid lines are fits to the form factor combined with structure factor as explained in section 3.1. b) Supercooling  $\Delta T_{BS}$  of confined water as a function of  $\omega$ , the solid line is a guide to the eyes, the dashed line indicates the possible supercooling caused by foreign dissolved particles. The grey rectangle shows the  $\omega$ -independent range of supercooling of water in reverse micelles as observed in a similar system [40]. The arrow on the left axis marks the supercooling corresponding to the homogeneous nucleation temperature of bulk water.

Figure 4.1 a) shows SANS curves of samples 3, 4, and 6. The data was analyzed as described in section 3.1 and solid lines in Fig. 4.1 show the resulting fits to the core-shell form factor and Baxter structure factor. We list the obtained fitting results for the core radii in Tab.: 4.1. As expected the droplet size is in accordance with results obtained on shell-contrast samples and we will desist from further discussing the structure and turn our attention to the investigation of the freezing behavior.

Figure 4.2 displays four out of the six performed elastic scans on samples with core contrast. We choose the shown temperature range such that it contains the freezing step of the respective oil. The core radius of the microemulsion droplets decreases from a)  $46 \text{ \AA}$ , b) and c)  $18 \text{ \AA}$  to d)  $7 \text{ \AA}$ , see Tab. 4.1. For the elastic temperature scans shown, the intensity is summed over all 22 (7) detectors of IN16 (IN10) corresponding to an average over the accessed  $Q$ -range. Arrows indicate cooling and heating cycles and the dotted vertical lines mark the freezing temperatures of bulk water and the corresponding oil (a) and b): n-decane-d22, c): n-heptane-d16, d): toluene-d8).

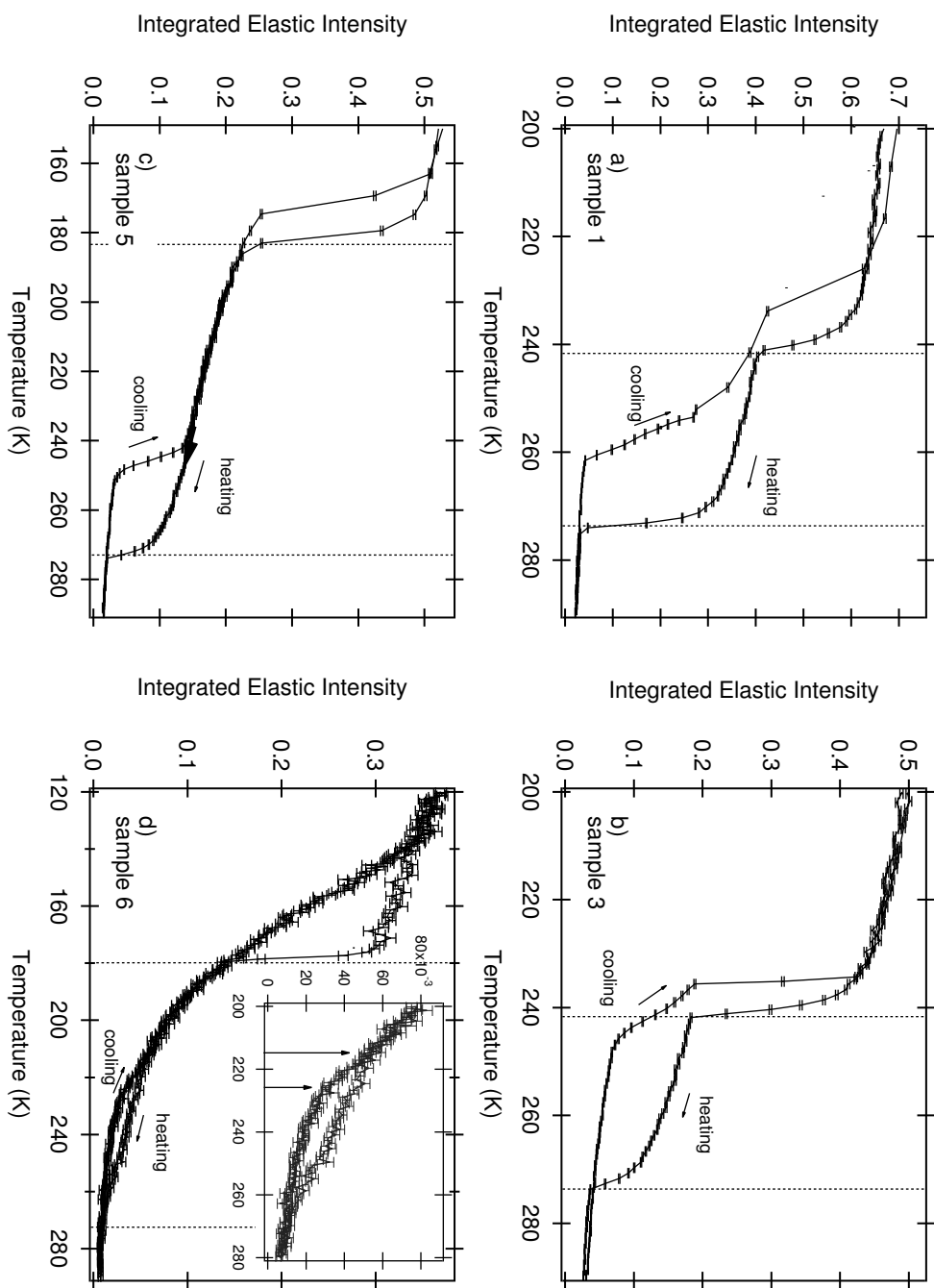


Figure 4.2.: Elastic temperature scans of microemulsions with varying droplet sizes performed on IN16 (a), b), c)) and IN10 (d)). Dotted vertical lines show the freezing points of bulk water (273.2 K) and the oil (a) and b): deuterated decane, c) deuterated heptane and d): deuterated toluene). Droplet radii decrease from a) 46 Å, b) 18 Å, c) 18 Å to d) 7 Å. The inset shows the relevant temperature enlarged, see text for further explanations.

Below the freezing point of the oil, the whole system can be considered as frozen and with increasing temperature only vibrational motions lead to a slight decrease in intensity due to an average Debye-Waller factor. Following the scattering on the heating curve a first steep drop in intensity occurs at the melting point of the bulk oil where the oil molecules start to move much faster than the time resolution of the instrument. (Note that coherent scattering, i.e. Bragg peaks and coherent short range order scattering from the deuterated oil contribute in a few detectors as well). Upon further heating a plateau region is observed, followed by a second steep drop at the melting temperature of bulk water,  $T_f = 273.2$  K. All scatterers in the sample are now mobile. These two steps in the heating curves occur for all samples exactly at the temperatures where the bulk liquids, oil and water, do melt.

Focusing now on the elastic intensity upon cooling, one notices that the increase, corresponding to a freezing of water on the ns-time scale, is clearly shifted towards lower temperatures compared to the freezing point of bulk water. For sample 1, having the biggest droplets investigated in this study, the elastic intensity increase caused by the freezing of water sets on at about  $T = 260$  K. For the smaller droplet sizes investigated here, the freezing occurs at even lower temperatures and reaches for the smallest droplets (sample 6) with a water core radius of about  $R_c \approx 7$  Å a freezing temperature close to 220 K. (Note that the homogeneous nucleation temperature of water lies at 236 K [103]. We thus hypothesize at this point that the observed strong supercooling is related to the fact that water might be closely attached to the AOT). The elastic scan of sample 6, shown in Fig. 4.2 d), is not as unambiguous as the elastic scans of the samples with bigger droplets. Due to the relatively small amount of water, the step in intensity caused by the slowing down of the water molecules is as expected very small. Moreover this scan has been performed on IN10 whose lower flux compared to IN16 complicates the interpretation of the scan because of the worse statistics. A clear change in slope of the integrated elastic intensity (indicated by the right arrow in the inset in figure 4.2 d)) led us to the conclusion that the water starts to freeze at this temperature.

For all samples we furthermore observed that freezing happens more gradually than melting, for which the elastic intensity drops more steeply. Note that by SANS we have observed the inverse: structural changes upon cooling happened more abruptly than those upon heating.

#### 4.2.1. Supercooling of confined water

Beginning and end of the intensity step attributed to the water freezing were determined from the elastic scans upon cooling (see arrows in figure 4.2 d)) and averaged to give the freezing temperature of confined water  $T_f^c$ . We then calculated the amount of

supercooling  $\Delta T_{\text{BS}}$  as follows:

$$\Delta T_{\text{BS}} = T_f - T_f^c \quad (4.1)$$

with water's bulk freezing temperature  $T_f$ . The width of the step is treated as the error of  $\Delta T_{\text{BS}}$ . The change in step height for different samples reflects the different relative amount of water but also the changing contrast with change in oil.

Resulting values for the supercooling  $\Delta T_{\text{BS}}$  of confined water are listed in Tab. 4.1. These values are plotted in Fig. 4.1 b) against the molar ratio  $\omega$  which defines the size of the confinement. The solid line is a guide to the eyes and we clearly see that with decreasing  $\omega$  the observed water freezing temperature decreases.

AOT is an anionic surfactant therefore we have to take into account the effect of the dissolved  $\text{Na}^+$  ions. It is known that the freezing point of a salt solution is lower than the freezing point of the pure liquid. We estimated the upper limit for a shift of the freezing temperature caused by AOT ions assuming that all AOT molecules are dissociated and the ions uniformly distributed inside the water core:

$$\Delta T_{\text{max}} = \frac{K_c}{\omega \cdot m[\text{H}_2\text{O}]} \quad (4.2)$$

with  $m[\text{H}_2\text{O}] = 18 \text{ g/mol}$  being the molar mass of water and the cryoscopic constant of water  $K_c = -1.86 \text{ K kg mol}^{-1}$  [104]. The  $\omega$ -dependence of  $\Delta T_{\text{max}}$  resulting from Eq. 4.2 is shown by the dashed line in Fig. 4.1 b).  $\Delta T_{\text{max}}$  does not further increase for  $\omega < 6$  because the maximal depression of the freezing point is 21 K for a saturated salt solution [104]. For all three sizes the water freezes at temperatures of more than 15 K below this estimation. The salt concentration in the water core can therefore not exclusively explain the observed supercooling. We find that stronger confinement leads to a bigger supercooling of the water.

Comparison of sample 3, 4 and 5 with  $\omega = 12$  shows that the surrounding oil matrix does not influence the freezing of water inside the droplets in a remarkable way. Freezing of the water in sample 3 and 4 (with n-decane-d22) and of the water in sample 5 (with n-heptane-d16) occurs within the error bars at the same temperature even though the viscosities of the oils differ in the range of interest about a factor of 2 - 3 (see Fig. A.1 for a plot of the viscosities of toluene, heptane, decane and water as a function of temperature).

The freezing behavior of reverse micelle confined water was previously investigated and results from different techniques are contradictory. Mid-infrared spectroscopy was used to investigate the freezing behavior of water inside droplets of a microemulsion consisting of water, AOT, and n-pentane with  $1 \leq \omega \leq 30$  [40]. Whereas these authors report a  $\omega$ -independent phase transition of the water occurring for all compositions in a interval between  $T = 335 \text{ K}$  and  $245 \text{ K}$  (indicated in figure 4.1 b) by the grey rectangle), there are also experimental results in agreement with our observation of a  $w$ -dependent

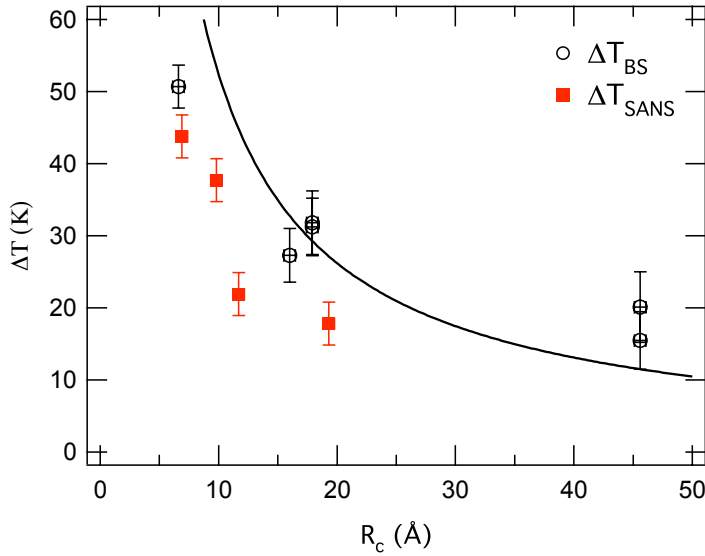


Figure 4.3: Supercooling  $\Delta T$  as a function of micelle core radius  $R_c$ . Hollow symbols are results from elastic scans on backscattering [86], full symbols correspond to SANS. Solid line shows the Gibbs-Thomson dependency (Eqn. 4.4) with the theoretical constant  $K_{GT} = 524 \text{ K } \text{\AA}$ .

freezing point of water. Fluorescent probing investigations on water/AOT/n-heptane microemulsions with  $5 \leq \omega \leq 20$  yielded a decrease in freezing temperature with decreasing  $\omega$  [50]. Confirming our results qualitatively, these authors found the freezing point of confined water to be shifted from  $T = 263 \text{ K}$  for  $\omega = 20$  to  $238 \text{ K}$  for  $\omega = 5$ .

#### 4.2.2. Relation between water freezing and droplet instability

Elastic scans have shown that the freezing point of the confined water is depressed compared to bulk water. Moreover the amount of supercooling was found to depend on micelle size: with decreasing micelle size the freezing temperature of the enclosed water decreases. This amount of supercooling  $\Delta T_{BS}$  is compared to the droplet stability:

$$\Delta T_{SANS} = T_f - T_s \quad (4.3)$$

with  $\Delta T_{SANS}$  being the difference between the freezing temperature  $T_f$  of deuterated water (for these SANS experiments shell contrast samples were used) and the shrinking temperature  $T_s$  of the droplets as observed in Fig. 3.9. In Fig. 4.3 we plot  $\Delta T$  from both experimental methods as a function of the droplet core radius  $R_c$ . Hollow symbols are BS results, full symbols are SANS results. It turns out that both data sets for  $\Delta T$  follow the same functional dependency on the radius  $R_c$ . We again want to underline that Fig. 4.3 compares structural findings and thus a static characteristic of the system ( $\Delta T_{SANS}$ ) with a dynamic observable ( $\Delta T_{BS}$ ). In this context it has to be mentioned that cooling rates for BS experiments were in the order of  $0.3 \text{ K/min} - 0.5 \text{ K/min}$ , which is very similar to those applied for the SANS experiments. The main experimental difference is the thickness of sample holders which was ten times thinner in the case of BS ( $0.1 \text{ mm}$ ).

If we assume that the ice formation occurs inside the droplets by the mechanism of homogenous nucleation then we can relate the supercooling to the confining radius  $R_c$ . Freezing of the water should only be possible at the temperature where the critical radius of an ice nuclei gets smaller than the radius  $R_c$  of the water core. The size of the critical nucleus depends on temperature therefore the supercooling  $\Delta T$  may now be expressed as a function of the droplet radius  $R_c$  [3]:

$$\Delta T \approx \frac{2 \gamma_{sl} T_f}{\rho L_{sl} R_c} = \frac{K_{GT}}{R_c} \quad (4.4)$$

with  $L_{sl}$  and  $\gamma_{sl}$  being the heat of fusion and surface tension between liquid water and ice respectively and  $\rho$  the density of water. Equation 4.4 is known as the Gibbs-Thomson equation and it predicts the supercooling  $\Delta T$  to be inversely proportional to the radius  $R_c$ . Inserting the values for  $\gamma_{sl}$  and  $L_{sl}$  of water at its bulk freezing temperature  $T_f$  we estimate the constant  $K_{GT} = 524 \text{ K } \text{\AA}$  [3] (and references therein). The solid line in Fig. 4.3 is a plot of the Gibbs-Thomson dependency, Eq. 4.4, without any adjustable parameter. We note that the supercooling  $\Delta T_{BS}$  for radii  $R_c > 10 \text{ \AA}$  is reasonably well described by that relationship, although the use of  $K_{GT}$  can only be a rough estimation since it does not take into account the temperature dependence of the involved constants. Recently it was observed by means of DSC that the melting point depression of water confined in mesoporous silica follows Eqn. 4.4 when taking into account a layer of non-freezable water close to the walls [3]. We conclude that hard and soft confinement seem to have similar effects on water freezing. Due to the restricted number of data points and the relatively large error bars we will restrict ourselves to this qualitative discussion of the relation between supercooling and confining size.

### 4.3. Summary and conclusions

We have investigated the freezing behavior of reverse micelle water cores by means of elastic temperature scans on backscattering spectrometers. We found that the freezing point of reverse micelle confined water is depressed with comparison to bulk water. The observed supercooling  $\Delta T_{BS}$  cannot be explained by the dissociation of the anionic surfactant molecules inside the water pool. The amount of supercooling  $\Delta T_{BS}$  of the water increases with decreasing droplet size confirming earlier results obtained by fluorescence probing [50]. This contradicts the finding of a  $\omega$ -independent freezing point as reported by [40]. Moreover the influence of the viscosity of the surrounding oil was investigated by changing the oil from decane to heptane while keeping the  $\omega$  constant and it was found to be weak. Comparing the freezing temperature of the confined water to the temperature of droplet shrinking determined by SANS, we note a similar dependency on droplet size.



## 5. Dynamics of microemulsion droplets

In chapter 3 we have discussed the static structure of the water/AOT/oil microemulsion as seen by SANS. Having characterized the droplet shape we now want to turn our attention to the dynamical behaviour of these droplets. We aim at investigating dynamics of water confined inside reverse micelles. So first we need to characterize the dynamics of the micelles itself in order to be able to properly separate water from droplet motion. Droplet microemulsions show dynamics over a wide range of time scales. The droplets perform thermally activated shape fluctuations around their mean spherical shape and they undergo translational diffusion in the surrounding oil matrix. On a longer time scale droplets collide, exchange water and surfactant material and re-form. NSE is well suited to measure both of these dynamic processes as it probes length scales comparable to the droplet size and time scales appropriate for the observation of bending modes and translational diffusion.

This chapter will start with a brief recapitulation of the theoretical description of droplet fluctuations. We will show how values for the bending modulus  $\kappa$  and the translational diffusion coefficient of droplets  $D_{\text{drop}}$  can be extracted from the time - and  $Q$ -dependence of the intermediate scattering function  $I(Q, t)$  measured by NSE.

For one structurally well characterized sample with D<sub>2</sub>O/AOT/toluene-d<sub>8</sub> ( $\omega = 8$ ,  $\phi = 0.1$ ), we have performed NSE measurements over a wide range of temperatures between  $T = 250$  K and 300 K. We have obtained the translational diffusion coefficient  $D_{\text{drop}}$  and the bending modulus  $\kappa$  of the AOT layer as a function of temperature. As an alternative way to measure  $D_{\text{drop}}$  we also have employed dynamic light scattering (DLS) on a sample with a similar composition to that studied by NSE.

We will relate dynamical observations made by NSE and DLS to structural results obtained from SANS and we arrive at a consistent picture about the phase behaviour of the microemulsion over the studied temperature range.

### 5.1. Micelle shell fluctuations and diffusion measured by NSE

We aim at investigating the confined water over the entire temperature range of structural stability of the microemulsion droplets. For this purpose we need to obtain a quantitative knowledge about the temperature dependent diffusion of the entire droplets.

This information is important to enable a proper separation of water from droplet dynamics. Moreover we want to make sure that not only the structure but also the "stiffness" of the confinement is preserved. As a measure for this stiffness we are interested in the bending modulus  $\kappa$  of the AOT surfactant membrane surrounding the water core. By means of NSE we can access both of these quantities as will be briefly outlined in the following.

### 5.1.1. Helfrich model for the bending energy of membranes

The surfactant mono-layer in microemulsions reduces the oil-water interfacial tension to about zero and the microemulsion structure is mainly determined by the spontaneous curvature  $C_s$  of the surfactant film. *Helfrich* related the surfactant film bending energy per unit area  $E_{el}$  to the bending modulus  $\kappa$ , saddle splay (or Gaussian) modulus  $\tilde{\kappa}$  and spontaneous curvature  $C_s = 1/R_s$  of the membrane [105]:

$$E_{el} = \frac{\kappa}{2} \left( \frac{1}{R_1} + \frac{1}{R_2} - \frac{2}{R_s} \right)^2 + \frac{\tilde{\kappa}}{R_1 R_2} \quad (5.1)$$

Here  $R_1$  and  $R_2$  are the principal radii of curvature, illustrated in Fig. 5.1 for a saddle surface. Equation 5.1 gives the energy cost for the deviation of the curvature from the spontaneous curvature  $C_s$ . Whereas for  $C_s = 0$  a flat surfactant film is favored, in the case of water-in-oil reverse micelles with the surfactant film curved towards the water,  $C_s$  is per definition negative. Values for the bending modulus  $\kappa$  can range from  $100 k_B T$  in the case of rigid structures like lipid bilayers to less than  $1 k_B T$  for microemulsions. Smaller  $\kappa < 0.1 k_B T$  typically result in emulsion instability [95].

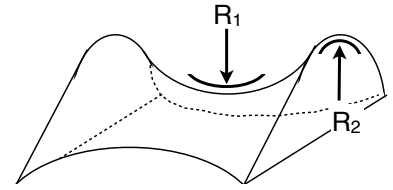


Figure 5.1.: Principal radii of curvature  $R_1$  and  $R_2$  for a saddle surface.

The second term in Eq. 5.1 is of importance for topologic changes of the microemulsion: a positive saddle-splay modulus  $\tilde{\kappa}$  favors bicontinuous structures while for negative  $\tilde{\kappa}$  lamellar or spherical phases occur [106].

For spherical droplets of radius  $R$ ,  $R_1 = R_2 = R$  holds and Eq. 5.1 reduces to:

$$E_{el} = 2 \kappa \left( \frac{1}{R} - \frac{1}{R_s} \right)^2 + \frac{\tilde{\kappa}}{R^2} \quad (5.2)$$

#### 5.1.1.1. Droplet shell fluctuations

On the basis of Eq. 5.1 *Safran* and *Milner* developed the theoretical description of thermally activated shell fluctuations of micelles and vesicles. The bending energy  $E_{el}$

associated with the deformation of a time-averaged spherical shell with radius  $R$  is described by an expansion in terms of spherical harmonics [107, 108]:

$$R'(\Omega) = R + R \sum_{l,m} u_{lm} Y_l^m(\Omega) \quad (5.3)$$

where  $Y_l^m(\Omega)$  denotes the spherical harmonic of degree  $l$  and order  $m$  with  $l \geq 0$  and  $|m| \leq l$  as a function of angle  $\Omega$ . For the derivation of the theory, both surfactant film area and droplet volume are conserved and the fluctuation-dissipation theorem is applied to calculate the amplitudes of the fluctuations. The droplet area can be assumed as constant, as the collision time  $t_c$  of diffusing droplets is much longer than the time scale  $\tau$  on which the fluctuations occur. It has further been shown by these authors that the principal contribution to the fluctuations arises from the ( $l = 0$ ) and ( $l = 2$ ) modes [107, 108]. In this approximation the zero order ( $l = 0$ ) deformation corresponds to the fluctuation in droplet size or in other words to the droplet size polydispersity  $p$  that may be determined by SANS. The mean squared amplitude  $\langle |u_0|^2 \rangle$  of the zero order mode is given by [109]:

$$\langle |u_0|^2 \rangle = k_B T \left[ 6(2\kappa + \tilde{\kappa}) - 8\kappa \frac{R}{R_s} + \frac{3k_B T}{2\pi} h(\phi) \right]^{-1} \quad (5.4)$$

with now taking also the entropy of mixing,  $h(\phi) \approx \ln \phi - 1$ , into account [106]. Implying that the observed polydispersity  $p$  is only determined by the amplitude of the zero order fluctuation  $u_0$ , one may relate  $p$  to  $\kappa$  and  $\tilde{\kappa}$  using Eq. 5.4 [110]:

$$p^2 = \frac{\langle |u_0|^2 \rangle}{4\pi} \quad (5.5)$$

The second order mode ( $l = 2$ ) describes "peanut-like" deformations of the droplet which may be observed in dynamic measurements; the corresponding mean squared amplitude is given by [109]:

$$\langle |u_2|^2 \rangle = k_B T \left[ 16\kappa \frac{R}{R_s} - 12\tilde{\kappa} - \frac{3k_B T}{4\pi} h(\phi) \right]^{-1} \quad (5.6)$$

Based on the theoretical model for viscoelasticity of vesicle dispersions proposed by *Seki* and co-workers [111], the associated relaxation rate  $\lambda_2$  calculates with [112]:

$$\lambda_2 = \frac{\kappa}{R_0^3} \left[ 4 \frac{R}{R_s} - 3 \frac{\tilde{\kappa}}{\kappa} - \frac{3k_B T}{4\pi\kappa} h(\phi) \right] \frac{24}{23\eta_w + 32\eta_t} \quad (5.7)$$

Here the viscosities inside  $\eta_w$  and outside  $\eta_t$  the fluctuating shell are explicitly considered.

Experimentally one may access the relaxation rate  $\lambda_2$  by NSE as outlined in the following. The intermediate scattering function  $I(Q, t)$  for a fluctuating thin shell is given by [107]:

$$I(Q, t) \propto \exp(-D_{\text{drop}}Q^2t) [4\pi[j_0(QR)]^2 + F_2(QR)\langle u_2(t)u_2(0)\rangle] \quad (5.8)$$

with the weighting factor  $F_2(QR) = 5[4j_2(QR) - QRj_3(QR)]^2$ . The exponential term describes the translational diffusion of the entire droplet, the first term in the brackets is the static form factor of the shell, and the time dependence of the fluctuations is contained in the autocorrelation function of the fluctuation amplitude  $u_2$ .

Rather than evaluating this sum in exponentials one takes the initial slope of the normalized intermediate scattering function [107]:

$$-\left. \frac{d I(Q, t)}{dt} \right|_{t=0} \frac{1}{I(Q)} = -\left. \frac{d}{dt} \ln(I(Q, t)) \right|_{t=0} = D_{\text{drop}}Q^2 + \frac{\lambda_2 \langle |u_2|^2 \rangle F_2(QR_0)}{4\pi[j_0(QR)]^2 + \langle |u_2|^2 \rangle F_2(QR)} \quad (5.9)$$

with the relaxation rate  $\lambda_2$  of the ( $l = 2$ ) mode.

The measured normalized intermediate scattering function  $I(Q, t)/I(Q, 0)$  can then be evaluated in terms of a single exponential:

$$\frac{I(Q, t)}{I(Q, 0)} = \exp(-D_{\text{eff}}(Q) \cdot Q^2t) \quad (5.10)$$

where the effective diffusion coefficient  $D_{\text{eff}}(Q)$  has a characteristic  $Q$ -dependence: it contains the  $Q$ -independent translational diffusion coefficient  $D_{\text{drop}}$  of the droplets and a  $Q$ -dependent term  $D_{\text{def}}(Q)$  representing the droplet shape fluctuations [113]:

$$D_{\text{eff}}(Q) = D_{\text{drop}} + D_{\text{def}}(Q) \quad (5.11)$$

where the deformation coefficient  $D_{\text{def}}$  is defined after Eq. 5.9 as:

$$D_{\text{def}} = \frac{1}{Q^2} \cdot \frac{\lambda_2 \langle |u_2|^2 \rangle F_2(QR)}{4\pi[(j_0(QR))]^2 + \langle |u_2|^2 \rangle F_2(QR)} \quad (5.12)$$

For  $QR = \pi$  the structure factor of the undistorted spherical shell has a minimum and the ( $l = 2$ ) mode has the largest weighting factor and still a large amplitude [107]. Therefore the contribution of  $D_{\text{def}}$  - as a measure of the shell fluctuations - to  $D_{\text{eff}}$  will be best visible around  $Q = \pi/R$ . For larger and smaller  $Q$  the predominant contribution will be the translational diffusion coefficient  $D_{\text{drop}}$  of the droplet.  $D_{\text{def}}$  has a peak centered at about the  $Q$ -value which corresponds to the minimum of the static form factor of the droplets and the peak form can now be evaluated to yield the mean squared dimensionless fluctuation amplitude  $\langle |u_2|^2 \rangle$  and the relaxation rate  $\lambda_2$  of the ( $l = 2$ ) mode.

Combining Eqs. 5.5 and 5.7 *Kawabata* and co-workers derived the following expression for the bending modulus  $\kappa$ , where  $\tilde{\kappa}$  and  $h(\phi)$  have cancelled out [112]:

$$\kappa = \frac{1}{48} \left( \frac{k_B T}{\pi p^2} + \lambda_2 R^3 \frac{23 \eta_w + 32 \eta_t}{3} \right) \quad (5.13)$$

Equation 5.13 expresses the bending modulus  $\kappa$  in terms of parameters that can be accessed experimentally: polydispersity  $p$  and droplet radius  $R$  measurable by SANS and  $\lambda_2$  measurable by NSE.

Since the pioneering work of *Huang* and co-workers [114], NSE was successfully applied to measure shell fluctuations of many different microemulsion systems. Besides bicontinuous phases, droplet microemulsion have extensively been studied [84,115] and especially water swollen AOT micelles with a variety of different surrounding oils and molar ratios  $\omega$  have been subject of a number of investigations [36,95,116–118]. Reported values for  $\kappa$  in water/AOT/oil systems range from  $0.2k_B T$  to several  $k_B T$  as summarized e.g. in [95]. To our knowledge no such investigations have been published for low temperatures  $T < 270$  K and none for toluene as oil surrounding the droplets.

## 5.2. Experimental details

For the investigation of the relationship between the bending modulus  $\kappa$  of the AOT shell and the structural stability of the droplets, we have chosen one sample composition with D<sub>2</sub>O/AOT/toluene-d<sub>8</sub> with  $\omega = 8$  and  $\phi = 0.1$ . Regarding the molar ratio  $\omega$  this composition corresponds to sample T3 whose temperature dependent structure is discussed under section 3.5. For this composition the SANS experiments showed that the initial core radius  $R_c = 12 \text{ \AA}$  is stable down to  $T_s \approx 255$  K (see Fig. 3.9). For the NSE experiment we have thus varied the temperature between  $T = 300$  K and 250 K to cover the range where the shrinking of the droplets occurs.

NSE experiments have been carried out at the spin-echo spectrometer IN15 at the ILL. The following configurations were used: a neutron wavelength  $\lambda = 6.3 \text{ \AA}$  ( $10 \text{ \AA}$ ) and scattering angles  $2\theta = 4.7^\circ, 7.7^\circ, 10.7^\circ$ , and  $13.7^\circ$  ( $4.7^\circ$  and  $7.7^\circ$ ) resulting in a  $Q$  ranging from  $0.065 \text{ \AA}^{-1}$  -  $0.314 \text{ \AA}^{-1}$  ( $0.039 \text{ \AA}^{-1}$  -  $0.094 \text{ \AA}^{-1}$ ) respectively. The probed time window was 0 ns - 12 ns (50 ns). NSE decouples resolution and intensity to the first order and therefore a relatively large wavelength band of 15% (FWHM) can be used.

Samples were measured in the same flat aluminum sample holders of 1 mm thickness used for the SANS measurements at low temperatures. The sample temperature was controlled by a standard ILL orange cryostat. At all measured temperatures the sample was equilibrated for at least one hour before starting to count.

The instrumental resolution was obtained by measuring graphite which is a coherent

elastic scatterer. Resolution corrections were then simply carried out by dividing all sample spectra with the appropriate resolution measurement. All spectra were further corrected for background scattering from the pure solvent and the sampleholder as explained in section 2.2.3.3.

The multi-detector signal was further sub-grouped into 2 to 9  $Q$ -values per scattering angle  $2\theta$ .

## 5.3. Results and discussion

### 5.3.1. Droplet translation and bending modulus

In Fig. 5.2 we show the normalized intermediate scattering function  $I(Q, t)/I(Q, 0)$  of the microemulsion at a temperature  $T = 265$  K for a selection of scattering vectors  $Q$ .

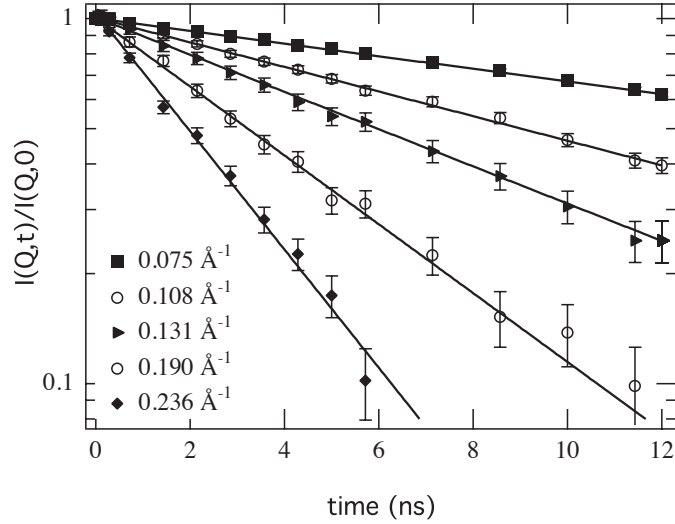


Figure 5.2.: Normalized intermediate scattering function  $I(Q, t)/I(Q, 0)$  at  $T = 265$  K. Scattering vectors  $Q$  are indicated next to symbols. Solid lines are fits to a single exponential function.

By fitting  $I(Q, t)/I(Q, 0)$  to a single exponential, shown as solid lines in Fig. 5.2, we obtain the effective diffusion coefficient  $D_{\text{eff}}$  defined by Eq. 5.10. Note that the single exponential function describes our data in an adequate way<sup>1</sup> and therefore we do see

<sup>1</sup>This is also the case for the data obtained with an initial wavelength of  $\lambda = 10$  Å attaining Fourier times up to 50 ns. The accessed  $Q$  is too small to probe the location of the peak in  $D_{\text{eff}}$  therefore we do not expect a deviation from the single exponential form.

no reason to use more complicated fitting models that have recently been proposed [119]. The resulting effective diffusion coefficient  $D_{\text{eff}}$  is shown in Fig. 5.3 as a function of the scattering vector  $Q$ . In the same figure we also plot the corresponding static structure factor that was before determined by SANS (at room temperature). From top to bottom the temperature varies from  $T = 300$  K to 250 K and indeed we observe a clear maximum of  $D_{\text{eff}}$  around the minimum of the static structure factor (at about  $Q = 0.14 \text{ \AA}^{-1}$ ) for all temperatures except for  $T = 250$  K.

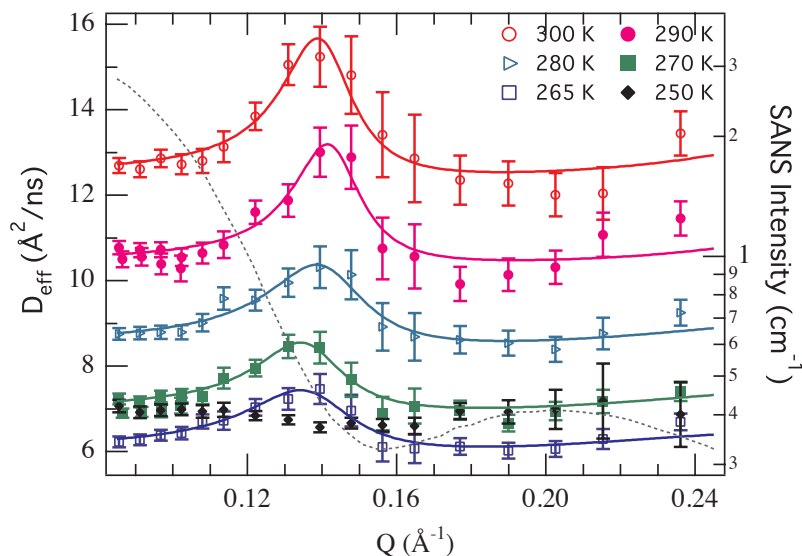


Figure 5.3.: Effective diffusion coefficient  $D_{\text{eff}}$  as obtained by fitting the NSE curves to a single exponential (Eqn. 5.10). Solid lines are fits to Eqn. 5.11. Note that no maximum around  $Q = 0.14 \text{ \AA}^{-1}$  is observed at the lowest temperature  $T = 250$  K. Grey dotted line shows the SANS intensity of the investigated microemulsion around room temperature.

Let us here recall that for the studied composition the shrinking of the droplets was observed around 255 K (see sample T3 in Fig. 3.9). For all temperatures above 255 K the sample thus consists of droplets dispersed in toluene with a core radius of  $R_c = 12 \text{ \AA}$ , whereas at 250 K the water core is diminished to  $6 \text{ \AA}$  to  $7 \text{ \AA}$ . Adding on  $R_c$  the thickness  $d$  of the AOT shell, we know that the total droplet radius,  $R = R_c + d$ , decreases from  $R(T > 255 \text{ K}) = 24 \text{ \AA}$  to  $R(T = 250 \text{ K}) = 19 \text{ \AA}$ .

We now fit the  $Q$ -dependence of  $D_{\text{eff}}$  by Eq. 5.11. The fits are shown as solid lines Fig. 7.3 and the resulting parameters are displayed in Fig. 5.4 as a function of temperature. At this point we want to remind that when using Eq. 5.11 for the description

of the shell fluctuations we neglect the higher order deformations ( $l > 2$ ) which may be the reason for the small discrepancies between the model and  $D_{\text{eff}}$  for  $Q > 0.2 \text{ \AA}^{-1}$  in Fig. 5.3. We will now discuss the fitting results shown in Fig. 5.4.

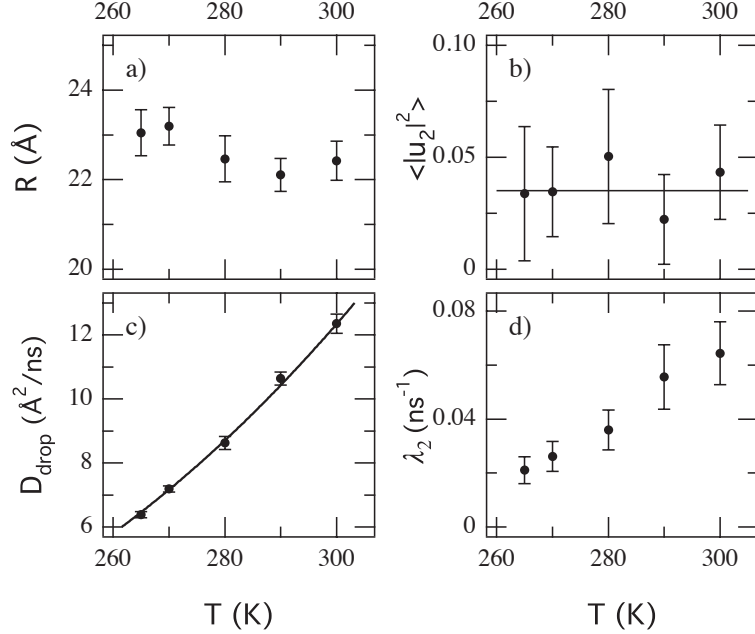


Figure 5.4.: Temperature dependencies of fitting parameters of Eq. 5.11. a): mean droplet radius  $R$ , b) dimensionless fluctuation amplitude  $\langle |u_2|^2 \rangle$ , c): translational diffusion coefficient  $D_{\text{drop}}$ , the line is a fit to Eq. 5.14 and d): relaxation rate  $\lambda_2$  of second order oscillation.

**5.3.1.0.1. Droplet radius:** The location of the maximum  $Q_{\text{max}}$  of  $D_{\text{eff}}$  is determined by the mean radius  $R$  of the fluctuating shell. In Fig. 5.3 it can be seen already with the naked eye that this maximum slightly shifts between the different temperatures. Figure 5.4 a) displays the NSE fitting results for  $R$  as a function of temperature. Below 280 K the radius seems to increase of about  $1 \text{ \AA}$  from  $R = 22.2 \text{ \AA}$  to  $23.1 \text{ \AA}$ . Due to the relatively large errors we do not attach too much importance to these small changes, though we note that also the SANS experiments showed that the thickness of the AOT shell (thus also the total radius) increases slightly with decreasing temperature. But contrary to the NSE results the SANS results, plotted in Fig. 3.10, show a continuous variation with temperature and much smaller relative errors. The absolute value for the NSE-radius of about  $R \approx 22 \text{ \AA} - 23 \text{ \AA}$  is in excellent agreement with  $R \approx 24 \text{ \AA}$  observed by SANS.



**5.3.1.0.2. Diffusion coefficient:** The level of  $D_{\text{eff}}$  at small  $Q$  gives the translational diffusion coefficient  $D_{\text{drop}}$  of the droplets (Fig. 5.4 c)). Using the modified Stokes-Einstein equation for a diffusing deformable droplet one may relate  $D_{\text{drop}}$  to the hydrodynamic radius  $R_h$  of the diffusing droplet [120]:

$$D_{\text{drop}} = (1 - \phi) \frac{k_B T}{2\pi \eta_t R_h} \cdot \frac{\eta_w + \eta_t}{3\eta_w + 2\eta_t} \quad (5.14)$$

where  $\phi$  denotes the volume fraction of droplets and  $\eta_t$  and  $\eta_w$  the temperature-dependent viscosities of toluene-d8 and heavy water respectively<sup>2</sup>. The viscosity  $\eta_t$  of deuterated toluene in the temperature range of interest was assumed to be similar to that of protonated toluene as given in [121],  $\eta_w$  of heavy water was calculated from the viscosity of protonated water found in [122] with the formula given in [123]. From the SANS experiments we know that neither the geometrical radius nor the interactions of the droplets significantly change with temperature (above 255 K). The variation of  $D_{\text{drop}}$  with temperature should then be completely contained in the temperature dependence of viscosities of toluene  $\eta_t$  and water  $\eta_w$ . The only free parameter in Eq. 5.14 is hence the hydrodynamic radius  $R_h$ .

In effect the absolute value of  $D_{\text{drop}}$  can, for all temperatures above 255 K, be expressed in an excellent way by the modified Stokes-Einstein equation 5.14 and a constant temperature independent  $R_h$  of 33 Å, shown by the solid line in Fig. 5.4 c). The deduced  $R_h$  is about 1.3 times larger than the geometrical radius ( $R = R_c + d$ ) of the droplets determined by SANS. A hydrodynamic radius  $R_h$  bigger than the geometrical radius has been observed in many different micellar systems and is explained by a shell of solvent molecules that moves along with the diffusing droplet [33].

Turning our attention now to the behaviour of  $D_{\text{eff}}$  at 250 K shown in Fig. 5.3 we remark that the effective diffusion coefficient  $D_{\text{eff}}$  is rather  $Q$ -independent and flat. At first glance it is surprising to see that despite the higher viscosity of toluene at  $T = 250$  K the effective diffusion coefficient  $D_{\text{eff}}$  is bigger than at 265 K. We estimate the translational diffusion coefficient  $D_{\text{drop}}$  at  $T = 250$  K by Eq. 5.14 taking into account the hydrodynamic radius of about 1.3 times the total geometrical radius,  $R_h \approx 1.3 \cdot R = 24$  Å and the droplet volume fraction that is due to the water expulsion reduced to  $\phi \approx 0.08$ . We get  $D_{\text{drop}} = 6.7$  Å<sup>2</sup>/ns which is about the level we observe. Shell fluctuations for droplets of this size should be best visible around  $Q = 0.19$  Å where within the errors we do not see maximum in  $D_{\text{eff}}$ . This might be due to the fact that the core is reduced to the AOT head groups and about two water molecules per AOT why the amplitude of the fluctuations is supposed to be very small.  $D_{\text{eff}}$  at 250 K is therefore mainly given by the  $Q$ -independent  $D_{\text{drop}}$ .

<sup>2</sup>It was shown by the authors that the exact form of the shape energy is irrelevant to the diffusion coefficient as far as the deformation of the droplet is small enough so that only the viscosities are of importance for the calculation of  $D_{\text{drop}}$  [120].

Overall the findings for the translational diffusion of the droplets (NSE) confirm the structural results (SANS) in the investigated temperature range.

**5.3.1.0.3. Bending modulus  $\kappa$ :** The nature of the fluctuations are contained in the dimensionless mean squared amplitude  $\langle |u_2|^2 \rangle$  and the decay rate  $\lambda_2$ . The variation of these two parameters with temperature is shown in Fig. 5.4 b) and d).

We note that within the errors the dimensionless mean squared amplitude is constant  $\langle |u_2|^2 \rangle \approx 0.03$ . Inspecting Eq. 5.6 this means that, if the mixing entropy  $h(\phi)$  is negligible and  $\tilde{\kappa} \propto k_B T$ , already at this point we expect a constant bending modulus  $\kappa$  as  $\langle |u_2|^2 \rangle$  is constant under temperature variation<sup>3</sup>.

The decay rate  $\lambda_2$  increases with increasing temperature about a factor of roughly 3.5 from  $T = 265$  K to 300 K which is partly explained by the decrease of viscosity with temperature, see Equation 5.7. (Figure A.1 in the appendix displays the temperature dependence of water and toluene viscosities.)

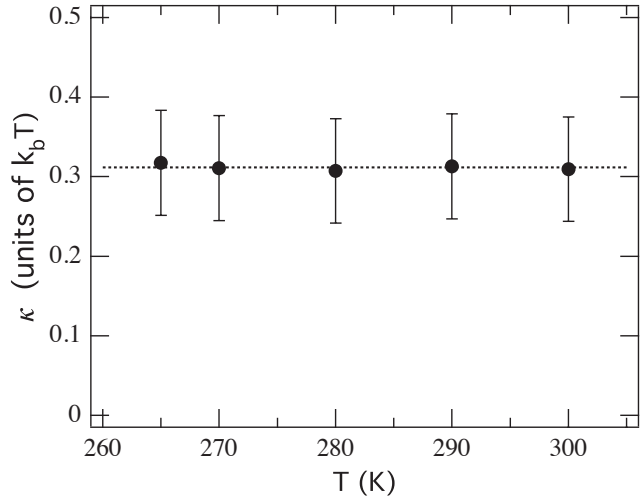


Figure 5.5: Temperature dependence of bending elasticity  $\kappa$  of the AOT shell calculated after equation 5.13. Dotted line shows the average bending elasticity  $\kappa = (0.31 \pm 0.06)k_B T$ .

Using Eq. 5.13 we may now calculate the bending modulus  $\kappa$ . Figure 5.5 displays  $\kappa$  as a function of temperature. For the whole investigated temperature range we find a constant bending modulus  $\kappa = (0.31 \pm 0.06)k_B T$ . Even though we have observed by SANS that the droplet instability for this sample composition occurred around  $T_s = 255$  K, the bending modulus  $\kappa$  does not decrease when approaching  $T_s$ . Thus we conclude that our experimental findings do not allow to relate the AOT membrane elasticity to the low temperature structural instability of the droplets. The absolute value of  $\kappa = 0.3k_B T$  compares very well with the previous studies on AOT reverse water swollen micelles in other oils than toluene [95].

<sup>3</sup>Note that when speaking of a constant bending modulus, one means that it contains only the simple temperature dependence  $\kappa \propto k_B T$ .

## 5.4. Droplet diffusion measured by DLS

An alternative way to determine the diffusion coefficient of microemulsion droplets is by means of dynamic light scattering (DLS). The intensity of light scattered by a droplet microemulsion fluctuates due to the Brownian motion of the droplets. These fluctuations can be analyzed through the normalized autocorrelation function of the scattered electrical field  $g_1(t)$ . For an ideal solution of monodisperse spherical diffusing particles  $g_1$  decays exponentially:

$$g_1(t) = \exp\left(-\frac{t}{\tau}\right) \quad (5.15)$$

The relaxation rate  $\tau^{-1}$  is related to the mutual diffusion coefficient  $D_m$  according to:

$$\tau^{-1} = D_m Q^2 \quad (5.16)$$

with the scattering vector,  $Q = \frac{4\pi}{\lambda} n \sin(\theta/2)$ , depending on the diffraction index  $n$ .  $g_1(t)$  can be derived from the measured intensity correlation  $g_2(t)$  by applying the Siegert-relation:

$$g_1(t) = \sqrt{g_2(t) - 1} \quad (5.17)$$

The measured mutual diffusion coefficient  $D_m$  is a function of the droplet volume fraction and for low concentrations,  $\phi \leq 0.1$ , the following relation holds [124]:

$$D_m = D_0(1 + k_D\phi) \quad (5.18)$$

with  $k_D$  denoting the diffusional virial coefficient which includes thermodynamic and frictional effects<sup>4</sup>.

### 5.4.1. Experimental

We have investigated a microemulsion composed of H<sub>2</sub>O/AOT/toluene-h8 with  $\omega = 8$  and  $\phi = 0.1$  at temperatures  $T = 260$  K, 273 K and 288 K. With respect to  $\omega$  and  $\phi$  this composition corresponds to the sample measured with NSE (see section 5.2). Contrary to the NSE sample, which contained D<sub>2</sub>O and toluene-d8, the DLS sample is fully protonated.

Experiments have been performed at the DLS apparatus at the TU Darmstadt. The DLS measurements are of marginal importance for this work therefore we desist from a lengthy discussion of theory and technique. The experimental set-up is in detail

<sup>4</sup>To extract the real free droplet diffusion coefficient one would have to measure  $\tau^{-1}$  with decreasing volume fraction and extrapolate it to zero concentration  $\phi \rightarrow 0$ .

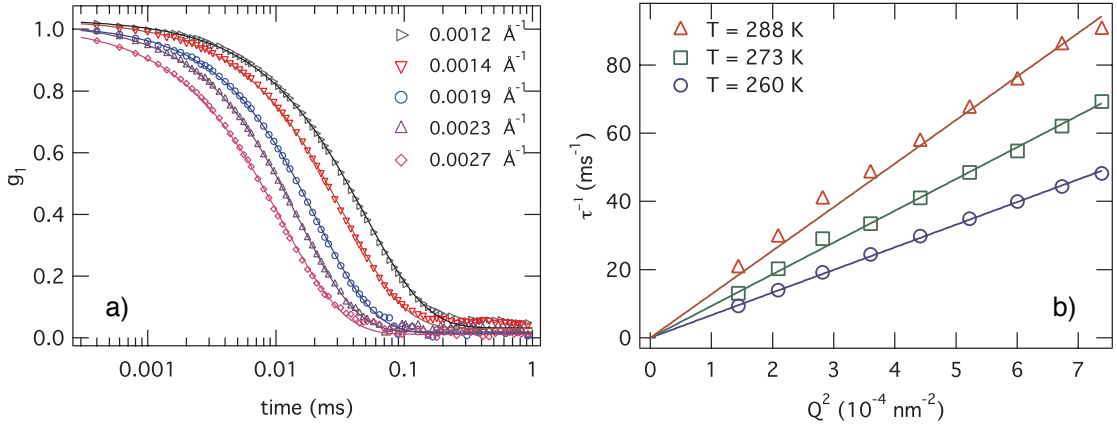


Figure 5.6.: a) Field autocorrelation function  $g_1$  for pure microemulsion ( $\text{H}_2\text{O}/\text{AOT}/\text{toluene-h8}$ ,  $\phi = 0.1$ ,  $\omega = 8$ ) at  $T = 288 \text{ K}$ . Solid lines are fits to a single exponential. b) Linear fit of the relaxation rate  $\tau^{-1}$  vs  $Q^2$  in order to determine temperature dependent diffusion coefficients (see Eq. 5.16).

described elsewhere [125]. As a special feature we only want to mention the cold finger cryostat which allows for measurements at temperatures between  $77 \text{ K} \leq T \leq 475 \text{ K}$ . Measured scattering angles ranged from  $\theta = 50^\circ$  to  $130^\circ$  in steps of  $\Delta\theta = 10^\circ$ , giving access to scattering vectors between  $0.0012 \text{ \AA}^{-1} \leq Q \leq 0.0027 \text{ \AA}^{-1}$ . (As light source a He-Ne Laser with a wavelength of  $\lambda = 632.8 \text{ nm}$  is used).

The sample was filtered with a  $0.2 \mu\text{m}$  Millipore filter inside a laminar flow box into the sample holder. Samples were measured in a cylindrical glass cell with a diameter of  $20 \text{ mm}$ . Before starting the measurement the sample was equilibrated for at least 15 minutes at the desired temperature.

#### 5.4.2. Results

Figure 5.6 a) shows field autocorrelation functions  $g_1$  for the microemulsion at a temperature of  $T = 288 \text{ K}$  at a selection of different scattering vectors. For each  $Q$  we fit  $g_1$  according to Eq. 5.15 with a single exponential to determine the relaxation rate  $\tau^{-1}$ . We note that the single exponential describes the data in a very satisfactory way which implies that the microemulsion does not contain aggregates of droplets. This is an additional information to what we see by NSE, where the probed length scale is much smaller. The resulting values of  $\tau^{-1}$  at all three investigated temperatures are plotted as a function of  $Q^2$  in Fig. 5.6 b). Solid lines are fits with Eq. 5.16 in order to extract the mutual diffusion coefficient  $D_m$ .

Figure 5.7 displays the obtained diffusion coefficients as a function of temperature.

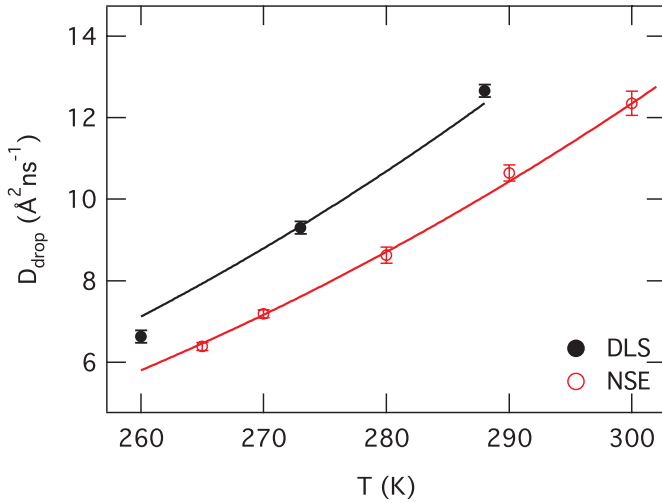


Figure 5.7: Temperature dependence of translational diffusion coefficient of pure microemulsion ( $\text{H}_2\text{O}/\text{AOT}/\text{toluene-h8}$ ,  $\phi = 0.1$ ,  $\omega = 8$ ). Black symbols represent DLS results. Red symbols are NSE results for a similar microemulsion ( $\text{D}_2\text{O}/\text{AOT}/\text{toluene-d8}$ ,  $\phi = 0.1$ ,  $\omega = 8$ ). Solid lines are fits with Eqn. 5.14. See text for further explanations.

We compare DLS results (black full symbols) to the previously discussed NSE results (red hollow symbols). We note that using DLS we see a slightly faster droplet diffusion than with NSE. The absolute difference is for all investigated temperatures with  $\Delta D_{\text{drop}} \approx (1 - 2) \text{\AA}^2 \text{ns}^{-1}$  rather small. We can alternatively say that the DLS results behave like the NSE results shifted to a temperature 10 degrees lower.

Part of this difference is probably explained by the samples differing with respect to their deuteration. As it is the case for other liquids, the viscosity of the deuterated form, i.e. toluene-d8, is likely to be higher than that of toluene-h8; the same objects should thus diffuse faster in toluene-d8, which is what we observe. Only knowing the temperature dependent viscosity of toluene-h8 we cannot explicitly account for this. Using the Stokes-Einstein relation, Eq. 5.14, we can only estimate the hydrodynamic radius of the diffusing droplet to be  $R_h = (27.7 \pm 0.7) \text{\AA}$  which is a few Ångström smaller than the value deduced from NSE ( $R_h \approx 33 \text{\AA}$ ).

All in all the discrepancies between DLS and NSE results are small and we tend to explain them by the different sample compositions and potentially also by small errors of the temperature.

## 5.5. Summary and conclusions

We used NSE to study AOT shell fluctuations and droplet diffusion as a function of temperature for a microemulsion ( $\text{AOT}/\text{D}_2\text{O}/\text{toluene-d8}$ ,  $\phi = 0.1$ ,  $\omega = 8$ ) between  $250 \text{ K} \leq T \leq 300 \text{ K}$ . SANS has shown that the investigated microemulsion consists of droplets with an initial room temperature water core of radius  $R_c \approx 12 \text{\AA}$ . When cooling

the microemulsion, the droplets shrink at a temperature of  $T_s \approx 255$  K, see sample T3 in 3.9. The chosen temperature range for the NSE study covered thus the temperature range of structural stability and shrinking.

The measured intermediate scattering function was analyzed in terms of single exponential,  $I(Q, t)/I(Q, 0) = \exp(-D_{\text{eff}}Q^2t)$ . The  $Q$ -dependent effective diffusion coefficient  $D_{\text{eff}}$  contains the translational diffusion coefficient  $D_{\text{drop}}$  as well the information about relaxation rates and amplitudes of the shell fluctuations. Confirming the SANS results,  $D_{\text{drop}}$  corresponds through the Stokes-Einstein relation (Eq. 5.14) to a constant hydrodynamic droplet radius of about 1.3 times the geometrical radius for all temperatures above  $T_s$ . At temperatures below  $T_s$ ,  $D_{\text{drop}}$  agrees with the estimated translational diffusion coefficient of shrunken droplets. Analyzing the shell fluctuations we observed a relaxation rate  $\lambda_2$  which increases with temperature. Following the model proposed by [113] for the determination of the bending modulus  $\kappa$  of the AOT shell, we did not see a variation with temperature. Contrary to results for water swollen AOT micelles in decane, where the shell became more floppy (corresponding to a decreasing  $\kappa$ ) with increasing temperature [119], our data analysis yields a constant bending modulus of  $\kappa \approx 0.3k_B T$  over the whole investigated temperature range where the droplets are stable. From our experimental results no relation between the droplet instability at  $T_s$  and the bending elasticity  $\kappa$  can be inferred.

We conclude that besides the structural stability, also concerning the droplet dynamics, this microemulsion system is well suited for the study of confined water over a large temperature range. Experimentally no change of the AOT shell elasticity with temperature is detected, this implies that the hardness of the confinement does not vary in a significant way.

Using DLS on a fully protonated sample with otherwise the same composition as for the NSE study, we measured slightly bigger diffusion coefficients for the droplets. We explain the small discrepancy mainly by the differing viscosity of protonated and deuterated toluene. An additional information obtained by DLS is that no large droplet clusters are present in the sample.

For the subsequent discussion of water dynamics inside these droplets we will rely on the NSE results for the droplet diffusion. Quasi-elastic neutron scattering methods NSE, TOF and BS all probe a much larger  $Q$  than DLS. By NSE (which we used to analyze coherent scattering!) we do therefore not expect to observe a signature of cooperative droplet diffusion. We are thus confident that the incoherently measured droplet diffusion is very well approximated by  $D_{\text{drop}}$  obtained by NSE.

## 6. Dynamical behavior of water in reverse micelles

Having characterized the droplet structure of the microemulsion (chapter 3) as well as diffusion and form fluctuations of the droplets (chapter 5) we shall now focus on the study of the confined water itself. By means of QENS, combining TOF and BS, the dynamical behavior of water inside reverse AOT micelles was investigated spanning a time range of three decades from pico- to nanoseconds. The influence of the micelle size on water dynamics was studied using two sets of samples with droplets of bigger and smaller sizes. We have chosen water inside micelles with  $\omega = 3$  and  $\omega = 8$  with respective core radii of about  $R_c \approx 12 \text{ \AA}$  and  $7 \text{ \AA}$ . The temperature was varied over the common range of stability for both systems, from room temperature down to the region where water is supercooled,  $260 \text{ K} \leq T \leq 300 \text{ K}$ .

We will begin this chapter with the description of models for the different kinds of water motion, namely rotational and translational diffusion, and the according scattering functions in the time and frequency domain. Few QENS studies have been reported in literature and we will briefly summarize their outcome. Our own experimental results follow under section 6.2; we will describe rotational and translational motion of confined water molecules separately and we compare the measured diffusion coefficients to the respective values of bulk water. The dependence of water's mobility on micelle size and temperature is in detail discussed.

### 6.1. Theoretical description of water motion

In the following we will discuss the incoherent dynamic scattering function as well as the intermediate scattering function describing different kinds of water motion.

For the temperature range studied here,  $\hbar\omega \ll (1/2)k_B T$  holds, and thus the classical approximation is valid. The scattering function may then be considered as symmetric  $S(Q, \omega) = S(-Q, -\omega)$  which implies an equal probability for energy gain and loss of the neutrons upon interaction with the sample which is the case only when all sample states are uniformly occupied.

Water molecules undergo different kinds of motion: they vibrate, they perform trans-

lational diffusion and they rotate. If these motions are decoupled, meaning they are independent of each other, one can write the total incoherent dynamic structure factor  $S_{\text{inc}}(Q, \omega)$  as a convolution product of the vibrational, translational and rotational parts,  $S_{\text{inc}}^{\text{V}}(Q, \omega)$ ,  $S_{\text{inc}}^{\text{T}}(Q, \omega)$  and  $S_{\text{inc}}^{\text{R}}(Q, \omega)$  respectively:

$$S_{\text{inc}}(Q, \omega) = S_{\text{inc}}^{\text{V}}(Q, \omega) \otimes S_{\text{inc}}^{\text{T}}(Q, \omega) \otimes S_{\text{inc}}^{\text{R}}(Q, \omega) \quad (6.1)$$

The maximum scattering vector up to which we will analyze our QENS data is  $Q \approx 1 \text{ \AA}^{-1}$ ; this means that the minimum direct spacing that we probe is  $6.3 \text{ \AA}$  compared to the length of an O-H bond of about  $1 \text{ \AA}$ . The decoupling approximation was shown to be valid by comparing results of MD simulations and experiments for water in the time and space range probed by QENS [9, 63, 126]. In the following we will therefore take the decoupling approximation for granted.

We will continue with the detailed description of each of the terms in Eq. 6.1 as they are commonly used to analyze QENS signals of water.

### 6.1.1. Vibrations

In the quasi-elastic region (timescale of picoseconds and longer) the vibrational dynamics have decayed and their apparent contribution to the scattered intensity is a Debye-Waller factor in the time domain [22]:

$$I^{\text{V}}(Q, t) \approx \exp\left(-\frac{1}{3}Q^2\langle u^2 \rangle\right) \quad (6.2)$$

Here  $\langle u^2 \rangle$  is the mean square vibrational amplitude of a hydrogen atom around its equilibrium position. In Fig. 6.1 the Debye-Waller factor is plotted over the  $Q$ -range of interest for our experiments to estimate the contribution of vibrations to  $I(Q, t)$ . We chose two literature values as limits for  $\langle u^2 \rangle$  of water [9, 85] to calculate  $I(Q, t)$  after Eq. 6.2.

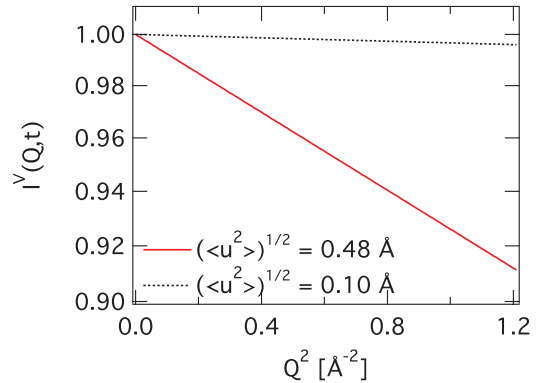


Figure 6.1: Estimation of upper and lower limit for vibrational intermediate scattering function  $I^{\text{V}}(Q, t)$  of water in the wavevector range up to  $Q = 1.1 \text{ \AA}^{-1}$ . The Debye-Waller factor (Eq. 6.2) for a maximum (red) [85] and minimum (black) [9] vibrational amplitude is plotted against  $Q^2$ . See text for further details.



A vibrational amplitude of  $\sqrt{\langle u^2 \rangle} \leq 0.1 \text{ \AA}$  was assumed by *Liu* and co-workers [9]. In the range probed by QENS the Debye-Waller factor can then be set to unity as illustrated by the black dotted line in Fig. 6.1.

As an estimation for an upper limit for the vibrational contribution we calculate  $I^V(Q, \omega)$  with  $\sqrt{\langle u^2 \rangle} = 0.48 \text{ \AA}$  as found by *Teixeira* and co-workers who used QENS to measure water dynamics [85]. The resulting intermediate scattering function is shown by the red line in Fig. 6.1. Over the investigated  $Q$ -range, the Debye-Waller factor would in this case decay to 90% of the value at  $Q = 0$ .

In the following any possible vibrational contributions to the scattering will be included in a pre-factor  $K$  which scales the total observed intermediate scattering function. As later discussed  $K$  contains intensity variations due to normalization with resolution spectra of crystallized samples and possible coherent contributions. Therefore we are not able to draw conclusions on vibrational motions of water.

### 6.1.2. Translational diffusion

In the limit of a continuous medium and a smooth density gradient a model describing long-range diffusion has to satisfy the Fick equation, which relates the time evolution of the system to the concentration gradient:

$$D\nabla^2 G_s(r, t) = \frac{\partial}{\partial t} G_s(r, t) \quad (6.3)$$

where  $G_s$  denotes the self-part of the autocorrelation function, giving the probability that a particle can be found at the position  $r$  at the time  $t$ , see section 2.1. Equation 6.3 is solved by a Gaussian form for  $G_s(r, t)$ :

$$G_s(r, t) = \frac{1}{\sqrt{(4\pi D_T t)^3}} \exp\left(-\frac{r^2}{4D_T t}\right) \quad (6.4)$$

with  $D_T$  denoting the translational diffusion coefficient. Fourier transforming Eq. 6.4 with respect to time and to space gives a Lorentzian-shaped incoherent dynamic scattering function  $S_{\text{inc}}^T(Q, \omega)$ :

$$S_{\text{inc}}^T(Q, \omega) = \frac{1}{\pi} \cdot \frac{D_T Q^2}{\omega^2 + (D_T Q^2)^2} = \mathcal{L}(\Gamma_T, \omega) \quad (6.5)$$

with its half width at half maximum,  $\text{HWHM} = \Gamma_T$ , varying in the case of free translational diffusion according to:

$$\Gamma_T(Q) = D_T Q^2 \quad (6.6)$$

In the time domain this corresponds to an intermediate scattering function  $I^T(Q, t)$  which decays exponentially:

$$I^T(Q, t) = \exp(-D_T Q^2 t) \quad (6.7)$$

The model of isotropic free translational diffusion is often insufficient to describe the measured scattering functions of diffusing particles. When the probed  $Q$  is larger than the inverse of the distance between neighboring molecules the neutrons will also detect the microscopic details of the diffusion process. In the case of water, the translational diffusion can in this range successfully be expressed by a random jump diffusion model presented first by *Singwi* and *Sjölander* in 1960 [127]. The underlying picture of this model is that water molecules are being trapped by their surrounding molecules. They alternately undergo oscillatory motion inside this cage for a time  $\tau_0$  and free diffusion for a time  $\tau_1$ , until they are trapped by different neighborhood. Assuming that the oscillation time is much longer than the diffusion time, i.e.  $\tau_1 \ll \tau_0$ , this model leads to a Lorentzian shaped translational dynamic scattering function  $S(Q, \omega)$  with a HWHM of:

$$\Gamma_T(Q) = \frac{D_T Q^2}{1 + D_T Q^2 \tau_0} \quad (6.8)$$

with the translational diffusion coefficient  $D_T$  and  $\tau_0$  denoting the residence time on one site before the water molecule jumps to the next site [22]. In the limit of  $D_T Q^2 \tau_0 \ll 1$ , corresponding to the real space long range limit, Eq. 6.8 reduces to the relation of free translational diffusion (Eq. 6.6). On the other hand, when probing small real space distances,  $D_T Q^2 \tau_0 \gg 1$ , the broadening tends to a plateau value  $\Gamma_T \rightarrow \tau_0^{-1}$ . Since the pioneering work of *Teixeira* and co-workers on bulk water [85], this model has successfully been applied to describe the translational part of QENS data for water in many different environments.

### 6.1.3. Isotropic rotation

The model for a molecule rotating on a sphere of radius  $a$  was developed by *Sears* under the assumption that the reorientations take place through small-angle, random rotations [128]. The resulting incoherent dynamic scattering function  $S_{\text{inc}}^R(Q, \omega)$  is an infinite sum over Lorentzians weighted by spherical Bessel functions  $j_l$  of increasing order  $l$ , plus an elastic part due to the spatial restriction to the sphere:

$$\begin{aligned} S_{\text{inc}}^R(Q, \omega) &= A_0(Qa)\delta(\omega) + \sum_{l=1}^{\infty} A_l(Qa) \cdot \frac{1}{\pi} \frac{\tau_l}{1 + \omega^2 \tau_l^2} \\ &= A_0(Qa)\delta(\omega) + \sum_{l=1}^{\infty} A_l(Qa) \cdot \mathcal{L}(\Gamma_R^l, \omega) \end{aligned} \quad (6.9)$$

where the HWHM of each Lorentzian is  $\Gamma_R^l = \tau_l^{-1}$ . The pre-factors  $A_l(Q)$  to the Lorentzians are called quasi-elastic structure factors and they are defined as follows<sup>1</sup>:

$$A_0(Qa) = [j_0(Qa)]^2 \quad (6.10)$$

$$A_l(Qa) = (2l + 1) [j_l(Qa)]^2 \quad (6.11)$$

with  $a$  being the radius of the sphere on which the molecule rotates. For protons of a water molecule this radius equals the length of an O-H-bond,  $a \approx 0.98 \text{ \AA}$ . The correlation time  $\tau_l$  of order  $l$  calculates from the rotational diffusion coefficient  $D_R$ :

$$\tau_l^{-1} = l(l + 1)D_R = \Gamma_R^l \quad (6.12)$$

When speaking of the rotational time  $\tau_R$  one generally refers to the second order correlation time  $\tau_R = \tau_2 = 1/(6 D_R)$ . This time corresponds to the relaxation time measured by T1 nuclear magnetic resonance (NMR). By means of dielectric relaxation one would access a time constant that has to be compared to  $\tau_1$ .

Looking back at Eq. 6.6, 6.8 and 6.12 we note that the width of the translational component depends in a characteristic way on the magnitude of the scattering vector  $Q$ , whereas the width  $\Gamma_R^l$  of every rotational Lorentzian is constant. The width of the total rotational component nevertheless shows a weak  $Q$ -dependence as the weight of the higher order terms increases with increasing  $Q$ .

#### 6.1.4. Total model function

Inserting Eq. 6.5 and 6.9 in Eq. 6.1 we may now write the total expression for the dynamic scattering function as:

$$S_{\text{inc}}(Q, \omega) = A_0(Qa) \cdot \mathcal{L}(\Gamma_T, \omega) + \sum_{l=1}^{\infty} A_l(Qa) \cdot \mathcal{L}((\Gamma_T + \Gamma_R^l), \omega) \quad (6.13)$$

(The convolution product of two Lorentzians gives one Lorentzian whose width is the sum of the initial two widths,  $\mathcal{L}(\Gamma_1, \omega) \otimes \mathcal{L}(\Gamma_2, \omega) = \mathcal{L}((\Gamma_1 + \Gamma_2), \omega)$ .)

Whereas a simple rotation gives rise to elastic intensity, this is no longer the case when the scatterer simultaneously performs translational motion.

Equation 6.13 is Fourier transformed with respect to time to yield the intermediate incoherent scattering function  $I_{\text{inc}}(Q, t)$  for rotational-translation motion. The convolution product in frequency becomes a simple product in the time domain:

$$\begin{aligned} I_{\text{inc}}(Q, t) &= I_{\text{inc}}^T(Q, t) \cdot I_{\text{inc}}^R(Q, t) \\ &= A_0(Qa) \cdot \exp[-\Gamma_T t] + \sum_{l=1}^{\infty} A_l(Qa) \cdot \exp[-(\Gamma_T + \Gamma_R^l)t] \end{aligned} \quad (6.14)$$

<sup>1</sup>Note that due to  $\sum_{l=0}^{\infty} (2l + 1) [j_l(x)]^2$  the normalization  $\int dQ S^r(Q, \omega) = 1$  is fulfilled.

The exact scattering function for rotational motion on a sphere contains an infinite sum over Lorentzians in the frequency domain or exponentials in the time domain. In practice this sum can be truncated after a few terms as the intensity of the higher order terms is negligible for the experimentally accessible  $Q$ -range. In Fig. 6.2 we plot the first 4 weighting factors  $A_l(Qa)$  of Eq. 6.9 for  $a = 0.98 \text{ \AA}$ . The grey line shows  $Qa$  corresponding to the maximum of the instrumentally accessible  $Q$ -range for the used instruments. We note that already the  $l = 3$  mode is of negligible intensity.

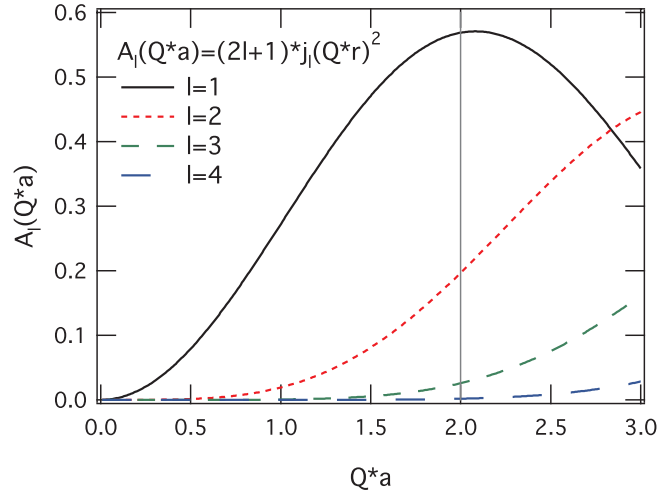


Figure 6.2: Weighting factors  $A_l$  of the Lorentzians in  $S_R^{\text{inc}}(Q, \omega)$  (Eq. 6.9) as a function of  $Qa$ , with the length of an O-H bond  $a \approx 0.98 \text{ \AA}$ . The grey vertical line shows the maximum accessible range for instruments IN5, IN16 and Basis. Note that all contributions with  $l > 2$  are of negligible intensity in this range.

#### 6.1.4.1. Fit function

Experimentally the dynamic scattering function is probed (convoluted) with the instrument specific resolution function  $R$ :

$$S(Q, \omega) = \int_{-\infty}^{\infty} S(Q, \omega') R(\omega' - \omega) d\omega' \quad (6.15)$$

$R$  is a peaked function of instrument specific width  $\Delta\omega$ , and the convolution product in the frequency domain becomes a simple product in the time domain. All data discussed in the following were measured in the frequency domain but we will nevertheless transform them to the time domain.  $I(Q, t)$  simply has to be divided by the instrument specific resolution and thereafter data from different spectrometers can be combined and simultaneously analyzed in a straightforward way.

For the fitting we will take into account only the first three rotational terms up to  $l = 2$ .

Our final fit function for rotational-translational water motion then reads:

$$I(Q, t) = K \left[ A_0(Qa) \exp[-\Gamma_T t] + \sum_{l=1}^2 A_l(Qa) \exp[-(\Gamma_T + l(l+1)D_R)t] \right] \quad (6.16)$$

with the pre-factor  $K$  and  $A_0$  and  $A_l$  being the quasi-elastic structure factors as defined before by Eq. 6.10.  $K$  includes both, the scaling of the total quasi-elastic intensity due to vibrations (see Eq. 6.2) and coherent contributions. Moreover a free  $K$  is needed for the fitting procedure as the division by the resolution spectrum introduces another intensity variation which is difficult to quantify, see also section 6.1.1.

### 6.1.5. QENS studies of water in AOT based microemulsions

Incoherent quasi-elastic neutron scattering (QENS) techniques are well adapted for the direct study of molecular motions in heterogeneous systems such as microemulsions as they probe both appropriate length and time scales. Water dynamics on time scales ranging from nano- to picoseconds are accessed. Moreover QENS investigations offer the possibility of selective deuteration so that motions of the water can be highlighted with respect to the other sample compounds. Starting in 1985 with the pioneering work of *Teixeira* and co-workers [85] there have up to now been a large number of experiments probing water dynamics by means of neutron scattering. QENS techniques have successfully been employed to study dynamics of water under many different conditions and in a wide range of environments. Studies include water attached to biomolecules [129], polymers [130], cement [7], porous silica [9, 131] or clay materials [10]. Whereas molecular dynamics in water/AOT/ oil microemulsions have been investigated by many different experimental methods, the number of QENS studies on water confined to these reverse AOT micelles is limited to only a few. In the following we will list the main outcome of these studies in chronological order.

To our knowledge the earliest QENS measurements on water in microemulsion droplets were performed more than 35 years ago by *Talboty* and co-workers [132, 133]. They used the IN6 TOF spectrometer to investigate monomer motions in water/AOT/cyclohexane-d7 microemulsions with  $4.5 \leq \omega \leq 16$  at room temperature. The measured line broadening was entirely attributed to motions of water molecules inside the micellar core; translational motions of the whole micelles were neglected. The spectra of the smallest micelles ( $\omega = 4.5$ ) could not be evaluated due to insufficient statistics. Water inside  $\omega = 9$  and  $\omega = 16$  micelles was found to behave similar. They observed free translational motion for the water with a diffusion coefficient of  $D_T = 1.2 \cdot 10^{-5} \text{cm}^2 \text{s}^{-1}$  which is half as small as  $D_T$  for bulk water. Furthermore fully deuterated samples with only protonated AOT surfactant were used to study their dynamics. For  $Q > 1.4 \text{ \AA}^{-1}$  free Fickian lateral diffusion on the shell with an  $\omega$ -independent AOT diffusion coefficient of

$D_T = 0.8 \cdot 10^{-5} \text{ cm}^2 \text{ s}^{-1}$  was found to dominate the motion. For smaller  $Q < 1.4 \text{ \AA}^{-1}$  a constant inelastic line width and an increasingly intensive elastic peak were qualitatively interpreted as dominating anisotropic rotational motion of the AOT molecules.

In a later study *Fletcher* and co-workers investigated the room temperature AOT mobility in octane-continuous droplet microemulsions under various additives in more detail by TOF [68]. Contrary to the prior study the AOT motion was found to be of diffusive nature over the whole  $Q$ -range. The effect of core viscosity on the AOT mobility was studied by changing the polar core from water to glycerol. They observed a considerable slowing down of the AOT molecules close to glycerol corresponding to a factor of about 2 compared to AOT close to water. Moreover they added different co-solvents which affected the upper phase transition temperature but did not influence the AOT motion in a significant way. Altogether these investigations led them to conclude that there is no correlation between local AOT mobility and droplet exchange kinetics. Concentrating again on the water dynamics, Chymotrypsin enzymes were dissolved inside the water core. A small fraction of the water was observed to be immobilized, whereas the dynamical behavior of the predominant part, 90% – 95% of the total water, was not affected by enzyme addition.

*Aliotta* and co-workers studied room temperature water motion inside AOT reverse micelles in cyclohexane-d8 [134]. The spectra were fitted with two Lorentzians, one describing the rotation and the other one describing translational motion of water. The observed rotational motion was comparable to that of bulk water. Concerning the translation they observed jump diffusive behavior, where the translational diffusion coefficient increased with increasing micelle size from  $D_T = 2.3 \cdot 10^{-5} \text{ cm}^2$  for  $\omega = 5$  to  $D_T = 3.4 \cdot 10^{-5} \text{ cm}^2$  for  $\omega = 10$ . Both values are larger than in bulk water; this result was considered as unphysical and was blamed on multiple scattering effects because of too thick samples.

*Freda* and co-workers focussed on hydration-dependent dynamics of AOT molecules in  $\text{D}_2\text{O}/\text{AOT}/\text{cyclohexane-d}_{12}$  with  $0.3 \leq \omega \leq 12$  around room temperature [135]. As the micelle size increases above  $\omega \approx 1$  they observed a wide quasielastic signal, which has been interpreted as the onset of intrinsic micelle dynamics related to the AOT with a characteristic time of 0.2 ns. The mobility of water molecules was not studied.

*Harpham* and co-workers recently combined MD simulations and QENS experiments to investigate water motion in water/ d-AOT/ isooctane-d8 microemulsions with  $1 \leq \omega \leq 5$  at room temperature [63]. The contribution of whole micelle translation was again not taken into account and the measured  $S(Q, \omega)$  was analyzed in terms of a convolution

product of a jump diffusion and an isotropic rotation. The translational component of water inside the smallest micelles with  $\omega \leq 2.5$  was too narrow to be resolved. In the case of  $\omega = 5$ , the observed translational diffusion was about five times slower than in bulk water. Extracted rotational diffusion coefficients were found to increase with increasing  $\omega$ , being only slightly smaller than for bulk water. All in all the rotational mobility was seen to be only little affected by the confinement whereas the translational mobility was considerably retarded. MD simulations compared very well with the measured spectra and they reasoned that the decoupling approximation for the different kinds of proton motions is valid for the investigated time and spatial range [63].

These studies agree in finding the rotational mobility of water inside reverse AOT micelles only to be little influenced whereas the translational motion seems to be considerably slowed down. Absolute values for diffusion coefficients are contradictory and moreover it remains unclear if all water inside the micelles is slowed down or if the determined values are averages over water fractions of different mobility. All these studies have been performed around room temperature - up to now no low temperature dependent studies have been conducted. Table 6.1 summarizes the mentioned investigations of water in reverse AOT micelles.

Table 6.1.: Published values for room temperature water dynamics in reverse AOT micelles: translational diffusion coefficient  $D_T$ , translational residence time  $\tau_0$  and rotational time  $\tau_R$ .

ref.	method	oil	$T$ (K)	$\omega$	$D_T$ ( $\text{cm}^2 \text{s}^{-1}$ )	$\tau_0$ (ps)	$\tau_R$ (ps)
[134]	QENS	iso-octane	room	10	3.4	0.7	
				5	2.3	1.6	
[63]	QENS	iso-octane	300	5	0.5	$12 \pm 4$	$1.6 \pm 0.1$
			300	2.5	-		$1.5 \pm 0.1$
			300	1	-		$2.6 \pm 0.1$
[132]	QENS	cyclohexane	room	9.5, 16	1.2	-	-
[62]	MD	iso-octane		3, 5, 7		-	-
[64]	MD	cyclohexane	298	7	0.91	-	99
[85]	QENS	-	293	bulk	2.22	1.25	1.16

## 6.2. Experimental results

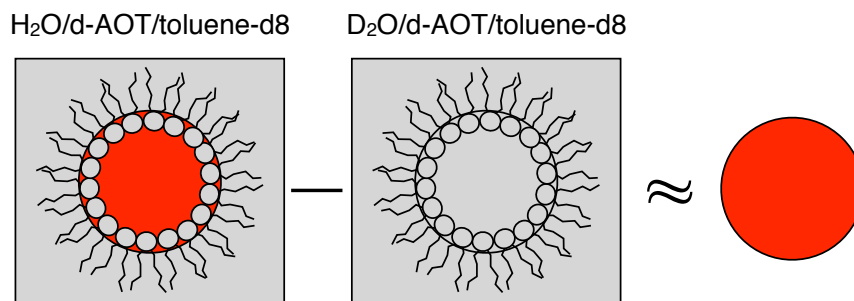


Figure 6.3.: Visualization of contrast variation study to access the signal of only water: From spectra of reverse d-AOT micelles filled with H<sub>2</sub>O dispersed in toluene-d<sub>8</sub>, spectra of completely deuterated samples with otherwise identical composition ( $\omega$  and  $\phi$ ) were subtracted.

Does the dynamical behavior of water inside reverse micelles differ from that of bulk water and how does the size of the micelles influence the water dynamics? In the following we will try to answer these questions based on results obtained by QENS. To study water inside bigger and smaller micelles we have chosen two well characterized microemulsion compositions with a molar ratio of water to surfactant of  $\omega = 3$  and  $\omega = 8$  and a droplet volume fraction of  $\phi = 0.1$ . The structure of these microemulsions was extensively studied before, see chapter 3. We determined the size of the core radii to be  $R_c = 7 \text{ \AA}$  and  $R_c = 12 \text{ \AA}$  for the small and big micelles respectively. After Eq. 1.3 the number of water molecules can then be estimated to be about  $n_w \approx 30$  inside a small and about 200 inside a big micelle. As proved by temperature dependent SANS, the structure of these microemulsions remains stable down to temperatures well below the freezing point of bulk water. To cover a wide range of temperatures we have therefore chosen to investigate the samples between  $T = 300 \text{ K}$  and  $260 \text{ K}$ . Within this temperature range droplets in both samples are far from their respective shrinking temperature (see samples T3 and T4 in Fig. 3.9) and the confining structure can be presumed as invariable.

The signal of water inside these droplets was accessed by measuring for both droplet sizes two samples with identical compositions except for the fact that one contains H<sub>2</sub>O and the other one D<sub>2</sub>O. Oil plus surfactant AOT make more than 90 vol% of the entire sample volume. Even though they are deuterated, their incoherent contribution is therefore not negligible. We thus subtracted the corrected D<sub>2</sub>O/d-AOT/toluene-d<sub>8</sub> signal from the H<sub>2</sub>O/d-AOT/toluene-d<sub>8</sub> signal; this should give, to a good approximation, the signal due to solely the confined water.

This principle of contrast variation is illustrated in Fig. 6.3.



Before starting now the detailed description of the data analysis we would like to anticipate the answer to the question if water dynamics depend on micelle size by showing dynamic scattering functions  $S(Q, \omega)$  of water in small and big micelles.

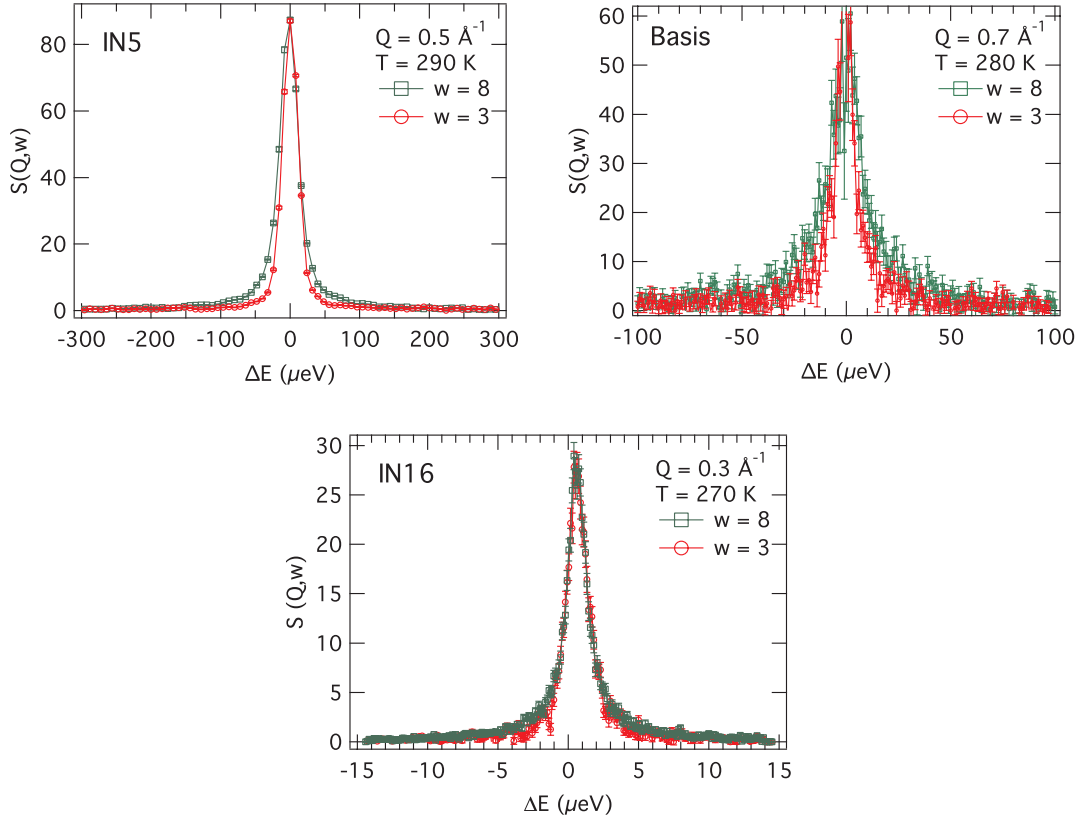


Figure 6.4.: Comparison of the dynamic scattering function  $S(Q, \omega)$  for water in micelles of two different sizes measured on IN5, Basis and IN16. We show difference spectra according to Fig. 6.3. Note that the signal of water confined to smaller micelles (red symbols) is always more narrow than that from bigger micelles (green symbols). Independent of any model this directly shows that water in smaller micelles is slower than in bigger ones.

Figure 6.4 displays three sets of  $S(Q, \omega)$  for water in big and small droplets measured on IN5, Basis and IN16. For each set we chose a different temperature  $T$  and scattering vector  $Q$ . The signal from water in the small droplets (red symbols) is, independent of temperature  $T$ , scattering vector  $Q$  and the used instrument, always more narrow than that from water in big droplets (green symbols). This observation is not only true for the shown spectra but holds for all investigated temperatures, scattering vectors  $Q$  and is true for the time range accessed by the three used spectrometers. At this point we

recall that if the signal would be governed by simple translational diffusion of the entire droplets we should observe a wider signal for smaller droplets as the droplet diffusion coefficient  $D_{\text{drop}}$  scales with the inverse of the droplet size. Therefore we can already at this stage conclude: yes, the dynamical behavior of the water is indeed influenced by the droplet size. On average, water in small droplets is slower than that confined to bigger ones. After this quantitative model-free observation qualitative results on the water dynamics will follow on the next pages.

### 6.2.1. Experimental details

We will report the results on water dynamics obtained from three QENS experiments. All data were analyzed in the time domain. The difference of the corrected dynamic scattering functions  $S(Q, \omega)$  of sample and background are Fourier transformed to yield the intermediate scattering function  $I(Q, t)$ . The Fourier transform algorithm *unift* was provided by R. Zorn, Jülich.

1. The first measurement was done at the **TOF spectrometer IN5**. With an incident wavelength of  $\lambda = 8 \text{ \AA}$  the investigated wavevector ranged from  $Q = 0.3 \text{ \AA}^{-1}$  to  $1.45 \text{ \AA}^{-1}$ . The chopper velocity was 12000 rpm and the frame overlap ratio was 4/5. The evaluated tested energy transfer ranged from -5 meV to +0.5 meV with an instrumental resolution (FWHM) of  $20 \mu\text{eV}$  to  $25 \mu\text{eV}$ . Flat aluminum sample holders with a wall to wall thickness of 1 mm were used and the sample was positioned at 135 degrees with respect to the incident beam. All spectra were collected for at least 2 h, up to 4 h for the background samples. At each of the five investigated temperatures between  $T = 260 \text{ K}$  and  $300 \text{ K}$  we obtained a set of  $I(Q, t)$  with  $Q$  increasing in steps of  $0.05 \text{ \AA}^{-1}$  from the minimum  $Q = 0.3 \text{ \AA}^{-1}$  on. We took into account all spectra up to  $Q = 1.1 \text{ \AA}^{-1}$ . For higher  $Q$ , artifacts due to Fourier transformation of the data become more and more important because of the finite accessed energy. Moreover by restricting the data analysis to this  $Q$ -range we avoided the interval where the maximum of the structure factor of liquid  $\text{D}_2\text{O}$  is located. An exemplary *Lamp* correction macro for IN5 data is given in the appendix A.4

2. A second experiment was performed on the **TOF-BS instrument Basis** at the SNS. Using an incident wavelength of  $\lambda = 6.4 \text{ \AA}$  (chopper frequency of 60 Hz) the tested wavevector ranged from  $Q = 0.2 \text{ \AA}^{-1}$  to  $2 \text{ \AA}^{-1}$ . The instrumental resolution was  $2.5 \mu\text{eV}$  and the accessible energy transfer ranged from  $-180 \mu\text{eV}$  to  $+180 \mu\text{eV}$ . Cylindrical aluminum sample holders with a wall to wall thickness of 0.25 mm were used. For temperatures  $T = 270 \text{ K}$ ,  $280 \text{ K}$  and  $290 \text{ K}$  we obtained a set of  $I(Q, t)$  with  $Q$  increasing in steps of  $0.2 \text{ \AA}^{-1}$  from the minimum  $Q = 0.3 \text{ \AA}^{-1}$  on. Spectra up to  $Q = 0.9 \text{ \AA}^{-1}$  will be considered.

3. The third experiment was performed on the **BS spectrometer IN16**. With an incident wavelength of  $\lambda = 6.271 \text{ \AA}$  an elastic  $Q$ -range of  $Q = 0.2 \text{ \AA}^{-1}$  to  $1.9 \text{ \AA}^{-1}$  was probed. The instrumental resolution was  $1 \mu\text{eV}$  and the accessible energy transfer ranged from  $-15 \mu\text{eV}$  to  $+15 \mu\text{eV}$ . Spectra have been measured at a single temperature of  $T = 270 \text{ K}$  with a collecting time of about 12 h per sample. The same sample holders as for IN5 were used, also positioned at 135 degrees with respect to the incident beam. Spectra with  $Q = 0.3$  and  $0.5 \text{ \AA}^{-1}$  will be considered.

For all instruments vanadium was measured for normalization and to correct for detector efficiency. A sample spectrum at  $T \leq 10 \text{ K}$  was measured to determine the instrumental resolution. For all samples the calculated transmission was higher than 0.86. No multiple scattering corrections were applied.

Table 6.2 summarizes the instrumental characteristic and in Fig. 6.5 we give an overview of the  $Q$ - and  $T$ -range covered by the different instruments.

Table 6.2.: Comparison of the characteristics of performed QENS experiments.  $\lambda_i$  denotes the incident neutron wavelength,  $\delta E$  is the instrumental resolution (FWHM). The given energy transfer  $\Delta E$  and elastic  $Q$ -range correspond to evaluable spectra.

Instrument	$\lambda_i$ ( $\text{\AA}$ )	$\delta E$ ( $\mu\text{eV}$ )	$\Delta E$ ( $\mu\text{eV}$ )	T (K)	$Q$ ( $\text{\AA}^{-1}$ ) (step)
IN5	8	20 - 25	-5000 - +500	300, 290, 280, 270, 260	0.3 - 1.1 ( $\Delta = 0.05$ )
Basis	6.4	2	-180 - +180	290, 280, 270	0.3 - 1.1 ( $\Delta = 0.2$ )
IN16	6.271	< 1	-15 - +15	270	0.3 - 0.5 ( $\Delta = 0.1$ )

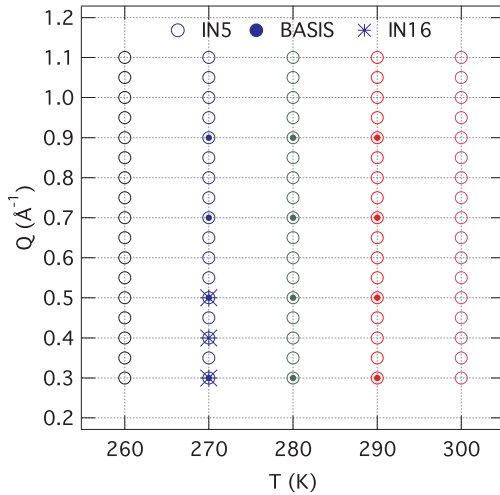


Figure 6.5: Summary of covered wavevector  $Q$  and sample temperature  $T$  for the three performed QENS experiments. Each point corresponds to an evaluable spectrum with sufficient statistics, the accessible  $Q$ -range as defined by the instrumental settings extends to larger  $Q$ .

### 6.2.2. Outline of the data analysis

Spectra of water confined to reverse micelles have been measured on three different instruments spanning a range of three decades in time. The final aim is to arrive at a coherent description of the water motion as seen by combining all data. Therefore we have decided to Fourier transform the data from the frequency domain to the time domain and to perform all data analysis on the thereby obtained intermediate scattering function  $I(Q, t)$ . We want to point out that the dynamic scattering function  $S(Q, \omega)$  contains just the same information but a simultaneous analysis of the data from different instruments is more complicated. In the time domain the intermediate scattering function  $I(Q, t)$  can be simply divided by the instrumental resolution - which is different for all of the three used instruments. In addition the combined representation of data from the different instruments is more evident in the time domain. Nevertheless we start the analysis with the data obtained on IN5 only. We decided to do so as we have obtained the largest number of spectra on IN5 - concerning  $Q$  as well as temperature, see Fig. 6.5. Moreover the statistics of the IN5 difference spectra are much better than those measured on Basis and IN16. Therefore as a first step towards an overall description of all data from the three instruments we treat the TOF-data. These results will then be used to constrict parameters for the analysis of the data from Basis and IN16.

### 6.2.3. Short times - fast processes: IN5

The fitting of  $I(Q, t)$  measured on IN5 was done in two stages. First, each set of data was fitted to Eq. 6.16 which describes the translational and rotational motion of the water molecules. The fit was performed on  $I(Q, t)$  up to times of  $t = 70$  to  $100$  ps. For the fitting procedure the radius of rotation was fixed to the distance of an O-H bond  $a = 0.98$  Å. For each temperature we performed a global fit of all  $I(Q, t)$  with Eq. 6.16. The rotational diffusion coefficient  $D_R$  was simultaneously optimized over the entire  $Q$ -range investigated. Looking back at Eq. 6.16 we see that the  $Q$ -dependence is contained in the weighting factors  $A_l$ . For each set of curves we obtain one  $D_R$  whereas the pre-factor  $K$  and the translational width  $\Gamma_T$  are fitted for each  $Q$ -value independently. Whereas the decay at the longer times is determined by  $\Gamma_T$ , the fast decay at the shortest accessible times depends on  $D_R$ .

#### 6.2.3.1. Rotational motion of water

Figure 6.6 a) shows the resulting rotational diffusion coefficient  $D_R$  as a function of temperature for both droplet sizes. For the bigger droplets (full circles)  $D_R$  clearly increases with increasing temperature. In the case of water confined to the smaller droplets (open circles)  $D_R$  shows the same tendency but much less pronounced. The temperature dependence of the rotational time  $\tau_R = 1/(6D_R)$  is shown in Fig. 6.6 b) in

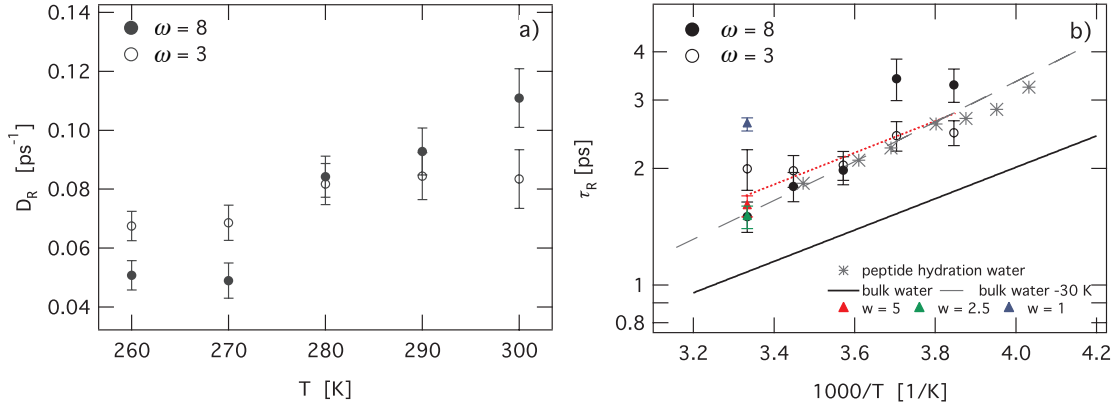


Figure 6.6.: a): Temperature dependence of the rotational diffusion coefficient  $D_R$  for water in small and big droplets. b): Arrhenius plot of the rotational time  $\tau_R$  over the temperature range of  $T = 312$  K to  $240$  K. The black solid line shows bulk water [85], grey stars correspond to rotational dynamics of water confined to peptides [129] and colored triangles represent results for water in reverse AOT micelles [63]. The red dotted line is a fit to the Arrhenius Eq. 6.17. Grey broken line is the bulk water dependency shifted by  $-30$  K.

the Arrhenius representation. By plotting the logarithm of  $\tau_R$  versus  $1000/T$  a thermally activated process with a single time constant gives a straight line as:

$$\tau_R = \tau_R^0 \exp(E_A/RT) \quad (6.17)$$

with the activation energy  $E_A$ , the gas constant  $R = 8.314$  J/mol/K and the pre-factor  $\tau_R^0$ . We compare our values for  $\tau_R$  to QENS results obtained for bulk water (solid line) [85], water confined by peptides (stars) [129] and water in reverse AOT micelles of varying size (colored triangles) [63]. *Harpham* and co-workers investigated water in reverse micelles with  $\omega = 1$ ,  $2.5$  and  $5$  at  $T = 300$  K. They did not see a difference between  $\tau_R$  for  $\omega = 5$  and  $\omega = 2.5$ . As the sizes of these micelles are comparable to ours we interpret our results accordingly: we presume that the water rotation is independent of droplet size. The simultaneous fit of  $\tau_R$  for water in small and big droplets to Eq. 6.17 is shown by the red dotted line in Fig. 6.6 b). Although our results for  $\tau_R$  scatter strongly and are subject to big errors, the fit is in good agreement with values found for water near peptides (represented by stars). This further supports our assumption of a rotation independent of the confining geometry.

From our results for water in  $\omega = 3$  and  $\omega = 8$  micelles we find an activation energy of  $E_A = (1.9 \pm 0.4)$  kcal/mol and a pre-factor of  $\tau_R^0 = (0.07 \pm 0.03)$  ps.

Water confined by peptides shows Arrhenius behavior with an activation energy of  $E_A \approx 2.07$  kcal/mol [129]. The respective value for bulk water was determined to be  $E_A \approx 1.85$  kcal/mol with a pre-factor of  $\tau_R^0 = 0.0485$  ps. In a previous study it was

demonstrated that diffusion of confined water is comparable to that of bulk water at temperatures typically 20 K - 30 K below the real temperature [136, 137]. When shifting the bulk water temperature dependency of the rotational time  $\tau_R$  accordingly by -30 K we obtain the grey broken line in Fig. 6.6 b). We note that our results for  $\tau_R$  are within the errors close to that dependency. Except from noting the excellent agreement between our results and literature values we will desist from a further discussion of  $E_A$  and  $\tau_R^0$ .

To stabilize the subsequent fits the rotational diffusion coefficient  $D_R$  is for each temperature in the following fixed to  $(6 \cdot \tau_R)^{-1}$  with  $\tau_R$  as determined by the Arrhenius fit. The values for  $D_R$  are given in Tab. 6.3.

Table 6.3.: Rotational diffusion coefficients  $D_R$  for water in small and big droplets.  $D_R$  is determined by assuming Arrhenius behavior of  $\tau_R$  (Eq. 6.17):  $\tau_R = (0.07 \text{ ps}) \cdot \exp(1.9 \text{ kcal}/(RT))$ . These values for  $D_R$  have been imposed to all subsequent fits.

$T$ [K]	260	270	280	290	300
$D_R$ [ $\text{ps}^{-1}$ ]	0.061	0.069	0.078	0.088	0.098

The thereby defined values for  $D_R$  may be inaccurate due to the scattering and the rather large errors of the measured points. For an exact determination of  $D_R$  our data is not appropriate as we do not probe the adequate time range of sub-ps and large  $Q$  where the rotational contribution to  $I(Q, t)$  becomes more important. We want to emphasize that the determination of  $\Gamma_T$  is nearly not affected by the exact value of  $D_R$  within the range where we fix it. Comparing the results for  $\Gamma_T$  obtained with imposed  $D_R$  to those with free  $D_R$ , we find that the difference is within the fitting error thus negligible.

At this point we have to mention that  $\tau_R$  should in principle correspond to the rotational correlation time that can be extracted from NMR T1 measurements. However it was found that QENS results for  $\tau_R$  are always shorter by at least a factor of 2-3 [138]. At  $T = 270$  K, values for micelle water and bulk water extracted from QENS are  $\tau_R = 2.4$  ps and 1.5 ps respectively. At the same temperature NMR finds  $\tau_R \approx 6$  ps for bulk water [139] and for water in micelles a more than two orders of magnitude longer rotational correlation time of 1.8 ns (at 260 K) [102]. A recent publication based on MD simulations deals with this discrepancy between values from QENS and NMR [140]. The line width measured by QENS contains the rotational parts  $\Gamma_R^l$  and the translational part  $\Gamma_T$  (see Eq. 6.13). It was quoted that water reorientation deduced from QENS is underestimated because of an incorrect extrapolation of the translational line width from small to large  $Q$ . This could explain an underestimation of  $\tau_R$  of a factor of 1.5. As we fit our data simultaneously for all  $Q$  values with Eq. 6.16 without assuming a

jump diffusion for  $\Gamma_T$  we think that this argumentation is not applicable in our case.

### 6.2.3.2. Translational motion of water as resolved by IN5

After having briefly discussed results for the rotational diffusion we will now concentrate on the translational dynamics of the water inside the droplets. All IN5 spectra were again fitted to Eq. 6.16 but this time imposing  $D_R$  to the value as given in Tab. 6.3. In Fig. 6.7 we show data for big and small droplets together with the resulting fits. The intermediate scattering function  $I(Q, t)$  for both droplet sizes at  $T = 270$  K is displayed for a selection of  $Q$ -values. Note that both graphs display the data over the same time range and it is again obvious that the signal from the smaller droplets decays slower. Data and fits for all other investigated temperatures are shown in the appendix A.7.

The  $Q$ -dependence of the resulting translational widths  $\Gamma_T$  are shown in Fig. 6.8. For both droplet sizes we plot  $\Gamma_T$  as a function of  $Q^2$  for all investigated temperatures. With increasing temperature  $\Gamma_T$  increases for both droplet sizes reflecting the fact that the higher the temperature is the faster becomes the translation.

For each temperature and  $Q$  the absolute value of  $\Gamma_T$  is smaller for water in smaller droplets than that of water confined to the bigger droplets.

In Fig. 6.9 we illustrate this difference for  $T = 270$  K. The translational width  $\Gamma_T$  of water in small and big droplets is plotted together with  $\Gamma_T$  of bulk water as measured by *Teixeira* and co-workers [85]. On average, water confined to both droplet sizes is slower than bulk water.

If we now intend to extract absolute values for the parameters characterizing the translational water motion we need to account for the diffusion of the entire droplets as discussed in detail in the previous chapter 5. Water inside the droplets is moved along by the diffusing droplet. At the same time the water molecules will perform translational motion inside the droplet. These two translational processes are supposed to be independent of each other and the total translational width  $\Gamma_T$  will then be the sum of both  $\Gamma_{\text{H}_2\text{O}}$  and  $\Gamma_{\text{drop}}$ . Assuming free Fickian diffusion (Eq. 6.6) for the droplets and jump diffusion (Eq. 6.8) for the water inside the droplet we obtain:

$$\begin{aligned}\Gamma_T &= \Gamma_{\text{drop}} + \Gamma_{\text{H}_2\text{O}} \\ &= D_{\text{drop}}Q^2 + \frac{D_T Q^2}{1 + \tau_0 D_T Q^2}\end{aligned}\quad (6.18)$$

Figure 6.9 shows  $\Gamma_{\text{drop}}$  for both droplet sizes at  $T = 270$  K. For the big droplets the droplet diffusion coefficient  $D_{\text{drop}}$  was set to the value measured by NSE<sup>2</sup> (see chapter 5). For the small droplets with  $\omega = 3$  the according diffusion coefficient  $D_{\text{drop}}$  was calculated from the Stokes-Einstein equation (Eq. 5.14) by assuming that the hydrodynamic

<sup>2</sup>Note that contrary to DLS the NSE experiments probed a  $Q$ -range which is close to that probed by TOF and BS.

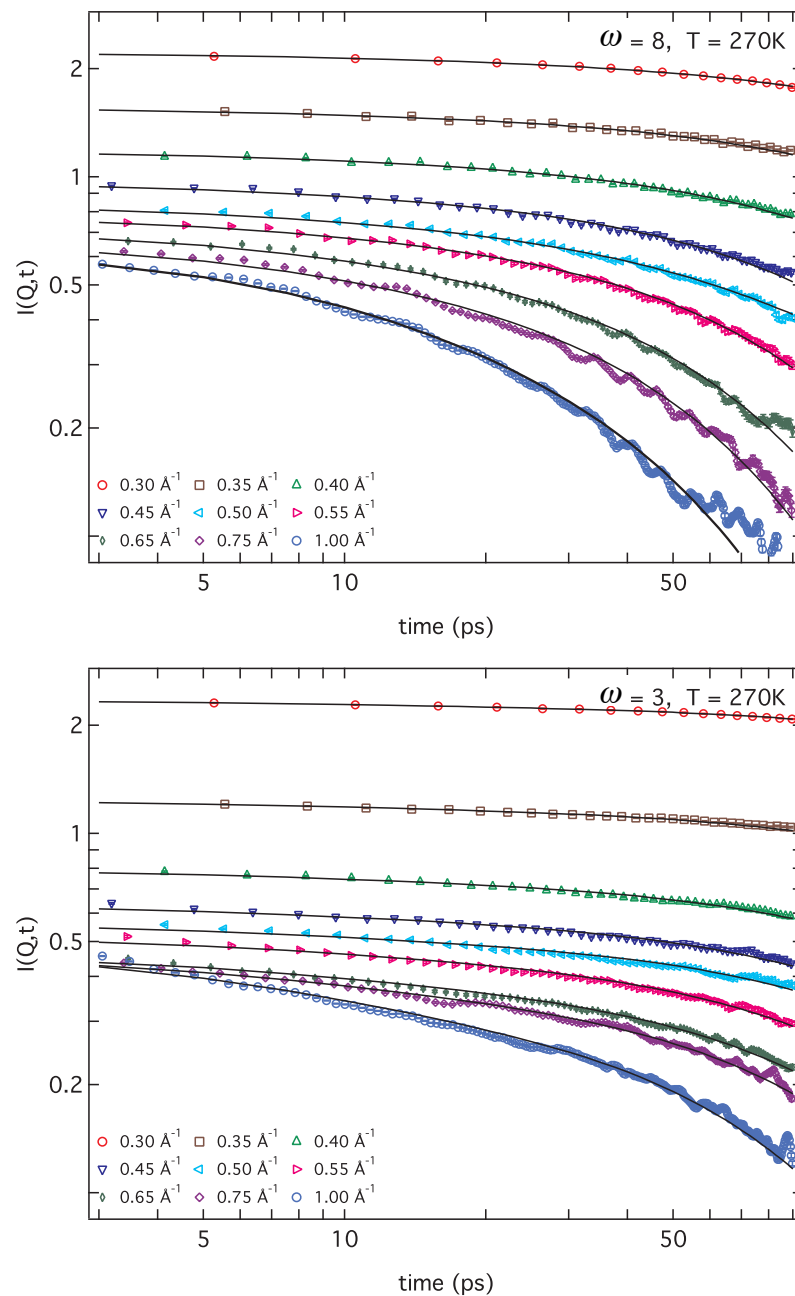


Figure 6.7.: Intermediate scattering function  $I(Q,t)$  of water in big droplets (top figure) and small droplets (bottom figure) at  $T = 270\text{ K}$ . The data were measured on IN5. Lines are fits to Eq. 6.16 with fixed rotational diffusion coefficient  $D_R = 0.069\text{ ps}^{-1}$ .



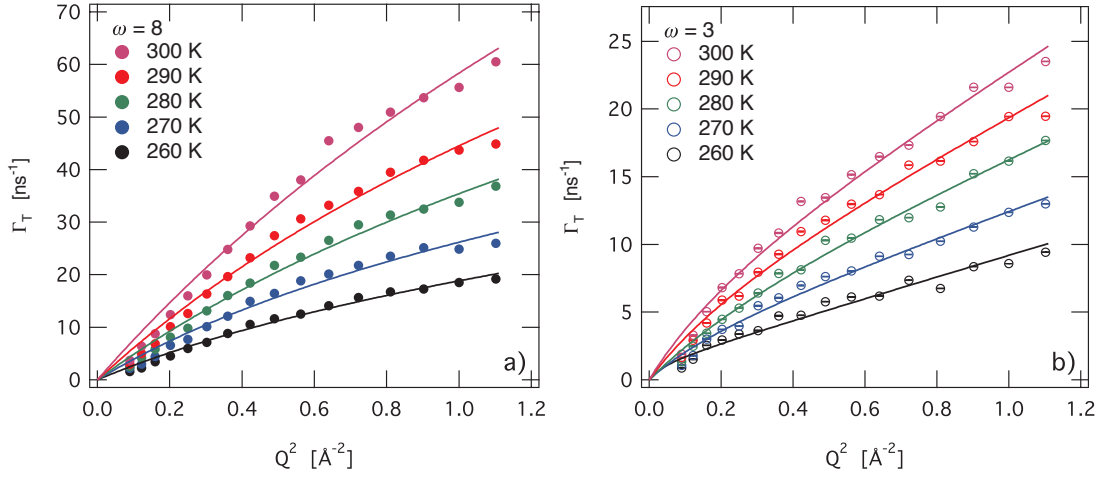


Figure 6.8.: Translational component  $\Gamma_T$  obtained from fitting of IN5 data with fixed  $D_R$  to Eq. 6.16.  $\Gamma_T$  as a function of  $Q^2$  for water in a) big droplets and b) small droplets. Solid lines are fits to Eq. 6.18 assuming free translational diffusion of the entire droplet and jump diffusion for the water.

radius scales with the geometrical droplet radius like  $R_h \approx 1.3 \cdot R_0$  as it was found for the larger droplets with  $\omega = 8$ . (See chapter 5).

For the small droplets the measured width  $\Gamma_T$  is only slightly larger than the corresponding  $\Gamma_{\text{drop}}$ . Even though this difference is smaller in the case of the big droplets it is obvious that we need to consider the droplet diffusion in both cases. If neglecting it, we would overestimate the translational motion of the water molecules itself to a great extent.

Fitting  $\Gamma_T$  to Eq. 6.18 with  $D_{\text{drop}}$  fixed to the values determined by NSE we obtain curves that are shown by blue solid lines in Fig. 6.9. The temperature dependence of the resulting translational diffusion coefficient  $D_T$  and the translational residence time  $\tau_0$  of the water is shown in Fig. 6.10. The respective values are listed in Tab. 6.4. Results for water in small (open circles) and big droplets (full circles) are compared to the respective values for bulk water (stars) [85] and water confined to reverse AOT micelles with  $\omega = 5$  (red triangle) [63].

For both droplet sizes  $D_T$  at all investigated temperatures is smaller than the bulk water value, whereas  $\tau_0$  is always larger. This means that on average, water diffuses slower inside droplets of both sizes than when in its bulk form.

With decreasing droplet size the average translational motion becomes slower reflected by decreasing  $D_T$  and increasing  $\tau_0$  with decreasing  $\omega$ . Compared to bulk water the residence time  $\tau_0$  is prolonged about a factor of 10 and 100 for water inside big and small droplets respectively.

Figure 6.9: Translational component  $\Gamma_T$  of small and big droplets at  $T=270$  K from fit of Eq. 6.16 to IN5 data with fixed  $D_R$ . For comparison we show the translational component of bulk water at  $T=273$  K [85] and the width  $\Gamma$  due to free diffusion of the droplet. Here we assume  $\Gamma = D_{\text{drop}}Q^2$  with the droplet diffusion coefficient  $D_{\text{drop}}$  measured by NSE (see chapter 5). Blue solid lines are fits to Eq. 6.18.

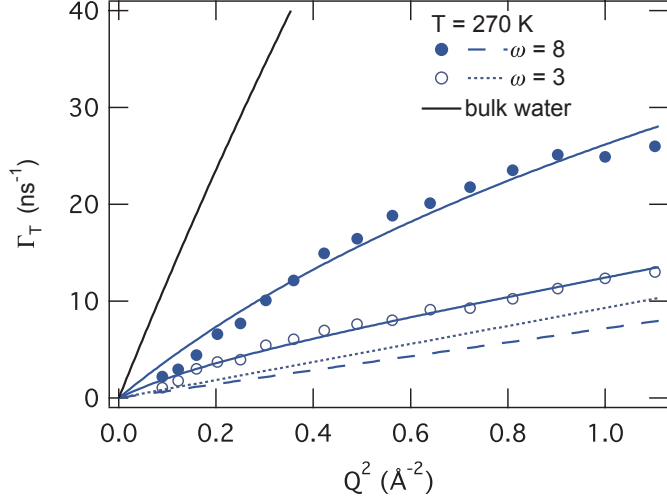


Table 6.4.: Translational diffusion coefficient  $D_T$  and residence time  $\tau_0$  for water in small and big droplets. Values result from fits of IN5 data to Eq. 6.16 with imposed rotational diffusion coefficient  $D_R$  as given in Tab. 6.3. These results are displayed in Fig. 6.10

$\omega$	$T$ [K]	260	270	280	290	300
3	$D_T$ [ $10^{-5}\text{cm}^2/\text{s}$ ]	$0.27 \pm 0.35$	$0.15 \pm 0.04$	$0.15 \pm 0.03$	$0.23 \pm 0.05$	$0.28 \pm 0.01$
	$\tau_0$ [ps]	$757 \pm 150$	$255 \pm 31$	$134 \pm 18$	$135 \pm 17$	$115 \pm 14$
8	$D_T$ [ $10^{-5}\text{cm}^2/\text{s}$ ]	$0.23 \pm 0.02$	$0.34 \pm 0.03$	$0.42 \pm 0.03$	$0.53 \pm 0.04$	$0.66 \pm 0.05$
	$\tau_0$ [ps]	$35 \pm 5$	$24 \pm 4$	$13 \pm 2$	$11 \pm 2$	$7 \pm 2$

For both droplet sizes,  $D_T$  increases with temperature but with a less steep slope than in the case of bulk water.

We compare our results to recently published values for water inside reverse AOT micelles of size between our small and big micelles ( $\omega = 5$ ) [63]. At  $T = 300$  K, the QENS experiments yielded  $D_T = (0.5 \pm 0.1) \text{ cm}^2/\text{s}$  and  $\tau_0 = (12 \pm 4) \text{ ps}$ . Both values lie between our respective results determined for water inside micelles with  $\omega = 3$  and  $\omega = 8$ . This further confirms the systematic slowing down of the translational motion with micelle size.

At this point we want to recall that the QENS signal is due to all protons in the sample. QENS cannot follow a single water molecule and therefore the here presented results have to be understood as average values over all present water molecules.

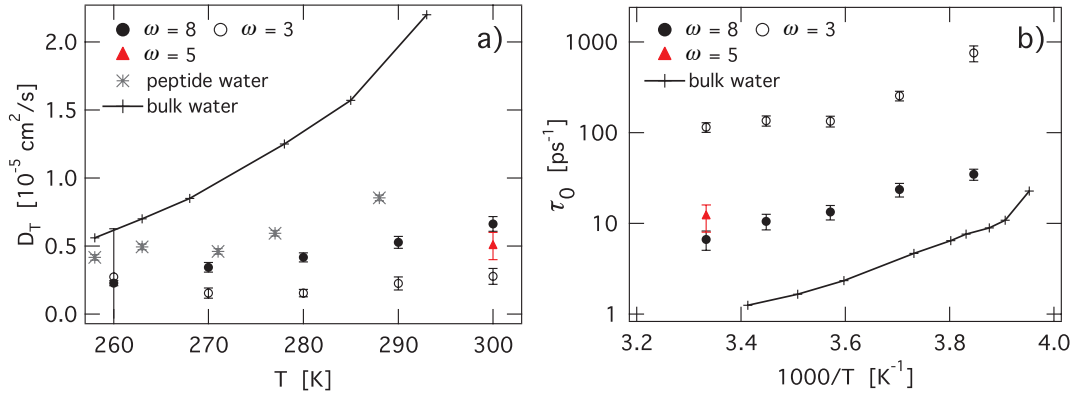


Figure 6.10.: a): Temperature dependence of the translational diffusion coefficient  $D_T$  for water in small and big droplets. b): Arrhenius plot of the translational residence time  $\tau_0$  over the temperature range of  $T = 300 \text{ K}$  to  $260 \text{ K}$ . Lines between crosses correspond to  $\tau_0$  for bulk water [85] and grey stars show results for water confined by peptides [129]. With decreasing droplet size the translational motion becomes slower:  $D_T$  decreases and  $\tau_0$  increases the smaller  $\omega$  gets.

#### 6.2.4. Longer times - slower processes: Basis and IN16

Having analyzed the data from IN5 we will now turn our attention to longer time scales probed by Basis and IN16. Figure 6.12 displays the intermediate scattering function  $I(Q, t)$  as measured on all three spectrometers for both droplets sizes. The lines show the before obtained fits to IN5 data extrapolated to longer times. Whereas the rotational translational model (Eq. 6.16) also describes the long time data from water in small droplets the model is insufficient in the case of water in bigger droplets. Here the model decays much faster than the data. The deviation between data and model at longer times implies that there must be an additional slower process in the case of water in big droplets that was not resolved by IN5.

##### 6.2.4.1. Number of water molecules bound per AOT molecule

As discussed before, results from other experimental techniques have been interpreted such that there exist different fractions of water inside reverse micelles [47]. For micelles of sufficient size a layer of slow water bound by the AOT as well as faster core water was observed.

Assuming that in our big micelles there exist two fractions of water molecules which we will call fast ( $A$ ) and slow ( $B$ ) water we introduce the ratio of fast over slow water

molecules:

$$x = \frac{A}{B} \quad (6.19)$$

As a simple attempt to describe the data from Basis and IN16 we modify Eq. 6.16 by adding a second term to describe the observed slower decay at longer times:

$$\begin{aligned} I(Q, t) &= I_{\text{slow}}(Q, t) + I_{\text{fast}}(Q, t) \quad (6.20) \\ &= \frac{K}{1+x} [A_0(Qa) \cdot \exp(-\Gamma_T^B t) + A_1(Qa) \cdot \exp(-(\Gamma_T^B + 2D_R^B)t)] \\ &\quad + \frac{K}{1+\frac{1}{x}} [A_0(Qa) \cdot \exp(-\Gamma_T^A t) + A_1(Qa) \cdot \exp(-(\Gamma_T^A + 2D_R^A)t)] \end{aligned}$$

where indices  $A$  and  $B$  stand for fast and slow water respectively.

The combined data sets are now fitted with Eq. 6.20.  $D_R$  is again fixed to the respective value listed in Tab. 6.3. Figure 6.11 shows the obtained values for  $\frac{A}{B}$  as a function of  $Q$  for temperatures of  $T = 270$ ,  $T = 280$  and  $T = 290$  K.

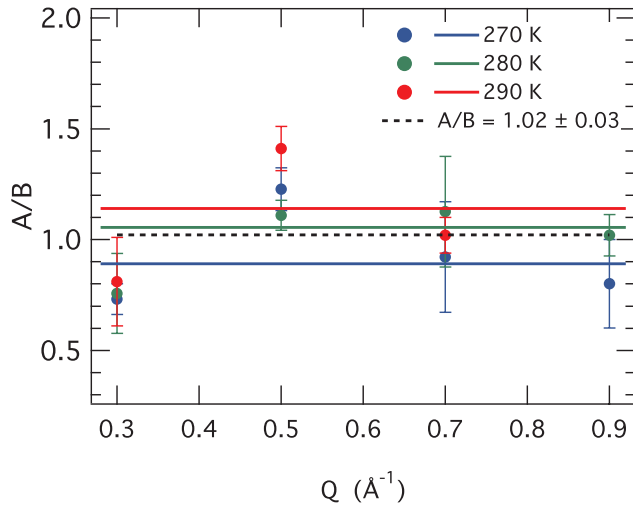


Figure 6.11: Ratio  $\frac{A}{B}$  of fast over slow water molecules obtained by fitting Eq. 6.20 to combined data from IN5, Basis and IN16. Colored lines are  $Q$ -averages at fixed temperature. With increasing temperature the ratio  $\frac{A}{B}$  slightly increases. The dotted line shows the average over all temperatures and  $Q$ -values.

By eye no systematic variation of  $\frac{A}{B}$  neither with temperature nor with  $Q$ -value is observed. Nevertheless when averaging  $\frac{A}{B}$  for every temperature independently we find that the ratio of fast over slow water molecules slightly increases with increasing temperature from  $\frac{A}{B} = (0.89 \pm 0.05)$  at  $T = 270$  K to  $\frac{A}{B} = (1.14 \pm 0.06)$  at  $T = 290$  K. Keeping in mind the picture of a number of water molecules closely bound to each AOT molecule this result would mean, that when going to higher temperatures less water molecules are attached to the AOT. Considering the large uncertainties in the fitted values for  $\frac{A}{B}$  we do not think that we can draw this conclusion from our data. We thus average  $\frac{A}{B}$

over all temperatures and  $Q$ -values. This implies that we assume that the fraction of retarded water molecules does not change with temperature over the investigated range which we think is justified for the analysis of our data.

We obtain  $\frac{A}{B} = 1.02 \pm 0.03$ , which corresponds to  $A \approx B \approx 4$  water molecules per AOT molecule, as the total number of water molecules per AOT molecule is given by  $\omega = 8$ . When identifying the slow fraction of water molecules with the molecules that compose the water layer bound to the AOT this quantitatively means that each AOT molecule dynamically binds on average a number of about 4 water molecules.

This number lies in the range of published values from other experimental methods including DSC, NMR and IR [48, 69, 102, 141].

The result of about 4 closely bound water molecules per AOT explains the observation that spectra of water in the small micelles ( $\omega = 3$ ) can be described by the model (Eq. 6.16) which contains only one fraction of water. Apparently in those micelles all water is bound and therefore no fast core water is observed.

#### 6.2.4.2. Two dynamically separated water fractions

The combined spectra from IN5, Basis and IN16 were then again fitted to Eq. 6.20 but this time imposing  $\frac{A}{B} = 1$  to stabilize the fitting procedure. In Fig. 6.12 a) combined data from all three spectrometers for water in big droplets at  $T = 270$  K together with the resulting fits (solid lines) is shown. For a direct comparison the previous fits to Eq. 6.16 are also included (dotted lines). The data at times  $t > 100$  ps are now well described by the model and we obtain two translational widths  $\Gamma_T^A$  and  $\Gamma_T^B$  for the fast and slow water molecules respectively. These two widths are plotted as a function of  $Q^2$  in Fig. 6.13 for temperatures  $T = 270$  K, 280 K and 290 K, values are listed in Tab. 6.5. We also show the before obtained width  $\Gamma_T$  extracted from the analysis of the IN5 data alone (solid line). The width  $\Gamma_{\text{drop}} = D_{\text{drop}}Q^2$  due to only droplet diffusion is displayed by the dotted lines. By broken lines we show the dependency of bulk water at a temperature 10 K below the temperature at which the spectra were measured. The lower line shows the measured width after [85], the upper line contains the enlarging due to droplet diffusion.

For all three temperatures we note that the width  $\Gamma_T^A$  of the faster component is very close to the estimated width of bulk water 10 K below. This is in agreement with the observation that dynamics of water confined by peptides is similar to that of bulk water about 10 - 30 degrees lower [85, 142]. The slower component  $\Gamma_T^B$  lies slightly below the respective values extracted from analysis of IN5 data alone.  $\Gamma_T^B$  is for  $Q > 0.5 \text{ \AA}^{-1}$  still significantly larger than what we would expect as width caused by droplet diffusion only. Hence the slow component still shows translational diffusion: on the probed timescale, the water molecules inside the shell layer are not entirely immobilized.

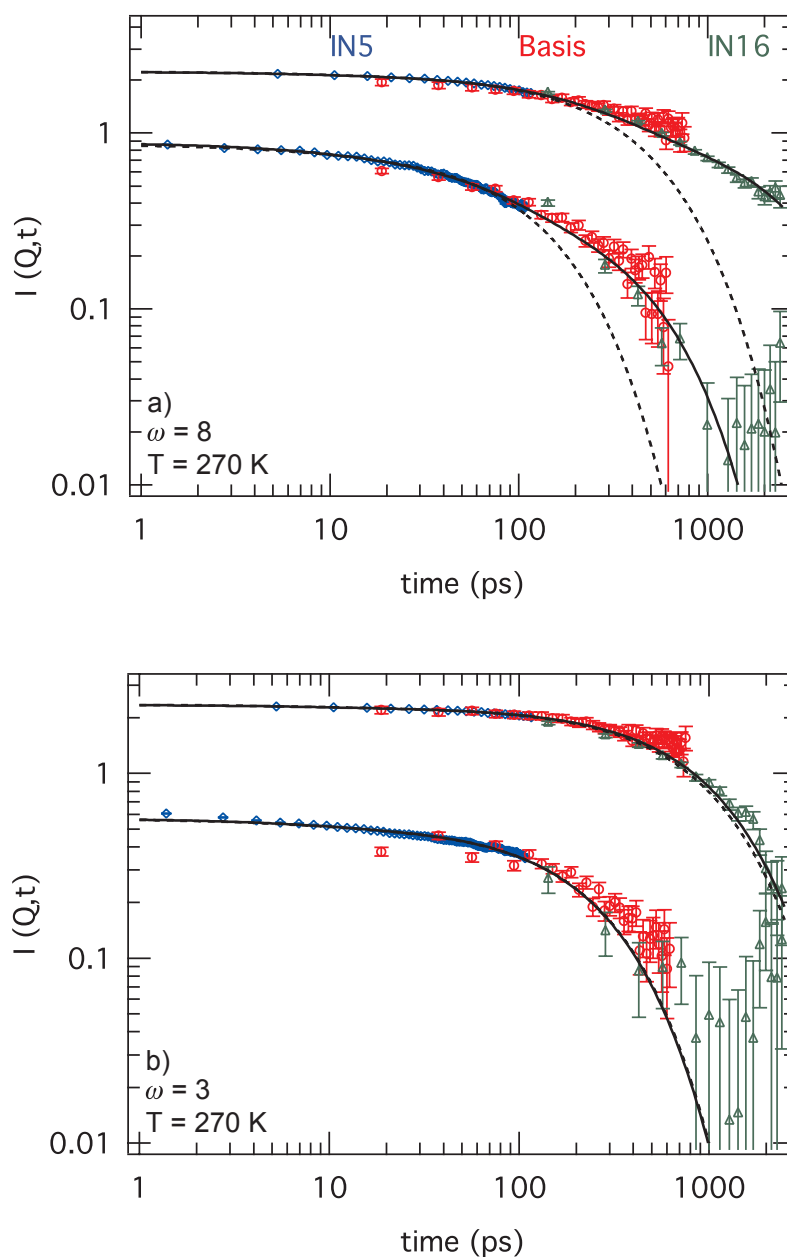


Figure 6.12.: Intermediate scattering function  $I(Q, t)$  for water in big droplets combining data from IN5, Basis and IN16 at  $Q = 0.3 \text{ \AA}^{-1}$  and  $0.5 \text{ \AA}^{-1}$ . a) Solid lines are fits to Eq. 6.20 fixing the ratio of fast over slow water molecules to  $\frac{A}{B} = 1$ . The dotted lines show the earlier fits to Eq. 6.16 considering only one fraction of water molecules. Note that both models differ only at longer times  $t > 100$  ps. b) Over the entire tested time range, the signal of water in small droplets can be described by Eq. 6.16. Dotted black lines show the fit considering only data from IN5, black solid lines show the fit to the same model taking into account all data. For  $Q = 0.3 \text{ \AA}^{-1}$  a slight difference can be observed, at  $Q = 0.5 \text{ \AA}^{-1}$  both fits are indistinguishable.

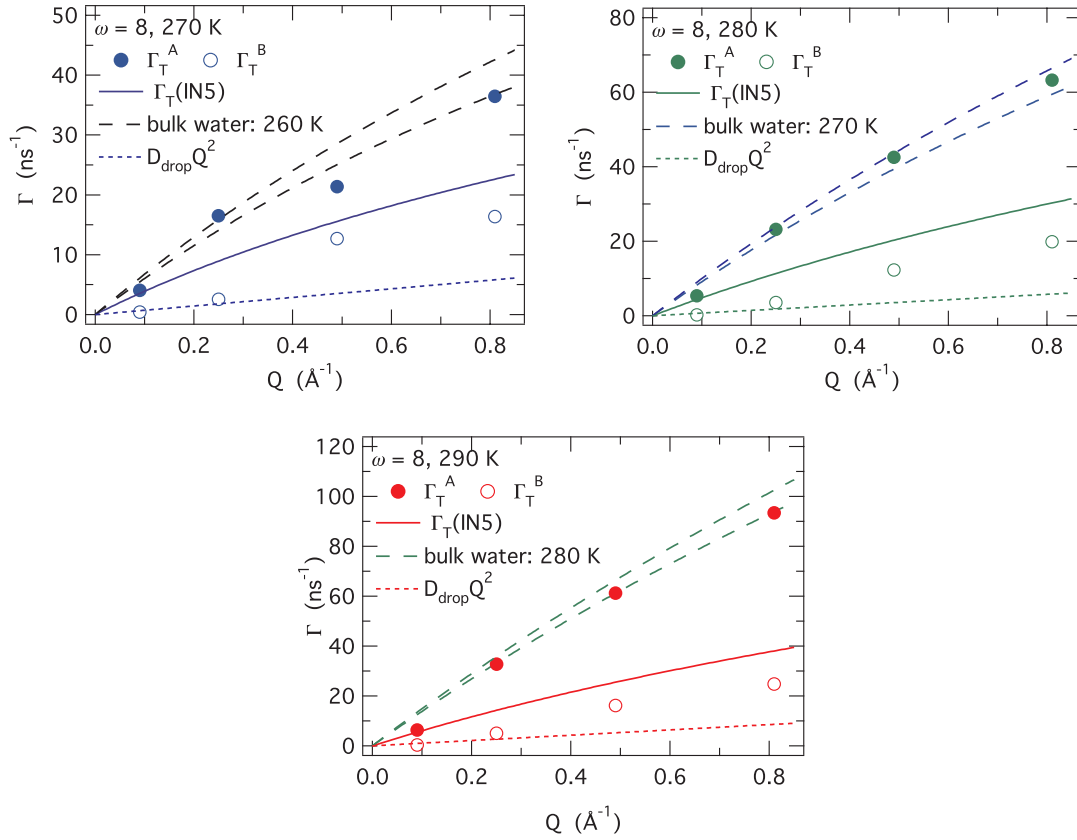


Figure 6.13.: Splitting of the translational component of water confined to big droplets at  $T = 270 \text{ K}$ ,  $280 \text{ K}$  and  $290 \text{ K}$ . Translational widths  $\Gamma_T^A$  and  $\Gamma_T^B$  of fast and slow water fractions as a function of  $Q^2$ . The solid lines show the single width  $\Gamma_T$  as before obtained from fits of IN5 data. Lower broken lines correspond to bulk water at a temperature 10 K lower [85] taking into account the droplet translation. Dotted lines show the estimated width due to entire droplet diffusion at the corresponding temperature. Fitting errors are smaller than symbols.

We want to bring out the fact that only for  $T = 270 \text{ K}$  and  $Q = 0.3^{-1}$  and  $0.5 \text{ \AA}^{-1}$  we possess data from all three spectrometers. For all other  $Q$  and  $T$  values the combined data consists of spectra from IN5 and Basis.

We interpret these results as follows: inside the big micelles there seem to be two fractions of water present. One fast fraction - called fraction  $A$  - behaves very similar to bulk water. The respective translational width is within experimental accuracy undistinguishable from what was measured for bulk water at a temperature 10 degrees lower. As the number of points for both,  $\Gamma_T^A$  and  $\Gamma_T^B$ , is restricted to only four we will not deduce diffusion constants  $D_T$  nor residence times  $\tau_0$ .

Table 6.5.: Fitting results for water in  $\omega = 8$  micelles. Combined analysis of data from TOF and BS with Eq. 6.20 imposing  $\frac{A}{B} = 1$ .  $\Gamma_T^A$  and  $\Gamma_T^B$  denote the translational widths of fast and slow water component. Fitting errors are smaller than  $0.001 \text{ ps}^{-1}$ . These results are displayed in Fig. 6.13.

$T$ (K)	$Q$ ( $\text{\AA}^{-1}$ )	$\Gamma_T^A$ ( $\text{ps}^{-1}$ )				$\Gamma_T^B$ ( $\text{ps}^{-1}$ )			
		0.3	0.5	0.7	0.9	0.3	0.5	0.7	0.9
270		0.004	0.017	0.021	0.036	<0.001	0.003	0.013	0.016
280		0.005	0.023	0.042	0.063	<0.001	0.004	0.013	0.020
290		0.006	0.033	0.061	0.093	<0.001	0.006	0.016	0.025

#### 6.2.4.3. Alternative models

*Piletic* and co-workers investigated water inside reverse AOT micelles by means of IR spectroscopy [48]. Micelle size dependent water spectra were reproduced by a weighted sum of bulk and bound water spectra. In this core-shell model the properties of the shell water were taken to be those of the water inside  $\omega = 2$  micelles. We tested if our QENS data can be interpreted accordingly. For this purpose we tried to fit the intermediate scattering function  $I(Q, t)$  of water in big micelles by a weighted sum of spectra for bulk and bound water. Bulk water parameters were taken from [85]. To describe the bound water fraction we took the spectra of water inside the small micelles. Again the entire droplet diffusion was taken into account as before. As only free parameter we varied the weighting of the bulk and bound fraction. This model could not describe the combined data in a satisfying way. We conclude that the **bulk core - bound shell model** is inappropriate for the analysis of our QENS data.

As an alternative model to describe translational motion of especially supercooled and confined water [136, 143] we also need to mention the **relaxing cage model** (RCM) which uses ideas from the mode-coupling theory and was recently developed by *Chen* and co-workers [144]. The RCM-model is based on the assumption that in supercooled water each molecule is confined to a tetrahedrally coordinated hydrogen-bonded cage for a certain relaxation time. The translation of a water molecule therefore requires the rearranging of a large number of neighboring water molecules and the translational diffusion is thus strongly coupled to the local structural relaxation. The intermediate scattering function can be written as a stretched exponential:

$$I_{RCM}(Q, t) = F_V(Q, t) \exp \left[ - \left( \frac{t}{\tau} \right)^\beta \right] \quad (6.21)$$

where the pre-factor  $F_V(Q, t)$  describes short time dynamics ( $< 2 \text{ ps}$ ) as vibrations of the



water molecules in the cage [9]. The stretched exponential describes the  $\alpha$ -relaxation process of the cage build of the neighboring molecules. The lower the temperature the more  $\beta$  should deviate from one [129].

Taking into account the rather large uncertainties in our data especially at higher  $Q$  and longer times we decided not to apply the RCM for the analysis of our data. Moreover the model is designed for water in the supercooled regime where we do not yet possess data at various temperatures (see 6.5 for an overview of measured  $Q$  and  $T$ ). Using the well-established rotational-translational model, Eq. 6.14, we were able to compare our results to results obtained by other groups, who applied exactly the same model. Especially dynamic properties of bulk water as investigated by QENS were directly comparable [85].

### 6.2.5. Do we see signs of geometrical confinement?

We would answer this question certainly with yes, if we look back on the results showing the confinement size dependence of water freezing and of structural stability of the micellar droplets with decreasing temperature (see Fig. 4.3), which could be described by the finite size effects, the Gibbs-Thomson relation (Eq. 4.4). But how about the behavior of the relaxation times?

For pure geometrical confinement one expects to observe a decrease of the relaxation time, i.e. an accelerated motion of the confined molecules. The basic idea is that in the bulk liquid correlations between neighboring molecules influence the single molecule dynamics. While at high temperature the thermal energy is large enough to easily overcome local potentials arising from surrounding molecules, at lower temperature the influence of the neighbor interaction becomes more stronger.

For most simple liquids the increasing importance of the neighbor potential with decreasing temperature leads to an exponential, i.e. Arrhenius increase of the viscosity and to single exponential relaxation functions until the system crystallizes (see Eq. 6.17). Static and dynamic heterogeneities, which are characteristic for glass forming liquids, lead for undercooled liquids to a viscosity which increases with decreasing temperature according to a Vogel-Fulcher law, i.e. stronger than for an Arrhenius dependence. It looks like the activation energy would continuously increase with decreasing temperature. There are many ideas describing this observation which is characteristic for a complex energy landscape. One major idea, first presented by *Adams* and *Gibbs* [145], is that there are cooperative re-arranging regions (CRR) that influence the single molecule motion. The size of the CRR thus corresponds to the length scale above which molecules can be considered as moving independently of each other. The growing size of this region leads with decreasing temperature to the observed dramatic increase of the viscosity.

The idea of geometrical confinement is now that enclosing the glass forming liquid in a restricted environment should prevent the size of these region from continuously

growing, as the maximum size of a CRR is limited by the size of the confining space. Below a certain temperature the individual molecule may thus move faster than in bulk because less other molecules have to re-arrange [145]. Figure 6.14 illustrates the picture of CRRs and geometrical confinement. But this scenario should be valid only if we could cut off the interaction to the environment, which is probably unphysical because walls always contribute to the interaction.

Mostly a slowing-down of the dynamics in confinement is observed when hard wall effects dominate, i.e. for the case of interaction with slow walls [12–14]. An acceleration of the dynamics was observed either for hard confinement with hydrophobically treated walls (*Alba-Simionesco* in [13]) or in soft confinement [146]. In our soft confined system the surrounding oil is also much faster than the water dynamics at

the same temperature (see Fig. A.1) but water is separated by the AOT shell from the oil. Thus the shell dynamics itself is relevant for the wall interaction. From NSE we know that the time scale of shell deformation modes is long compared to the time scale of water motion (see discussion of shell fluctuations in chapter 5). The slow AOT shell motion should therefore rather decrease the water mobility, which is what we observe. Another important question is, over which length-scale the wall dynamics influences the dynamics of the enclosed water molecules. Assuming we would have only a single hydration layer of water disturbed by the AOT shell, real geometrical confinement could then eventually be realized for the core water and we could expect this water to be accelerated compared to bulk water. But why do we observe a slowing-down of all water inside the micelles? (We recall that even in the bigger micelles the faster water fraction was slowed down compared to bulk water at the same temperature.) The most probable explanation is that the two-fraction model is too simple. Wall effects are expected to decrease quickly towards the interior of the droplet but they are very likely still noticeable in the middle of the droplet core. A smooth gradient from very slow relaxation times close to the AOT shell to faster relaxation times probably approaching those of bulk water in the center of large droplets could be more realistic and neutrons average of course over all the core content. Thus again, like in most confinement studies, wall effects seem to play an important role also in soft confinement and the ideal situation of a purely geometrical confinement is not achieved by reverse micelles. Nevertheless soft

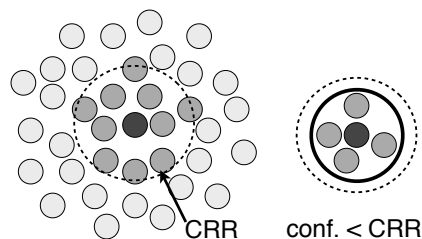


Figure 6.14.: Idea of geometrical confinement: for the motion of the black molecule all dark grey molecules inside the cooperative re-arranging region (CRR) have to re-arrange. Confining molecules into a defined volume smaller than the CRR, less molecules influence each other and the individual molecules could move faster.

confinement has advantages, some of them were already mentioned: the confinement size is easily tunable, the interaction between different droplets can be varied and the viscosity of the surrounding oil can be changed (though this change is mediated by the surfactant shell to the confined liquid), contrary to hard confinement, density and pressure changes between confined and bulk liquid can be neglected. Last but not least of importance is that micellar droplets present an environment for water which resembles those in systems of biological relevance.

### 6.3. Summary and conclusions

Combining the three QENS spectrometers IN5, Basis and IN16 we characterized the dynamical behavior of soft confined water over more than three decades in time from pico- to nanoseconds. By preparing microemulsion samples with  $\omega = 8$  and  $\omega = 3$  we studied the influence of confinement size on the water dynamics. The water signal was accessed by subtracting background spectra from fully deuterated samples with otherwise identical composition.

In a first step of the analysis we determined the rotational diffusion coefficient  $D_R$  of water taking into account only IN5 data. We observed the rotation to be within the errors independent of droplet size. Assuming an Arrhenius behavior of the rotational time  $\tau_R$  we find an activation energy of  $E_A = (1.9 \pm 0.4)$  kcal/mol which is close to the bulk water value. Our results for  $\tau_R$  agree with results for water confined by peptides [129] and reverse micelles [63]. For subsequent fits the rotational diffusion coefficient was fixed to the averaged values.

Translational motion of water as resolved by IN5 follows a jump diffusion dependency. The average translational mobility of water inside reverse AOT micelles was found to be reduced with comparison to bulk water at the same temperature. Furthermore our data revealed an increasing slowing down of the translation with decreasing droplet size. The extracted diffusion constants decreased with decreasing droplet size whereas residence times increased with decreasing droplet size. Absolute values are in agreement with QENS results for water confined to  $\omega = 5$  micelles [63].

Taking into account BS data we extended the probed time range up to several thousands of picoseconds. Whereas data for water inside small droplets was well described by the model extrapolated from shorter times accessed by IN5, in the case of big droplets we observed a significant difference. At longer times the intermediate scattering function decayed much slower than predicted by the fit to IN5 data where we considered only one fraction of water molecules performing rotation and translation. Taking into account the results from other experimental techniques which revealed two dynamically separated

fractions of water corresponding to core and shell water we refined the fitting model. Spectra from water inside big micelles could successfully be described by a weighted sum of a fast (A) and a slow (B) component performing rotational translation motion (Eq. 6.20). For both components the rotational diffusion coefficient  $D_R$  was fixed to the before determined values and only the translational widths  $\Gamma_T^A$  and  $\Gamma_T^B$  were fitted.

We determined the ratio of fast over slow water molecules independent of  $Q$ -value and of insignificant temperature dependence to  $\frac{A}{B} \approx 1$ . For the here studied micelles with  $\omega = 8$  this corresponds to about 4 slow or bound water molecules per AOT molecule. This result is in agreement with a number of about 4 bound water molecules per AOT as found by IR spectroscopy [46]. Moreover we want to recall our SANS, which showed that at least two molecules of water per AOT do not freeze. Within the uncertainties these two numbers are that close that it suggests that the water which is seen by QENS as bound is identical with the un-freezable fraction determined by SANS.

Imposing  $\frac{A}{B} = 1$  we find the translational behavior of the fast core component to resemble that of bulk water at a lower temperature. At all three investigated temperatures  $T = 270$  K,  $280$  K and  $290$  K the fast translational width  $\Gamma_T^A$  is within the errors identical with QENS results for free water [85] at a temperature reduced by  $10$  K, respectively. The slower water component still shows translational motion faster than we estimated for the entire droplet diffusion. Contrary to IR spectra [48] our QENS spectra could not be reproduced by a weighted sum of bulk and bound water spectra.

Any further quantitative analysis to determine values for translational diffusion constants and residence times of the slow component is impossible due to the restricted number of points.

QENS measures quantities averaged over all scattering protons. Nevertheless, due to the large range of probed time scales we could distinguish between two fractions of water molecules which are very different with respect to their dynamical behavior. Whereas the existence of fast and slow water molecules were observed by other techniques [46, 48] probing mainly the vibrational behavior of water's hydrogen bonds, this is to our knowledge the first time that QENS experiments showed the existence of two water fractions.

## 7. Perspective: polymer loaded micelles

One possible way to modify the elastic properties of surfactant membranes in microemulsions is by addition of polymers. This chapter presents preliminary results on the effect of hydrophilic homo-polymers on structure and dynamics of a w/o droplet microemulsion. As basic microemulsion we have chosen the previously well characterized system  $D_2O/AOT/toluene-d_8$  ( $\omega = 8$  and  $\phi = 0.05, 0.1$  and  $0.15$ ) whose structure is in detail described in section 3.4. As polymer polyethyleneoxide ( $PEO_{3000}$ ) was added to the microemulsion, with a concentration corresponding to  $Z \approx 2$  polymer molecules per droplet. The effect of PEO addition on droplet structure was then investigated by means of SANS and size and polydispersity of pure and polymer-containing microemulsion droplets are compared in the following. Furthermore NSE was used in order to study droplet diffusion as well as droplet shell fluctuations of the PEO loaded microemulsion ( $D_2O/AOT/toluene-d_8$ ,  $\omega = 8$ ,  $\phi = 0.1$  and  $Z = 1.5$ ). We try to deduce elastic properties of the AOT membrane under PEO addition and we relate these results to the respective observations made for the pure microemulsion (see chapter 5). Altogether we will confine ourselves to showing tentative interpretations of first trial experiments. For quantitative statements further systematic studies need to be conducted.

### 7.1. PEO in reverse water swollen AOT micelles

Microemulsions form selective solvents for polymers. Depending on their affinity - hydrophilic or hydrophobic - the polymers will either reside inside the oil or inside the water domains. Appropriate hydrophilic homo-polymers of moderate weight may therefore be dissolved inside the water cores of a w/o droplet microemulsion. One simple model system is that of reverse water swollen AOT micelles containing the water soluble polymer PEO. The exact location of the polymers inside the droplets depends on the nature of the surfactant. Repulsive polymer-surfactant interactions in the case of non-ionic surfactants should cause the PEO chains to reside in the middle of the core away from the surfactant shell. In the case of attractive interactions between PEO and the here discussed anionic surfactant AOT, the polymer chains are expected to be adsorbed at the surfactant interface [147]. This adsorption should have an impact on the elastic

properties of the interface hence also on phase behavior and microemulsion structure. A variety of experimental techniques, including SANS [148,149], DLS [150,151] and conductivity [152–156], were applied to study structure and dynamical behaviour of PEO containing AOT-based w/o microemulsions.

Depending on the size of the polymer with respect to the size of the droplet core, two different cases were observed. Polymers with radii of gyration smaller than the core radii were found to be located inside one single droplet, whereas polymers larger than the droplets induced either phase separation [152] or connected several droplets [157]. This so-called droplet necklace structure was observed by SANS [148] and it was also theoretically studied [158].

The effect on PEO on the elastic modulus of the AOT mono-layers was investigated by Kerr measurements and conductivity studies [152,157]. These rather indirect methods indeed showed a slight increase of the stiffness of the AOT membrane upon PEO addition. Direct experimental evidence for the PEO to be adsorbed at the AOT interface is still missing.

A more straightforward way to determine elastic properties of surfactant membranes is by means of NSE. As discussed in chapter 5, this technique has successfully been applied to measure bending moduli in different microemulsion systems. But while the effect of many parameters, e.g. temperature, pressure or even protein addition to an AOT based water-in-oil droplet microemulsion was studied [36], to our knowledge there exist up to now no NSE investigations to directly monitor PEO induced changes of the AOT membrane stiffness.

## 7.2. Experimental results

### 7.2.1. Experimental details

**Microemulsion** stock solutions were prepared by mixing pre-calculated amounts of AOT, D<sub>2</sub>O, and toluene-d<sub>8</sub>, see appendix A.1. The molar ratio was prepared to be  $\omega = 8$  which determines the water core radius of the droplets to  $R_c \approx 12 \text{ \AA}$ , see section 3.4. For the SANS experiments the droplet volume fraction was varied from  $\phi = 5\%$ , 10% to 15%.

We used the hydrophilic **homo-polymer** polyethyleneoxide (PEO) with a mean molecular weight of  $M = 3000 \text{ g/mol}$ , which corresponds to an average polymerization number of  $n = 67$ . Prior to the mixing experiments we applied SANS to determine the radius of gyration of free PEO<sub>3000</sub> in heavy water to be  $R_G \approx 19 \text{ \AA}$  (Data and discussion of SANS on PEO can be found in the appendix A.8). The undisturbed PEO chain is hence bigger than the droplet core:  $R_G > R_c$ .

**Polymer-containing microemulsions** were prepared by adding appropriate amounts of PEO to the microemulsion stock solutions and stirring until the samples were single-phase and optically clear. The concentration of polymer in the microemulsion is expressed by the parameter  $Z$  which is defined as the number of polymer chains per microemulsion droplet. For the SANS study we prepared microemulsions with  $Z = 2$ . The NSE study focused on the middle droplet volume fraction  $\phi = 0.1$  and a slightly lower polymer concentration corresponding to  $Z \approx 1.5$ .

Note that no significant amount of PEO can be dissolved in toluene therefore we are confident that the predominant amount of polymer is located inside the water core of the droplets.

**SANS** experiments were carried out on the D11 diffractometer (see section 2.2.4.2) using an incident neutron wavelength of  $\lambda = 4.6 \text{ \AA}$  with three sample to detector distances 1.1 m, 5 m and 20 m with respective collimations of 8 m, 8 m and 20 m. The chosen configurations covered a range of scattering vectors from  $0.01 \text{ \AA}^{-1} \leq Q \leq 0.47 \text{ \AA}^{-1}$ . Samples were measured in 1 mm thick standard quartz cells at a temperature of  $T = (288 \pm 1) \text{ K}$ . The raw data was treated according to the procedure described in section 2.2.4.3.

**NSE** experiments were carried out at the neutron spin echo spectrometer IN15 using two different set-ups (see section 2.2.3.2). Using a wavelength of  $\lambda = 6.3 \text{ \AA}$  ( $10 \text{ \AA}$ ) and scattering angles  $2\theta = 4.7^\circ, 7.7^\circ, 10.7^\circ$ , and  $13.7^\circ$  ( $4.7^\circ$  and  $7.7^\circ$ ) the accessed scattering vector ranged between  $0.065 \text{ \AA}^{-1} \leq Q \leq 0.314 \text{ \AA}^{-1}$  ( $0.039 \text{ \AA}^{-1} \leq Q \leq 0.094 \text{ \AA}^{-1}$ ) respectively. The resulting time window was 0 ns - 12 ns (50 ns). Due to experimental difficulties at the highest Fourier times we had to constrain the data analysis to 10 ns. Samples were measured in flat aluminum sample holders of 1 mm thickness at temperatures  $T = 260 \text{ K}, 280 \text{ K}, 290 \text{ K}$  and  $300 \text{ K}$  with  $\Delta T < 0.5 \text{ K}$ . The sample temperature was controlled by a standard ILL orange cryostat and at all measured temperatures the sample was equilibrated for at least 30 minutes. All spectra were corrected for background scattering from the pure solvent and the sampleholder and divided by the experimental resolution as explained in section 2.2.3.3.

### 7.2.2. PEO effect on droplet structure

The PEO containing microemulsions are to be compared to the pure microemulsions. The structure of the relevant pure microemulsion has before been studied by SANS. In the following we will refer to corresponding results that are subject of section 3.4.

Scattering curves of the PEO containing microemulsions are shown in Fig. 7.1 a). Each sample contains  $Z \approx 2$  molecules of PEO<sub>3000</sub> per droplet. Scattering of the corresponding pure microemulsions is shown aside in Fig. 7.1 b). Similar colors in both figures

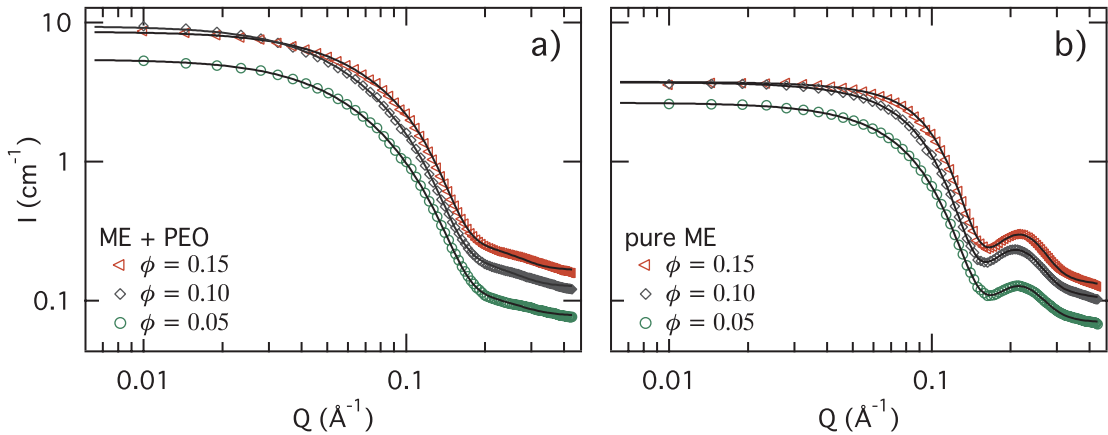


Figure 7.1.: a) Scattering of microemulsion in shell contrast containing  $Z \approx 2$  molecules of PEO<sub>3000</sub> per droplet. b) Scattering of corresponding pure shell contrast microemulsions. Solid lines are fits the model for polydisperse spherical core-shell particles with mutual interactions described by a Baxter sticky sphere potential. The errorbars are smaller than symbols.

mark identical droplet volume fractions  $\phi$ . For all three PEO containing samples, the minimum of the form factor is smeared out and slightly shifted to larger  $Q$  compared to the pure microemulsion. Under the assumption of a preserved underlying droplet structure, this signifies a decrease of the droplet size upon polymer addition. Less sharp features of the scattering curves in Fig. 7.1 a) can be due to the following two points. First we have to take into account that the contrast profile of the PEO containing microemulsions is less sharp than that of the pure shell contrast microemulsions. The addition of protonated PEO to the deuterated water core will reduce the coherent scattering length density difference between shell and core. A second reason could be an increased polydispersity of droplets which contain PEO chains.

In literature it is reported that the underlying microemulsion droplet structure can be preserved upon PEO addition even for polymers being considerably larger than the droplets [149]. For this reason we analyze the SANS data with the model introduced in section 3.1. This model includes a core-shell form factor for polydisperse spherical particles and a Baxter sticky hard sphere structure factor (see appendix A.5 for a description of the structure factor). The same model was earlier successfully applied to describe the scattering of the pure droplet microemulsion. In the case of PEO containing microemulsions we fixed the coherent scattering length density  $\rho_m$  of the matrix to the calculated value for toluene-d8 and that of the shell to the value obtained by fitting of the corresponding pure microemulsions. In addition the thickness  $d$  of the AOT shell was constrained to the before obtained result. The scattering length density  $\rho_c$  of the



core was varied by the fitting procedure as the core is now composed of D<sub>2</sub>O and PEO. The obtained fits are shown in Fig. 7.1 by solid lines. The fitted values for the total droplet radius  $R = R_c + d$  and the droplet polydispersity  $p$  are displayed in Fig. 7.2.

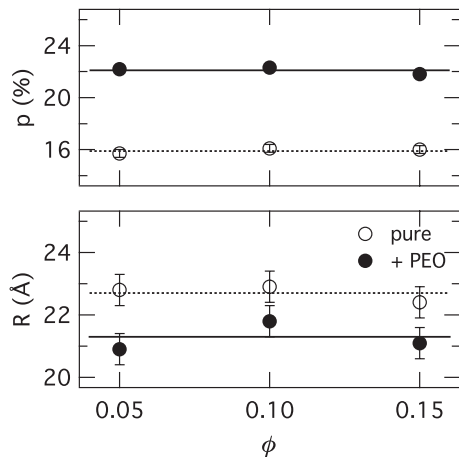


Figure 7.2: Total droplet radius  $R$  (core plus shell) and size polydispersity  $p$  of pure (hollow symbols) and PEO containing (full symbols) microemulsion droplets. Values are listed in Tab. 7.1. Experiments were performed at  $T \approx 288$  K. Values for pure microemulsions are discussed under section 3.4.

We compare  $R$  and  $p$  of pure (hollow symbols) and the PEO containing (full symbols) microemulsion as a function of the droplet volume fraction  $\phi$ . All results are listed in Tab. 7.1. For pure and PEO-containing microemulsions we observe that neither the radius  $R$  nor the polydispersity  $p$  depend on the droplet concentration in the investigated range of  $0.05 < \phi < 0.15$ . These two parameters are within the errors constant. Fitting results confirm that upon PEO addition the total droplet radius decreases from  $R \approx 22.7$  Å to  $21.1$  Å whereas the droplet size polydispersity increases from  $p \approx 15.9\%$  to  $22.1\%$ . Both, a decreasing size as well as an increasing polydispersity of the droplets induced by addition of PEO larger than the droplet cores to AOT/water/oil microemulsions, are in agreement with observations by others [148,149].

A possible reason for this could be the modified elastic properties of the AOT membrane. As the PEO chains are expected to arrange close to the AOT membrane [147,152] they are probably altering its stiffness. This would then change the spontaneous curvature of the AOT shell what may explain the droplet decrease as well as the increased polydispersity. We will further discuss this point on the next pages when presenting the NSE results on bending elasticity under section 7.2.3.

Fitting results for  $\rho_c$  lay in the order of  $2 \cdot 10^{-6}$  Å<sup>-2</sup>. Making the simplified assumption of PEO being uniformly distributed inside the water core, we estimated the mean scattering length density of the core to be about  $3 \cdot 10^{-6}$  Å<sup>-2</sup> to  $3.5 \cdot 10^{-6}$  Å<sup>-2</sup>. The observed difference between fitted and calculated value may point to the fact that a form factor for a spherical particle with two shells could be more appropriate because the PEO is expected to be located close to the AOT instead of being distributed homogeneously.

We nevertheless contented ourselves with the easier model to keep the number of free parameters to a minimum. The number of shells should not affect the absolute droplet radius nor the polydispersity in a significant way.

Table 7.1.: Listing of fitting parameters for pure and PEO containing microemulsions of D<sub>2</sub>O/AOT/toluene-d8 with varying droplet volume fraction  $\phi$ . The fitted droplet volume fraction is  $\phi_f$ .  $\rho_c$ ,  $R_c$ ,  $d$  are core radius and shell thickness respectively and  $p$  is the polydispersity index. Measurements were performed at  $T = (288 \pm 1)$  K. Errors are estimated to be in the order of 0.5 Å for  $R_c$  and  $d$  and 1% for  $p$ . Stars mark constrained parameters.

	$\phi$ (%)	$\phi_f$ (%)	$\rho_c$ ( $10^{-6}$ Å <sup>-2</sup> )	$R_c$ (Å)	$d$ (Å)	$p$ (%)
1	5	3	6.38*	10.8	12.0	15.7
2	10	7	6.38*	11.9	11.0	16.1
3	15	10	6.38*	11.7	10.7	16.0
1+PEO		4	2.1	8.9	12.0*	21.9
2+PEO		7	2.5	10.8	11.0*	22.5
3+PEO		10	2.7	10.6	10.7*	21.9

### 7.2.3. Droplet diffusion and bending modulus - NSE

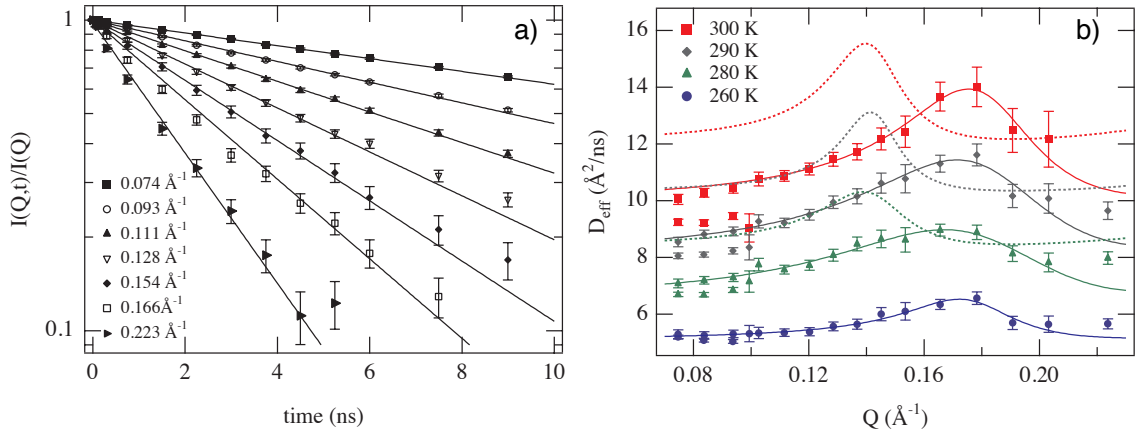


Figure 7.3.: a) Normalized intermediate scattering function of PEO containing microemulsion at  $T = 290$  K. Solid lines are fits to a single exponential. b)  $Q$ -dependance of effective diffusion coefficient  $D_{\text{eff}}$  for PEO containing microemulsion at different temperatures. Dotted lines correspond to  $D_{\text{eff}}$  for pure microemulsions (see chapter 5). Upon PEO addition the peak shifts to higher  $Q$  and it becomes broader.

Let us now turn to the dynamical behaviour of pure and polymer-containing mi-

croemulsions as seen by NSE. Figure 7.3 a) shows normalized intermediate scattering curves of the microemulsion with  $Z \approx 1.5$  PEO<sub>3000</sub> molecules per droplet at  $T = 290$  K. We note that the data is well described by single exponentials, shown by solid lines in Fig. 7.3 a). Analyzing the NSE data of PEO containing microemulsions as it was earlier done with results of pure microemulsions (see chapter 5) we determined the effective diffusion coefficient  $D_{\text{eff}}$  from the fits with single exponentials. In this context we desist from repeating the according equations but we point back to Eqs. 5.10 to 5.12 in section 5.1.1.1. Colored symbols in Fig. 7.3 b) show resulting  $D_{\text{eff}}$  as a function of scattering vector  $Q$  for temperatures between  $T = 300$  K and 260 K. Dotted lines correspond to  $D_{\text{eff}}$  of the respective pure microemulsion at the same temperatures (marked by similar colors). Upon polymer addition the plateau value of  $D_{\text{eff}}$  decreases compared to the pure microemulsions. Moreover the peak becomes systematically broader and its maximum shifts for all temperatures to a larger scattering vector  $Q_{\text{max}} \approx 0.18 \text{ \AA}^{-1}$ . We

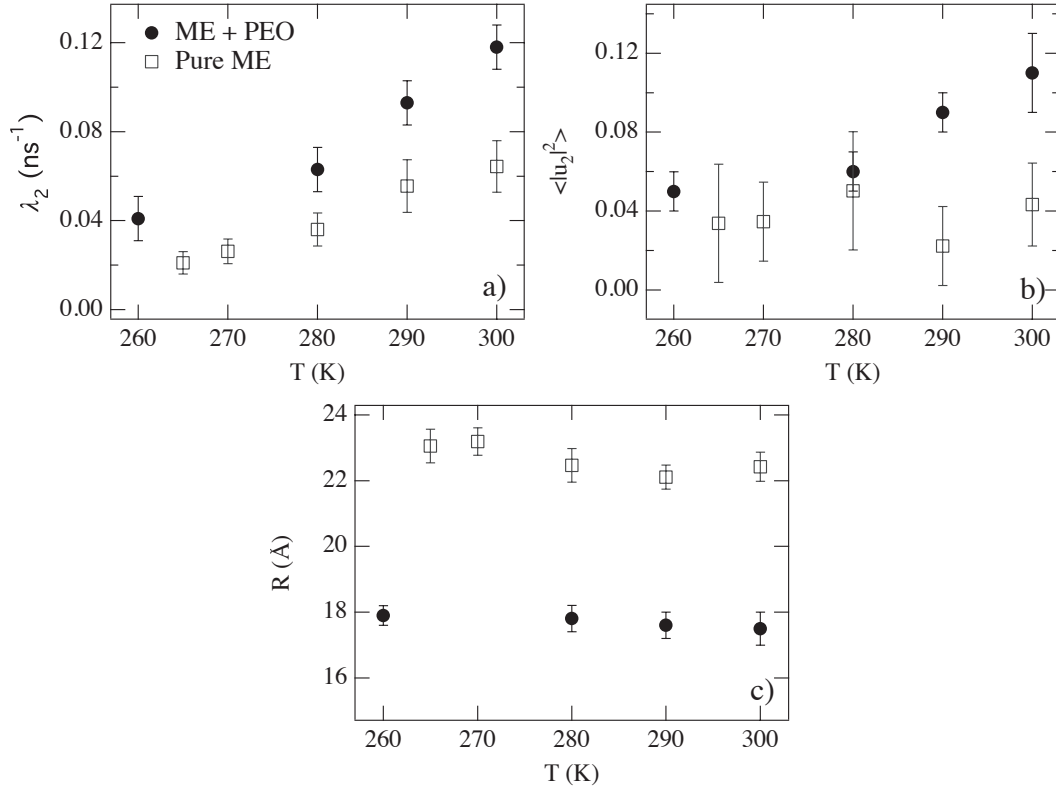


Figure 7.4.: Temperature dependency of fitting parameters of the effective diffusion coefficient  $D_{\text{eff}}$  to Eq. 5.11 for pure (hollow symbols) and PEO containing microemulsions (full symbols). a) Relaxation rate  $\lambda_2$  of second order oscillation, b) dimensionless fluctuation amplitude  $\langle |u_2|^2 \rangle$  and c) mean droplet radius  $R$ .

further fit the data with Eq. 5.12 which expresses the effective diffusion coefficient  $D_{\text{eff}}$  as a function of the translational diffusion coefficient  $D_{\text{drop}}$ , the average shell radius  $R$ , and relaxation rate  $\lambda_2$  and the dimensionless mean squared amplitude  $\langle |u_2|^2 \rangle$  of the second order form fluctuation. In Fig. 7.4 these parameters are compared to the respective results for polymer free droplets.

**Radius:** the location of the peak in  $D_{\text{eff}}$  is determined by the average radius  $R$  of the fluctuating shell. Figure 7.4 c) compares NSE results for  $R$  of pure and PEO containing micelles. Radii of pure and polymer containing droplets both stay rather constant over temperature. In accordance with the SANS results we observe the decrease of the droplet size upon polymer addition. PEO-loaded droplets are about 4 Å to 5 Å smaller than the respective PEO-free droplets.

**Fluctuations:** The fluctuations are described by their relaxation rate  $\lambda_2$  and dimensionless amplitude  $\langle |u_2|^2 \rangle$  shown in Fig. 7.4 a) and b). We will desist from discussing those parameters in detail because they were obtained using the model derived for fluctuating particles that are on average spherical, which might not be the case for the PEO containing droplets.

$\lambda_2$  increases upon PEO addition, this probably points at an increasing elastic modulus. On average  $\langle |u_2|^2 \rangle$  is larger for the PEO containing droplets. Contrary to the dimensionless squared amplitude of polymer-free droplets,  $\langle |u_2|^2 \rangle$  of PEO containing droplets shows a clear temperature dependence. We hypothesize that this might be related to the decreasing water solubility of PEO with increasing temperature. Presumably this also affects the adsorption of PEO on the AOT shell and thus the fluctuation amplitude.

**Diffusion coefficient:** Figure 7.5 shows the temperature dependence of the translational diffusion coefficient  $D_{\text{drop}}$  of pure microemulsion droplets (grey broken line, data from Fig. 5.4 c)) and PEO loaded droplets (black symbols).  $D_{\text{drop}}$  is given by the constant  $Q$ -independent plateau value on which the  $Q$ -modulated deformational part sits (see 5.11). Figure 7.3 b) shows that sufficiently low  $Q$  are probed to allow for an accurate determination of  $D_{\text{drop}}$  independent of the exact form of  $D_{\text{drop}}$ .

The black solid line Fig. 5.4 c)) is a fit with the Stokes-Einstein relation, Eq. 5.14, which yields the hydrodynamic radius of the diffusing objects  $R_h \approx 41$  Å. Taking into account the previously discussed factor of about 1.3 between hydrodynamic and geometric radius, we still find a radius of  $R \approx 31$  Å. This value is significantly bigger than the SANS result of  $R \approx 21$  Å. We therefore have to conclude that the diffusing objects cannot be single droplets.

As the undisturbed PEO<sub>3000</sub> chains are about 1.5 times larger than the water core of one droplet, one may assume that one PEO chain connects on average two droplets. SANS

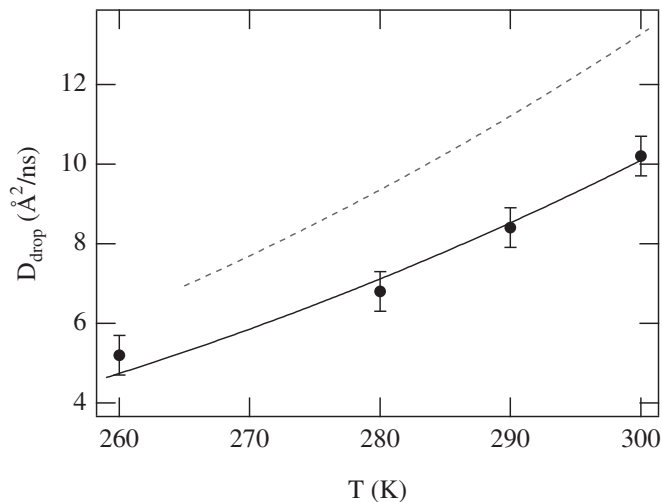


Figure 7.5: Translational diffusion coefficients  $D_{\text{drop}}$  of PEO containing micelles as a function of temperature. Black solid line is a fit with the Stokes-Einstein relation (Eq. 5.14). The dashed grey line corresponds to  $D_{\text{drop}}$  of pure water swollen micelles.

showed that no significant structural changes occur upon PEO addition, therefore we further assume that the form of the interconnected droplets remains similar to that of a PEO free droplet. We approximate the form of the two-droplet-cluster by a prolate ellipsoid with a major axis of twice the droplet radius  $2R$  and a minor axis of the droplet radius  $R$ . The hydrodynamic radius  $R_h$  of such an object calculates to [159]:

$$R_h = \frac{\sqrt{3} R}{\ln(2 + \sqrt{3})} \quad (7.1)$$

From the observed  $D_{\text{drop}}$  we estimate with Eqs. 5.14 and 7.1 a droplet radius of  $R \approx 24 \text{ \AA}$ , which is indeed closer to the SANS droplet radius and thus supports the picture of PEO-interconnected two-droplet-clusters.

### 7.3. Summary and conclusions

We have performed SANS and NSE measurements in order to investigate the PEO induced structural and dynamical changes in w/o droplet microemulsions. The basic microemulsion consisted of water swollen reverse AOT micelles with a water core radius of  $R_c \approx 12 \text{ \AA}$  dispersed in toluene-d8. As a hydrophilic homo-polymer we added PEO<sub>3000</sub> whose radius of gyration is about 3/2 as big as the water core of the droplets. To the microemulsion we added a number of  $Z \approx 2$  molecules PEO<sub>3000</sub> per droplet. PEO<sub>3000</sub> has a radius of gyration of  $R_G \approx 19 \text{ \AA}$ , which is slightly bigger than the droplet water core radius. SANS investigations showed that the structure of the polymer containing microemulsion is very similar to that of the pure microemulsion. Upon polymer addition we observed a small decrease of the droplet radius and an increase of the polydisper-

sity. Both observations indicate that the AOT membrane elasticity changes upon PEO addition.

Using NSE we found the PEO containing droplets to diffuse slower than free droplets. For the PEO loaded droplets the hydrodynamic radius estimated from the translational diffusion coefficient corresponded to clusters of 2 droplets. This observation is in agreement with so-called necklace structures reported in literature [148, 152].

A first tentative analysis indicated that the nature of the fluctuations changes upon PEO addition. We observed increasing relaxation rates  $\lambda_2$  corresponding to an increased bending modulus  $\kappa$ . Moreover the dimensionless amplitude increased with temperature. This may be related to the temperature dependent solubility of PEO in water.

We did not derive absolute values for the bending modulus  $\kappa$  as the in section 5.1.1.1 discussed model was derived for fluctuating particles that are on average spherical. Apparently the PEO containing droplets do not fulfill this precondition on the time scale relevant for NSE.

All in all we see these first results as a strong indication for the possibility to modify the elastic properties of the AOT shell by adding PEO. Further systematic studies with varying polymer concentration and primarily by using PEO of different molecular weights are required to obtain a quantitative understanding maybe allowing a controlled modification of the elastic modulus in future.

## 8. Summary

In the presented thesis we have investigated the suitability of reverse micelles as a model system for the study of the dynamical behavior of soft confined water, next to hydrophilic ionic groups. For this purpose we have used the droplet phase of a water-in-oil (w/o) microemulsion consisting of water, oil (decane, toluene or heptane) and the anionic surfactant AOT (sodium bis[ethylhexyl] sodium sulfosuccinate). Over a wide range of compositions this ternary mixture forms spherical water droplets coated by a mono-molecular layer of surfactant (so-called reverse micelles), which are thermodynamically stable dispersed in the continuous oil matrix. In the first part of this work we have thoroughly investigated structure and dynamics of the droplets. In the second part of this thesis we have then focussed on the mobility of confined water as a function of micelle size and temperature.

We started this work with the detailed characterization of the microemulsion structure. We have used small angle neutron scattering (SANS) to determine form, size and polydispersity of the droplets as a function of microemulsion composition. We have verified that the radius  $R_c$  of the polar water core increases at room temperature linearly with  $\omega$ , where  $\omega$  denotes the molar ratio of water to AOT [19]. The following relation holds:  $R_c/\text{\AA} \approx 1.4 \cdot \omega + 2.3$ , as we have shown for  $\omega \leq 40$  and droplet volume fractions  $\phi \leq 0.2$ . One may thus vary the size of the water core in a controlled way between a few Ångström and several nanometer by choosing the appropriate  $\omega$ . In the following we have extended the phase diagram of this microemulsion to lower temperatures. Using SANS we have proved that the droplet phase is stable down to temperatures below the freezing point  $T_f$  of free water and we have determined form, size and polydispersity of the droplets as a function of temperature. The smaller  $\omega$  was, i.e. the smaller the droplets were at room temperature, the lower was the temperature  $T_s$  down to which the droplets remained stable.  $\Delta T_{\text{SANS}} = T_f - T_s$  was found to be proportional to the inverse of the radius  $1/R_c$ . Further cooling of the microemulsions below  $T_s$  caused the shrinking of the droplets to a  $\omega$ -independent final size. A comparison of the size of shrunken droplets to that of "dry" reverse AOT micelles ( $\omega = 0$ ) has shown that even at the lowest investigated temperatures of  $T \approx 220$  K the shrunken micelles still contain about 2 water molecules per AOT molecule.

As a next step we addressed the question if the structural instability of the droplets and the freezing behavior of the confined water are related. We have carried out elastic fixed window scans on neutron backscattering (BS) in order to investigate the water freezing under variation of droplet size. We observed a clear depression of the freezing point  $T_f^c$  of confined water compared to that of bulk water  $T_f$ . With decreasing droplet size the supercooling,  $\Delta T_{\text{BS}} = T_f - T_f^c$ , of the confined water increased.  $\Delta T_{\text{BS}}$  and  $\Delta T_{\text{SANS}}$  hence showed a qualitatively similar dependence on  $\omega$ , i.e. on droplet water core size. In this context it should be emphasized that with  $\Delta T_{\text{BS}}$  and  $\Delta T_{\text{SANS}}$  we compared quantities extracted from a dynamical and a structural observation. The measured relation between the supercooling  $\Delta T_{\text{BS}}$  and the droplet core radius  $R_c$  follows the Gibbs-Thomson equation for homogenous nucleation, if we identify  $R_c$  with the critical radius of a nucleus. This means that soft confinement, as realized by reverse micelles, influences the freezing behavior of water in a similar manner as hard confinement as e.g. mesoporous silica [3]. We could not definitely clarify if the "shrinking temperature"  $T_s$  corresponds to the lower phase boundary of the microemulsion or if it is caused by the freezing of the confined water.

The structural characterization of the microemulsion was followed by the investigation of droplet dynamics by means of neutron spin echo (NSE). One aim was the determination of the temperature dependent diffusion coefficient  $D_{\text{drop}}$  of the entire droplets in the oil matrix, as the exact knowledge of  $D_{\text{drop}}$  is an essential pre-condition for the separation of water and droplet dynamics. Structural properties of microemulsions are essentially determined by the elasticity of the surfactant membrane. Values of the bending modulus  $\kappa$  of the AOT shell in w/o droplet microemulsions have been determined by different methods to range between  $0.2k_B T \leq \kappa \leq 3k_B T$  [95]. Furthermore it is known that softer membranes with  $\kappa < 0.1k_B T$  typically result in an instability of the structure [95]. The second aim of our experiment was thus to test if the previously by SANS observed droplet shrinking at  $T_s$  can be explained by a change of the bending modulus at just this temperature.

We have chosen to investigate a microemulsion with droplets of an average size ( $\omega = 8 \rightarrow R_c \approx 12 \text{ \AA}$ ); for this composition the shrinking temperature was determined to be at  $T_s \approx 255 \text{ K}$ . We measured the intermediate scattering function from room temperature down to below the shrinking temperature,  $250 \text{ K} \leq T \leq 300 \text{ K}$ . We extracted the effective diffusion coefficient  $D_{\text{eff}}$ , which contains the droplet diffusion coefficient  $D_{\text{drop}}$  and the  $Q$ -dependent deformation part  $D_{\text{def}}$  [114]. Above  $T_s$  the temperature dependence of the droplet diffusion coefficient  $D_{\text{drop}}$  follows in an excellent way the Stokes-Einstein relation, where the resulting hydrodynamic radius  $R_h$  corresponds over the entire tested temperature range to about 1.3 times the geometrical droplet radius.



---

Analyzing the  $Q$ -dependence of the deformation part  $D_{\text{def}}$  we determined the dimensionless amplitudes and relaxation times of the form fluctuations. The therefrom calculated bending modulus  $\kappa$  of the AOT shell was found to be constant  $\kappa = (0.31 \pm 0.06)k_B T$  over the investigated temperature range of droplet stability [107, 113]. Thus  $\kappa$  does not change in a significant way when approaching  $T_s$ . Hence there is no experimental indication that changing elastic properties of the AOT shell cause the droplet instability. Results on droplet dynamics obtained by NSE confirm the before by SANS obtained results on droplet structure. Combining both methods, SANS and NSE, we arrived at a consistent picture of the temperature dependent phase behavior of the investigated microemulsion.

At this point we have obtained a comprehensive knowledge about structure and droplet dynamics of the chosen AOT based w/o microemulsion in the relevant range of compositions ( $0 \leq \omega \leq 12$ ,  $0.05 \leq \phi \leq 0.2$ ). We have successfully shown that this system offers the possibility to study water in well-defined soft confinement, where both, confinement size and temperature, may be varied over a large range. We want to underline that the droplet structure is stable down to temperatures  $T < 270$  K. Hence these reverse micelles are suited to study water in the supercooled state.

In the second part of this work we focussed on the study of the dynamical behavior of water inside reverse micelles of H<sub>2</sub>O/d-AOT/toluene-d<sub>8</sub> microemulsions. We have performed incoherent quasi-elastic neutron scattering measurements using three different instruments which are complementary with respect to their dynamical range. Combining time-of-flight (TOF) and backscattering (BS), we accessed the water dynamics over three decades in time from pico- to nanoseconds. To study the influence of confinement size on water mobility we have prepared two systems with different micelle sizes,  $\omega = 3$  and  $\omega = 8$ , corresponding to respective water core radii of  $R_c \approx 7$  Å and  $R_c \approx 12$  Å. The temperature was varied over the for both systems common range of structural stability  $260 \text{ K} \leq T \leq 300 \text{ K}$ . For both systems fully deuterated samples with otherwise identical compositions (same  $\omega$  and  $\phi$ ) were measured as background and subtracted from the spectra of H<sub>2</sub>O containing samples. By doing so we minimized the scattering contribution of d-AOT and toluene-d<sub>8</sub> and approximately obtained the signal originating from the water. We analyzed Fourier-transformed data in the time domain using a model which describes the water motion by independently performed rotational diffusion on a sphere and jump diffusion [85]. Within experimental accuracy, measured rotational diffusion coefficients  $D_R$  for water inside micelles of both sizes were identical and only slightly smaller than for bulk water [85]. The rotational time,  $\tau_R = 1/(6D_R)$ , follows Arrhenius behaviour,  $\tau_R = \tau_R^0 \exp(E_A/RT)$ , with an activation energy of  $E_A = (1.9 \pm 0.4) \text{ kcal/mol}$  and a pre-factor of  $\tau_R^0 = (0.07 \pm 0.03) \text{ ps}$ . While

the rotational motion appears to be almost unaffected by the confinement, we observed a clear effect on the translational motion. For all investigated temperatures the translational motion slowed down with decreasing micelle size. The translational diffusion coefficient  $D_T$  decreased and the residence time  $\tau_0$  increased with decreasing  $\omega$  about a factor of 10 (100) for  $\omega = 8$  ( $\omega = 3$ ).

Owing to the large dynamical range we could separate two fractions of water with different mobility inside the bigger droplets with  $\omega = 8$ . We determined the ratio of fast ( $A$ ) over slow ( $B$ ) water to be  $\frac{A}{B} \approx 1$ , which corresponds to about 4 retarded water molecules per AOT molecule. The mobility of the faster water fraction was comparable to that of free water at a temperature of about 10 K lower. Inside smaller micelles with  $\omega = 3$  we observed only one fraction of very slow water. These observations suggest that slow water can be identified with water closely bound by the surfactant AOT. There seems to be a minimum molar ratio of  $\omega \approx 4$  above which water inside the reverse micelles begins to behave similar to bulk water. However, also this "core" water has a decreased mobility compared to bulk water at the same temperature.

Finally we conducted first experiments on a trial basis to study the effect of the hydrophilic homo-polymer polyethyleneoxide (PEO) on structure and dynamics of a  $D_2O/AOT/Toluol-d_8$  microemulsion with  $\omega = 8$ . Our intention was to investigate if the elastic properties of the AOT-shell may be varied in a controlled way by PEO addition because this would offer the possibility to change the confinement from soft to hard. Interactions between PEO and AOT have been predicted to be attractive which should cause the PEO to be adsorbed at the AOT shell and to stiffen it [147]. A rather indirect experimental determination of the elastic modulus of PEO modified AOT membranes has confirmed this, but a direct experimental proof is missing [152, 157].

For our study the microemulsion droplets were loaded with  $PEO_{3000}$  (polyethyleneoxide, molecular weight: 3000 g/mol), corresponding to  $Z \approx 2$  PEO molecules per droplet. By means of SANS we showed that the underlying droplet structure is stable upon PEO addition. The radius of the droplets slightly decreases while the polydispersity increases with addition of PEO; both observations point at a changing bending modulus  $\kappa$ .

The measured translational diffusion coefficient of the PEO containing droplets was significantly smaller than that of the respective "empty" ones. The derived hydrodynamic radius suggests that on the time scale relevant for NSE on average two droplets are linked together by the PEO. At the same time the form of the loaded droplets seems to remain similar to that of the droplets of the pure microemulsion.

As expected, PEO addition alters the shell fluctuations - no absolute values for  $\kappa$  have been determined, nevertheless our results show that PEO addition modifies the stiffness of the AOT membrane. Further systematic experiments need to be conducted in order to obtain quantitative results.

## 8.1. Zusammenfassung

In der vorliegenden experimentellen Arbeit untersuchten wir die Eignung von inversen Mizellen als Modellsystem zum Studium des dynamischen Verhaltens von Wasser in weicher geometrischer Einschränkung, nahe an hydrophilen ionischen Gruppen. Zu diesem Zweck wurde die Tröpfchenphase einer Wasser-in-Öl (w/o) Mikroemulsion bestehend aus Wasser, Öl (Dekan, Heptan oder Toluol) und dem anionischen Tensid AOT (sodium bis[ethylhexyl] sodium sulfosuccinate) genutzt. Durch geeignete Wahl der Zusammensetzung bilden sich in dieser ternären Mischung sphärische Wasserkerne, umschlossen von einer monomolekularen Schicht des Tensids (inverse Mizellen genannt), die in der kontinuierlichen Ölmatrix thermodynamisch stabil dispergiert sind. Nachdem Struktur und Dynamik der Tröpfchen im ersten Teil der Arbeit ausführlich untersucht wurden, wurde im zweiten Teil der Arbeit die Mobilität des eingeschlossenen Wassers in Abhängigkeit von Mizellengröße und Temperatur bestimmt.

Zu Beginn der Arbeit widmeten wir uns der sorgfältigen strukturellen Charakterisierung der Mikroemulsion. Wir nutzten Kleinwinkelneutronenstreuung (SANS), um Form, Größe und Polydispersität der Tröpfchen in Abhängigkeit von der Zusammensetzung zu bestimmen. So konnten wir den bekannten Zusammenhang [19] bestätigen, nach dem der Radius  $R_c$  des polaren Wasserkerns bei Raumtemperatur linear mit  $\omega$ , dem molaren Verhältnis von Wasser zu AOT, anwächst.  $R_c/\text{Å} \approx 1.4 \cdot \omega + 2.3$ , wobei  $\omega$  zwischen 0 und 40 variiert wurde und der Volumenanteil an Tröpfchen unterhalb  $\phi \leq 0.2$  lag. Basierend auf dieser Erkenntnis ist es möglich, die Größe des Wasserkerns zwischen einigen Ångström und mehreren Nanometern kontrolliert einzustellen. Im Folgenden wurde das Phasendiagramm der Mikroemulsion auf tiefe Temperaturen ausgeweitet. Wir zeigten mit SANS direkt, dass die Tröpfchenphase bis zu Temperaturen unterhalb des Gefrierpunktes  $T_f$  von freiem Wasser stabil ist und bestimmten Form und Polydispersität der Tröpfchen als Funktion der Temperatur. Je kleiner  $\omega$  ist, d.h. je kleiner die Tröpfchen bei Raumtemperatur sind, desto tiefer ist die beobachtete untere Stabilitätstemperatur  $T_s$ , dabei skaliert  $\Delta T_{\text{SANS}} = T_f - T_s$  mit dem Inversen des Radius  $1/R_c$ . Wurde die Mikroemulsion weiter unter  $T_s$  gekühlt, so schrumpften die Tröpfchen auf eine  $\omega$ -unabhängige Endgröße. Der Vergleich mit reinen inversen AOT Mizellen ( $\omega = 0$ ) zeigte, dass sich selbst bei den tiefsten untersuchten Temperaturen,  $T \approx 220$  K, noch ca. 2 Wassermoleküle pro AOT Molekül in den geschrumpften Mizellen befinden.

In einem nächsten Schritt gingen wir dann der Frage nach, inwiefern die strukturelle Instabilität der Tröpfchen und das Frierverhalten des eingesperreten Wassers zusammenhängen. Dazu führten wir elastische Scans auf Neutronenrückstreu-Spektrometern (BS) durch, anhand derer das Gefrieren des eingesperreten Wassers bei Variation der Mizellengröße untersucht wurde. Verglichen mit dem Gefrierpunkt von freiem Wasser ist der des eingesperreten Wassers deutlich herabgesetzt. Je kleiner die ursprünglichen Tröpfchen sind, desto größer ist die gemessene Unterkühlung  $\Delta T_{\text{BS}}$  des sich in den

Tröpfchen befindlichen Wassers. Somit ist der Verlauf von  $\Delta T_{\text{BS}}$  und  $\Delta T_{\text{SANS}}$  mit  $\omega$  qualitativ ähnlich. In diesem Zusammenhang möchten wir erneut betonen, dass wir mit  $\Delta T_{\text{BS}}$  und  $\Delta T_{\text{SANS}}$  eine dynamische mit einer strukturellen Observablen vergleichen. Die von uns gemessene Unterkühlung  $\Delta T_{\text{BS}}$  als Funktion des Kernradius  $R_c$  folgt der durch die Gibbs-Thomson Gleichung gemachten Vorhersage für homogene Nukleation, wenn wir den kritischen Keimradius mit dem Kernradius  $R_c$  der Tröpfchen identifizieren. Dies bedeutet, dass die von uns gewählte weiche Einschränkung das Frierverhalten des Wassers vergleichbar beeinflusst wie harte Einschränkung, realisiert durch beispielsweise mesoporöses Silica [3]. Nicht eindeutig geklärt werden konnte, ob die "Schrumpftemperatur"  $T_s$  der unteren Phasengrenze der Mischung entspricht, oder ob sie das Resultat des Gefrierens des eingeschlossenen Wassers ist.

Diese somit über einen weiten Temperaturbereich strukturell charakterisierte Mikroemulsion wurde anschließend mit Neutronen-Spin-Echo (NSE) spektroskopisch untersucht. Zum einen sollte so die temperaturabhängige Diffusion der Tröpfchen in der Ölmatrix gemessen werden, da die genaue Kenntnis des Diffusionskoeffizienten  $D_{\text{drop}}$  eine grundlegende Voraussetzung ist, um später Wasser- und Tröpfchendynamik separieren zu können. Die strukturellen Eigenschaften von Mikroemulsionen sind in erster Linie bestimmt durch die Elastizität der Tensidschicht. Mit unterschiedlichen Methoden experimentell bestimmte Werte für den Biegemodul  $\kappa$  der AOT-Schicht in w/o Mikroemulsionen liegen bei Raumtemperatur im Bereich  $0.2k_B T \leq \kappa \leq 3k_B T$  [95]. Weiter ist bekannt, dass weichere Membranen,  $\kappa < 0.1k_B T$ , typischerweise eine Instabilität der Struktur bewirken [95]. Zum anderen sollte anhand des Experiments deshalb eine Aussage darüber gemacht werden, ob das zuvor mit SANS beobachtete Schrumpfen der Tröpfchen bei  $T_s$  in Zusammenhang steht mit einer Veränderung des Biegemoduls bei eben dieser Temperatur.

Die NSE Untersuchungen wurden an einer Mikroemulsion mit einer mittleren Tröpfchengröße ( $\omega = 8 \rightarrow R_c \approx 12 \text{ \AA}$ ) durchgeführt, für die die Schrumpftemperatur zu  $T_s \approx 255 \text{ K}$  bestimmt wurde. Wir maßen die intermediäre Streufunktion, ausgehend von Raumtemperatur bis unter  $T_s$ ,  $250 \text{ K} \leq T \leq 300 \text{ K}$ , und bestimmten so den effektiven Diffusionskoeffizienten, der sich aus dem Translationsdiffusionskoeffizienten  $D_{\text{drop}}$  und dem  $Q$ -abhängigen Deformationsanteil  $D_{\text{def}}$  zusammensetzt [114]. Der Temperaturverlauf des gemessenen Diffusionskoeffizienten  $D_{\text{drop}}$  oberhalb  $T_s$  ließ sich in exzellenter Weise über die Stokes-Einstein Gleichung beschreiben, wobei der daraus resultierende hydrodynamische Radius  $R_h$  in etwa 1.3 mal dem geometrischen Radius entsprach. Über die  $Q$ -Abhängigkeit des Deformationsanteils  $D_{\text{def}}$  liessen sich Amplitude und Relaxationszeit der Formfluktuationen bestimmen und daraus weiter Biegemodul  $\kappa$  der AOT Schicht [107, 113]. Wir ermittelten ein konstantes  $\kappa = (0.31 \pm 0.06)k_B T$  für den gesamten Temperaturbereich, in dem die Tröpfchen stabil waren.  $\kappa$  ändert sich also nicht messbar mit Annäherung an  $T_s$ , was bedeutet, dass wir keinen experimentellen

Hinweis darauf sehen, dass die Unstabilität der Tröpfchen durch veränderte elastische Eigenschaften der AOT Schicht verursacht wird.

Zusammenfassend läßt sich sagen, dass die mit NSE gemessene Tröpfchendynamik die zuvor mit SANS gewonnene Erkenntnis über die Struktur bestätigt. Die Kombination beider Methoden, SANS und NSE, ergibt ein konsistentes Bild des temperaturabhängigen Phasenverhaltens der untersuchten Mischung.

Die gewählte auf AOT basierte w/o Mikroemulsion ist nun im relevanten Zusammensetzungsbereich, ( $0 \leq \omega \leq 12$ ,  $0.05 \leq \phi \leq 0.2$ ), umfassend charakterisiert, sowohl was die Struktur, als auch was die Dynamik der Tröpfchen betrifft. Sie bietet die Möglichkeit, Wasser in wohldefinierter weicher Einschränkung zu untersuchen, wobei sowohl Größe als auch Temperatur über einen weiten Bereich variiert werden können. Hervorzuheben ist insbesondere die Tatsache, dass die Tröpfchen stabil sind bis zu Temperaturen  $T < 270$  K. Dieses System eignet sich demnach auch, um Wasser im unterkühlten Zustand zu untersuchen.

Im zweiten Teil der Arbeit untersuchten wir die Wasserdynamik in den inversen Mizellen der  $\text{H}_2\text{O}/\text{d-AOT}/\text{Toluol-d}_8$  Mikroemulsion. Wir führten inkohärente quasi-elastische Neutronenstreuungen an drei sich bezüglich ihres dynamischen Bereichs ergänzenden Spektrometern durch. Durch diese Kombination von Flugzeit- (TOF) und Rückstreu-Spektroskopie (BS) konnte die Wasserdynamik über drei Zeitdekaden von Piko- bis zu Nanosekunden verfolgt werden. Um den Einfluss der Einschränkungsgröße zu untersuchen, präparierten wir zwei Systeme mit unterschiedlichen Tröpfchengrößen,  $\omega = 3$  und  $\omega = 8$ , was jeweiligen Kernradien von  $R_c \approx 7$  Å und  $R_c \approx 12$  Å entsprach. Die Temperatur wurde über den gemeinsamen Bereich struktureller Stabilität von  $T = 260$  K bis  $T = 300$  K variiert. Für beide Systeme wurden volldeuterierte Proben  $\text{D}_2\text{O}/\text{d-AOT}/\text{Toluol-d}_8$  mit ansonsten identischer Zusammensetzung (gleiches  $\omega$  und  $\phi$ ) als Untergrund gemessen und von dem Signal der Proben mit  $\text{H}_2\text{O}$  entsprechend abgezogen. Auf diesem Weg minimierten wir den Streubeitrag durch d-AOT und Toluol-d8 und erhielten näherungsweise das Signal des eingeschlossenen Wassers.

Wir analysierten die Fourier-transformierten Daten anhand eines Modells, welches die Wasserdynamik durch Rotation auf einer Kugeloberfläche und Sprungdiffusion beschreibt [85]. Die so bestimmten Rotationsdiffusionskoeffizienten  $D_R$  für Wasser in Mizellen beider Größen unterscheiden sich im Rahmen der Messgenauigkeit nicht voneinander und sind nur wenig kleiner als bei freiem Wasser [85]. Die Rotationskorrelationszeit,  $\tau_R = 1/(6 D_R)$ , folgt einem Arrheniusverhalten,  $\tau_R = \tau_R^0 \exp(E_A/RT)$ , mit der Aktivierungsenergie  $E_A = (1.9 \pm 0.4)$  kcal/mol und dem Vorfaktor  $\tau_R^0 = (0.07 \pm 0.03)$  ps. Während die Rotationsbewegung durch die Einschränkung demnach nahezu unbeeinflusst scheint, ergab sich für die Translationsbewegung ein deutlicher Effekt. Kon-

sistent für alle untersuchten Temperaturen war mit abnehmender Mizellengröße eine zunehmende Verlangsamung der Translationsdiffusion zu beobachten: der Translationsdiffusionskoeffizient  $D_T$  nimmt ab und die Verweildauer  $\tau_0$  nimmt mit kleiner werdendem  $\omega$  um einen Faktor 10 (100) für  $\omega = 8$  ( $\omega = 3$ ) zu.

Anhand der Resultate bei den längsten untersuchten Zeiten ließen sich in den größeren Tröpfchen mit  $\omega = 8$  zwei Wasserfraktionen auflösen, die ein unterschiedliches dynamisches Verhalten zeigten. Wir bestimmten das Verhältnis von schnellem ( $A$ ) zu langsamen ( $B$ ) Wasser zu  $\frac{A}{B} \approx 1$ , was bedeutet, dass pro AOT Molekül 4 Wassermoleküle verlangsamt erscheinen. Die Mobilität der schnelleren Wasserfraktion ist vergleichbar zu der von freiem Wasser bei einer um 10 K tieferen Temperatur. Innerhalb der kleinen Tröpfchen mit  $\omega = 3$  konnte nur langsames Wasser gemessen werden. Diese Beobachtungen legen nahe, die langsamen Wassermoleküle mit Tensid-gebundenem Wasser zu identifizieren. Innerhalb der Tröpfchen scheint erst bei einem molaren Verhältnis von  $\omega > 4$  Wasser mit Eigenschaften von annähernd freiem Wasser vorzuliegen. Auch dieses "Kern"-Wasser ist jedoch verlangsamt verglichen mit freiem Wasser.

Abschließend führten wir erste Experimente durch, um die Auswirkung eines hydrophilen Homopolymers Polyethylenoxid (PEO) auf Struktur und auch Dynamik der  $D_2O/AOT/Toluol-d_8$  Mikroemulsion mit  $\omega = 8$  zu untersuchen. Motivation dafür war die Frage, ob sich so die elastischen Eigenschaften der AOT-Schicht kontrolliert ändern lassen und auf diesem Weg die Art der Einschränkung des Wassers von weich zu hart variiert werden könnte. Theoretisch vorhergesagt wurde eine attraktive Wechselwirkung zwischen PEO und AOT aufgrund derer sich das Polymer von innen an die Tensidschicht anlagert und zu einer Versteifung der AOT-Schicht führt [147]; eine erste indirekte experimentelle Bestimmung des elastischen Moduls bestätigte dies auch [152, 157].

Wir beluden die Mikroemulsion mit 2 Ketten PEO (Molekulargewicht: 3000 g/mol) pro Tröpfchen. Unsere SANS Untersuchungen zeigten, dass die Polymere die Tröpfchenstruktur der Mikroemulsion nicht signifikant veränderten. Der Tröpfchenradius verkleinerte sich leicht bei Zugabe von PEO, gleichzeitig nahm die Polydispersität zu - beide Beobachtungen weisen auf eine Veränderung des Biegemoduls  $\kappa$  hin.

Der mit NSE gemessene temperaturabhängige Translationsdiffusionskoeffizient  $D_{\text{drop}}$  der PEO-beladenen Tröpfchen war wesentlich kleiner als der der unbeladenen Tröpfchen. Der daraus bestimmte hydrodynamische Radius läßt darauf schließen, dass auf der mit NSE zugängigen Zeitskala im Mittel jeweils zwei Tröpfchen durch die PEO Ketten verbunden sind, wobei die Form der Tröpfchen ähnlich der der Unbeladenen bleibt. Wie erwartet veränderten sich die Formfluktuationen unter Zugabe des Polymers - absolute Werte für  $\kappa$  wurden nicht bestimmt, jedoch können die Resultate als Hinweis darauf gedeutet werden, dass durch PEO die Steifigkeit der AOT Schicht modifiziert werden kann. Weiter Versuche sind notwendig, um quantitative Aussagen zu machen.

# A. Appendix

## A.1. Sample preparation

The microemulsions were prepared by mixing appropriate amounts of AOT, water, and oil (toluene-d8, heptane-d16 or decane-d22) and shaking for several minutes until the samples were single-phase and optically clear. Depending on the method and the intention of the experiment, AOT and water were used either in the protonated or deuterated form. For neutron scattering experiments the solvents were always deuterated. N-heptane-d16, toluene-d8, n-decane-d22 (Acros Organics, Euriso-Top, >98%), D<sub>2</sub>O (Euriso-Top, >99.9%) and AOT (Acros Organics) were used without further purification. Deionized water was taken from a Millipore Direct-Q 3 system.

The composition of a microemulsion is characterized by the droplet volume fraction  $\phi$  and the molar ratio  $\omega$  of water to AOT. With the desired total sample volume,  $v_{tot} = v_{AOT} + v_w + v_o$ , the required volume  $v_o$  of oil is:

$$v_o = (1 - \phi) \cdot v_{tot} \quad (\text{A.1})$$

Required water volume  $v_w$  and AOT mass  $m_{AOT}$  calculate as follows:

$$v_w = \frac{v_{tot} \cdot \phi}{1 + \frac{\rho_w \cdot M_{AOT}}{\omega \cdot \rho_{AOT} \cdot M_w}} \quad (\text{A.2})$$

$$m_{AOT} = \rho_{AOT} \left[ v_{tot} \cdot \phi - \frac{v_{tot} \cdot \phi}{1 + \frac{\rho_w \cdot M_{AOT}}{\omega \cdot \rho_{AOT} \cdot M_w}} \right] \quad (\text{A.3})$$

Here  $M$  denotes the molar mass,  $\rho$  is the mass density and subscripts  $w$ ,  $o$  and  $AOT$  stand for water, oil and AOT respectively. Liquid components were added by volume using high-precision laboratory pipettes. AOT was added by weight. In order to economize the expensive deuterated components only the sample volume needed for the experiment was prepared (depending on the instrument  $v_{tot}$  was in the order of 0.5 ml to 2 ml). This implies larger errors in the wanted composition ( $\phi$  and  $\omega$ ) than when bigger volumes of the microemulsion can be prepared. Using the measured weight of every component, the absolute errors (decreasing with increasing  $\phi$  and increasing sample volume  $v_{tot}$ ) in molar ratio and volume fraction were calculated to be for all

samples at maximum  $\Delta\omega \leq 0.25$  and  $\Delta\phi \leq$  respectively .

Usually samples were prepared 1 to 7 days before the beginning of the experiment. When filled sample holders were stored for a later experiment their weight was controlled to ensure that no sample evaporated. Except for the sample used for the DLS measurement at the TU Darmstadt, all other samples were prepared in the chemistry laboratory of the ILL.

## A.2. Properties of toluene, heptane, decane and water

For the preparation of the microemulsions three different oils were used: toluene ( $C_7H_8$ ), heptane ( $C_7H_{16}$ ) or decane ( $C_{10}H_{22}$ )<sup>1</sup>. In the following their physical properties relevant for this work are listed and compared to those of water.

### Freezing point, mass density, coherent scattering length density

In Tab. A.1 molar mass  $M$ , freezing point  $T_f$ , density  $\rho$  and scattering length density  $\rho_{coh}$  are listed for decane, heptane, toluene and water in deuterated and protonated form<sup>2</sup>.

Table A.1.: Properties of water, decane, heptane and toluene. Values given for mass density  $\rho$  and coherent scattering length density  $\rho_{coh}$  refer to room temperature.

		$T_f$ [K]	$M$ [g/mol]	$\rho$ [g/ml]	$\rho_{coh}$ [ $10^{-14}\text{cm}^{-2}$ ]
toluene	-h8	178	92.1	0.87	0.94
	-d8	178*	100.2	0.94	5.67
decane	-h22	241	142.3	0.73	-0.49
	-d22	241*	164.4	0.85	6.64
heptane	-h16	182	100.2	0.68	-0.54
	-d16	182*	116.3	0.79	6.27
water	-h2	273.2	18.0	1.00	-0.56
	-d2	276.9	20.0	1.10	6.38

### Viscosity

For the deuterated oils no reference data for the viscosity  $\eta$  could be found in literature. The viscosities of the deuterated oils were therefore approximated by those of their non-deuterated forms. Figure A.1 shows the temperature dependent viscosity  $\eta$  for the three

<sup>1</sup>Protons H have to be replaced by deuterions D in case of deuterated solvents.

<sup>2</sup>\*-marked values for freezing points  $T_f$  are approximated by  $T_f$  of the protonated form.



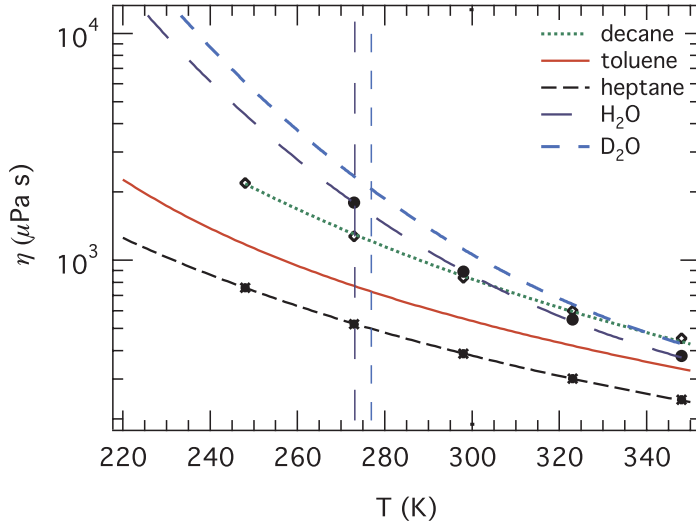


Figure A.1: Viscosity  $\eta$  of decane and heptane [122] and toluene [121]. The viscosity of water [122] is shown as well,  $\eta$  at temperatures below the bulk water freezing point (indicated by the vertical line) was extrapolated from the data above 273 K.

used oils and water.

### Toluene

In the case of toluene  $\eta$  was calculated after the formula given in [121] by:

$$\ln(\eta^*) = A + \frac{B}{T^*} + \frac{C}{(T^*)^2} + \frac{D}{(T^*)^3} \quad (\text{A.4})$$

With the dimensionless variables  $\eta^*$  and  $T^*$ :

$$T^* = \frac{T}{298.15 \text{ K}} ; \quad \eta^* = \frac{\eta}{\eta(298.15 \text{ K})} \quad (\text{A.5})$$

$$A = -5.220; \quad B = 8.964 \quad (\text{A.6})$$

$$C = -5.834; \quad D = 2.089 \quad (\text{A.7})$$

### Decane, Heptane and Water

For decane, heptane and water a continuous description for the viscosity  $\eta$  was obtained by interpolation the data from [122] in the following way:

$$\eta = A \cdot \exp\left(\frac{B}{T}\right) + C \quad (\text{A.8})$$

Within experimental precision, the viscosity of deuterated water at a given temperature

Table A.2.: Parameters for the interpolation of  $\eta$  after equation A.8.

	A ( $\mu$ Pa s)	B (K)	C ( $\mu$ Pa s)
decane	$8.17 \pm 0.51$	$1384.7 \pm 23.3$	0
heptane	$14.20 \pm 0.23$	$985.6 \pm 4.9$	0
water	$0.128 \pm 0.04$	$2581.6 \pm 82.8$	$160.4 \pm 18.9$

and pressure was found to equal that of protonated water at a temperature 6.498 K lower and the same pressure, corrected for the difference in molar mass [123]:

$$\eta_{\text{D}_2\text{O}} = 1.0544 \cdot \eta_{\text{H}_2\text{O}}(T - 6.498 \text{ K}) \quad (\text{A.9})$$

### A.3. Self absorption corrections for BS and TOF data

To deduce the correct sample intensity  $I_s$  from the measured intensity of both sample and cell  $I_{sc}^e$  and empty cell  $I_c^e$  one has to perform corrections for self absorption in sample and cell. In the following I will outline the theoretical considerations and principle calculations as given in detail in the *SQW* manual [79].

$I_{sc}^e$  can be expressed in terms of the double differential cross section  $\frac{d^2\sigma}{d\Omega dE} = \frac{1}{h} \frac{d^2\sigma}{d\Omega d\omega}$  (Eq. 2.7) and the instrumental resolution function  $R(Q, \omega - \omega')$ :

$$\begin{aligned} I_{sc}^e(Q, \omega) &= \frac{n_s}{A_s} \left( \int \frac{d^2\sigma_s}{d\Omega d\omega} R(Q, \omega - \omega') d\omega' \right) \int_s T_{sc}^i(\mathbf{x}, E_i) \cdot T_{sc}^f(\mathbf{x}, E_f, Q) d\mathbf{x} \\ &+ \frac{n_c}{A_s} \left( \int \frac{d^2\sigma_c}{d\Omega d\omega} R(Q, \omega - \omega') d\omega' \right) \int_c T_{sc}^i(\mathbf{x}, E_i) \cdot T_{sc}^f(\mathbf{x}, E_f, Q) d\mathbf{x} \end{aligned} \quad (\text{A.10})$$

$A_s$ ,  $n$  and  $z$  denote the illuminated sample area, number density of scatterers and path length respectively. Subscript  $s$  and  $c$  stand for sample and can. The measured intensity  $I_{sc}^e$  depends on the probability  $T_{sc}^i(\mathbf{x}, E_i)$  for an incoming neutron with energy  $E_i$  to reach the point  $\mathbf{x}$  without scattering nor absorption. In analogy  $T_{sc}^f(\mathbf{x}, E_f, Q)$  is the probability that the neutron, now with energy  $E_f$ , leaves the sample without further interaction into direction  $2\theta^3$ . The integration has to be performed over the illuminated volume; in Eq. A.10 we split it into a part concerning the can and one concerning the sample itself.

$$I_{sc}^e(Q, \omega) = A_{s,sc} \cdot I_s(Q, \omega) + A_{c,sc} \cdot I_c(Q, \omega) \quad (\text{A.11})$$

---

<sup>3</sup>In the case of BS  $k_i \approx k_f$  and  $Q \approx 2k_i \sin(\theta)$

where  $A_{s,sc}$  and  $A_{c,sc}$  are defined as follows:

$$\begin{aligned} A_{s,sc} &= \frac{1}{A_s z_s} \int_s T_{sc}^i(\mathbf{x}, E_i) \cdot T_{sc}^f(\mathbf{x}, E_f, Q) d\mathbf{x} \\ A_{c,sc} &= \frac{1}{A_s z_c} \int_c T_{sc}^i(\mathbf{x}, E_i) \cdot T_{sc}^f(\mathbf{x}, E_f, Q) d\mathbf{x} \end{aligned} \quad (\text{A.12})$$

The measured intensity  $I_c^e$  from the empty sample cell is described in the same way:

$$I_c^e(Q, \omega) = A_{c,c} \cdot I_c(Q, \omega) \quad (\text{A.13})$$

with:

$$A_{c,c} = \frac{1}{A_s z_c} \int_c T_c^i(\mathbf{x}, E_i) \cdot T_c^f(\mathbf{x}, E_f, Q) d\mathbf{x} \quad (\text{A.14})$$

Combining Eqs. A.10 and A.13 the theoretical intensity from the sample alone can now be expressed in terms of measured intensities and the volume integrals (Eqs. A.12 and A.14):

$$I_s(Q, \omega) = A_1 \cdot I_{sc}^e(Q, \omega) - A_2 \cdot I_c^e(Q, \omega) \quad (\text{A.15})$$

with the sample geometry dependent Paalman-Pings absorption coefficients  $A_1$  and  $A_2$  [160]:

$$A_1 = \frac{1}{A_{s,sc}}, \quad A_2 = \frac{A_{c,sc}}{A_{c,c} \cdot A_{s,sc}} \quad (\text{A.16})$$

*SQW* allows to perform the corrections for flat and cylindrical sample holders. The explicit calculation of the scattering angle dependent Palmann-Pings coefficients for these two sample geometries can be found in [79].

## A.4. Correction macro for IN5 data

```

Lamp-Correction Macro for IN5 -data
-----
RDSET, inst="NexuS"
RDSET, base="Current Path"
-----
t1 = 0.886      ; transmission of sample
t2 = 0.943      ; transmission of background sample
-----
load sample and background data:
-----
w1 = rdun('tof_59787_59789_inorm_LAMP.hdf') ; Fin1_8A_270K
w11 = rdun('tof_59835_59838_inorm_LAMP.hdf') ; Fin2_8A_270K
load empty cell
-----
w2=rdun('tof_59811_59815_inorm_LAMP.hdf') ; empty_8A_300K
-----
Remove bad spectra from sample data
-----
w1 = remove_spectra(w1,BadSpectra=1,80,372,384)
-----
Remove bad spectra from empty cell data
-----
w2 = remove_spectra(w2,BadSpectra=1,80,372,384)
-----
Remove bad spectra from background sample data
-----
w11 = remove_spectra(w11,BadSpectra=1,80,372,384)
-----
Subtract empty cell from sample
-----
t = 0.886      & e1 = sqrt(e1^2 + (t*e2)^2)
w1 = w1 - t*w2      & e1 = sqrt(e1^2 + (t*e2)^2)
-----
Subtract empty cell from background sample
-----
t=0.943
w11 = w11 - t*w2      & e11 = sqrt(e11^2 + (t*e2)^2)
-----
Corrections for usual detection efficiency, background
Detectors similar to IN6 (and all the same type)
-----
RDSET,inst="IN6"
w1 = corrfct(w1,/deleff,/background,window=20)
w11 = corrfct(w11,/deleff,/background,window=20)
RDSET,inst="IN5"
-----
Self-attenuation/self-shielding corrections for data
-----
data = H2O + d-AOT + d-oil
-----
w12 =
salfcorr(w11,thick=1,0,angle=135,0,sigma_a=0,158,sigma_s=119.6,rho=0.96,Mass=95,/verbose)
w2 =
salfcorr(w1,thick=1,0,angle=135,0,sigma_a=0,063,sigma_s=98.2,rho=0.97,Mass=95,/verbose)
x2 = x1 ; Back to channels instead of energies
-----
Normalise to the vanadium
-----
absorption correction for Vana is done by running the same before with V as sample
store into w40 after that
w3 = vnorm(w2,w40)
w13 = vnorm(w12,w40)
w14=w3-w13
-----
Transform in energy (to elastic peak of Vanadium!!)
-----
w4 = 12e(w14,w40)
-----
Group into n spectra with constant Q and Q-spacing = 0.05 1/Å,
take data > 10meV, swap energy and Q
-----
w5=sqw_rebin(w4,dQ=<Q>, Emin=<Emin>/neg, angles[/,pos, angles[/,all, angles])
w5=sqw_rebin(w4,dQ=0.05, Emin=-10/pos, angles,/swap, QE)
-----
Rebin energy, energy step: 0.008 meV, Emin = -5 meV
-----
w6 = energy_rebin(w5,de = 0.008, emin = -5,0/force)
-----
Write data in Inx-Format
-----
write_lamp, "In1_2_270K.dat", w = 6,format = "Inx"
-----
w34 = w6
print, "data sample in W34."

```

Figure A.2.: Exemplary *Lamp* correction macro for IN5 data. Explicatory comments are marked in blue; actual commands are black.

## A.5. Sticky hard sphere structure factor

The so-called Baxter structure factor describes the inter-particle structure factor  $S(Q)$  for a hard sphere fluid with a narrow attractive well of width  $\Delta$  [91]. The interaction potential  $u(x)$  is given by:

$$u(x) = \begin{cases} \infty & x < 2R \\ -u_0 & 2R < x < 2R + \Delta \\ 0 & x > 2R + \Delta \end{cases} \quad (\text{A.17})$$

where  $R$  denotes the "hard" radius of the sphere. The strength of attractive interaction is described in terms of "stickiness"  $\tau$ :

$$\tau = \frac{1}{12 \cdot \epsilon} \exp\left(\frac{u_0}{k_b T}\right) \quad (\text{A.18})$$

which is a function of the perturbation parameter  $\epsilon$ :

$$\epsilon = \frac{\Delta}{\Delta + 2 \cdot R} \quad (\text{A.19})$$

and the depth of the attractive potential square well  $u_0$  (in units of  $k_b T$ ). The smaller  $\tau$  the stronger the attraction.

A perturbative solution of the Percus-Yevick closure is used to calculate the dimensionless structure factor  $S(Q)$  [88,92]. In practice the perturbation parameter  $\epsilon$  has to be held fixed between 0.01 and 0.1 and only  $\tau$  is varied by the fitting procedure.

Defining the following parameters:  $R$  as the total droplet radius (core + shell),  $\phi$  as the droplet volume fraction,  $\epsilon$  as the perturbation parameter and  $\tau$  as the stickiness parameter the structure factor  $S(Q)$  is calculated to be:

$$S(Q) = \frac{1}{a^2 + b^2} \quad (\text{A.20})$$

with functions  $a$  and  $b$  calculated according to:

$$\eta = \frac{\phi}{(1 - \epsilon)^3} \quad (\text{A.21})$$

$$\sigma = 2 \cdot R \quad (\text{A.22})$$

$$A = \frac{\sigma}{1 - \epsilon} = \frac{2 \cdot R}{1 - \epsilon} \quad (\text{A.23})$$

$$(\text{A.24})$$

$$q_a = \frac{\eta}{12} \quad (\text{A.25})$$

$$q_b = -\left(\tau + \frac{\eta}{1-\eta}\right) \quad (\text{A.26})$$

$$q_c = \frac{1+\eta/2}{(1-\eta)^2} \quad (\text{A.27})$$

$$P = q_b^2 - 4 \cdot q_a \cdot q_c \quad (\text{A.28})$$

$$\lambda = \frac{-q_b \pm \sqrt{P}}{2 \cdot q_a} \quad (\text{A.29})$$

$$\mu = \lambda \cdot \eta \cdot (1-\eta) \quad (\text{A.30})$$

$$\alpha = \frac{1+2 \cdot \eta - \mu}{(1-\eta)^2} \quad (\text{A.31})$$

$$\beta = \frac{\mu - 3 \cdot \eta}{2 \cdot (1-\eta)^2} \quad (\text{A.32})$$

$$q_v = x \quad (\text{A.33})$$

$$\kappa = q_v \cdot A \quad (\text{A.34})$$

$$d_s = \sin(\kappa) = \sin(q_v \cdot A) \quad (\text{A.35})$$

$$d_c = \cos(\kappa) = \cos(q_v \cdot A) \quad (\text{A.36})$$

$$a_1 = \frac{(d_s - \kappa \cdot d_c) \cdot \alpha}{\kappa^3} \quad (\text{A.37})$$

$$a_2 = \frac{\beta \cdot (1 - d_c)}{\kappa^2} \quad (\text{A.38})$$

$$a_3 = \frac{\lambda \cdot d_s}{12 \cdot \kappa} \quad (\text{A.39})$$

$$a = 1 + 12 \cdot \eta \cdot (a_1 + a_2 - a_3) \quad (\text{A.40})$$

$$b_1 = \alpha \cdot \left( \frac{1}{2\kappa} - \frac{d_s}{\kappa^2} + \frac{1-d_c}{\kappa^3} \right) \quad (\text{A.41})$$

$$b_2 = \beta \cdot \left( \frac{1}{\kappa} - \frac{d_s}{\kappa^2} \right) \quad (\text{A.42})$$

$$b_3 = \frac{\lambda}{12} \cdot \left( \frac{1-d_c}{\kappa} \right) \quad (\text{A.43})$$

$$b = 12 \cdot \eta \cdot (b_1 + b_2 - b_3) \quad (\text{A.44})$$

## A.6. SANS data and fits for $T$ -variation

On the next pages we show additional spectra and fits for the temperature dependent SANS experiments on w/o microemulsions with  $0 < \omega \leq 12$  discussed in section 3.5. Showing every single measured spectrum would go beyond the scope of this work as in total about 500 data sets have been obtained. We limit ourselves to a selection of spectra at 6 relevant temperatures per sample. Figures A.3 to A.6 show SANS data obtained upon cooling, see Tab. 3.2 for a listing of the sample compositions. The solid lines correspond to fits with the formfactor plus structure factor model explained in section 3.1.

Resulting fit parameters for high ( $T = 290$  K), average ( $T = 260$  K) and low temperatures ( $T = 230$  K) are given in Tab. A.3.

Table A.3.: Fit results for D<sub>2</sub>O/AOT/oil microemulsion samples T1, T2, T3 and T4 at three different temperatures. In the first column the oil (hep = heptane-d16, tol = toluene-d8) and  $\omega$  of the sample are given.  $R_c$  denotes the core radius,  $d$  is the shell thickness (AOT-tail), and  $p$  the polydispersity. The errors of the fit are of the order of the precision of the values given in the table.

sample	$T = (290 \pm 1)$ K			$T = (260 \pm 1)$ K			$T = (230 \pm 1)$ K		
	$R_c$ (Å)	$d$ (Å)	$p$ (%)	$R_c$ (Å)	$d$ (Å)	$p$ (%)	$R_c$ (Å)	$d$ (Å)	$p$ (%)
T1 (hep, 12)	19.2	11.0	17.1	19.3	11.7	17.4	6.4	13.0	10.2
T2 (hep, 5)	9.7	11.7	13.1	9.7	12.1	13.3	7.7	12.4	13.1
T3 (tol, 8)	11.9	12.4	16.3	12.0	12.6	16.8	5.4	11.1	10.1
T4 (tol, 3)	6.8	12.5	12.2	6.9	12.8	12.1	6.4	12.5	13.4

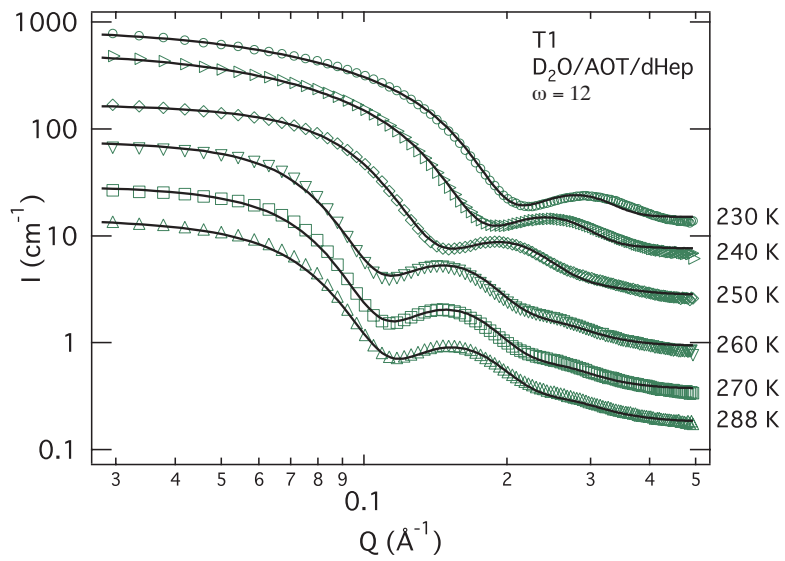


Figure A.3.: Temperature evolution of the SANS intensity of sample T1. Solid lines are fits to the form factor plus structure factor model as explained in section 3.1.

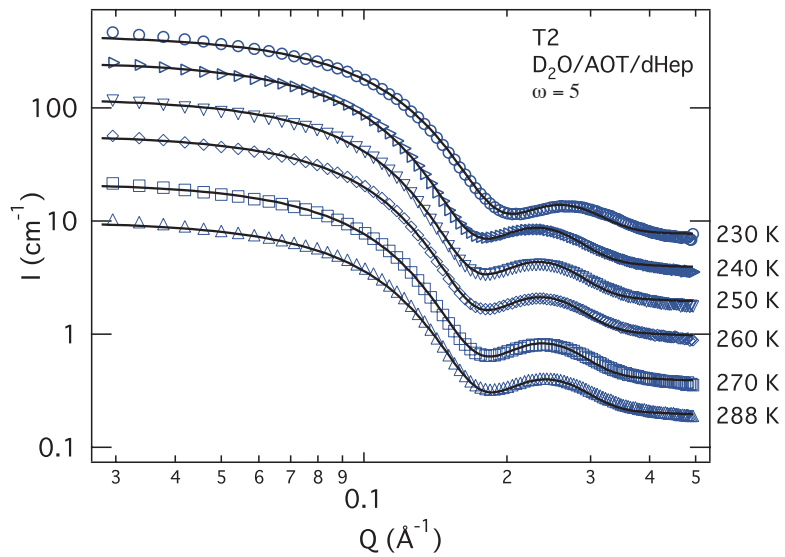


Figure A.4.: Temperature evolution of the SANS intensity of sample T2. Solid lines are fits to the form factor plus structure factor model as explained in section 3.1.



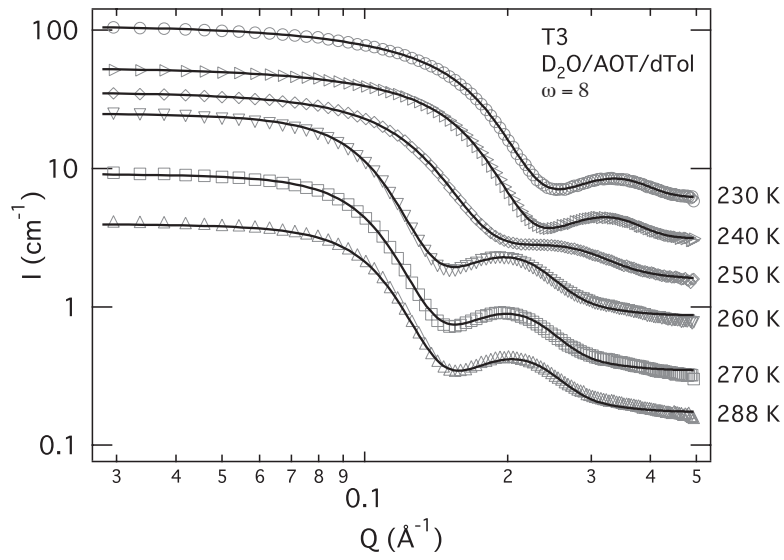


Figure A.5.: Temperature evolution of the SANS intensity of sample T3. Solid lines are fits to the form factor plus structure factor model as explained in section 3.1.

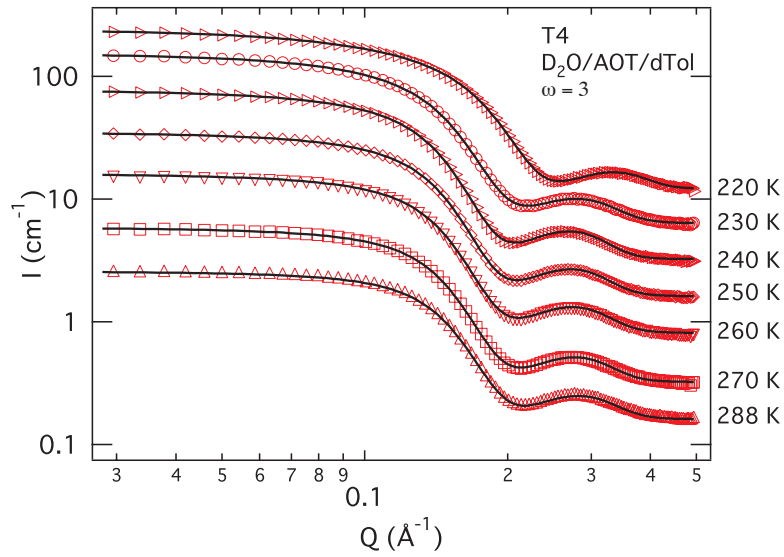


Figure A.6.: Temperature evolution of the SANS intensity of sample T4. Solid lines are fits to the form factor plus structure factor model as explained in section 3.1.

## A.7. TOF data and fits

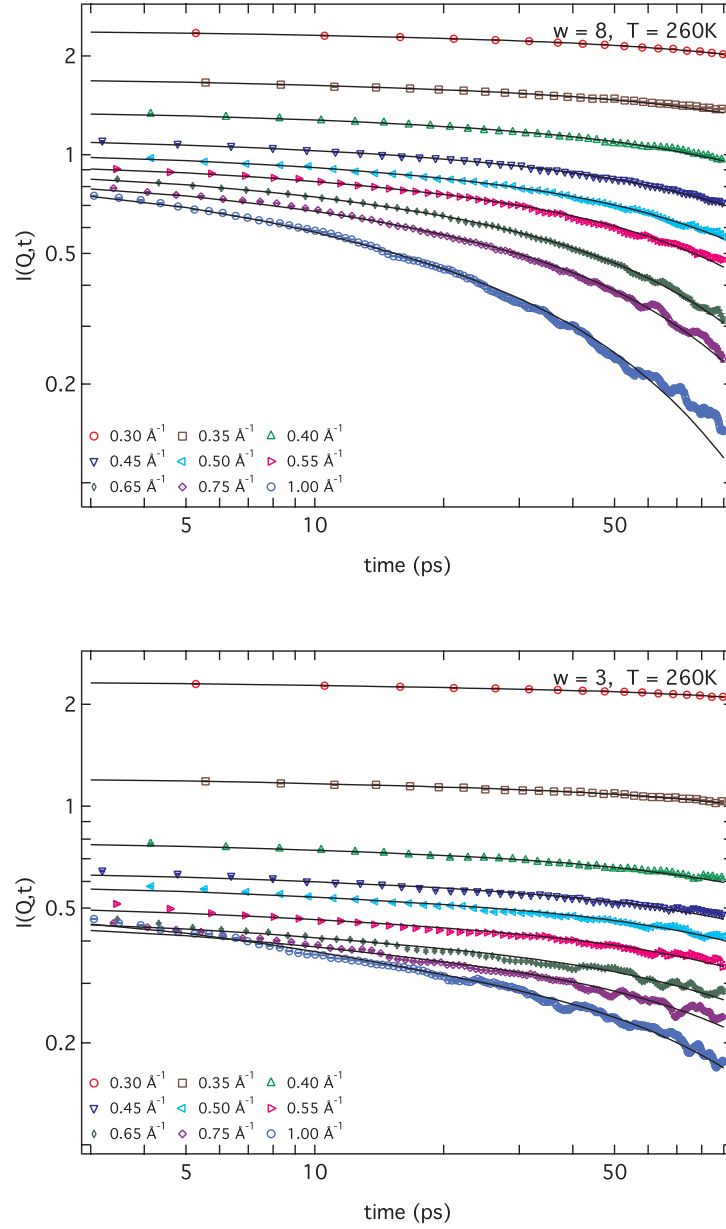


Figure A.7.: Intermediate scattering function  $I(Q,t)$  for water in big and small droplets at  $T = 260$  K. Lines are fits to Eq. 6.16 with fixed rotational diffusion coefficient  $D_R = 0.061 \text{ ps}^{-1}$ .

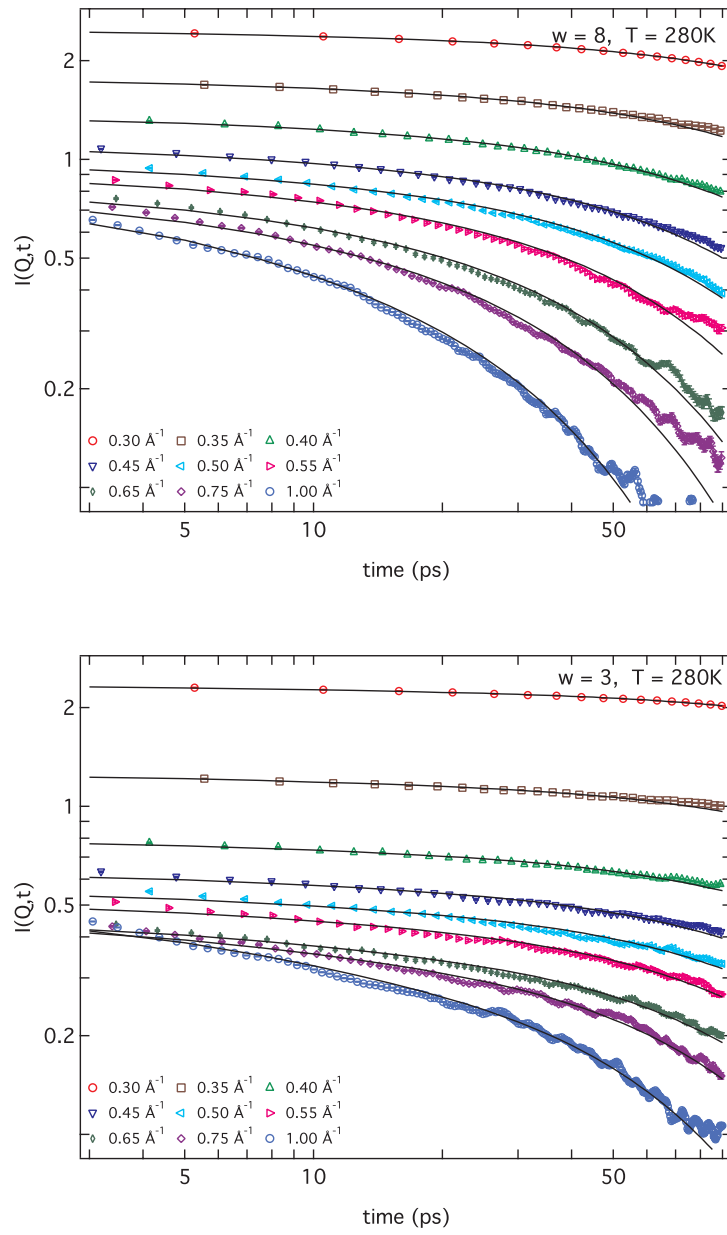


Figure A.8.: Intermediate scattering function  $I(Q,t)$  for water in big and small droplets at  $T = 280$  K. Lines are fits to Eq. 6.16 with fixed rotational diffusion coefficient  $D_R = 0.078 \text{ ps}^{-1}$ .

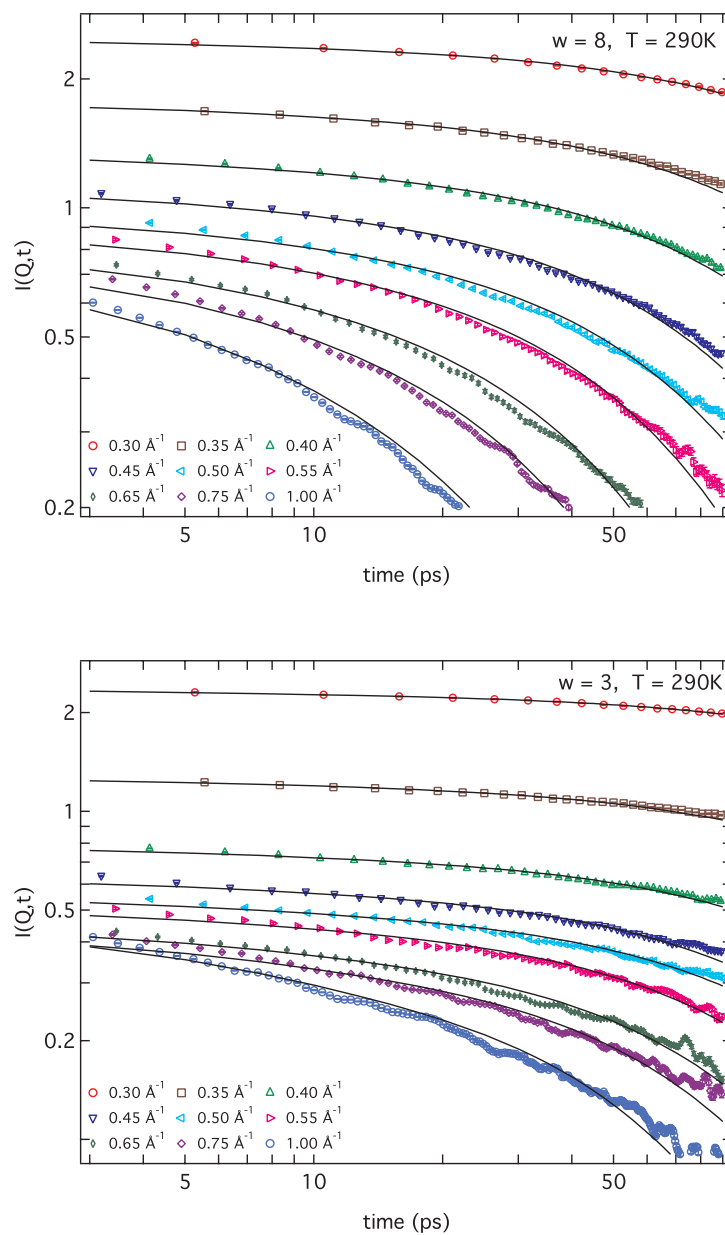


Figure A.9.: Intermediate scattering function  $I(Q, t)$  for water in big and small droplets at  $T = 290$  K. Lines are fits to Eq. 6.16 with fixed rotational diffusion coefficient  $D_R = 0.088$  ps $^{-1}$ .

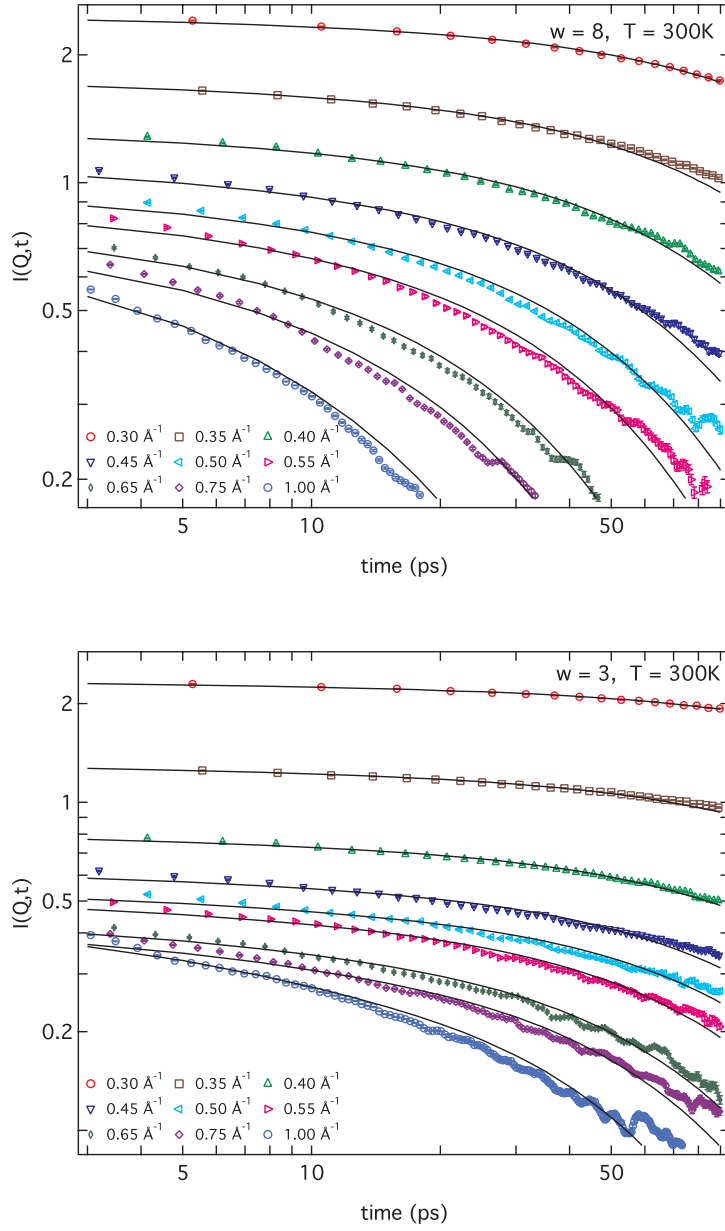


Figure A.10.: Intermediate scattering function  $I(Q, t)$  for water in big and small droplets at  $T = 300\text{ K}$ . Lines are fits to Eq. 6.16 with fixed rotational diffusion coefficient  $D_R = 0.098\text{ ps}^{-1}$ .

## A.8. Structural characterization of PEO<sub>3000</sub>

In chapter 7 we discuss the effect of PEO addition on structure and dynamics of a w/o droplet microemulsion. In order to obtain a knowledge about the dimensions of PEO in D<sub>2</sub>O we have performed a SANS study on the D11 diffractometer; experimental details can be found in 3.2. Characteristics of PEO (hydrophilic homo-polymer) are listed in Tab. A.4:

Table A.4.: Characteristics of polyethyleneoxide (PEO)<sup>4</sup>.  $n$  denotes the polymerization number.

	PEO <sub>3000</sub>
molecular formula	C <sub>2n+2</sub> H <sub>4n+6</sub> O <sub>n+2</sub>
molecular mass $M$ (g/mol)	(44n + 62)
density $\rho$ (g/cm <sup>3</sup> )	1.13
scattering length density $\rho_{coh}$ ( $\cdot 10^{-14}$ cm <sup>-2</sup> )	0.64

The absolute scattering intensity  $I(Q)$  of a Gaussian polymer chain is proportional to the Debye structure factor  $D(Q)$ :

$$I(Q) = \underbrace{\phi_{pol}(\Delta\rho)^2 n v_m}_{=A} \cdot \underbrace{\frac{2(e^{-(QR_g)^2} + (QR_g)^2 - 1)}{(QR_g)^4}}_{=D(QR_g)} + I_{inc} \quad (\text{A.45})$$

with  $R_g$  being the radius of gyration of the polymer chain,  $\phi_{pol}$  the volume fraction of polymer,  $\Delta\rho$  the scattering contrast between polymer and solution,  $n$  the polymerization number and  $v_m$  the volume of a monomer.  $I_{inc}$  denotes the incoherent flat background. This expression is only valid for a dilute solution with the volume fraction of polymer smaller than the so called overlap concentration:  $\phi_{pol} < \phi_{pol}^*$ .  $\phi_{pol}^*$  of PEO<sub>3000</sub> has been calculated from the polymerization number  $n$  to be  $\phi_{pol}^* \sim n^{-\frac{4}{5}} = 3.4\%$ . The scattering from three dilute solutions of PEO<sub>3000</sub> in D<sub>2</sub>O is shown in Fig. A.11. Solid lines are fits to Eq. A.45, parameters resulting from the fit are listed in Tab. A.5. Polydispersity of the chains is not considered, also water is not a theta solvent but a good solvent around room temperature [161].

By extrapolation to zero polymer concentration,  $\phi_{pol} = 0$ , we find a radius of gyration of  $R_g = (19.0 \pm 0.2)$  Å, see Fig. A.11. This value is slightly smaller than calculated according to literature [162, 163] :

$$R_g/\text{\AA} = 0.215 \cdot M_w^{0.583 \pm 0.031} = (22.9 \pm 6) \quad (\text{A.46})$$

$$R_g/\text{\AA} = (0.0408 \cdot M_w^{1.16 \pm 0.01})^{1/2} = (21.0 \pm 0.9) \quad (\text{A.47})$$

From the proportionality constant  $A$  in Eq. A.45 we estimate the molar volume  $V_{PEO}$  of one chain of PEO<sub>3000</sub> in D<sub>2</sub>O  $\Delta\rho = 5.74 \cdot 10^{10} \text{ cm}^{-2}$ , results for  $V_{PEO}$  are listed in Tab. A.5. We find a smaller chain volume  $V_{PEO}$  than calculated from density and molecular weight:  $V_{th} = \frac{M_w}{\rho \cdot N_A} \approx 4.4 \cdot 10^{-21} \text{ cm}^3$ . The origin of the PEO<sub>3000</sub> polymer and further characteristics like polydispersity are unknown therefore we rely on the parameters determined by SANS.

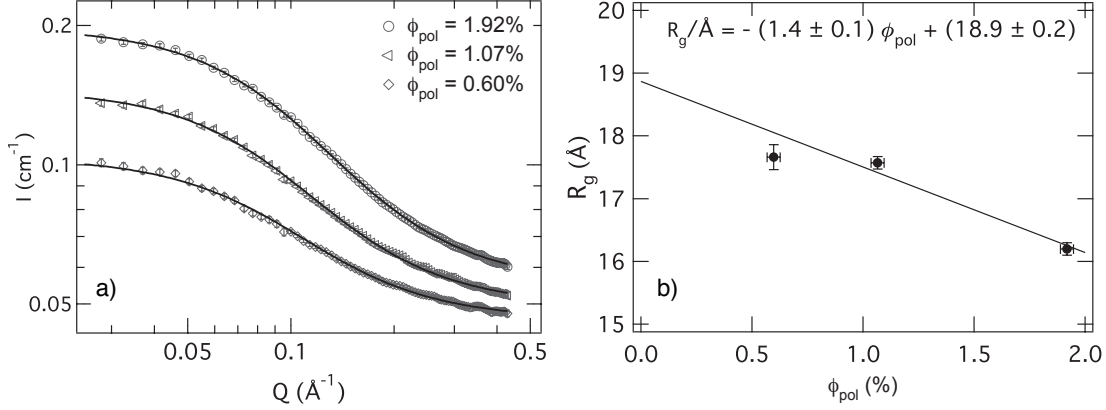


Figure A.11.: Scattering of varying concentration  $\phi_{pol}$  of PEO<sub>3000</sub> dissolved in D<sub>2</sub>O at  $T \approx 288 \text{ K}$ ; the errors are smaller than symbols. Solid lines are fits to Eq. A.45. Parameters resulting from the fit are listed in Tab. A.5.

Table A.5.: Summary of the fitting results for PEO<sub>3000</sub> in D<sub>2</sub>O, shown in figure A.11.  $R_g$  denotes the radius of gyration of the PEO-chain,  $A$  is the proportionality constant as defined in equation A.45. The error  $A$  was estimated to be 20% of  $A$  (corresponding to uncertainty of absolute intensity), this value is about 10 times bigger than the fit error of  $A$ .  $V_{PEO}$  was calculated from  $A$  using Eq. A.45.

$\phi_{pol}(\%)$	$R_g (\text{Å})$	$A (\text{cm}^{-1})$	$V_{PEO} (10^{-21} \text{cm}^3)$
$0.60 \pm 0.03$	$17.7 \pm 0.2$	$0.058 \pm 0.012$	$2.9 \pm 0.6$
$1.07 \pm 0.03$	$17.6 \pm 0.1$	$0.096 \pm 0.019$	$2.7 \pm 0.6$
$1.92 \pm 0.03$	$16.2 \pm 0.1$	$0.143 \pm 0.029$	$2.3 \pm 0.5$





# Bibliography

- [1] P. BALL, *Nature* **452**, 291 (2008/03/20/print).
- [2] D. C. STEYTLER, J. C. DORE, and C. J. WRIGHT, *J. Phys. Chem.* **87**, 2558 (1983).
- [3] A. SCHREIBER, I. KETELSEN, and G. FINDENEGG, *Phys. Chem. Chem. Phys.* **3**, 1185 (2001).
- [4] M ROVERE, editor, *J. Phys.: Condensed Matter* **16** (2004).
- [5] E. MEYER, *Protein Sci.* **1**, 1543 (1992).
- [6] L. ALDRIDGE, H. BORDALLO, and A. DESMEDT, *Physica B: Condensed Matter* **350**, E565 (2004).
- [7] E. FRATINI, S.-H. CHEN, P. BAGLIONI, and M. BELLISSENT-FUNEL, *J. Phys. Chem. B* **106**, 158 (2002).
- [8] I. BROVCHENKO and A. OLENIKOVA, editors, *Interfacial and confined water*, Elsevier, 2008.
- [9] L. LIU, C. MOU, C. YEN, and S.-H. CHEN, *J. Phys.: Condens. Matter* **16**, S5403 (2004).
- [10] N. MALIKOVA, A. CADÉNE, V. MARRY, E. DUBOIS, P. TURQ, J.-M. ZANOTTI, and S. LONGEVILLE, *Chem. Phys.* **317**, 226 (2005).
- [11] E. MAMONTOV, C. BURNHAM, S.-H. CHEN, A. MORAVSKY, C. LOONG, N. DE SOUZA, and A. KOLESNIKOV, *J. Chem. Phys.* **124**, 194703 (2006).
- [12] B. FRICK, H. BÜTTNER, and R. ZORN, editors, *Proceedings of the International Workshop on Dynamics in Confinement, Journal de Physique IV* **10**(PR7), 2000.
- [13] B. FRICK, M. KOZA, and R. ZORN, editors, *Proceedings of the second International Workshop on Dynamics in Confinement, Eur. Phys. J. E* **12**(1), 2003.

- [14] M. KOZA, B. FRICK, and R. ZORN, editors, *Proceedings of the 3rd International Workshop on Dynamics in Confinement*, *Eur. Phys. J. Special Topics* **141**(4), 2007.
- [15] L. WANG, F. HE, and R. RICHERT, *Phys. Rev. Lett.* **92**, 095701 (2004).
- [16] M. KOTLARCHYK, S. H. CHEN, and J. HUANG, *J. Phys. Chem* **86**, 3273 (1982).
- [17] M. KOTLARCHYK, S. H. CHEN, J. HUANG, and M. KIM, *Phys. Rev. A* **29**, 2054 (1984).
- [18] S.-H. CHEN, J. ROUCH, F. SCIORTINO, and P. TARTAGLIA, *J. Phys.: Condens. Matter* **6**, 10855 (1994).
- [19] M. VAN DIJK, J. JOOSTEN, Y. LEVINE, and D. BEDEAUX, *J. Phys. Chem.* **93**, 2506 (1989).
- [20] S. H. CHEN, *Ann. Rev. Phys. Chem.* **37**, 351 (1986).
- [21] I. GRILLO, *Soft-Matter Characterization*, chapter 13: Small-Angle Neutron Scattering and Applications in Soft Condensed Matter, Springer, 2008.
- [22] M. BEE, *Quasielastic Neutron Scattering: Principles and Applications in Solid State Chemistry, Biology and Materials Science*, Adam Hilger, 1988.
- [23] G. D. M BELLETETE, M LACHAPELLE, *J. Phys. Chem.* **94**, 7642 (1990).
- [24] T. HOAR and J. SCHULMAN, *Nature* **152**, 102 (1943).
- [25] K. HOLMBERG, *Surfactants and Polymers in Aqueous Solution*, Wiley, 2003.
- [26] C. STUBENRAUCH, editor, *Microemulsions - Background, New Concepts; Applications, Perspectives*, Wiley, 2009.
- [27] I. HAMLEY, *Introduction to soft matter*, Wiley, 2000.
- [28] T. DE and A. MAITRA, *Adv. Colloid Interface Sci.* **59**, 95 (1995).
- [29] B. TAMAMUSHI and N. WATANABE, *Colloid & Polymer Sci.* **258**, 174 (1980).
- [30] M. ZULAUF and H.-F. EICKE, *J. Phys. Chem.* **83**, 480 (1979).
- [31] L. ARLETH and J. S. PEDERSEN, *Phys. Rev. E* **63**, 061406 (2001).
- [32] H. SETO, M. NAGAO, Y. KAWABATA, and T. TAKEDA, *J. Chem. Phys.* **115**, 9496 (2001).

- 
- [33] T. BLOCHOWICZ, C. GÖGELEIN, T. SPEHR, M. MÜLLER, and B. STÜHN, *Phys. Rev. E* **76**, 041505 (2007).
- [34] A. MAITRA, *J. Phys. Chem* **88**, 5122 (1984).
- [35] G. SCOTT and D. KILGOUR, *J. Phys. D.* **2**, 863 (1969).
- [36] M. HIRAI, R. KAWAI-HIRAI, H. IWASE, Y. KAWABATA, and T. TAKEDA, *Appl. Phys. A* **74**, 1254 (2002).
- [37] H. STAMATIS, A. XENAKIS, and F. KOLISIS, *Biotech. Adv.* **17**, 293 (1999).
- [38] N. T. HUNT, A. A. JAYE, and S. R. MEECH, *Chem. Phys. Lett.* **416**, 89 (2005/11/29/).
- [39] M. PILENI, *J. Phys. Chem.* **97**, 6961 (1993).
- [40] N. NUCCI and J. VANDERKOOI, *J. Phys. Chem. B* **109**, 18301 (2005).
- [41] G. ONORI and A. SANTUCCI, *J. Phys. Chem.* **97**, 5430 (1993).
- [42] D. CHRISTOPHER, J. YARWOOD, P. BELTON, and B. HILLS, *J. Colloid Interface Sci.* **152**, 465 (1992).
- [43] D. MOILANEN, E. FENN, D. WONG, and M. FAYER, *J. Chem. Phys.* **131**, 014704 (2009).
- [44] D. MOILANEN, E. FENN, D. WONG, and M. FAYER, *J. Phys. Chem. B* **113**, 8560 (2009).
- [45] H. MACDONALD, B. BEDWELL, and E. GULARI, *Langmuir* **2**, 704 (1986).
- [46] A. DOKTER, S. WOUTERSEN, and H. BAKKER, *Phys. Rev. Lett.* **94**, 178301 (2005).
- [47] A. DOKTER, S. WOUTERSEN, and H. BAKKER, *Proc. Natl. Acad. Sci.* **103**, 15355 (2006).
- [48] I. PILETIC, D. MOILANEN, D. SPRY, N. LEVINGER, and M. FAYER, *J. Phys. Chem. A* **110**, 4985 (2006).
- [49] M. WONG, J. THOMAS, and T. GRÄTZEL, *J. Am. Chem. Soc.* **98**, 2391 (1976).
- [50] C. A. MUNSON, G. A. BAKER, S. N. BAKER, and F. V. BRIGHT, *Langmuir* **20**, 1551 (2004).
- [51] R. RITER, D. WILLARD, and N. LEVINGER, *J. Phys. Chem. B* **102**, 2705 (1998).

- [52] P. MORAN, G. BOWAMKER, and R. COONEY, *Langmuir* **11**, 738 (1995).
- [53] H.-S. TAN, I. PILETIC, R. RITER, N. LEVINGER, and M. FAYER, *Phys. Rev. Lett.* **94**, 057405 (2005).
- [54] G. CARLSTRÖM and B. HALLE, *J. Phys. Chem.* **93**, 3287 (1989).
- [55] H. HAUSER, G. HAERING, A. PANDE, and P. LUISI, *J. Phys. Chem.* **93**, 7869 (1989).
- [56] A. SIMORELLIS, W. VANHORN, and P. FLYNN, *J. Am. Chem. Soc.* **128**, 5082 (2006).
- [57] B. BARUAH, L. SWAFFORD, D. CRANS, and N. LEVINGER, *J. Phys. Chem. B* **112**, 10158 (2008).
- [58] B. BARUAH, J. RODEN, M. SEDGWICK, N. CORREA, D. CRANS, and N. LEVINGER, *J. Am. Chem. Soc.* **128**, 12758 (2006).
- [59] G. MUDZHIKOVA and E. BRODSKAYA, *Coll. J.* **68**, 800 (2006).
- [60] G. MUDZHIKOVA and E. BRODSKAYA, *Coll. J.* **68**, 738 (2006).
- [61] E. BRODSKAYA and G. MUDZHIKOVA, *Mol. Phys.* **104**, 3635 (2006).
- [62] S. ABEL, F. STERPONE, S. BANDYOPADHYAY, and M. MARCHI, *J. Phys. Chem. B* **108**, 19458 (2004).
- [63] M. R. HARPHAM, B. M. LADANYI, N. E. LEVINGER, and K. W. HERWIG, *J. Phys. Chem.* **121**, 7855 (2004).
- [64] M. POMATA, D. LARIA, M. SKAF, and M. ELOLA, *J. Chem. Phys.* **129**, 244503 (2008).
- [65] J. FAEDER and B. M. LADANYI, *J. Phys. Chem. B* **104**, 1033 (2000).
- [66] M. D'ANGELO, D. FIORETTO, G. ONORI, L. PALMIERI, and A. SANTUCCI, *Phys. Rev. E* **54**, 993 (1996).
- [67] D. MITTLEMAN, M. NUSS, and V. COLVIN, *Chem. Phys. Lett.* **275**, 332 (1997).
- [68] P. FLETCHER, B. ROBINSON, and J. TABONY, *J. Chem. Soc., Faraday Trans. 1* **82**, 2311 (1986).
- [69] C. BONED, J. PEYRELASSE, and M. MOHA-OUCHANE, *J. Phys. Chem.* **90**, 634 (1986).

- 
- [70] H. TAN, I. PILETIC, and M. FAYER, *J. Chem. Phys.* **122**, 174501 (2005).
- [71] A. DOKTER, *Water in Confinement*, PhD thesis, University Amsterdam, 2008.
- [72] G. SQUIRES, *Introduction to the Theory of Thermal Neutron Scattering*, Dover Publications, 1978.
- [73] W. MARSHALL and S. LOVESEY, *Theory of Thermal Neutron Scattering: the Use of Neutrons for the Investigation of Condensed Matter*, Oxford University Press, 1971.
- [74] S. LOVESEY, *Theory of Neutron Scattering from Condensed Matter*, volume 1, Oxford Science Publications, 1984.
- [75] A. DIANOUX and G. LANDER, editors, *Neutron Data Booklet*, Old City Publishing, Philadelphia, 2003.
- [76] H. MAIER-LEIBNITZ, *Bayerische Akademie der Wissenschaften* **16**, 173 (1966).
- [77] B. ALEFELD, *Bayerische Akademie der Wissenschaften* **11**, 109 (1966).
- [78] B. FRICK, E. MAMONTOV, L. VAN EIJCK, and T. SEYDEL, *Z. Phys. Chem.* **224** (2010).
- [79] O. RANDL, *SQW - a comprehensive user manual*, Institute Laue-Langevin, 1.0 edition, 1996, ILL96RA07T.
- [80] F. RIEUTORD, *INX - program for time-of-flight data reduction*, Institute Laue-Langevin, 1.0 edition, 1990, 90RI 17T.
- [81] F. MEZEI, editor, *Neutron Spin Echo*, Springer, 1980.
- [82] A. GUINIER, *Ann. Phys. Paris* **12**, 161 (1939).
- [83] R. GHOSH, S. EGELHAAF, and A. RENNIE, *A Computing Guide for Small-Angle Scattering Experiments*, Institute Laue Langevin, 5 edition, 2006, ILL06GH05T.
- [84] T. HELLWEG, A. BRULET, and T. SOTTMANN, *Phys. Chem. Chem. Phys.* **2**, 5168 (2000).
- [85] J. TEIXEIRA, M. BELLISSENT-FUNEL, S. CHEN, and A. DIANOUX, *Phys. Rev. A* **31**, 1913 (1985).
- [86] T. SPEHR, B. FRICK, I. GRILLO, and B. STÜHN, *J. Phys.: Condensed Matter* **20**, 104204 (2008).

- [87] T. SPEHR, B. FRICK, I. GRILLO, P. FALUS, M. MÜLLER, and B. STÜHN, *Phys. Rev. E* **79**, 031404 (2009).
- [88] S. R. KLINE, *J. Appl. Cryst.* **39**, 895 (2006).
- [89] M. KOTLARCHYK and S. H. CHEN, *J. Chem. Phys.* **79**, 2461 (1983).
- [90] M. KOTLARCHYK, R. STEPHENS, and J. HUANG, *J. Phys. Chem.* **92**, 1533 (1988).
- [91] R. J. BAXTER, *J. Chem. Phys.* **49**, 2770 (1968).
- [92] S. MENON, C. MANOHAR, and K. S. RAO, *J. Chem. Phys.* **95**, 9186 (1991).
- [93] I. GRILLO, Technical Report ILL01GR08T, Institute Laue-Langevin, 2001.
- [94] T. SPEHR, Polymer-induzierte transiente Netzwerke in Wasser-in-Öl-Mikroemulsionen, Master's thesis, TU Darmstadt, 2005.
- [95] C. KITCHENS, D. BOSSEV, and C. ROBERTS, *J. Phys. Chem. B* **110**, 20392 (2006).
- [96] J. ERIKSSON and S. LJUNGGREN, *Langmuir* **11**, 1145 (1995).
- [97] X. LI, C. LOONG, P. THIYAGARAJAN, G. LAGER, and R. MIRANDA, *J. Appl. Cryst.* **33**, 628 (2000).
- [98] S. NAVE, J. EASTOE, R. K. HEENAN, D. STEYTLER, and I. GRILLO, *Langmuir* **16**, 8741 (2000).
- [99] Y. HENDRIKX, H. KELLAY, and J. MEUNIER, *Europhys. Lett.* **25**, 735 (1994).
- [100] M. NAGAO, H. SETO, M. SHIBAYAMA, and N. YAMADA, *J. Appl. Cryst.* **36**, 602 (2003).
- [101] A. LONGO, G. PORTALE, W. BRAS, F. GIANNICI, A. RUGGIRELLO, and V. LIV-ERI, *Langmuir* **23**, 11482 (2007).
- [102] P.-O. QUIST and B. HALLE, *J. Chem. Soc., Faraday Trans. 1* **84**, 1033 (1988).
- [103] C. A. ANGELL, *Ann. Rev. Phys. Chem.* **34**, 593 (1983).
- [104] L. PAULING, *Grundlagen der Chemie*, Verlag Chemie, 1973.
- [105] W. HELFRICH, *Z. Naturforsch. C* **28**, 693 (1973).
- [106] F. SICOLI, D. LANGEVIN, and L. T. LEE, *J. Chem. Phys.* **99**, 4759 (1993).
- [107] S. MILNER and S. SAFRAN, *Phys. Rev. A* **36**, 4371 (1987).

- 
- [108] S. SAFRAN, *J. Phys. Chem.* **78**, 2073 (1983).
- [109] M. GRADZIELSKI, D. LANGEVIN, and B. FARAGO, *Phys. Rev. E* **53**, 3900 (1996).
- [110] S. SAFRAN, *Phys. Rev. A* **43**, 2903 (1991).
- [111] K. SEKI and S. KOMURA, *Physica A* **219**, 253 (1995).
- [112] Y. KAWABATA, H. SETO, M. NAGAO, and T. TAKEDA, *J. Neutron. Res.* **10**, 131 (2002).
- [113] Y. KAWABATA, M. NAGAO, S. KOMURA, T. TAKEDA, D. SCHWAHN, N. YAMADA, and H. NOBUTOU, *Phys. Rev. Lett.* **92**, 056103 (2004).
- [114] J. HUANG, S. MILNER, B. FARAGO, and D. RICHTER, *Phys. Rev. Lett.* **59**, 2600 (1987).
- [115] T. HELLWEG and D. LANGEVIN, *Phys. Rev. E* **57**, 6825 (1998).
- [116] M. NAGAO and H. SETO, *Phys. Rev. E* **78**, 011507 (2008).
- [117] B. FARAGO and M. GRADZIELSKI, *J. Chem. Phys.* **114**, 10105 (2001).
- [118] B. FARAGO, J. HUANG, D. RICHTER, S. SAFRAN, and S. MILNER, *Prog. Colloid Polym. Sci.* **81**, 60 (1990).
- [119] Y. KAWABATA, H. SETO, M. NAGAO, and T. TAKEDA, *J. Chem. Phys.* **127**, 044705 (2007).
- [120] S. KOMURA and K. SEKI, *Physica A* **192**, 27 (1993).
- [121] F. SANTOS, C. N. DE CASTRO, J. DYMOND, N. DALAOUTI, M. ASSAEL, and A. NAGASHIMA, *J. Phys. Chem. Ref. Data* **35**, 1 (2005).
- [122] D. R. LIDE, editor, *CRC Handbook of Chemistry and Physics*, CRC Press, Florida, 2004.
- [123] K. HARRIS and L. WOOLF, *J. Chem. Eng. Data.* **49**, 1064 (2004).
- [124] T. HELLWEG and D. LANGEVIN, *Physica A* **264**, 370 (1999).
- [125] M. MARSILIUS, Aufbau einer Lichtstreuuanlage zur Untersuchung der Dynamik niedermolekularer Glasbildner, Master's thesis, TU Darmstadt, 2007.
- [126] S. H. CHEN, P. GALLO, F. SCIORTINO, and P. TARTAGLIA, *Phys. Rev. E* **56** (1997).
- [127] K. S. SINGWI and A. SJÖLANDER, *Phys. Rev.* **119**, 863 (1960).

- [128] V. SEARS, *Can. J. Phys.* **45**, 237 (1967).
- [129] C. MALARDIER-JUGROOT and T. HEAD-GORDON, *Phys. Chem. Chem. Phys.* **9**, 1962 (2007).
- [130] V. CRUPI, S. MAGAZU, D. MAJOLINO, P. MIGLIARDO, U. WANDERLINGH, and W. KAGUNYA, *Physica B* **979**, 241 (1998).
- [131] A. FARAONE, L. LIU, C. MOU, C. YEN, and S.-H. CHEN, *J. Chem. Phys.* **121**, 10843 (2004).
- [132] J. TABONY, A. LLOR, and M. DRIFFORD, *Colloid & Polymer Sci.* **261**, 938 (1983).
- [133] J. TABONY, *Chem. Phys. Lett.* **113**, 75 (1985).
- [134] F. ALIOTTA, M. FONTANELLA, R. LECHNER, M. PIERUCCINI, B. RUFFLE, and C. VASI, *Colloid. Polym. Sci.* **280**, 193 (2002).
- [135] M. FREDA, G. ONORI, A. PACIARONI, and A. SANTUCCI, *Phys. Rev. E* **68**, 021406 (2003).
- [136] M.-C. BELLISSENT-FUNEL, *Eur. Phys. J. E* **12**, 83 (2003).
- [137] J. TEIXEIRA, J.-M. ZANOTTI, M.-C. BELLISSENT-FUNEL, and S.-H. CHEN, *Physica B* **234-236**, 370 (2008).
- [138] J. TEIXEIRA, M.-C. BELLISSENT-FUNEL, and S.-H. CHEN, *J. Mol. Liquids* **48**, 111 (1991).
- [139] J. ROPP, C. LAWRENCE, T. C. FARRAR, and J. L. SKINNER, *J. Am. Chem. Soc.* **123**, 8047 (2001).
- [140] D. LAAGE, *J. Phys. Chem. B* **113**, 2684 (2009).
- [141] M. FREDA, G. ONORI, A. PACIARONI, and A. SANTUCCI, *Phys. Chem. Lett.* **348**, 311 (2001).
- [142] M. BELLISSENT-FUNEL, J.-M. ZANOTTI, and S.-H. CHEN, *Faraday Discussions* **103**, 281 (1996).
- [143] J.-M. ZANOTTI, M.-C. BELLISSENT-FUNEL, and S.-H. CHEN, *Phys. Rev. E* **59**, 3084 (1999).
- [144] S.-H. CHEN, C. LIAO, F. SCIORTINO, P. GALLO, and P. TARTAGLIA, *Phys. Rev. E* **59**, 6708 (1999).



- [145] G. ADAM and J. GIBBS, *J. Chem. Phys.* **28** (1965).
- [146] T. BLOCHOWICZ, E. GOUIRAND, A. FRICKE, T. SPEHR, B. STÜHN, and B. FRICK, *Chem. Phys. Lett.* **475**, 171 (2009).
- [147] P. DE GENNES, *J. Phys. Chem* **94**, 8407 (1990).
- [148] S. RADIMAN, L. FOUNTAIN, C. TOPRAKCIOGLU, A. VALLERA, and P. CHIEUX, *Prog. Colloid. Polym. Sci.* **81**, 54 (1990).
- [149] D. SCHÜBEL, O. BEDFORD, G. ILGENFRITZ, J. EASTOE, and K. HEENAN, *Phys. Chem. Chem. Phys.* **1**, 2521 (1999).
- [150] D. PAPOUTSI, P. LIANOS, and W. BROWN, *Langmuir* **9**, 663 (1993).
- [151] C. GÖGELEIN, Experimente mit Photonenkorrelationsspektroskopie an transient vernetzten Mikroemulsionen, Master's thesis, TU Darmstadt, 2005.
- [152] W. MEIER, *Langmuir* **12**, 1188 (1996).
- [153] D. SCHÜBEL and G. ILGENFRITZ, *Langmuir* **13**, 4246 (1997).
- [154] M.-J. SUAREZ, H. LEVY, and J. LANG, *J. Phys. Chem.* **97**, 9808 (1993).
- [155] S. MEHTA and S. SHARMA, *J. Colloid Interface Sci.* **296**, 690 (2006).
- [156] D. PAPOUTSI, P. LIANOS, and W. BROWN, *Langmuir* **10**, 3402 (1994).
- [157] W. MEIER, *J. Phys. Chem. B* **101**, 919 (1997).
- [158] J. BROOKS and M. CATES, *Chem. Phys.* **149**, 97 (1990).
- [159] L.-Z. HE, V. GARAMUS, B. NIEMEYER, H. HELMHOLZ, and R. WILLUMEIT, *J. Mol. Liquids* **89**, 239 (2000).
- [160] H. PAALMAN and C. PINGS, *J. Appl. Phys.* **33**, 2635 (1962).
- [161] R. COOK, H. KING, and D. PFEIFFER, *Phys. Rev. Lett.* **69**, 3072 (1992).
- [162] K. DEVANAND and J. SELSER, *Macromolecules* **24**, 5943 (1991).
- [163] S. KAWAGUCHI, G. IMAIT, J. SUZUKI, A. MIYAHARA, T. KITANOLL, and K. ITO, *Polymer* **38**, 2885 (1996).



# Lebenslauf

## Persönliche Daten

Name Spehr  
Vornamen: Tinka Luise  
Geburtsdatum: 18.06.1979  
Geburtsort: Albany (N.Y.), USA  
Nationalität: deutsch  
Familienstand: verheiratet

## Promotionsstudium, Wissenschaftliche Mitarbeit

12/2005-01/2010 Technische Universität Darmstadt  
12/2005-11/2008 Institut Laue-Langevin Grenoble

## Hochschulausbildung

11/2005 Diplom der Physik  
09/2002-07/2003 Studium der Physik, Institut National Polytechnique de Grenoble  
10/1999-11/2005 Studium der Physik, Technische Universität Darmstadt  
10/1998-08/1999 Studium der Medizin, Universität des Saarlandes

## Schulbildung

06/1998 Abitur  
08/1989-06/1989 Gymnasium: Georg-Büchner-Schule, Darmstadt  
08/1986-07/1989 Grundschule: Eichesschule, Ober-Ramstadt

## Praktische Tätigkeit

07/1998-08/1998 Krankenpflegepraktikum: Elisabethenstift, Darmstadt



## Danksagung

Ich bedanke mich bei all den Personen, die mir während der letzten Jahre mit fachlichem Rat zur Seite standen und mich bei Experimenten unterstützten.

Allen voran möchte ich meine Dankbarkeit meinen beiden Betreuern, Prof. Dr. Bernd Stühn und Dr. Bernhard Frick, gegenüber ausdrücken, die nicht nur wissenschaftlich, sondern auch menschlich in vieler Hinsicht Vorbilder für mich sind. Ich danke ihnen beiden sehr für ihr kontinuierliches Interesse an meiner Arbeit, ihre Unterstützung in jeglicher Hinsicht und ihr Vertrauen in mich. Danke, dass mir die Doktorarbeit in dieser Form ermöglicht wurde.

Ich habe das doppelte Glück, mich bei zwei Arbeitsgruppen für den freundschaftlichen Umgang und die kollegiale Zusammenarbeit bedanken zu können: bei der TOF/HR Gruppe unter der Leitung von Prof. Dr. Helmut Schober am ILL in Grenoble und bei der AG Stühn an der TU Darmstadt. Namentlich erwähnen möchte ich Martin Müller, Gustav Nyström, Emmanuel Gouirand und Robert Wipf, die aus Darmstadt nach Grenoble kamen, um mich bei Experimenten zu unterstützen und Sebastian Schramm und Dr. Thomas Blochowicz für Hilfe bei der DLS; außerdem meine Neutronen-Kollegen, die das ILL für mich zu einem traumhaften Arbeitsplatz machten: Dr. Lambert van Eijck aus dem IN16 Dream-Team, meine SANS-Lehrerin Dr. Isabelle Grillo, Dr. Marek Koza - der Fahrstuhlschreck mit viel pädagogischem Geschick, Dr. Jacques Ollivier, der bescheiden ein großartiger Diskussionspartner ist und Prof. Dr. Torsten Soldner.

Meinen liebsten Mitdoktoranden, Markus Hild und Dr. Felix Schmitt in Darmstadt und Julia Rasch, Stefan Eibl, Dr. Andreas Stadler und Jochen Krempel in Grenoble danke ich dafür, dass ich wenig geteiltes Leid und sehr viel geteilte Freude in Erinnerung behalten werde.

Außerdem danke ich Dr. Peter Falus, Dr. Bela Farago, Dr. Henrich Frielinghaus, Dr. Amir Murani, Dr. Michaela Zamponi und Dr. Jean-Marc Zanotti, die mich als Instrumentverantwortliche bei Experimenten betreuten.

Viele Menschen haben dazu beigetragen, dass Grenoble ein zweites Zuhause für mich wurde. Allen voran waren das Cosima und Bernhard Frick, mit ihren großen Herzen und ihrem für mich immer offenen Haus.

Meinen Eltern, meinen Schwestern und meinem Mann danke ich für ihre Unterstützung aus der Nähe und der Ferne und vieles mehr! Und besonders danke ich meinem Vater, der uns Töchtern das naturwissenschaftliche Interesse vermittelt hat.